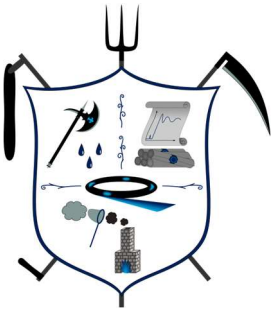

DISSERTATION

vorgelegt von:

SVEN STRÜBBE, M. SC.

Geburtsname: Sven Wendholt

INVESTIGATIONS OF NI-BASED METHANATION CATALYSTS UNDER DYNAMIC CONDITIONS VIA HARD X-RAY SPECTROSCOPY

UNIVERSITÄT PADERBORN
FAKULTÄT FÜR NATURWISSENSCHAFTEN

zur Erlangung der Würde eines

DOKTORS DER NATURWISSENSCHAFTEN (DR. RER. NAT.)

im Department Chemie

2023

Universität Paderborn
Arbeitsgruppe Prof. Dr. Matthias Bauer
Fakultät für Naturwissenschaften
Department Chemie – Anorganische Chemie
Warburger Straße 100
33098 Paderborn

Sven Strübbe:

Investigations of Ni-based methanation catalysts under dynamic conditions via hard X-ray spectroscopy.

Promotionskommission:

Prof. Dr. Jan Paradies	*Vorsitz*
Prof. Dr. Matthias Bauer	*Erstgutachter*
Prof. Dr. Mirijam Zobel	*Zweitgutachterin*
Prof. Dr. Thomas Werner	*Drittprüfer*

Tag der mündlichen Prüfung: 10.05.2023

UNIVERSITÄT PADERBORN
FAKULTÄT FÜR NATURWISSENSCHAFTEN
DEPARTMENT CHEMIE

Eidesstattliche Erklärung

Hiermit versichere ich, die vorliegende Arbeit selbständig angefertigt und keine anderen als die von mir angegebenen Hilfsmittel verwendet zu haben. Wörtliche und sinngemäße Zitate wurden als solche gekennzeichnet und die Genehmigungen zur Veröffentlichung der urheberrechtlich geschützten Publikationen wurden eingeholt.

Paderborn, den 23.03.2023 ……

Sven Strübbe

In den Wissenschaften ist viel Gewisses,
sobald man sich von den Ausnahmen nicht irremachen läßt
und die Probleme zu ehren weiß.

JOHANN WOLFGANG VON GOETHE

Abstract

Within the energy transition, the power-to-gas concept plays a crucial role in production of new energy carriers or development of alternative production routes to already known energy carriers, such as methane. To make the production of methane sustainable, carbon dioxide can be reduced with hydrogen generated from renewable energy sources. Since fluctuations in the energy flow, and consequently in hydrogen production can occur due to weather conditions, the catalyst system performance must be stable concerning this fluctuation. A promising approach for stable and highly active methanation catalysts are Ni catalysts based on the thermal decomposition of MOFs. This produces highly dispersed carbonaceous Ni pre-catalysts. However, this requires a detailed understanding of the underlying chemical mechanisms and associated electronic structures of the catalyst systems. Therefore, this work aims to establish spectroscopic methods for highly amorphous nickel-based catalyst systems within a carbon matrix based on X-ray absorption spectroscopy and X-ray emission spectroscopy. These methods provide information on the oxidation states, electronic structure and interactions, and geometric information from the pre-catalysts as well as from the activated catalysts.

Detailed analysis of the *ex-situ* catalyst precursors showed that slightly reductive conditions were sufficient to produce suitable pre-catalysts. A mixture of Ni(0) and Ni(II) encapsulated in a carbon matrix is present in all the samples investigated and a pure Ni_{fcc} structure is not achieved, allowing the assumption of particle formation. Moreover, a combination of HERFD-XANES, calculations under the application of the FEFF software package, and VtC-XES demonstrated that electronic interactions exist between the carbon matrix and the nickel centers. This does not occur by immediate, direct interaction in the first coordination environment, but by somewhat distant proximity. Furthermore, it could be shown that NiO traces are present in the catalyst precursors which show high activity in methanation. Accordingly, Ni(II)-containing species seem to have an improving effect on the structure-activity-correlation. Thus, a better understanding of these highly dispersed amorphous structures could be achieved by these findings. Building on these results, *in-situ* investigations were subsequently carried out. With regard to the activation process of the pre-catalyst, it could be shown that the temperature region which is decisive for the structural changes in the form of the decrease of a formed oxide layer can be narrowed down to a range of about 80 to 200 °C. The catalysts showed increased stability for as long as hydrogen was present in the gas atmosphere. Furthermore, an unambiguous correlation between the loss of a stabilizing carbon layer and the loss of activity could be shown. Here, a drop in the hydrogen supply was simulated in the form of three

different gas composition scenarios. The loss of the carbon layer in the case of a complete hydrogen failure was decisive for the deactivation of the catalyst system.

Kurzzusammenfassung

Innerhalb der Energiewende spielt das Power-to-Gas-Konzept eine entscheidende Rolle, um neue Energieträger zu gewinnen oder alternative Herstellungsrouten zu bereits bekannten Energieträgern, wie beispielsweise Methan, zu entwickeln. Um eine nachhaltige Methanherstellung zu realisieren, sollen Kohlenstoffdioxid und aus erneuerbaren Energien erzeugter Wasserstoff genutzt werden. Da wetterbedingt Fluktuationen im Stromnetz und daraus resultierend in der Wasserstoffproduktion entstehen können, bedarf es eines Katalysatorsystems, welches gegenüber diesen Schwankungen stabil ist. Einen vielversprechenden Ansatz stellen stabile und hochaktive Methanisierungskatalysatoren dar, die auf der thermischen Zersetzung von MOFs basieren. Dabei entstehen hochdisperse Ni-Katalysator-Vorstufen, die in einer Kohlenstoffmatrix eingebettet sind. Für ein derartiges Katalysatorsystem ist jedoch ein detailliertes Verständnis der zugrunde liegenden chemischen Mechanismen und damit einhergehender elektronischer Strukturen der Katalysatorsysteme notwendig. Ziel dieser Arbeit ist daher die Etablierung von spektroskopischen Methoden für hochamorphe nickelbasierte Katalysatorsysteme innerhalb einer Kohlenstoffmatrix unter Anwendung von Röntgenabsorptionsspektroskopie und Röntgenemissionsspektroskopie. Dadurch können Informationen über die Oxidationszustände, elektronische Wechselwirkungen und geometrische Informationen über die Präkatalysatoren und aktivierten Katalysatoren gewonnen werden.

Durch die detaillierte Analyse der *ex-situ* Katalysator-Vorstufen konnte gezeigt werden, dass leicht reduktive Bedingungen ausreichen, um geeignete Präkatalysatoren herzustellen. Jedoch wurde dabei auch deutlich, dass in allen untersuchten Proben ein Gemisch aus Ni(0) und Ni(II) vorliegt und keine pure $Ni(0)_{fcc}$ Struktur erreicht wird, was die Annahme der Partikelbildung stärkt. Außerdem konnte durch eine Kombination aus HERFD-XANES, FEFF-basierter theoretischer Rechnungen und VtC-XES eindeutig belegt werden, dass Wechselwirkungen zwischen der Kohlenstoffmatrix und den Nickelzentren stattfinden. Dies geschieht nicht durch eine direkte Wechselwirkung in der ersten Koordinationsumgebung, sondern in entfernteren Koordinationssphären. Zudem konnte dargelegt werden, dass NiO Spuren in den Präkatalysatoren vorliegen, die eine hohe Aktivität in der Methanisierung aufweisen. Dementsprechend scheinen Ni(II) Spezies einen positiven Effekt auf die Struktur-Aktivitätskorrelation zu haben. Mittels dieser Erkenntnisse konnte folglich ein erhöhtes Verständnis dieser hochdispersen, amorphen Strukturen gewonnen werden. Aufbauend auf diesen Ergebnissen wurden anschließend *in-situ* Untersuchungen durchgeführt. In Bezug auf den Aktivierungsprozess der Präkatalysatoren konnte dabei gezeigt werden, dass die Temperaturregion, die entscheidend für die strukturellen Veränderungen in Form der Abnahme einer sich gebildeten Oxidschicht ist, sich

auf einen Bereich von etwa 80 bis 200 °C eingrenzen lässt. Die Stabilität des Katalysators war deutlich erhöht, solange sich Wasserstoff in der Gasatmosphäre befand. Des Weiteren konnte ein eindeutiger Zusammenhang zwischen dem Verlust einer stabilisierenden Kohlenstoffschicht und einem Rückgang der Aktivität belegt werden. Hierbei wurde durch Veränderung der Gaszusammensetzung ein Ausfall der Wasserstoffversorgung in Form von drei verschieden Szenarien simuliert. Der Verlust der Kohlenstoffschicht bei einem vollständigen Ausfall des Wasserstoffs war dabei entscheidend für die Desaktivierung des Katalysatorsystems.

Danksagung

Meine Arbeit möchte ich mit einem Dank beginnen, einem Dank bei all jenen Menschen, die mich in dieser intensiven Zeit immerzu fachlich wie persönlich unterstützt haben.

Ein erster Dank gilt Matthias Bauer für die herzliche Aufnahme in seinen Arbeitskreis. Innerhalb eines Projektes, welches im weiten Feld der Katalyse angesiedelt ist, schenkte er mir das Vertrauen, mich in die mir bis dahin fremde Methodik der Röntgenspektroskopie einzuarbeiten. Dadurch ergab sich mir die einzigartige Möglichkeit meine im Studium entwickelte Begeisterung für die Katalyse mit einem außergewöhnlichen Messverfahren zu verbinden und zu einem anspruchsvollen Promotionsthema werden zu lassen. Durch ihn habe ich nicht nur das DESY in Hamburg – sehr gut – kennengelernt, sondern er unterstützte jede Gelegenheit meiner persönlichen Weiterbildung durch die Teilnahme an zahlreichen Konferenzen und Summer Schools in nah und fern. So durfte ich die große Welt der Wissenschaften näher erfahren, neue Kontakte knüpfen und vorherige Wegbegleiter wiedertreffen. Ich danke dir für die hervorragende Betreuung und den wertvollen Austausch.

Innerhalb des Kooperationsprojektes, in das sich mein Promotionsvorhaben eingliedert, bin ich auf ein großartiges Team getroffen. Hier möchte ich mich zunächst bei Mirijam Zobel von der Rheinisch-Westfälischen Technischen Hochschule Aachen und bei Wolfgang Kleist von der Rheinland-Pfälzischen Technischen Universität Kaiserslautern-Landau bedanken. Ihr habt die Projekttreffen neben eurem Fachwissen und eurer Erfahrung stets auch mit dem nötigen Humor bereichert.

Besonders freut es mich, dass sich Mirijam Zobel nach den Jahren der gemeinsamen Zusammenarbeit in dem Projekt bereiterklärt hat, den Abschluss meines Promotionsvorhabens nunmehr als Zweitgutachterin zu begleiten.

Zu meiner Promotionskommission zählen weiter Jan Paradies und Thomas Werner. Auch ihnen gilt mein ausdrücklicher Dank für die Übernahme des Vorsitzes und der Drittprüfung.

Ein spezieller Dank gebührt Leif Rohrbach und Nils Prinz. Als „die drei Wikinger“ – so etablierte sich schnell die Kurzform für unser Doktorandentrio – haben wir bei reichlich Kaffee und dem ein oder anderen Kaltgetränk neben all den wissenschaftlichen Rätseln auch all die großen und kleinen Fragen des Lebens ausgiebig bereden können. Mit euch war jedes Projekttreffen, jede Konferenz, jede Messzeit und jeder Zoomcall am Ende doch immerzu ein unglaublicher Spaß. In euch habe ich nicht nur die besten Projektpartner, sondern zwei gute Freunde gewonnen.

An alle aktuellen und ehemaligen Kolleginnen und Kollegen aus dem AK Bauer möchte ich einen Dank richten für die lebendige und hervorragende Arbeitsatmosphäre, konstruktive Diskussionen und hilfreiche Anregungen während und nach der Arbeitszeit. Es ist mir eine große Freude Teil der „Bauer-Ranger“ sein zu dürfen.

Besonders danken möchte ich meiner ersten Bürokollegin Anke Schoch. Neben der Betreuung in allen organisatorischen Angelegenheiten war es mir immer wieder ein Vergnügen mit dir von den aktuellen Arbeitsthemen abzuschweifen, sich auszutauschen und nicht zuletzt auch aufzuregen über all die Dinge, die auf der Welt – unserer Meinung nach – nicht gut laufen.

Ein weiterer spezieller Dank gilt meinem zweiten Büromitbewohner Michał Nowakowski. Er hat nicht nur die Einarbeitung in XES und das Feld der theoretischen Berechnungen übernommen, sondern war mir ein zuverlässiger und erfahrener Begleiter auf vielen Messzeiten. Dank deines Physikerblicks auf die Spektroskopie konnte so manche komplizierte Fragestellung im Ergebnis doch beantwortet werden. Dziękuję!

Roland Schoch danke ich für die umfangreiche Einarbeitung in XAS und die Weitergabe wertvoller Techniken, die zu dem Erfolg so mancher Messzeiten und Dienstreisen beigetragen haben. Danke für deine ständige Diskussions- und Hilfsbereitschaft.

Den finalen Charakter dieser Arbeit verdanke ich im Besonderen Anke, Michał, Roland und Sam, die sich der Korrekturdurchsicht angenommen haben. Danke, dass ihr jederzeit für mich erreichbar wart.

Abschließend danke ich von ganzem Herzen meiner Familie und meinen Freunden für die fortwährende Unterstützung, Rücksichtnahme und Zuspruch, die die Erstellung dieser Arbeit erfordert hat. Danke für euer Vertrauen über all die Zeit. Im Besonderen danke ich Johanna, meiner Frau. Ohne dein Verständnis, deinen Antrieb, deine Motivation und deine bedingungslose Unterstützung hätte ich diese Promotion niemals geschafft.

List of Beamtimes

Deutsches Elektronensynchrotron (DESY), Hamburg, Germany

Beamline 02.1

- 20.08.2021 – 23.08.2021

Beamline P64

- 11.04.2019 – 17.04.2019
- 07.11.2019 – 13.11.2019
- 04.05.2020 – 13.05.2020
- 06.10.2020 – 12.10.2020
- 27.04.2021 – 03.05.2021
- 23.09.2021 – 27.09.2021
- 05.10.2021 – 10.10.2021
- 21.04.2022 – 27.04.2022
- 09.06.2022 – 15.06.2022

Beamline P65

- 12.04.2019 – 17.04.2019
- 23.05.2019 – 27.05.2019
- 29.05.2020 – 03.06.2020
- 11.06.2020 – 17.06.2020
- 13.08.2020 – 18.08.2020
- 28.08.2020 – 01.09.2020
- 12.05.2021 – 17.05.2021
- 27.10.2022 – 01.11.2022

List of Publications

Publications in Journals

1. N. Prinz, L. Schwensow, S. Wendholt, A. Jentys, M. Bauer, W. Kleist, M. Zobel “Hard X-ray based techniques for structural investigations of CO_2 methanation catalysts prepared by MOF decomposition”
   Nanoscale, **2020**, *12*, 15800-15813. (DOI: 10.1039/d0nr01750g)
2. S. Weber, R. T. Zimmermann, J. Bremer, K. L. Abel, D. Poppitz, N. Prinz, J. Ilsemann, S. Wendholt, Q. Yang, R. Pashminehazar, F. Monaco, P. Cloetens, X. Huang, C. Kübel, E. Kondratenko, M. Bauer, M. Bäumer, M. Zobel, R. Gläser, K. Sundmacher, T. L. Sheppard “Digitization in Catalysis Research: Towards a Holistic Description of a Ni/Al_2O_3 Reference Catalyst for CO_2 Methanation”
   ChemCatChem, **2022**, *14*, e2021018. (DOI: 10.1002/cctc.202101878)
3. S. Strübbe, M. Nowakowski, R. Schoch, M. Bauer “High resolution X-ray absorption and emission spectroscopy for detailed analysis of new CO_2 methanation catalysts”
   ChemPhysChem, *submitted.*
4. L. Rohrbach, S. Strübbe, N. Prinz, C. Wilhelm, P. Müller, M. Nowakowski, A. Schökel, M. Zobel, M. Bauer, W. Kleist “Investigation of MOF derived Ni@carbon catalysts in the methanation of CO_2 under dynamic gas feed conditions during different dropout scenarios”
   ChemCatChem, *in revision.*
5. N. Prinz, S. Strübbe, M. Bauer, M. Zobel “Accessing the structural processes during the formation of Ni nanoparticles by decomposition of Ni-containing metal-organic framework using *in-situ* scattering”
   New. J. Chem., *accepted.*

Talks

1. S. Wendholt, M. Bauer “Synchrotron X-ray Spectroscopy in Catalysis Research”
   9th German-Russian Travelling Seminar, Russia, **2019**, 30.07.-10.08.

Poster

1. S. Wendholt, N. Prinz, L. Schwensow, M. Zobel, W. Kleist, M. Bauer “XAS studies of Ni-based methanation catalysts obtained from controlled decomposition of metal-organic frameworks”
   SPP2080 Status Meeting, Leipzig, **2020**, 17.02.-18.02.

2. S. Wendholt, N. Prinz, L. Schwensow, M. Zobel, W. Kleist, M. Bauer “XAS studies of Ni-based methanation catalysts obtained from controlled decomposition of metal-organic frameworks”
   2. “Bring-your-own-poster”-session (JCF Paderborn), Paderborn, **2020**, 26.02.
3. S. Wendholt, N. Prinz, L. Schwensow, M. Zobel, W. Kleist, M. Bauer “X-ray spectroscopy in the characterization of novel Ni-based methanation catalysts”
   SPP2080 Status Meeting, Online, **2021**, 23.02.-24.02.
4. S. Wendholt, N. Prinz, L. Schwensow, M. Zobel, W. Kleist, M. Bauer “X-ray spectroscopy in the characterization of novel Ni-based methanation catalysts”
   54. Jahrestreffen Deutscher Katalytiker, Online, **2021**, 16.03.-19.03.
5. S. Wendholt, N. Prinz, L. Schwensow, M. Zobel, W. Kleist, M. Bauer “Ni-based catalysts for CO_2 methanation probed by X-ray spectroscopy under *in-situ* conditions”
   758. WE Heraeus Seminar (From Wind and Solar Energy to Chemical Energy Storage: Understanding and Engineering Catalysis under Dynamic Conditions), Online, **2022**, 09.01.-13.01.
6. S. Wendholt, N. Prinz, L. Schwensow, M. Zobel, W. Kleist, M. Bauer “Ni-based catalysts for CO_2 methanation probed by X-ray spectroscopy under *in-situ* conditions”
   27th North American Catalysis Society Meeting, New York, NY, USA, **2022**, 22.05.-27.05.
7. S. Wendholt, N. Prinz, L. Schwensow, M. Zobel, W. Kleist, M. Bauer “Ni-based catalysts for CO_2 methanation probed by X-ray spectroscopy under *in-situ* conditions”
   55. Jahrestreffen Deutscher Katalytiker, Weimar, **2022**, 27.06.-29.06.
8. S. Strübbe, N. Prinz, L. Rohrbach, W. Kleist, M. Zobel, M. Bauer “X-ray spectroscopy investigations of novel Ni-based catalysts for CO_2 methanation”
   3. “Bring-your-own-poster”-session (JCF Paderborn), Paderborn, **2022**, 24.10.
9. S. Strübbe, N. Prinz, L. Rohrbach, M. Zobel, W. Kleist, M. Bauer “Analysis of Ni@C methanation catalysts using a methodical combination of hard X-rays”
   56. Jahrestreffen Deutscher Katalytiker, Weimar, **2022**, 15.03.-17.03.

Table of Content

1 Motivation

The climate crisis is one of the greatest challenges faced by modern mankind.[1] To constrain global warming, a reduction of CO_2 emissions is imperative. To even come close to this goal new and efficient energy techniques are required. Currently used renewable energy sources are mainly photovoltaics, biomass, wind- and hydropower.[2] In 2021, 238 TWh, around 40% of total electricity generation in Germany, were produced from renewable resources. Most of the energy supply is still generated from fossil fuels, which emit carbon dioxide and pollute the environment (cf. Figure 1).[3]

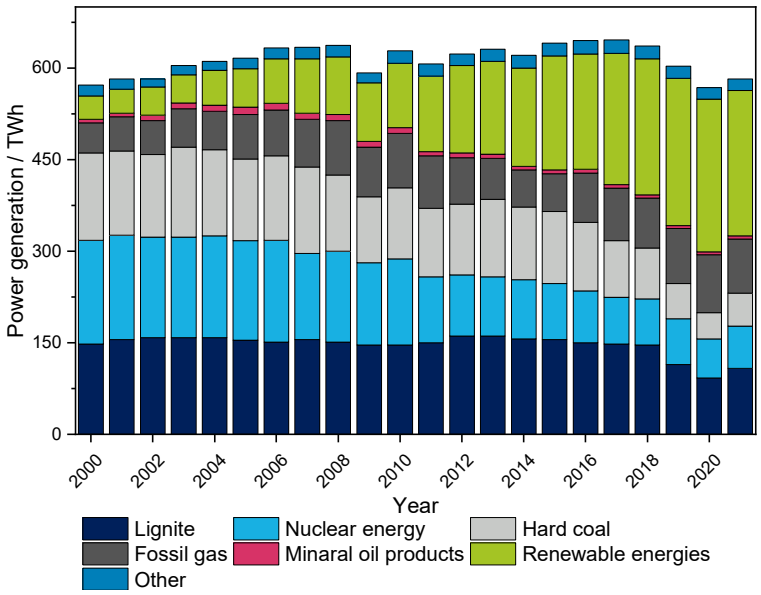

Figure 1: Gross electricity generation in Germany by energy source in the years 2000 to 2021.[3]

Due to the unstable availability of the weather-dependent renewable sources, a time and weather-dependent fluctuation in the energy grid can occur.[4] Effective storage concepts must be designed to sufficiently stabilize these fluctuations and to compensate electricity overproduction by renewable resources. Thus, energy storage is crucial and plays a key role in the transition towards sustainable energy usage.[5] One approach is the *power-to-X* concept. It describes a possible solution for short- and long-term energy storage in different sectors such as electricity, gas, heat, chemicals, and transport.[6] One implementation of this approach could be to use energy overproduction from renewable energy in electrochemical cells for water splitting. In a further step, this sustainably produced hydrogen can for example be used for the synthesis of energy carriers. For instance, a possible energy carrier could be based on the catalytic methanation of CO_2 to close the carbon cycle through the *power-to-gas* concept, via the SABATIER reaction (Eq. 1):[7,8]

$$CO_2 + 4\,H_2 \rightleftharpoons CH_4 + 2\,H_2O \quad \Delta H_{298K} = -165\,kJ/mol \qquad \textbf{Eq. 1}$$

Regarding the well-established and given infrastructure, methane can be stored and transported efficiently using the already existing gas distribution grid. Furthermore, the volumetric energy density of methane is three times higher than H_2, and it can be used directly in conventional gas power plants for electrical power production.[9] Moreover, the storage of hydrogen is a challenge and confronts scientists with the task of developing effective storage options for hydrogen,[10] since pure hydrogen suffers from losses in the storage process, which can be caused by diffusion or evaporation.[11] For application in the catalytic reaction of CO_2 towards methane, Ni-based catalysts are well known, due to their high activity and relatively low production costs.[12] Nevertheless, MUTZ *et al.* reported that Ni-catalysts immobilized on γ-Al_2O_3 support, tend to strongly deactivate during the catalytic methanation of CO_2 if they are confronted with losses of hydrogen flow.[13] Accordingly, highly stable catalyst systems are required, especially for dynamic gas feeds resulting from fluctuations in energy supply.[14] Therefore, much research has been invested in the immobilization and stabilization of metal nanoparticles on support materials to avoid deactivation processes such as high-temperature sintering.[15] Spatial entrapment of Ni nanoparticles stabilized by suitable support systems is a promising approach for the development of improved catalysts.[16] Confinement of the catalysts in a matrix, e.g. a carbon matrix, as in the context of this work, can prevent sintering of the catalytically active metal centers. An unconventional approach of thermal decomposition of metal-organic framework (MOF) precursors can be adopted to manufacture carbon encapsulated Ni catalysts. The high flexibility in the synthesis and the extremely defined structure of the framework compound allows for a high degree of precision when tailoring the properties of the resulting carbon-supported enhanced functional nanomaterials.[17,18] The surface properties are not only influenced by the composition of the MOF itself, but also by possible post-synthetic modifications of the MOF or the decomposition conditions.[19]

The subject of this thesis is the application of hard X-ray-based spectroscopic methods, namely X-ray absorption spectroscopy (XAS) and X-ray emission spectroscopy (XES), to get deep insights into the manufactured catalysts properties. XAS is an important tool for structural investigations of systems without long-range order, for example, amorphous structures of the gained catalysts. The method enables element-specific measurement of the samples and, as a result, precise analysis of the compound. The ability for the short-range ordering of X-ray absorbing elements in a sample to be precisely addressed, differentiated, and determined independent of the physical state is a feature that makes XAS extremely versatile.[20] Although the first approaches of X-ray-based absorption spectroscopy, as well as the first attempts to

explain it, have been known since the 1920s, only the advent of synchrotron radiation sources have allowed the development and verification of a general theoretical description of the extended X-ray absorption fine structure (EXAFS). This technique allows the analysis of the structural parameters of the coordinating atoms around the absorbing atom. The X-ray absorption near-edge structure (XANES), on the other hand, is mainly used to obtain valuable information about the unoccupied electronic states, the oxidation state of the X-ray absorbing atom and the geometric structure of the surrounding atoms.[21] Moreover, XES will be used to obtain information about the electronic structure of the sample. XES offers the possibility to probe the occupied states of the measured element, and so enables more precise statements about the atomic environment. Thus, for the first time, a methodological application of XES could be applied to such undefined Ni@C systems, which are based on the thermal decomposition of MOFs. Using a combination of this information, the present work aims to characterize highly amorphous pre-catalysts and catalysts at the electronic and structural levels. At the same time, the high specificity and versatility of both methods, XAS and XES, will be shown, while the possibilities of characterization and analysis will be presented, where other methods are not sufficient.

2 Catalysis

In the last centuries, reactions based on catalytic processes were discovered on a regular basis. In 1823, for example, JOHANN WOLFGANG DÖBEREINER developed the DÖBEREINER lamp, a lighter in which the reaction of sulfuric acid and zinc was used to produce hydrogen.[22] The hydrogen was flushed over a platinum sponge in oxygen, thus initiating a catalytic reaction between the two gases, at ambient temperature. The resulting heat was sufficient to ignite the hydrogen. Therefore, the DÖBEREINER lighter represents the first commercial application of a heterogeneous catalytic reaction. The current term *catalysis* was first introduced in 1835 by JÖNS JACOB BERZELIUS to the Royal Swedish Academy of Science. The expression originates from the Greek word *katalysis* which means *to untie*. The name derived from the fact that it was assumed that the bond breaking process was the crucial step of the reaction. He put forward the thesis that the observed chemical phenomenon only occurs when a certain substance is present but this substance remains unchanged after the reaction. In doing so, he relied, among all, on the work of DÖBEREINER and found that Pt merely awakens the “sleeping" gases.[23] A little more than half a century later, in 1895, FRIEDRICH WILHELM OSTWALD defined the term catalysis in German. The translation can be read approximately: "Catalysis is the acceleration of a slowly proceeding chemical process by the presence of a different substance".[24] In doing so, he already implied the fact that a catalyst causes a reaction to take place that would not occur without it, and at the same time accelerates a chemical reaction without changing the chemical equilibrium.[25] OSTWALD was awarded with the Nobel Prize in Chemistry in 1909 for his outstanding results in catalysis.[26] Based on OSTWALD's results, catalysis was no longer just a chemical phenomenon. Instead, it became one of the most researched topics and, at the same time, a powerful tool for chemists. Thus, as early as 1898, an employee of the *Badische Anilin- und Soda Fabrik* (BASF) scaled up the process developed by OSTWALD for the production of sulfuric acid to an industrial scale as a so-called *contact process*.[23] In 1904 FRITZ HABER began his attempts to produce ammonia from its elemental components, nitrogen and hydrogen, and achieved his first results.[27] HABER applied for a patent for the production of ammonia in 1908, which was granted in 1911.[28,29] BASF, which HABER was able to win as a partner, administered the patent and applied it industrially. In the following years, CARL BOSCH worked together with ALWIN MITTASCH on a technical realization of the newly developed process.[23,30] In 1913, the first large-scale plant of the HABER-BOSCH process went into operation at the BASF plant in Ludwigshafen am Rhein (Germany).[28,31] Based on the chemistry and the findings in the field of catalysis leading to the industrial process of ammonia synthesis, three Nobel Prizes in Chemistry were awarded in the next 100 years

connected to this reaction: in 1918 to FRITZ HABER, in 1931 to CARL BOSCH, and in 2007 to GERHARD ERTL, who was able to solve the mechanism of the reactions (cf. Eq. 2 to Eq. 8).[32]

$$H_2 \rightleftharpoons 2\,H_{ad} \qquad \textbf{Eq. 2}$$

$$N_2 \rightleftharpoons N_{2,ad} \qquad \textbf{Eq. 3}$$

$$N_{2,ad} \rightleftharpoons 2\,N_{ad} \qquad \textbf{Eq. 4}$$

$$N_{ad} + H_{ad} \rightleftharpoons NH_{ad} \qquad \textbf{Eq. 5}$$

$$NH_{ad} + H_{ad} \rightleftharpoons NH_{2,ad} \qquad \textbf{Eq. 6}$$

$$NH_{2,ad} + H_{ad} \rightleftharpoons NH_{3,ad} \qquad \textbf{Eq. 7}$$

$$NH_{3,ad} \rightleftharpoons NH_3 \qquad \textbf{Eq. 8}$$

In addition, based on HABER's 1909 results, OSTWALD was able to develop a process that produces nitric acid from ammonia, catalyzed by a Pt catalyst.[23,33] The development of the OSTWALD process and the HABER-BOSCH process forever changed the situation worldwide agriculture. For the first time, it was possible to produce fertilizers on an industrial scale, allowing them to feed the world's population, which has been growing faster ever since.[34] The first findings in catalysis apart from biocatalysis e.g. fermentation processes, were heterogeneously catalyzed reactions.[35] The origins of homogeneous catalysis as we know it today started in 1938 with OTTO ROELEN'S discovery of *oxo-synthesis*, more generally known as hydroformylation.[23,36] In this process, an alkene reacts directly with syngas (a mixture of CO and H_2) to form a higher valence aldehyde. ROELEN found that the mechanism proceeds via a cobalt carbonyl hydride species. RICHARD F. HECK and DAVID BRESLOW were able to clarify the cobalt-catalyzed reaction mechanism of the catalytic process without ligands in 1960 (cf. Figure 2).[37]

Based on a patent filed in 1938, the corresponding industrial process went into operation at the *Ruhrchemie* Company.[38] Another milestone, not only for chemistry but for the modern world, was the discovery of the polymerization of ethene or propene by KARL ZIEGLER and GIULIO NATTA.[39] This process uses a mixed catalyst consisting of an organometallic main group (I-III) compound, e.g. triethylaluminum, and a transition metal compound of groups IV to VI (e.g. titanium tetrachloride).[40] The two chemists were awarded the Nobel Prize in 1963 for the development of the ZIEGLER-NATTA process, which is still used today.

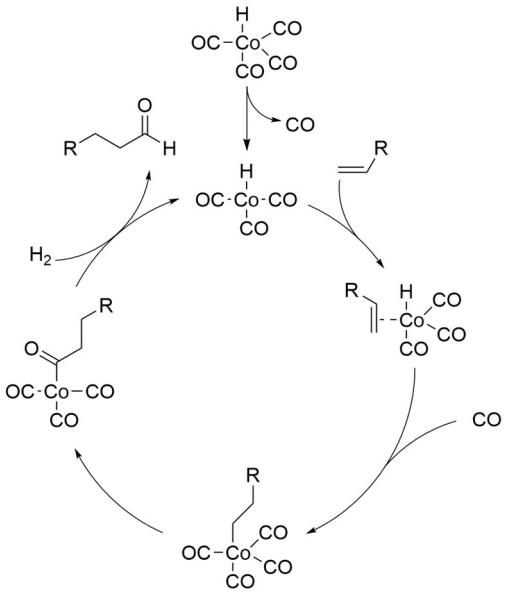

Figure 2: Reaction mechanism of the hydroformylation according to HECK and BRESLOW.[37]

In principle, the activation energy of a chemical process can be lowered by using catalysts. Furthermore, a suitable catalytic system can influence the reaction in such a way that the selectivity for the desired product is significantly increased.[41] Catalysts are an elementary part of the green chemistry concept, as they help to avoid waste, save energy, and they provide access to the conversion of raw materials.[42] The processes presented in this chapter are intended to only provide an outline of the rapid success story of catalysis and to underpin its importance for the modern age. Today, catalysis is one of the most important tools in the chemical industry. More than 90% of the total product range of the chemical industry went through a catalytic reaction cycle at least once in their manufacturing process.[43]

2.1 The methanation of carbon dioxide

The SABATIER reaction, which describes the reduction of carbon monoxide (cf. Eq. 10) or carbon dioxide (cf. Eq. 9) to methane, is a reaction that is well developed under steady-state conditions.[44,45] The formation of water as a by-product of methane generates a driving force that makes the reaction exothermic. Since the equilibrium of the SABATIER reaction shifts to the product side with increasing pressure, high-pressure reactions are ideal for the formation of methane. At the same time, since the increased formation of CO can be observed at temperatures above 450 °C by reverse water gas shift reaction (RWGS; cf. Eq. 11), the temperature should be lower for the reaction to methane. In addition, a decrease in the conversion of

CO_2 at high temperatures can be observed.[46] Most publications on the topic of CO_2 methanation note the use of temperatures between 200 and 400 °C and pressures between 1 and 30 bar.[45]

$$CO_2 + 4\,H_2 \rightleftharpoons CH_4 + 2\,H_2O \quad \Delta H_{298K} = -165\,kJ/mol \qquad \textbf{Eq. 9}$$

$$CO + 3\,H_2 \rightleftharpoons CH_4 + H_2O \quad \Delta H_{298K} = -206\,kJ/mol \qquad \textbf{Eq. 10}$$

$$CO_2 + H_2 \rightleftharpoons CO + H_2O \quad \Delta H_{298K} = -41\,kJ/mol \qquad \textbf{Eq. 11}$$

Even though the methanation reactions are exothermic, adequate conversion is not observed until the reaction is catalyzed.[45] Depending on the substrate, the two reactions Eq. 9 and Eq. 10 proceed differently. Different selectivities and conversions have been observed for both reactions, the methanation of CO_2[12,47] and the methanation of CO,[48,49] depending on the catalytic conditions.

2.2 Catalytically active systems for CO_2 methanation

Different metal-based catalysts for the methanation of CO_2 have been reported in the literature. The most notable, those exhibiting high activities are based on Pd,[50] Fe,[51] Co,[52] Pt,[53] Rh,[49,54,55] Ru,[56,57] or Ni.[56,58–62] In particular, Ru-based catalysts show great activities even at temperatures below 200 °C.[44,45,63,64] In contrast Ni shows very good performances in the high-temperature range between 300 and 500 °C.[65,66] Based on their good availability and low costs, nickel-based catalysts are among the most widely used methanation catalysts.[63] In the temperature range from 220 to 290 °C, high activities can be enabled by a high dispersion of the catalytically active nickel. However, modified surface defects or low-coordinated Ni centers also achieve satisfactory results in this temperature range.[59] High stabilities of about 290 hours have also been reported in long-term experiments.[59] Usually, the nickel catalysts are supported on materials such as Al_2O_3,[56,62,64–66] SiO_2,[67] or TiO_2.[60,68] However, studies have shown that redox-active supports such as ZrO_2,[69–71] CeO_2,[61] or even mixed oxides of both compounds[72,73] can also lead to promising results. The works report, that the high activity of nickel at low temperatures are further enhanced by the mild basic properties of these supports.[61,69–71] Al_2O_3 as support material provides a combination of higher redox-activity with high thermal stability and specific surface area.[66,74] Doping options such as MgO[67,75] or ZrO_2[76] were also used, and it has been found that this increased both selectivity and catalytic activity in most applications. Furthermore, nickel can be embedded in a carbon matrix,[17,18] as shown in this work. In addition to doping of the support material, there are also publications presenting doping of the catalyst species by an additional metal.[71,77] For example, it has been

shown that catalysts, which are doped with Fe exhibit improved CO dissociation,[78] increasing the activities for both the methanation of CO[79] and CO_2,[80] as well as for a reaction mixture of both gases.[80,81] Furthermore, iron doping can increase activities of CO_2 methanation at lower temperatures, whilst also improving the stability for temperatures above 350 °C.[82]

2.3 The mechanism of the SABATIER reaction

A clear mechanism for the CO_2-based SABATIER reaction is still open to scientific discussion, especially when factoring in the large variety of different catalyst metals or the doping reagents and conditions. In addition, not only the support can be varied or doped, but mixtures of different support materials are also used. Multiple different reaction paths can occur, which must be considered individually. Two reaction pathways of CO_2 methanation are widely accepted, one involves a CO species, in the other formates are formed.[83,84] The first mentioned mechanism is the dissociation of CO_2 via an RWGS reaction (Eq. 11) followed by methanation of CO (Eq. 10). After dissociative adsorption of CO, the reduction then proceeds by hydrogenation of the adsorbed carbide species on the surface.[83,85] Subsequently, the two individual components, oxygen, and carbon, are then hydrogenated step by step to form water and methane.[48,85,86] Although the carbide-based reaction pathway of CO is often cited,[83,84,87] WANG attempted to break down an alternative mechanism of CO reduction to methane which seems especially suitable for single-site approaches. His proposed mechanism is shown in Figure 3.[88]

In the mechanism described, first, two hydrogen molecules and two CO molecules are coordinated **(1)**. Afterwards, a bond reorientation takes place, and the CO ligand is reduced to an aldehydic group **(2)**. As a next step, this group is reduced to an alcohol with the simultaneous insertion of another CO ligand **(3)**, followed by a reaction of hydrogen with another CO ligand forming an aldehyde **(4)**. After molecular esterification **(5)** and the rearrangement of electrons, carbon dioxide is released **(6)**. In the last step, a final reduction of methane takes place and at the same time, a new carbonyl ligand is complexed together with a new hydrogen molecule **(7)**, thereby completing the cycle.

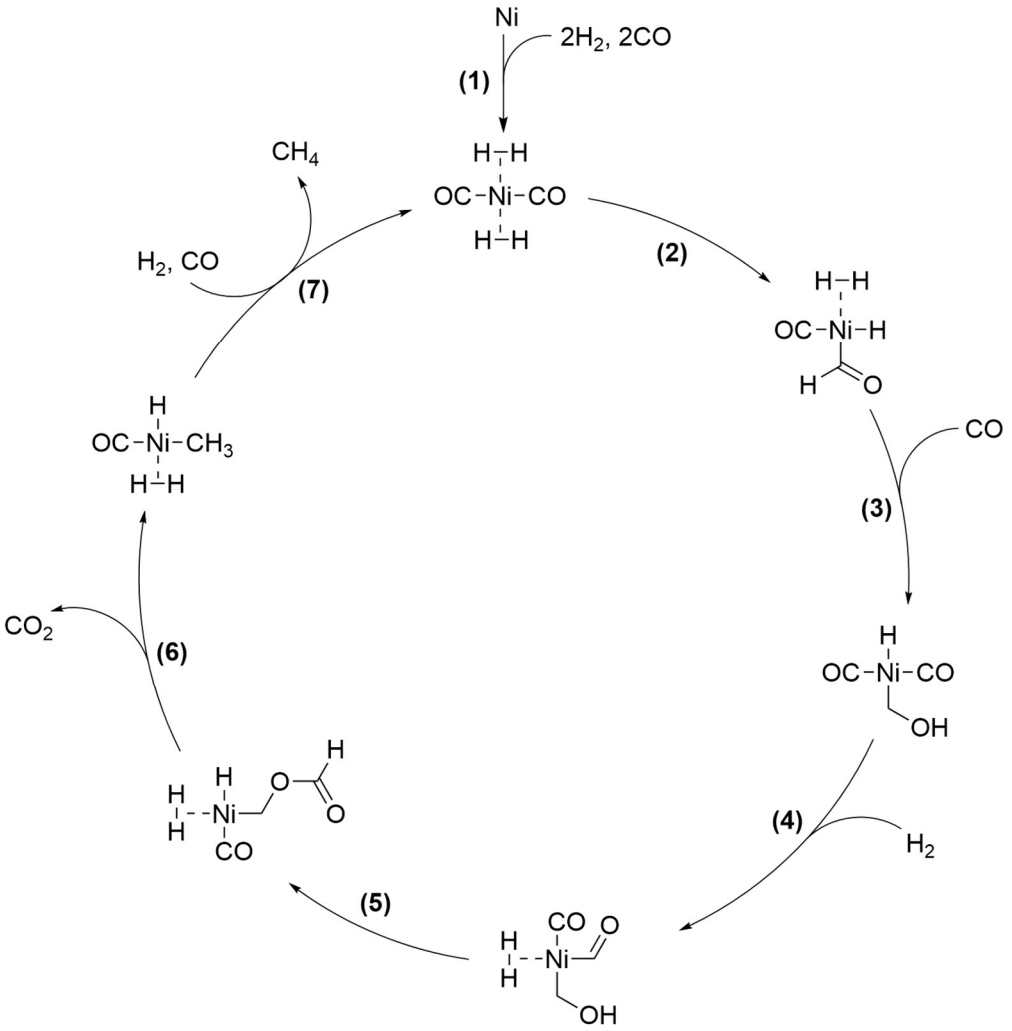

Figure 3: Reaction mechanism of the SABATIER-SENDERENS-Reduction according to WANG.[88]

The RWGS reaction mechanism via CO_2 dissociation is proposed to be used for the low-temperature methanation of CO_2 over a Rh@Al_2O_3 catalyst. In this example, the reaction takes place *via* CO_2-induced oxidation of Rh, followed by the well-known mechanism of CO methanation (cf. Eq. 10).[54]

As beforementioned, the second reaction pathway, which is largely agreed upon in the literature, proceeds via the direct hydrogenation of CO_2 and the formation of a formate species.[83,84,89,90] WESTERMANN *et al*. describe that a formate is directly formed on Ni when using a Ni@zeolite catalyst.[90] FISHER *et al.* report a SiO_2-supported Rh catalyst in which the hydrogenation of CO resulting from the dissociation of CO_2 proceeds directly *via* an H_2CO species without the formation of surface carbon.[49] ALDANA *et al.*[73] and PAN *et al.*[91] investigated Ni on a $Ce_{0.5}Zr_{0.5}O_2$[73] and γ-Al_2O_3[91] supports, respectively. It was found that the reaction pathway

differs mostly in that the reaction on the $Ce_{0.5}Zr_{0.5}O_2$ support proceeds primarily *via* a monodentate formate species,[84] whereas on a γ-Al_2O_3 support, a bidentate formate species is formed.[84] It was also shown by PAN *et al.* that the reaction proceeds preferentially at the mediate basic sites. Therefore, the CO_2 adsorbed on the strong basic sites of Ni@γ-Al_2O_3 participates at a slower rate in the methanation.[84,91] The reaction of Ni@γ-Al_2O_3 described by PAN *et al.* is shown in Figure 4.[84]

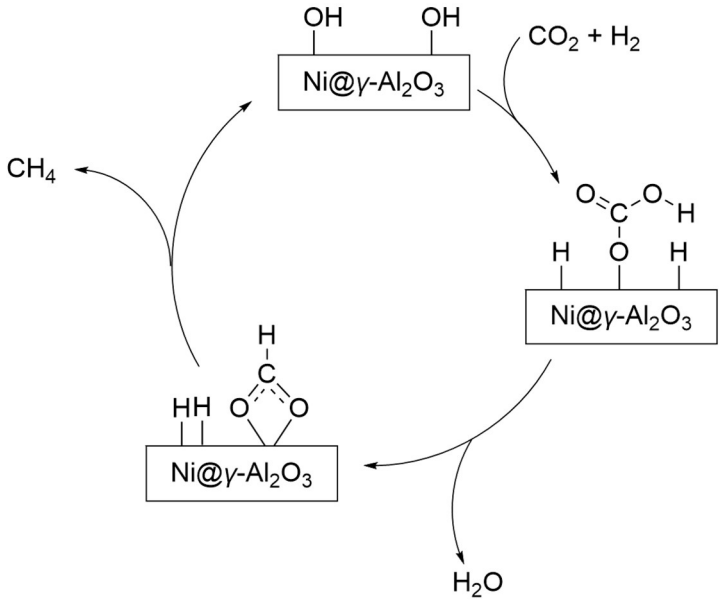

Figure 4: CO_2 methanation reaction route as described by PAN *et al.* on Ni@γ-Al_2O_3.[84]

Alternative mechanisms are also reported in the literature for Ni on SiO_2 supports. VOGT *et al.* argue that a third reaction pathway can be considered for the SABATIER reaction.[92] They have shown, using *operando* infrared spectroscopy, that Ni@SiO_2 catalyst does not follow a reaction pathway *via* the previously proposed formate species (cf. Figure 4).[93] In addition, it is suggested that a reaction pathway via a carboxylate species can occur. Contrary to the observation of FISHER *et al.* for Rh, where CO does not dissociate. The reaction pathway for Ni@SiO_2 is considered most likely to proceed *via* a carbide pathway based on the dissociation of CO.[8,94]

LIN *et al.* have investigated Ni@C systems obtained by the thermal decomposition of MOFs,[95] analogous to what was performed for the catalysts characterized in this work. It have been shown that in this case the methanation of CO_2 on Ni@C catalysts also proceeds *via* the formate pathway.[95] In the approach chosen by LIN *et al.* a MOF was used which is based on a hollow ball-in-ball structure consisting of Ni and trimesic acid.[95] Whereas in the approach used in this work, a MIL-53 based Ni-MOF is the basis for the pre-catalysts.

In the investigations of the reaction mechanism, numerous methods were used to study intermediates and reactants and thus to unravel the mechanism. However, precise targeting of the metallic species is a separate challenge, especially in the study of thermally decomposed MOFs, as this results in an undefined mixture of different metal-containing species. Therefore, the application of element-specific methods such as XAS or XES is required. To make this possible, both spectroscopic methods will be applied in this work to gain further insight into the mechanism and the catalytically active species.

3 Optical Fundamentals

3.1 Interaction of X-ray with matter

When matter is irradiated with X-rays, they can interact in four different ways: X-ray absorption, elastic scattering, inelastic scattering, and the production of electron-positron pairs. The latter occurs exclusively in confrontations with very high energies over 1.022 MeV (cf. Figure 5) and is irrelevant in the energy ranges of X-ray measurements. For the methods applied in this work, namely XAS and XES, the interactions of interest are photoelectric absorption and elastic scattering.[96]

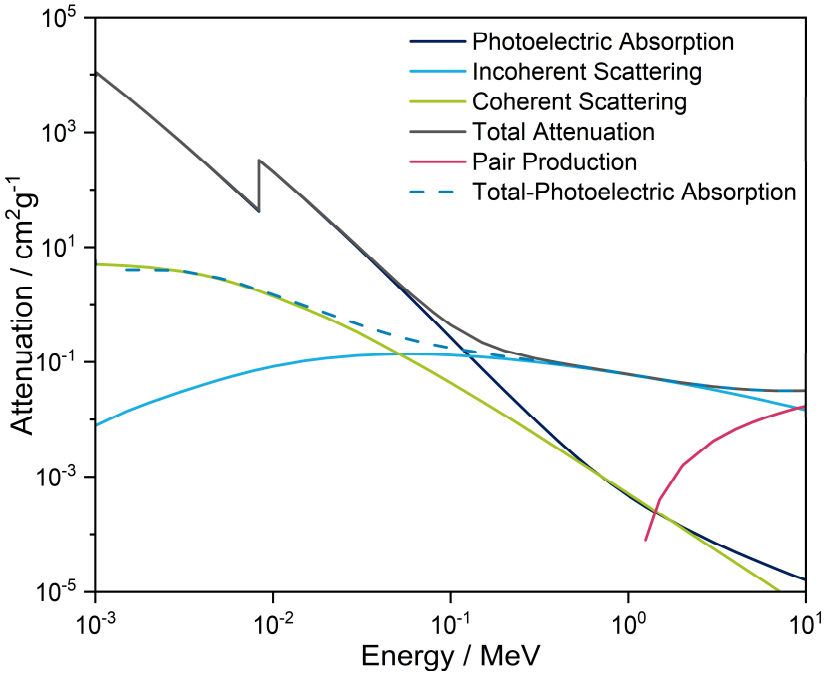

Figure 5: Different attenuation effects for Nickel over increasing energy.

Elastic scattering, which is also called coherent, unmodified, or RAYLEIGH scattering, is observed when a photon with certain energy hits a sample and is backscattered by atomic electrons. Neither ionization nor excitation of the electrons occurs, but a photon of the same frequency with a different spatial direction is emitted. Thus energy remains constant while the momentum changes.[97] Referring to a classical explanation, a bound electron of an atom is set into oscillation by the incidence of an electromagnetic wave. By this, a secondary wave of the same frequency is generated.[96] In most cases, elastic scattering plays a minor role compared to absorption in the low energy range or for light atoms, but not for high energies above 4 keV, which means for hard X-rays.[97] X-rays can also be scattered inelastically or via COMPTON scattering, whereby the energy of the scattered photon is not equal to that of the incident

photon. Due to this energy transfer, electronic transitions, such as excitations in the irradiated atom take place and a photon of different energy and momentum is emitted.[96,97]

The process when energy is transferred from a photon to an electron, which leads to the consumption of the photon, is called absorption. A core electron of an atom can be excited to higher states or into the continuum by incident photon *via* absorption process with simultaneous core hole creation. This process is called the photoionization process (cf. Figure 6).[97]

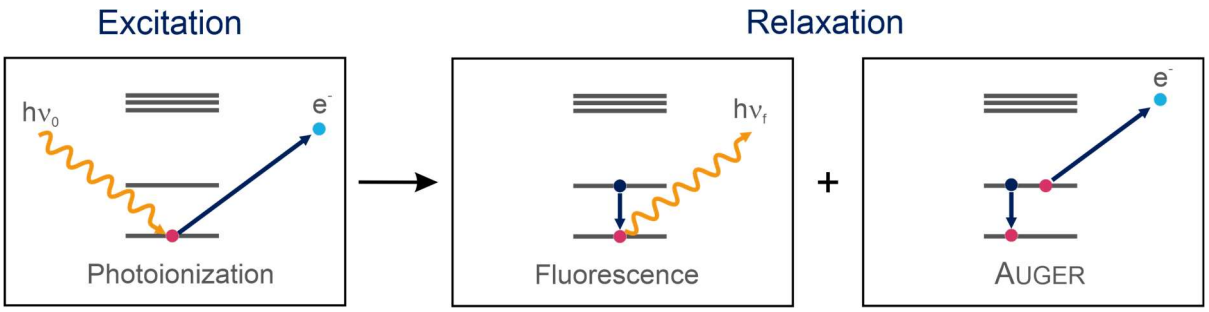

Figure 6: Different ways of interaction between X-ray photons and matter.[97]

The (photo)electron-hole exciton is metastable, and a relaxation of electrons from higher energy levels into the previously generated vacancies takes place. The two main relaxation pathways that can occur are fluorescence and AUGER relaxation. In the element characteristic fluorescence, energy is released which matches the energy difference of the two states involved. The type of fluorescence depends on the shell in which the vacancy is located and by which it is filled, when the electron vacancy is located in the *K*-shell, i.e. in the *1s* orbital, relaxations from the *L*-shell occur, correspondingly $L \rightarrow K$ transitions are called $K\alpha$ emission lines. If, in contrast, the relaxation takes place from the *M*-shell, this $M \rightarrow K$ transition is called a $K\beta_1$ or $K\beta_3$ emission line. Although, a $N \rightarrow K$ ($K\beta_2$ or $K\beta_5$) transition can also occur giving rise to weak valence emission in *3d* metals. The shells are designated according to the SOMMERFELD notation[98] and the transitions according to SIEGBAHN.[99] Figure 7 shows other possible transitions and detailed designations. The ratio of the emitted X-ray photons to the number of vacancies generated is called the fluorescence yield or radiation probability. The fluorescence yield increases as a function of atomic number and is consequently larger for the *K*-lines than for the subsequent lines.[97] Accordingly, for *3d* metals investigated in this work, the *K*-line is preferentially probed.

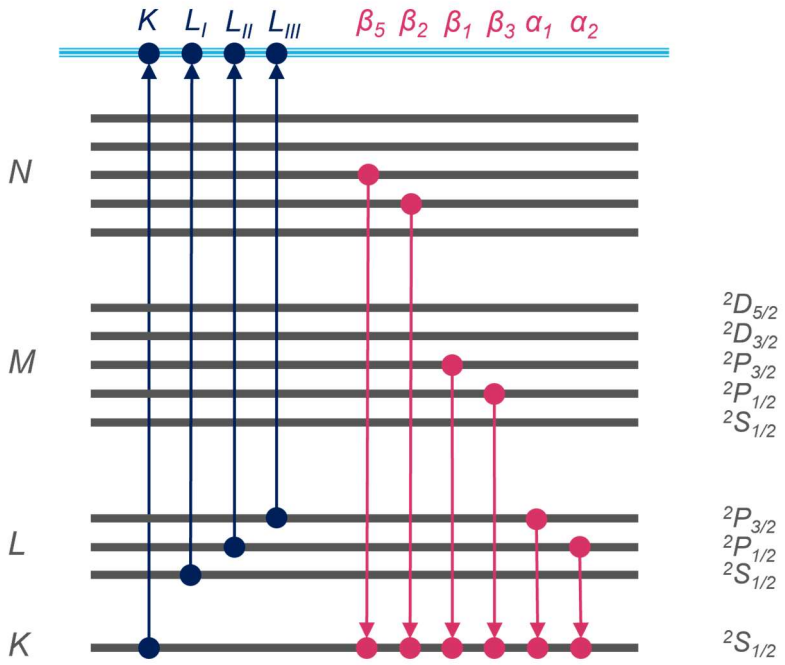

Figure 7: Selected absorption edges and fluorescence emission lines.[97]

In addition to the described radiative decay, also a non-radiative relaxation by emission in the form of an AUGER electron can compensate the energy difference between states involved.[96,97] In this case, the core hole is filled by an electron from a higher shell. The gained energy during this process is transferred to a second electron in the higher shell which is then emitted. Accordingly, the AUGER-effect is a non-radiative process. Consequently, the detection of AUGER electrons, by means of AUGER spectroscopy, provides detailed information about the energy levels involved in a transition.[96,97] The probability that AUGER electrons are produced is particularly high for light atoms and low energies. Thus, below Z=31 (Ga) the AUGER signal dominates and only at higher atomic numbers fluorescence becomes dominant.[100] Moreover, there may be radiative decay, as the energy increases, or non-radiative decay, due to the production of secondary electrons. In the latter, electrons are ejected from higher shells due to the emitted fluorescence photons or AUGER electrons. Both phenomena described are closely related and occur simultaneously. However, in the context of this work mainly X-ray absorption and X-ray emission spectroscopy are used.

3.2 Selection Rules

Electronic transitions studied by X-ray spectroscopy are governed by the electric dipole selection rules defined by:

$$\Delta \mathrm{J} = 0, \pm 1 \qquad \textbf{Eq. 12}$$

$$\Delta \mathrm{L} = \pm 1 \qquad \textbf{Eq. 13}$$

$$\Delta \mathrm{M} = 0, \pm 1 \qquad \textbf{Eq. 14}$$

In Eq. 12 *J* is defined as *J=L+S* and describes the total angular momentum. *L* in Eq. 13 is the azimuthal quantum number, which determines the orbital angular momentum, and *M* in Eq. 14 is the so-called magnetic quantum number. It must be noted in general that *0→0* transitions are prohibited.

The angular momentum must be transferred with every emission or absorption of a photon. But since each photon has its spin, the condition of conservation of angular momentum must be true, but a flip of spins is forbidden by the selection rule in Eq. 15.

$$\Delta S = 0 \qquad \textbf{Eq. 15}$$

When considering transitions, the LAPORTE rule must also always be satisfied.[101] This rule prohibits the preservation of parity concerning the center of inversion. Consequently, only transitions involving a parity change, i.e. *u→g* or *g→u*, (*u: ungerade,* german for odd, or *g*: *gerade,* german for even) are allowed. This is particularly important for centrosymmetric connections since information about the geometry can be obtained from the prohibited parity changes in *d-d* transitions. Nevertheless, when the center of symmetry is distorted, for example by asymmetric oscillations or JAHN-TELLER distortion,[102,103] the transition becomes partially allowed again, leading to characteristic spectroscopic signatures.

Dipole-forbidden transitions are characterized by higher order corrections to the dipole transition-based description, for example, the quadrupole correction. The selection rule of the azimuthal quantum number for electronic quadrupole transitions according to the following formula is decisive:[102,103]

$$\Delta \mathrm{L} = 0, \pm 2 \qquad \textbf{Eq. 16}$$

The transition probability of electric quadrupole transitions, however, is orders of magnitude lower compared to dipole-governed ones, making them almost insignificant in spectral intensity in many cases.

4 X-ray absorption spectroscopy

Just over a century ago, in 1913, the first absorption edge was measured. MAURICE DE BROGLIE mounted a single crystal on a rotating plate and irradiated it with X-rays produced by an X-ray tube. As the crystal rotated, it worked like a monochromator, tuning the energy of the beam falling on the photographic plate. Simultaneously, the absorption edges of the plate materials Ag and Br were probed and produced an intense white signal.[104] The first intense peak after the absorption edge is called *white line* in memory of this observation.[96] Another significant work in the development of XAS was the fine structure discovered by HUGO FRICKE in 1920, when he recorded the energy dependence of the absorption coefficient (μE) near the X-ray absorption *K*-edges of different elements, e.g. Mg, Ti, Cr.[105] At the same time, also in 1920, GUSTAV HERTZ published the results of his research on *L*-edge fine structures for the elements from Cs to Nd.[106] In the following years, further X-ray absorption experiments were carried out by AXEL E. LINDH on different elements.[107] In the process, experimental approaches were adapted and improved,[108] and initial explanations for observed phenomena were proposed.[109] Despite this, over the following fifty years, there remained a great deal of disagreement in the field.[110]

When DALE E. SAYERS, EDWARD A. STERN, and FARREL W. LYTLE published their work on the FOURIER-transformed EXAFS data in 1971,[111] expectations were raised by the analysis of the X-ray fine structure. The scientists established a hypothesis that allowed the extraction of the radial distribution functions sum from the experimental absorption spectrum. Based on these data, numerous publications followed proving that EXAFS can be used to find local structures, such as the type, number and distance of backscatterers around the absorbing atom.[112–115] In particular, the development of synchrotron facilities in the 1970s (cf. Chapter 6) providing intense and monochromatic X-ray radiation with adjustable energy has led to a great improvement in the application of X-ray absorption fine structure (XAFS). Due to the dependence of the absorption edge energy on the element's atomic mass, XAS is an element- and oxidation state-specific method. It can be applied as well for low concentrations and is independent of the sample's aggregate state. In addition, XAS allows *in-situ* measurements of reactions[116] and thus opens up versatile applications in, e.g., the investigation of catalysts.[65] In addition, because X-rays have a high transmission rate through bulk materials, the sensitivity of the method to bulk materials makes XAS a versatile scientific tool. XAS is combining these features and possibilities making it a manifold and powerful method.[96,117–119]

4.1 The principles of X-ray absorption spectroscopy

If a free atom is irradiated with X-rays, there is a continuous decrease of the absorption coefficient *μ(E)* with increasing energy. An explanation for this phenomenon offers the probability of photoelectric absorption. It is directly proportional to *μ(E)* and, along with the coherent and incoherent radiation, has a decisive impact on the observed energy range of the XAS measurement.[96,120]

$$\sigma = constant \cdot \frac{Z^n}{E^{3.5}} \qquad \textbf{Eq. 17}$$

In Eq. 17, *σ* can be described as the photoelectric absorption cross-section that determines the probability of an absorption process on a specific area at a specific time. *Z* is the atomic number and *E* is the photon number. The parameter *n* can vary between 4 and 5. As a result of this equation, the absorption coefficient approximately decreases proportionally to E^{-3}.[96,117]

In an XAS experiment, the sample of interest is irradiated with an energetically tunable and monochromatic X-ray beam. Particular X-ray energies are absorbed by specific atoms in the sample, which undergo excitation and can eject core electrons.[121] The X-ray beam is attenuated by the sample with thickness *d*. The decrease of beam intensity after penetrating a sample proportional to its thickness and the initial beam intensity is described by:[97,117]

$$dI = -\mu(E) I \, dx \qquad \textbf{Eq. 18}$$

The integral of the formula gives LAMBERT-BEER's law.[122]

$$I(E) = I_0 \cdot e^{-\mu(E)d} \qquad \textbf{Eq. 19}$$

I(E) is the transmitted and I_0 is the incident X-ray intensity. *μ(E)* describes the mass absorption coefficient, which decreases with the increasing energy of the incident photon and represents the main physical parameter.[96,97]

The absorption coefficient increases abruptly when a specific energy is reached and forms an absorption edge.[123] At the absorption edge, the absorbed X-ray radiation energy (*hν*) is exactly equal to the binding energy (E_{bind}) of an atom electron and can excite this electron to the lowest unoccupied molecular orbital (LUMO) level. Around 30 eV above the absorption edge, the X-ray beam has enough energy to promote a core electron in the continuum.[97,117,124] If the energy increases further after the absorption edge, the absorption coefficient decreases monotonically until the next absorption edge (s. Figure 8).

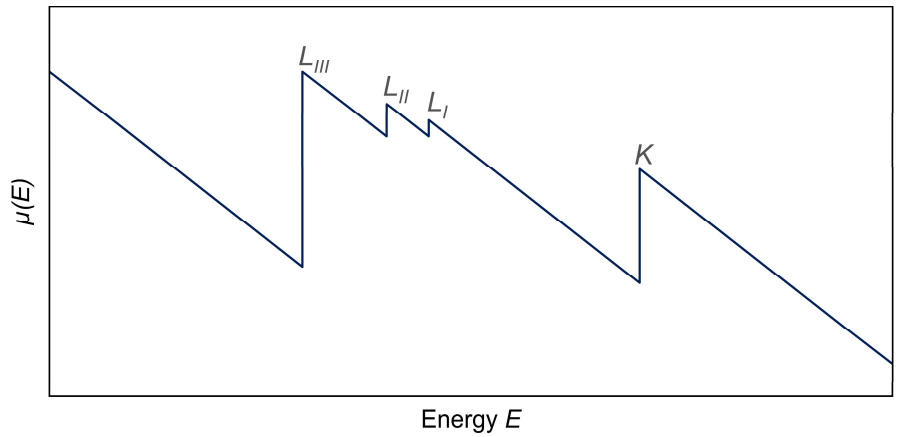

Figure 8: Schematic representation of the absorption coefficient *μ(E)* as a function of the incident photon energy *E*. The absorption edges are named according to the SOMMERFELD notification.[97]

The photoelectric effect (Eq. 20) describes the kinetic energy E_{kin} of the ejected electron.

$$E_{kin} = h\nu - E_{bind} \qquad \textbf{Eq. 20}$$

The kinetic energy of the ejected electron is described as E_{bind} in general physics. In context of absorption it is defined as E_0, which is called zero-point energy or *inner potential*.[117] Therefore applies $E_{bind} = E_0$. In one-electron approximation,[123,125] the probability of an inner shell electron absorbing X-ray photons relies on the starting and final state of the atom. The transition rate is defined by FERMI's Golden Rule:

$$\Gamma_{i\to f} = \frac{2\pi}{\hbar}\left|\langle f\left|\widehat{H}\right|i\rangle\right|^2 \delta(E_f - E_i - \hbar\omega) \qquad \textbf{Eq. 21}$$

In the simplest approach, the absorption coefficient is obtained when the equation is solved within the dipole approximation for a photon-induced transition of an electron from an initial state $|i\rangle$ to a final state $|f\rangle$ and $\widehat{H}$ is a perturbation Hamiltonian.[97] Here, the initial state of the ejected electron at *K* edges XAS corresponds to a *1s* core state. The defined final state corresponds to that of an excited electron. The *δ* function describes the DIRAC unit function. It confines the energies of the states within the frame of the Energy Conservation Rule. According to FERMI's Golden Rule, the absorption coefficient is directly related to the matrix element:[123]

$$\mu \propto \left|\langle f|\widehat{H}|i\rangle\right|^2 \qquad \textbf{Eq. 22}$$

A typical XAS spectrum can be divided into three regions: the pre-edge region, the near edge region around the absorption edge, and the extended X-ray absorption fine structure (EXAFS) region as shown in Figure 9. The pre-edge region and the absorption edge are summarized in the X-ray absorption near edge structure (XANES). Each region contains specific transitions

of an electron from core levels to higher unoccupied states or eventually to the continuum. The first part of the spectrum is located around 5 to 20 eV below the absorption edge and is called the pre-edge or the pre-peak.[123] The structure of the pre-edge can be complex, and one or more features can occur, which are the result of *1s*→LUMO transitions (cf. Figure 10). The transition can be precisely described as a transition from the *1s* to *nd/(n+1)p* hybridized orbitals. Because pure *1s*→*nd* quadrupole transitions are forbidden according to the LAPORTE rule, the probability of transition to the hybridized orbital is significantly lowered and the signal intensity is decreased. However, the pre-peak signal intensity is strongly influenced by the local geometry since it is the result of a *3d/4p* and *3d/2p*(ligand) overlap. Thus, the pre-peak signal serves as an indication of minor geometric changes.[123,126]

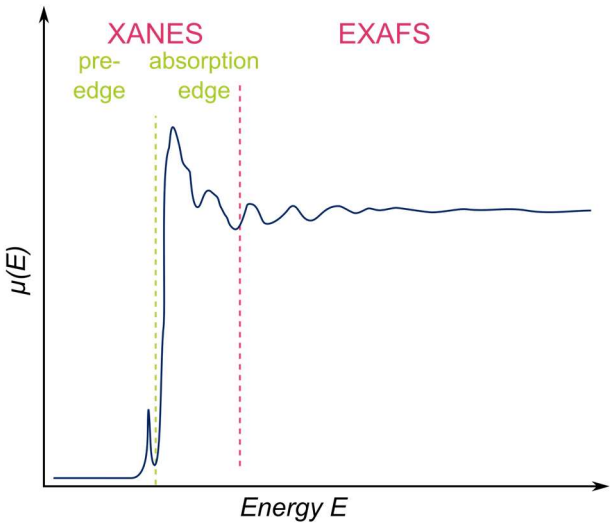

Figure 9: Division of an XAS spectrum into the XANES region and the EXAFS region.

For tetrahedral coordination (point group T_d) the pre-peak is the most intense as the result of the effective hybridization between $p_{x,y,z,}$ and $d_{xy,xz,yz}$ orbitals. Thus, the formation of hybridized orbitals and the parity selection rule of the electric dipole is satisfied, leading to the transition of a *1s* electron to the *p* component of the *nd/(n+1)p* hybridized orbital. On the contrary, octahedral coordination (point group O_h) shows an inversion in symmetry. This results in almost no pre-peak signal with only very low intensity due to quadrupole transitions.[127] Still, if the inversion symmetric octahedral geometry is distorted, the increased mixing of *p* and *d* orbitals results in a visible pre-peak signal. Since the orbital occupancy changes with different oxidation states, as a consequence the pre-peak will be modified as well. Additionally, for most cases, the pre-edge features shift to higher energy upon oxidation and towards lower energies for reduction, respectively.[128] Thus, the oxidation state of the absorbing element can be, to the limited extent, probed by the pre-peak signal.[129]

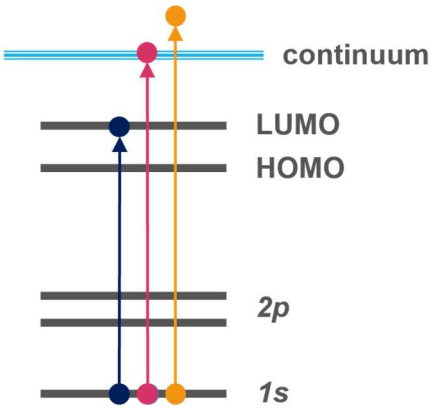

Figure 10: The transitions occurring for XANES [pre-edge (blue) and the absorption edge (red)] and EXAFS (orange).

At higher energies, the sharp and intense increase of the absorption coefficient *μ(E)* is the result of the high probability of the transitions which can occur at the energy of the corresponding edge. At this specific energy, a core electron is excited above the FERMI level energy or the continuum. The absorption edge position can be probed to determine the oxidation state of the absorbing atom. With a higher oxidation state, the absorbing atom has a higher positive charge, and the electrons are more attracted by the nucleus. Consequently, a higher amount of energy is necessary to excite a core electron.[96,123] Furthermore, the coordination environment of the absorbing atom can influence the edge position. The number and the type of ligands, and therefore the bond lengths, affects the electron density of the involved orbitals, changing the ionization threshold.[96] Taking all these factors into account, the determination of the absorption edge position can be facilitated by incorporating information gained from the pre-peak analysis, if available. Despite these issues, an analysis of the oxidation state is possible by measuring reference spectra, even mixtures, and evaluating by linear combination fitting of XANES spectra.[96,130]

In the energy region above the absorption edge, the energy is high enough to excite core electrons into the continuum, giving rise to the EXAFS region. The spherical wave of the produced photoelectron with wavelength *λ* is proportional to:

$$\Psi_{out}(r) \propto \frac{\sin\left(\frac{2\pi}{\lambda}r\right)}{r} \qquad \textbf{Eq. 23}$$

Whereby it is necessary to note, that the amplitude is decreasing with *1/r*.[123] The scattering wave is influenced by the surrounding atoms. If there are other atoms nearby backscattered

waves interfere with the outgoing wave (cf. Figure 11) and oscillating signals of the fine structure are generated.[97,131] The fine structure starts at around 50 eV above the edge energy, can extend until approximately 1000 eV above the edge, and the amplitude of the oscillations is around 1 to 20% of the edge jump.[97] During most XAS measurements, the energy range of only one absorption edge is measured and usually, the *K*-edge is the edge of interest. In the case of heavier elements, the L_{III}-edge is selected to gain better-resolved signal-to-noise ratios. Furthermore, the L_{III}-edge XAS-measurements allow to measure the spectra in the *3d* metal *K*-edge energy range, which is more easily reached by most synchrotron sources.

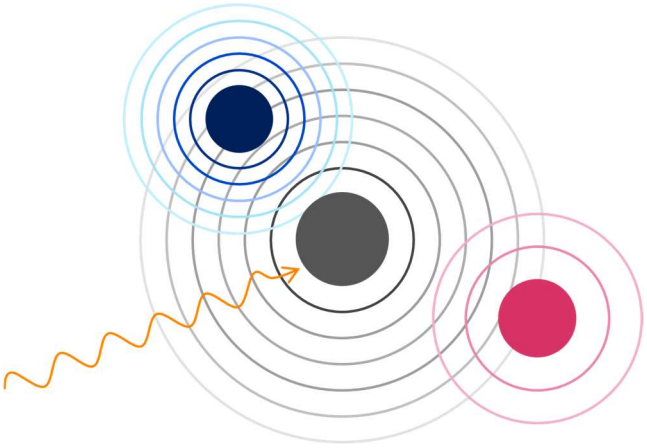

Figure 11: Backscattering behavior of the ejected photoelectron wave towards the absorbing atom.

The fine structure oscillations in the EXAFS region can be analyzed to obtain information about the type, and number of and distances of the neighboring atoms.[97,114,115,117,119] Thus, theoretical fits of the geometrical parameters based on the EXAFS equation need to be implemented as described in the following chapter.

4.2 Theory of EXAFS

The EXAFS region fine structure is a result of the interference between generated and backscattered photoelectron waves. Analysis of the EXAFS region gives information on the types of neighboring atoms, their number and distances to the absorbing atom. Additionally, EXAFS includes details about the static and thermal disorder of nearby atoms.[96,97,117,123,131] In recent years, a number of derivations from EXAFS theory have been presented.[111,132,133] For the purposes of this work, hereafter, a *short-range single-electron single-scattering* approach will be used to explain the EXAFS phenomenon.[112,115,132,133,134] More precisely, the approach describes the idea that the photoelectron is scattered only once before returning to the absorbing

atom and multiple scattering processes are not considered. Another approach is the Full Multiple Scattering (FMS) theory.[135] Here, the photoelectrons are scattered again and again and thus a scattering pattern is created, which also considers the interatomic backscattering. FMS is not considered in the EXAFS theory of this thesis.

For detailed EXAFS analysis, the fine structure must be isolated from the spectra. Therefore, the atomic background $\mu_0(E)$ is subtracted from the absorption coefficient $\mu(E)$ as described in Eq. 24. The obtained difference is normalized to $\Delta\mu_0(E_0)$ (cf. Figure 12) to gain the energy-dependent EXAFS function.[97,117,123]

$$\chi(E) = \frac{\mu(E) - \mu_0(E)}{\Delta\mu_0(E_0)} \qquad \textbf{Eq. 24}$$

In Eq. 24 the $\chi(E)$ corresponds to the isolated and normalized energy-dependent fine structure. It is important to mention that $\mu_0(E)$ is the absorption coefficient of an atom in which the chemical environment with the effect of neighboring atoms being "switched off".[123] The extracted fine structure function $\chi(E)$ is transferred from the energy E towards the photoelectron wave vector k to get the $\chi(k)$ which can be correlated with structural parameters through FOURIER transform.

The kinetic energy E_{kin} of the photoelectron in the photoelectric effect (cf. Eq. 20) is given by:

$$E_{kin} = h\nu - E_{bind} \qquad \textbf{Eq. 25}$$

The photon energy is described by $h\nu$ and E_{bind} is the electron binding energy. By using the *DE BROGLIE* equation $\lambda = \frac{h}{p}$ and the wave vector definition $k = \frac{2\pi}{\lambda}$, the kinetic energy can be written as:[97]

$$E_{kin} = \frac{p^2}{2m} = \frac{h^2k^2}{8\pi^2 2m} = \frac{\hbar^2k^2}{2m} \qquad \textbf{Eq. 26}$$

Where $\hbar = \frac{h}{2\pi}$ and h is PLANCK's constant, the electron momentum is given as p and m describe the electron mass. By comparing Eq. 25 and Eq. 26, a formula for the wave vector k, which will be used for the following equations, can be obtained:

$$k = \sqrt{\frac{2m}{\hbar^2}(E - E_{bind})} \qquad \textbf{Eq. 27}$$

The fine structure $\chi(k)$ can be described as a summation of all interferences of the spherical waves of the neighboring atoms with the outgoing wave of the absorbing atom. The scattering intensity is represented by the multiple amplitude factors:

$$\chi(k) = \sum_{j=1}^{shells} A_j(k) \cdot sin\phi_{ij}(k) \qquad \textbf{Eq. 28}$$

The formula contains two main components $A_j(k)$, which is expressing the amplitude of scattering intensity of the j^{th} coordination shell, and the sine function with the argument $\phi_{ij}(k)$ which is defined as the total phase shift. It includes the interatomic distance between the absorbing and the scattering atoms and can also be expressed in more detail as follows:

$$sin\phi_{ij}(k) = \sin\left[2kr_j - \phi_{ij}(k)\right] \qquad \textbf{Eq. 29}$$

Here r_j is defined as the distance of the absorbing atom and the scattering atom in the j^{th} shell. As the argument of the sine function can be related to the time needed for the photoelectron to travel to the neighboring atom and back, $2kr_j$ can be interpreted as the electron traveling the entire way to the scattering atom and back with constant velocity. Due to the positive charge of the nuclei, the electron is attracted and accelerated when it approaches the scattering atom or the absorbing atom again, resulting in a phase shift that shortens the total time required.[117] The total phase shift $\phi_{ij}(k)$ is equal to the phase shift of the backscattering atom plus twice that of the absorbing atom, for the outgoing and returning photoelectron.[97,117]

$$\phi_{ij}(k) = 2\phi_i(k) + \phi_j(k) \qquad \textbf{Eq. 30}$$

Where $\phi_i(k)$ is describing the phase shift of the absorbing atom and $\phi_j(k)$ describes the phase shift of the backscattering atoms in the j^{th} shell, respectively. Eq. 29 and Eq. 30 can be combined as:

$$\chi(k) = \sum_{j=1}^{shells} A_j(k) \cdot \sin\left[(2kr_j + \phi_{ij}(k)\right] \qquad \textbf{Eq. 31}$$

Eq. 31 shows that each coordination shell contributes to the fine structure signal in the form of a sine function multiplied by the corresponding amplitude. In the term $\sin[2kr_j + \phi_{ij}(k)]$ the sinusoidal oscillations as a function of the interatomic distances $(2kr_j)$ and the already described phase shift ϕ_{ij} are represented.[97,117] In EXAFS analysis, all sinusoidal functions from all coordination shells must be considered.[97,117] Within the amplitudes of the individual contributions, different information is included:

$$A_j(k) = \frac{N_j}{kr_j^2} S_i(k) F_j(k) e^{-2k^2\sigma_j^2} e^{-\frac{k_j}{\lambda_j(k)}} \qquad \textbf{Eq. 32}$$

The individual parameters will be explained in the description of the following formula which is a combination of Eq. 31 and Eq. 32.

$$\chi(k) = \sum_{j=1}^{shells} \frac{N_j}{kr_j^2} S_i(k) F_j(k) e^{-2\sigma_j^2 k_j^2} e^{-\frac{2k_j}{\lambda_j(k)}} \cdot \sin[2kr_j + \phi_{ij}(k)] \qquad \textbf{Eq. 33}$$

This formula is known as the EXAFS equation.[97,117] In N_j the number of nearby atoms in the j^{th} shell is addressed. The index *j* can be simplified as atom type because all atoms, with similar distance and type, are defined as a single coordination shell. The distance dependence of the vibration amplitude is reflected by the term $1/kr_j^2$. Thereby, the corresponding EXAFS signal appears weaker, the larger the distances between absorbing and backscattering atoms are. This results in a dominant influence of the nearest and next-nearest neighbors in EXAFS signal and the contributions from shells with larger distances are attenuated. The backscattering amplitude $F_j(k)$ from each of the N_j neighboring atoms in the j^{th} shell is also considered. Due to the resonant nature of the backscattering process, the backscattering amplitude is increased, when the photoelectron energy is equal to the energy of the orbitals of the backscattering atom. Since the electronic configuration of each atom is unique, the backscattering amplitude results in element-specific pattern.[117] Furthermore, the radial distance of the atom is averaged, so the distribution can be approximated by a GAUSSian function with square deviation σ_j^2. In reference to X-ray and neutron scattering, it is called the DEBYE-WALLER factor. It includes contributions from static disorder (σ_{stat}) and vibrational disorder (σ_{vib}). The latter is caused by lattice vibrations of the atoms and is temperature dependent. At low temperatures, these contributions can be suppressed and determined separately.[97]

The last two terms of the EXAFS formula belong to the processes of inelastic scattering and occur when a photoelectron is excited by the absorbing atom and the amplitude of the photoelectron is attenuated.[97] The first term $S_i(k)$ is the amplitude attenuating factor and is caused by multiple excitations of the absorbing atom *i.* The second process of inelastic scattering in EXAFS measurements is the excitation of neighboring atoms by excited photoelectrons and is expressed by the term $e^{-\frac{2k_j}{\lambda_j(k)}}$. Accordingly, the intensity is attenuated due to inelastic scattering of the electron and decreases as a function of the inelastic mean free path length $\lambda_j(k)$ of the photoelectron, leading to an amplitude loss.[97,117]

Taking these considerations into account, the relationship between energy and X-ray absorption coefficient allows the analysis of the local structure around certain atoms.[119]

4.3 Data reduction

After conversion of the experimental data into a spectrum, further steps of data reduction must be performed:[117,123] First, pre-edge line and post-edge line have to be determined to normalize the spectra. As a second step, background removal and fine structure extraction must then be performed to obtain the structural parameters from the EXAFS data. It is necessary to be able to resolve the experimental data into the individual wave signals of the different backscattering atoms in different coordination spheres.[97] In the third step, the fine structure is converted to *k*-space. Then the $\chi(k)$ data is FOURIER transformed which yields a function depending on the radial distribution function of the distance *r* to the absorbing atom.

4.3.1 Determination of pre-edge, post-edge and normalization

In an EXAFS analysis, the energy region above the absorption edge is extracted. In the first step, a raw XAS spectrum must be background-reduced and normalized.

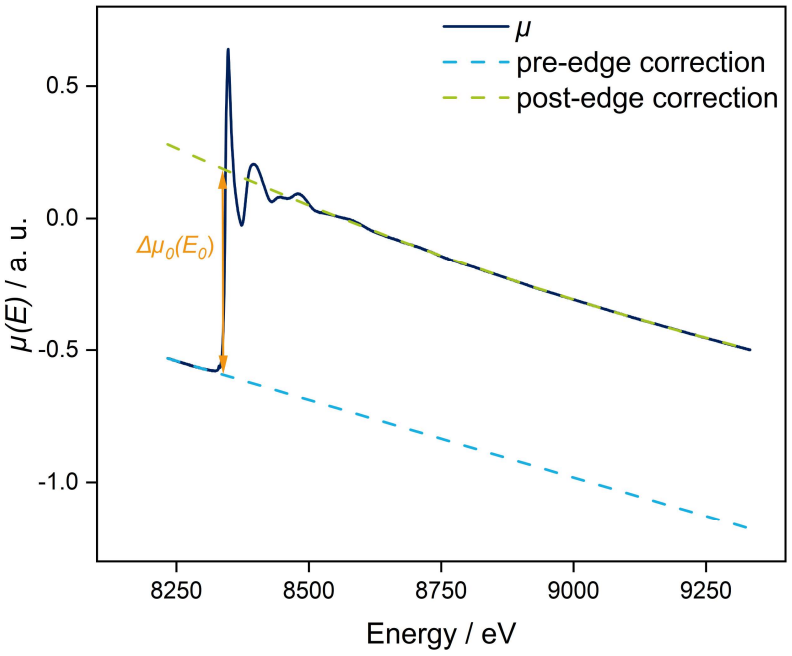

Figure 12: Experimental XAS spectrum of the Ni(II) based MOF Ni(BDC)(PNO) in dark blue. The fitted pre-edge line is shown dashed and in light blue. The post-edge line is plotted dashed and light green.

In most cases, a Victoreen-spline of the form $\mu_{pre\text{-}edge}=cE^{-3} - dE^{-4}$ is used to approximate the shape of the pre-edge region, alternatively simple linear or quadratic polynomials can be used.[123] The fitted background function is extrapolated and subtracted from the spectrum by the formula $\mu(E)=\mu - \mu_{pre\text{-}edge}$, as shown in Figure 12. In addition, the post-edge line is determined by approximating the spectrum after the white-line using a polynomial function. Afterwards, this line is extrapolated analogous to the pre-edge line and subtracted from the spectrum. With the help of the distance between both lines, the normalization factor $\Delta\mu_0(E_0)$ is obtained. This serves as denominator for the normalization of μ-μ_0. Thus, the *elemental* absorption coefficient of the chemical element under investigation is obtained.[113,123]

4.3.2 Background removal and extraction of the fine structure

The next step is to subtract from the absorption coefficient $\mu(E)$ the atomic background $\mu_0(E)$. This is supposed to represent the absorption coefficient of just that atom in an isolated environment without backscatterers. Since the atomic background is affected by non-specific background factors such as the baseline of the spectrometer, beam harmonics, elastic scattering, etc., it is usually not known and cannot be calculated or experimentally determined. Therefore, the atomic background $\mu_0(E)$ is often approximated as the smooth part of the measured total absorption $\mu(E)$ (cf. Figure 13), which can be modeled by different fitting procedures. Usually, least-square fits with polynomial splines or B-splines are used.

If the *least-squares method* is chosen to fit the oscillations, low-frequency background signals can be removed from $\mu(E)$ without attenuating the more frequent EXAFS oscillations. To investigate whether the background has been correctly determined, the FOURIER transform can be examined. Low-frequency oscillations and signals are visible at unphysically small distances of about 1 Å indicate wrong background subtraction. In Figure 13 a spline adjusted to the shown absorption spectrum can be seen. This spline shows the optimal shape since both, the edge position and a low-frequency oscillation, are represented.[97,123]

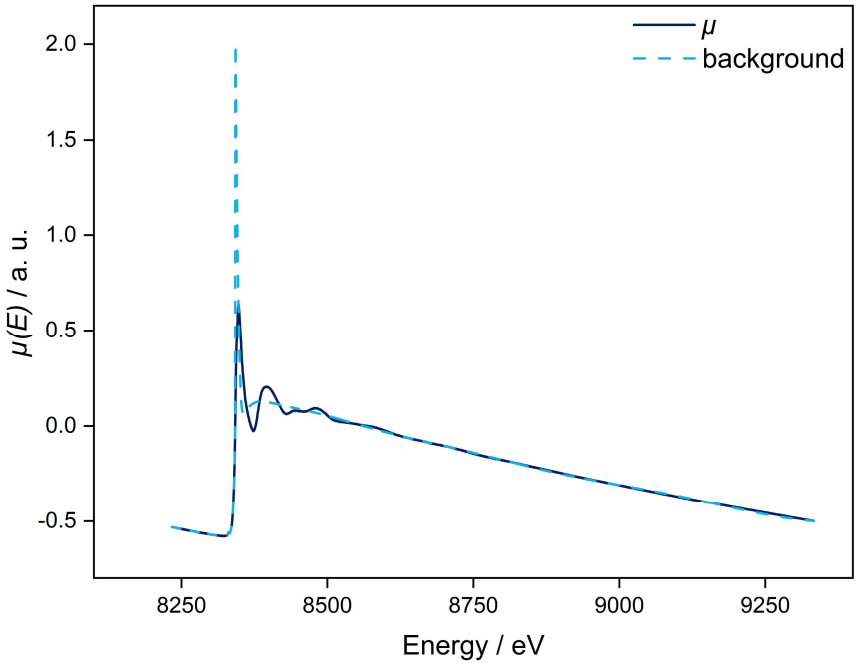

Figure 13: Experimental XAS spectrum of the Ni(II) based MOF Ni(BDC)(PNO) in dark blue. The atomic background function $\mu_0(E)$ is shown dashed and in light blue.

4.3.3 Conversion to *k*-space and FOURIER transformation

Lastly, the energy-dependent fine structure formula, obtained in the beforementioned step, $\chi(E)$ must be converted from E to k-space. Therefore Eq. 27 is used. According to CHANTLER, the absorption edge E_0 is defined as strong increase of the linear absorption coefficient that occurs when the energy of the photon is equal to that of a corresponding atomic shell (K, L_I, L_{II}, L_{III}, etc., equal to the formation of electron holes in the atomic subshells $1s$, $2s$, $2p_{1/2}$, $2p_{3/2}$, etc. respectively).[136] The inflection point, that corresponds to the allowed transition, in the XAS spectrum is usually denoted as E_0. However, the exact position of the local maximum can be superimposed due to the presence of electronic transitions and pre-edge peak.[97,117,123] Although an analysis of the spectrum can also be made in k-space, a FOURIER transform is usually performed using the following equation:[117,123]

$$FT(r) = \frac{1}{\sqrt{2\pi}} \int_{k_{min}}^{k_{max}} k^n \chi(k) e^{i2kr} dk \qquad \textbf{Eq. 34}$$

In the equation, $\chi(k)$ corresponds to the term obtained from Eq. 33. The parameter n can vary between 0 and 3 and weights the EXAFS spectrum in order to promote oscillations at different k ranges. Using the FOURIER transform of $\chi(k)$, a pseudo-radial distribution function with peaks at distances of the atoms in the vicinity is obtained. Since the phase factors in the sinusoidal function (cf. Eq. 30) depend on the energy, atomic distances are obtained in the FOURIER

transform, which are about 0.2 to 0.5 Å shorter than the physical distances. FOURIER transform is a complex function by which real and imaginary parts are obtained. The real part is mainly influenced by the number of neighbors and the disorder. The imaginary part is responsible for an accurate determination of the distance between the absorber and backscatterer as well as for the detection of unknown contributions within the EXAFS analysis.[117]

5 X-ray emission spectroscopy

At the beginning of the 20th century, the foundation for today's X-ray emission spectroscopy (XES) was established. In the 1910s X-ray diffraction was discovered and investigated. WILLIAM L. BRAGG, WILLIAM H. BRAGG and MAX VON LAUE found that when waves are scattered from a periodic crystal structure, the scattering angle changes as a function of the wavelengths, and thus the energy.[137] During that time, the fundamental physical processes of the discovery posed a great challenge to the scientists working on it, especially the development of measuring instruments for experiments was of great interest.[138] The observation was made that through the energy dependence of the diffraction angle, the arrangement of atoms in the crystal can be determined and conversely used to resolve the energy distribution of X-rays.[138] These first experiments, full of new observations, were conducted with a simple setup. A crystal was mounted on a flat rotating plate and an X-ray tube produced radiation which was directed through several slits toward the crystal. The scattered X-rays were collected on a photographic plate.[138] This opened up the possibility of investigating the properties of X-rays in detail. Thus, the energies of the characteristic X-ray lines could be determined, and the mechanisms of X-ray scattering could be studied in more detail. Thanks to these findings, in the following years X-ray spectroscopy played a major role in the elaboration and establishment of atomic structure models and theories of quantum physics.[139,140] In 1913, HENRY G. J. MOSELEY succeeded in establishing systematics of the wavelengths of the characteristic X-ray emission line of an element, thus proving the concept of atomic number. This played a decisive role in establishing the periodic table of the elements as it is known today.[141] As the research based on X-rays progressed, the need for highly efficient detection systems with better time resolution emerged. Different approaches were developed in the 1930s, of which mainly two provided the desired progress. The first was based on reflection geometry (BRAGG optics) and the second was on transmission geometry (LAUE optics) using curved diffraction optics. Based on these systems, various geometric arrangements have been proposed. Scientists such as YVETTE CAUCHOIS, JESSE DUMOND, H. H. JOHANN, TRYGGVE JOHANSSON, and L. VON HAMOS developed different detector systems, but most were based on the so-called ROWLAND circle geometry.[142–144,145] Even today, modern X-ray spectrometers are based on these geometric arrangements, although significantly modified. Nowadays, X-ray emission is detected based on different methods. For example, X-ray fluorescence spectrometry (XRF) can be used for the elemental analysis of materials.[146] In addition, due to the now highly resolved emission lines, analysis can be done on the atomic species, the atomic environment, and the chemical states such as the oxidation or spin state.[102,139]

5.1 The principles of X-ray emission spectroscopy

The phenomenon of XES is a photon-in/photon-out process and is thus classified as X-ray scattering.[147] For simplification, it can be defined as a two-step event. In the first step, an electron is excited from the core state by a photon. In the second step, the created vacancy at a core level is filled by an electron from an energetically higher state. The excess of energy due to the energy difference between involved states is emitted in form of X-ray fluorescence radiation. XES can be theoretically described by the KRAMERS-HEISENBERG formula:[139,148]

$$F_{HK}(\omega_{in},\omega_{out}) = \frac{\omega_{out}}{\omega_{in}} \sum_f \left| \sum_n \frac{\langle f|\hat{O}'^{\dagger}|n\rangle \langle n|\hat{O}|g\rangle}{E_n - E_g - \hbar\omega_{in} - i\Gamma_n} \right|^2 \frac{\frac{\Gamma_f}{\pi}}{\left[E_f - E_g - \hbar\omega)\right]^2 + \Gamma_f^2} \qquad \textbf{Eq. 35}$$

In the formula, $\hbar\omega$ is the photon energy, $\hat{O}'^{\dagger}$ and $\hat{O}$ is describing the outgoing and incoming transition operators, respectively. E_g, E_n and E_f are ground, intermediate and the final states. The lifetime energy broadenings of the intermediate and final states are described by Γ_n and Γ_f, respectively. Only one ground state, but all intermediate and final states are considered and summed up. Both denominators are described by LORENTZian profiles. The first LORENTZian is a complex expression with the energy broadening Γ_n of the intermediate state, which appears in the imaginary part. The second LORENTZian, on the other hand, is represented by the lifetime of the final state. Here, the energy transfer must be equal to an energy difference in the system.[139] The interference effects that can occur only influence the intensities of the signals, but not the transition energies. Consequently, these can be neglected which leads to Eq. 36.

$$F_{HK}(\omega_{in},\omega_{out}) \approx \frac{\omega_{out}}{\omega_{in}} \sum_f \sum_n \frac{\left|\langle f|\hat{O}'^{\dagger}|n\rangle\right|^2 \left|\langle n|\hat{O}|g\rangle\right|^2}{(E_n - E_g - \hbar\omega_{in})^2 + \Gamma_n^2} \times \frac{\frac{\Gamma_f}{\pi}}{\left[E_f - E_g - \hbar(\omega_{in} - \omega_{out})\right]^2 + \Gamma_f^2} \qquad \textbf{Eq. 36}$$

In the given formula the cross-section is proportional to the product of the absorption, in which an electron is promoted from the ground state to the intermediate state, and the emission, where a transition from intermediate to final state occurs.[139] XES can be divided into three different variants,[149] which are described by the KRAMERS-HEISENBERG equation, but only two of them are commonly used: non-resonant and resonant. In the former, the electron is excited into the continuum. The intermediate state here is described by an excited ion with a core hole. Contrary, in the resonant XES, the excitation energy is chosen close to the absorption edge.

This leads to a scenario where the excited photoelectron is excited into the LUMO generating a core hole, while the charge of the atom is not changed.

Generally, in XES occupied orbitals are probed. The possible X-ray emission lines of a *3d* element are shown in Figure 14. The lowest energy emission line, shown in dark blue in Figure 14, results from the relaxation from a *2p* electron into the *1s* vacancy, is called *Kα*, and is a core-to-core (CtC) transition. Hereby two distinguishable features of $K\alpha_1$ and $K\alpha_2$ are measured, which are the result of the spin-orbit splitting into $2p_{1/2}$ and $2p_{3/2}$ (s. Figure 15).

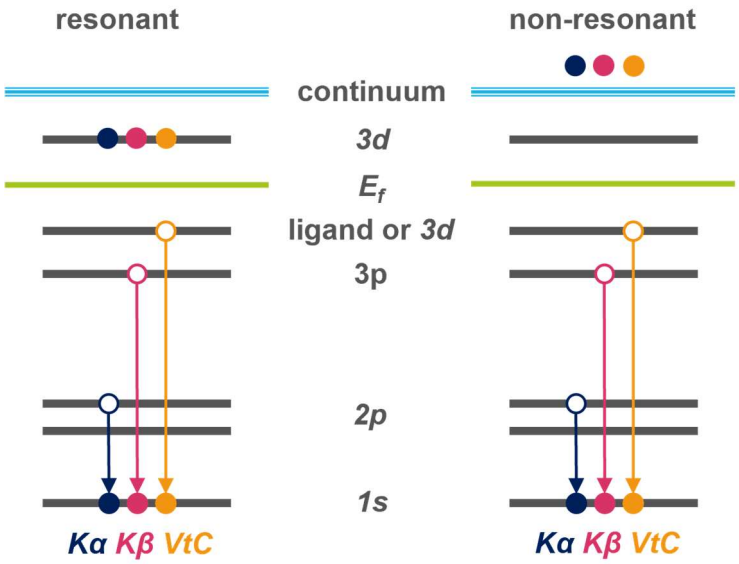

Figure 14: Scheme of transitions occurring for different emission lines. *Kα* is shown in dark blue, *Kβ* is shown in red, and valence-to-core (VtC) is shown in orange.

Due to the high transition probability, this is the XES signal with the highest intensity.[150] The technique of *Kα* measurement can also be used to collect high-energy resolution fluorescence detected (HERFD) XANES spectra, which will be explained later. The chemical insight of *Kα* is mainly focused on spin sensitivity since the *2p* orbitals are spatially and energetically separated from the valence orbitals.[151] The *Kα* emission can show different oxidation states of the element when the contraction of *3s* and *3p* orbitals are taken into account, even though they are not directly involved in the chemical bonding. If elements are probed, higher oxidation states lead to shifts towards higher energies in the *Kα* emission energy, since the electron density near the nucleus, is decreased when the valence electron is removed.[152,153] *Kα* line can behave differently in *3d* metals, and the competing effects are proposed as an explanation to this phenomena.[153]

With higher incident energies the *Kβ*, which is the result of a *3p*→*1s* transition, and the *3d*→*1s* based valence-to-core (VtC) features become visible (cf. Figure 15).

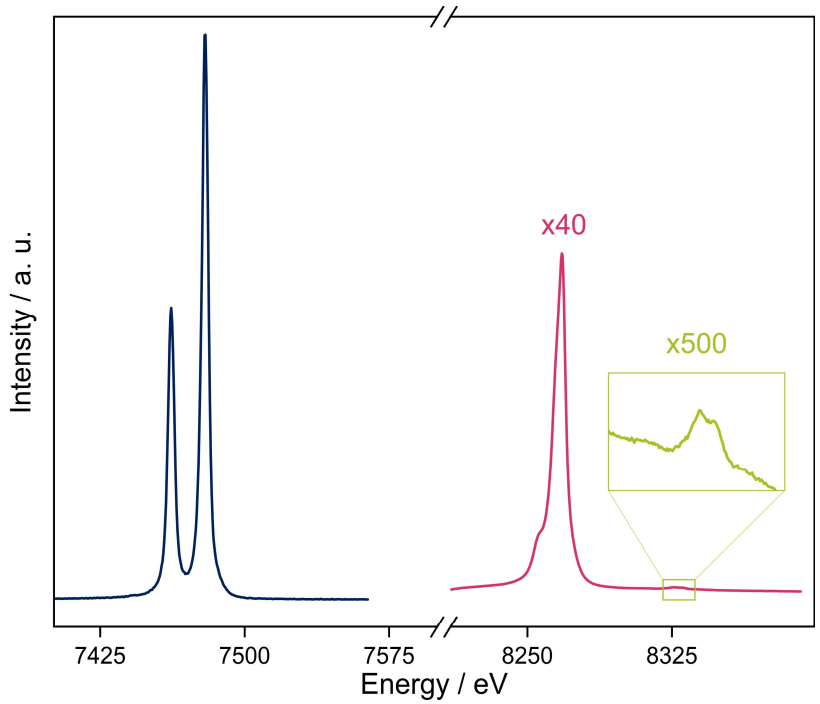

Figure 15: XES spectra of NiO for the transitions of *Kα₁* and *Kα₂* (dark blue), *Kβ* (red), and VtC (inset, green).

5.2 The Kβ emission line

The *Kβ* emission line is measured due to its high chemical sensitivity. Thus, the *Kβ*-based transitions are explained in more detail in the following chapters.

5.2.1 Core-to-core X-ray emission spectroscopy

In *3d* elements, the core-to-core (CtC) XES measurements are either the result of *2p→1s Kα* transitions or *3p→1s Kβ* transitions (cf. chapter 5.1, Figure 14 and Figure 15). Similarly to the case of *Kα* emission, in the beginning, *1s* electron is excited to create a core hole. The vacancy is filled by a *3p→1s* relaxation and the energy is emitted in form of X-ray fluorescence radiation, equal to the energetic difference between the involved states. The energy profile of this radiation can be detected providing information about the oxidation and spin states. Depending on the element and its spin state, the CtC-XES spectrum of a *3d*-metal is usually divided into two main features: the weaker and low-energy peak *Kβ'* or *Kβ* satellite feature, and the high energy *Kβ* mainline or, $K\beta_{1,3}$ line.[102,154] The *Kβ* mainline can be split by spin-orbit coupling and thus be separated into a $K\beta_1$ ($3p_{3/2} \rightarrow 1s$) and a $K\beta_3$ ($3p_{1/2} \rightarrow 1s$) transition.[155] The shape of the

CtC emission line is the result of *3p-3d* exchange interaction, due to the core-hole creation in the *3p* state upon *3p→1s* relaxation. An unpaired *3p* electron is created which then interacts with an unpaired *3d* electron. This electronic interaction is the reason for the splitting between *Kβ'* and $K\beta_{1,3}$ features. The *Kβ'* feature is located and is highly sensitive to spin configuration. With a higher spin state, the *Kβ'* feature is moving further from the $K\beta_{1,3}$ main feature, simultaneously the intensity of *Kβ'* is increasing, while $K\beta_{1,3}$ is decreasing.[154] Thus, it is possible to discriminate between low-spin (LS) and high-spin (HS) states with CtC-XES (cf. Figure 16).[102] With a higher spin state, more *3d* electrons are unpaired, resulting in increased *3p-3d* interaction. This leads to an enlarged intensity and a $K\beta_{1,3}$ shift towards higher energies in the spectrum.[139,141]

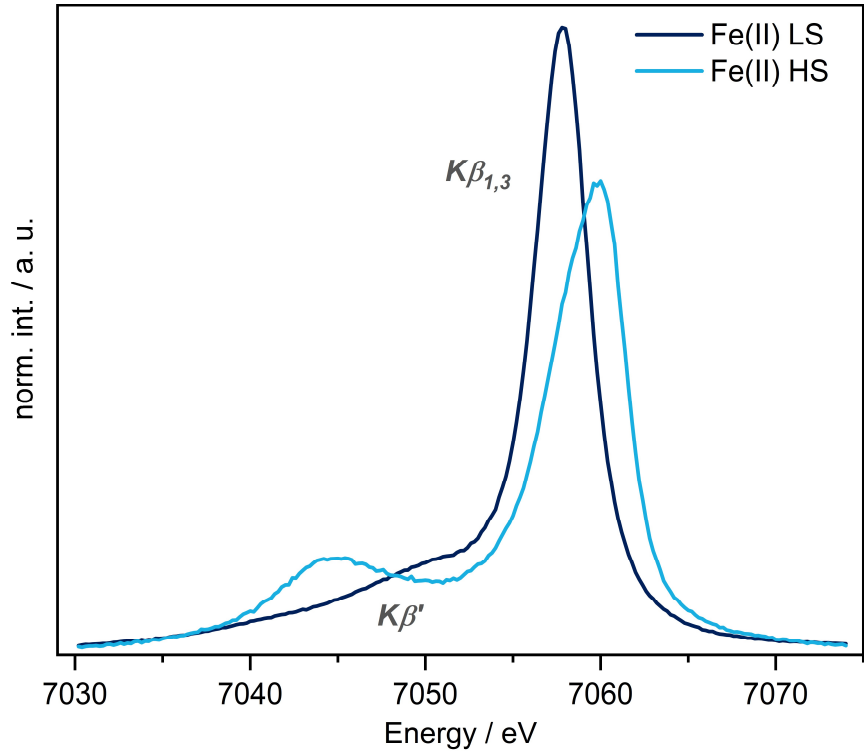

Figure 16: CtC-XES spectra of Fe(II) *Kβ* lines. The low-spin (LS) complex is shown in dark blue, and the high-spin (HS) complex is shown in light blue.

A further effect that influences the features of the spectrum is caused by the screening of the core hole potential. As the effective number of *3d* electrons decreases at higher oxidation states, the valence charge density is also reduced, thus changing the position and shape of the *Kβ* line. GLATZEL was able to show that this shift in the $K\beta_{1,3}$ feature is not due to changes in core-hole screening but to changes in the *3p-3d* exchange splitting.[156] The impact of the core-hole screening is indirect since it modifies the *3p-3d* exchange splitting rate.[102,139] Furthermore, the valence charge density is affected by the amount of covalent character of the bond, since as the amount of covalency of the bond increases, the electron cloud between the

metal and ligand is more delocalized. Several publications in recent years have focused on the study and monitoring of the spin state using the *Kβ* emission line. In particular, the change of the magnetic moment on the *3d* orbitals and the associated change of the spin state of a system has been described.[157,158]

5.2.2 Valence-to-core X-ray emission spectroscopy

Valence-to-core (VtC) emission is of particular interest from a chemical point of view since it is directly influenced by the coordination environment of the metal center. In VtC, transitions from the valence orbitals, including the highest occupied molecular orbital (HOMO) and ligand orbitals, to the metal *1s* core hole are probed.[102,139,158,159,160–162] Due to the dependence of the HOMO on the composition and the spin state at the metal center, the shape of the VtC spectrum varies. For a *3d* transition metal, e. g. Ni or Fe, the $K\beta_{2,5}$ is responsible for VtC signal through a $3d \rightarrow 1s$ transition (cf. chapter 5.1, Figure 14 and Figure 15), which is dipole forbidden and hence about the factor 100 weaker than the $K\beta_{1,3}$ signal. In addition, due to the higher energy difference of the involved states, the probability of the VtC emission is lower. However, it has been shown that, just as in the case of the pre-peak signal, there is a direct correlation of the $K\beta_{2,5}$ with *nd/(n+1)p* hybridization.[163,164] The extent to which this hybridization is possible depends on the coordination geometry.[161,162] If the configuration is centrosymmetric, e.g. an octahedron, no *nd/(n+1)p* hybridization can be detected. The ligand orbitals involved in bond creation, e.g. *2p*, lead to effective hybridization that allows electronic transitions to happen. If, on the other hand, a tetrahedral geometry is present, the strong hybridization increases the dipole character, and thus the transition probability increases as well.[127] Furthermore, the $K\beta_{2,5}$ intensity is affected by the metal-ligand bond length. If the distance is increasing, the $K\beta_{2,5}$ is decreased, since the overlap of the hybridized metal orbitals and the ligand orbitals is weakened.[158,160,162] As shown in Figure 17 a VtC spectrum consists of the $K\beta_{2,5}$ signal and its lower energy satellite, the *Kβ''* feature.

The *Kβ''* features are mainly the result of an electron relaxation from ligand *2s* orbitals to metal *1s* orbital and are therefore called cross-over transition. Consequently, the *Kβ''* feature is very sensitive to the ligand environment and the metal-ligand bond length.[102,158] Accordingly, unlike many other X-ray-based techniques such as EXAFS, VtC-XES can discriminate between light ligands of similar molecular weight such as C, N, or O, as the *Kβ''* feature shifts by approximately the *2s* binding energy of the atom.[102,158]

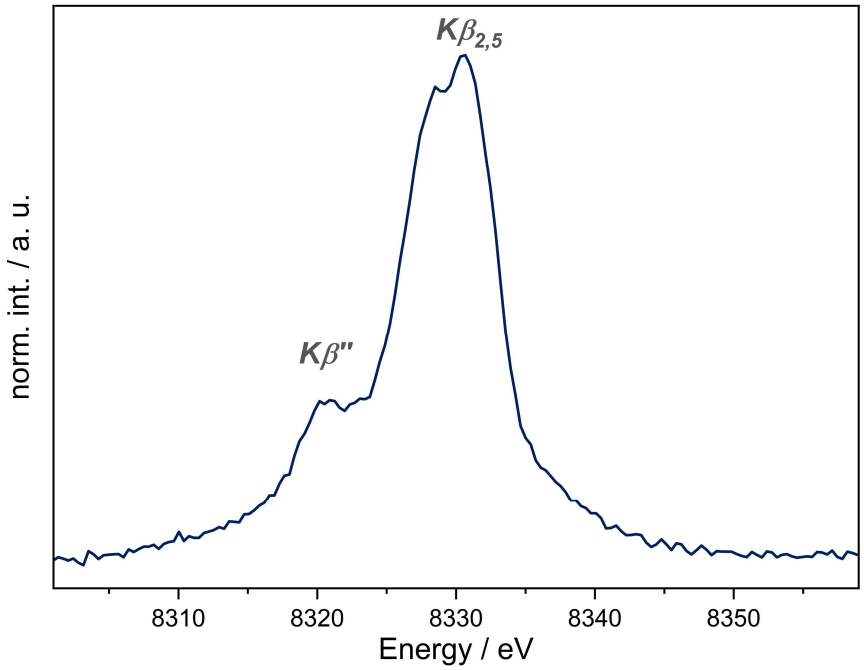

Figure 17: VtC spectrum of Ni_3C with the $K\beta_{2,5}$ line at higher energies and the $K\beta''$ at lower energies.

5.3 HERFD-XANES

In chapter 4.1 it was explained that the XAS pre-edge region provides information about the oxidation state and the local geometry. However, the detailed features in the pre-edge region are usually obscured in conventional XANES because of the *1s* core-hole lifetime broadening of the final states. According to HEISENBERG's Uncertainty Principle, for such short times, the intrinsic resolution is inversely proportional to the lifetime of the state.[154] A possibility to overcome these issues is to collect high-energy resolution fluorescence detected (HERFD) XANES spectra from the emission lines.[165] In HERFD-XANES, spectra are measured by monitoring a selected fluorescence decay channel with an energy bandwidth that is smaller than the natural lifetime broadening of the involved final state. Accordingly, an appropriate instrumental resolution is a prerequisite for HERFD-XANES measurements. In experimental practice, this causes the incident energy to scan the absorption edge, while simultaneously an analyzing crystal is used to discriminate the X-ray fluorescence with high resolution. As shown in Figure 18, the resulting HERFD-XANES spectrum for a *3d* transition metal, e.g. Ni, matches the features of the conventional XANES spectrum.[102,139] Looking closer at the pre-peak region, the key advantage of HERFD-XANES is the significantly better resolution, which allows for detecting features that are otherwise not visible. This allows additional information to be obtained, especially when combined with theoretical calculations.[166]

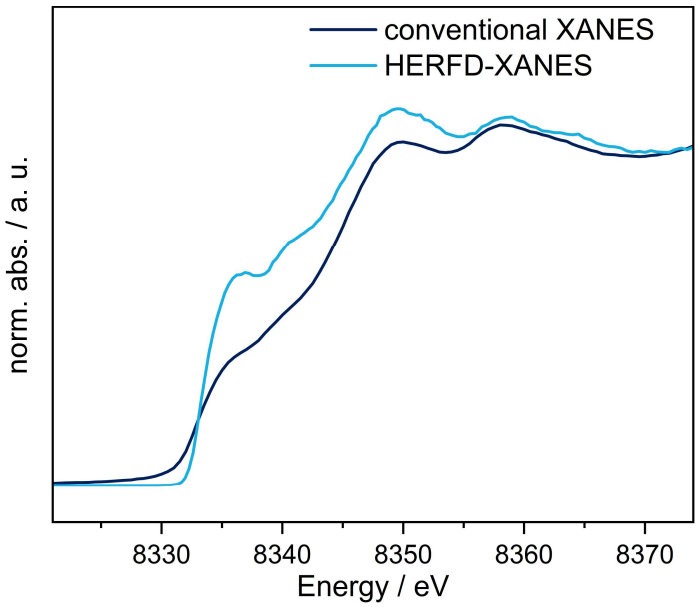

Figure 18: Comparison of the conventional XANES spectrum (dark blue) of Ni foil with the corresponding HERFD-XANES spectrum (light blue).

6 Synchrotron radiation as an X-ray source

For the usage of XAS and XES, the development of synchrotron radiation facilities as X-ray sources was crucial.[96,167] The advantage of synchrotron radiation can be, among other things, the higher flux of 10^6 to 10^9 more photons compared to an X-ray tube. Originally, 1st generation synchrotron facilities were cyclotrons (colliders) built only to perform experiments in high-energy physics. Synchrotron radiation was an undesirable by-product of the kinetic energy loss, but they were later modified to produce high-energy electromagnetic radiation.[96] To generate radiation in a synchrotron, charged particles are accelerated to a velocity close to the speed of light in a vacuum tube, which has a circular geometry. During this process, external magnetic fields maintain the trajectory of the particles. Each time the accelerated particles are deflected from a straight path, a cone of electromagnetic radiation with a tangential normal vector is generated. According to MAXWELL's equations,[96,168] this phenomenon applies to any kind of charged particle in a relativistic approach. Nevertheless, in most synchrotrons electrons are used, because they exhibit the highest ratio of energy to mass. This means that less energy is needed to accelerate the electrons to high energies.[169] In the 70s of the 20th century when SAYERS, STERN, and LYTLE published their work about EXAFS and made it a feasible analytic tool for non-crystalline species,[111] the second generation of synchrotron radiation facilities was developed. These improved and modified second-generation synchrotrons use bending magnets (cf. Figure 19) to deflect electrons and maintain their circular orbit.

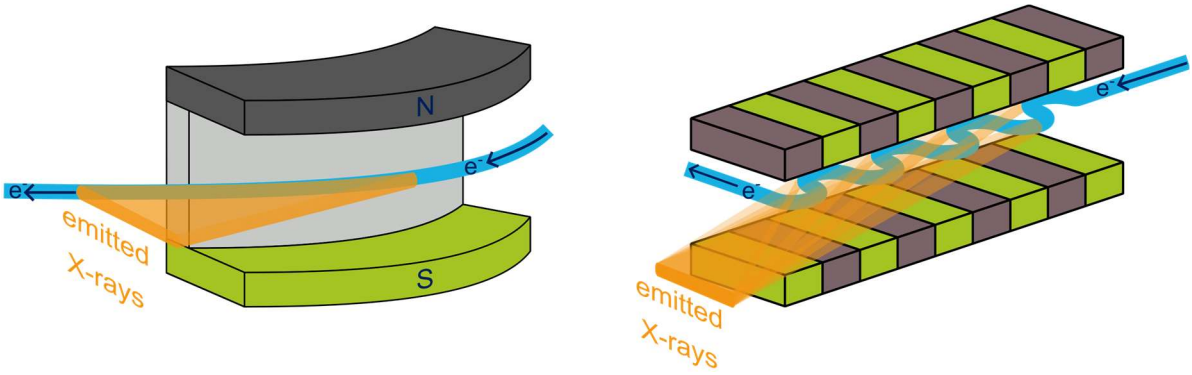

Figure 19: A schematic representation of a bending magnet (left) and an insertion device (right).

The flux, defined as the brightness per area, is only one of several parameters that further classify the quality of an X-ray source. The brightness is defined as the number of photons per second. Another important property is the intensity, given by the flux per area. The fourth parameter considered in the context of X-rays is brilliance (cf. Figure 20). It is the number of photons at a given source area together with specific angular divergence. It is given in photons per second, per 0.1% bandwidth, per source area, and unit of solid angle.[96] To ensure the low

particle beam cross-section required for high brilliance, a low spatial scattering of electrons, correspondingly a low emittance, is needed. Electrons in the accumulation ring are grouped in bunches. Consequently, the synchrotron radiation is not constant, but appears pulsed with defined time-period and phase.[169]

Figure 20: Schematic representation of the parameters used to calculate the flux, intensity, and brilliance of an X-ray source.

In addition to the bending magnets, in the third-generation synchrotrons, straight elements or insertion devices in particular wigglers, and undulators (cf. Figure 19) were introduced yielding ~10^4 times higher brilliance[96,170] of the X-ray source. These insertion devices are used in straight elements in the ring. An insertion device is composed of many linearly arranged magnets with subsequent opposite orientations of the magnetic field. Periodic magnetic fields force the electrons onto an undulating path. In the process, a tangential emission of radiation takes place at the turning point with each change of direction. The main difference between wigglers and undulators is the spatial period between the magnets, which describes the distance of an alternating pair of magnets. By tuning the distances between the magnets in the undulator, more coherent and intense emitted radiation over a smaller bandwidth can be achieved. With the wiggler, on the other hand, the beam is showing no coherence.

The latest development is the free-electron laser (FEL) technology. The pulses of FELs are much more intense than those of synchrotrons. They surpass the performance of earlier sources by many orders of magnitude,[171] improving essential parameters such as brightness, coherence, and shortness of the pulse duration.[170] Due to their high intensity and low repetition rate characteristics, FELs are perfectly suited for so-called single-shot and time-dependent (pump-probe) measurements.[171,172] Due to the high intensity of the beam, the sample is usually destroyed immediately, however, the flux is sufficient to generate a complete diffraction pattern or a spectrum in a single shot, which can then be detected with a position-sensitive, charge integrating detector.[96,173]

6.1 Principle of an XAS measurement

In an XAS measurement, there are typically three experimental modes to probe the sample: transmission, total fluorescence yield, and total electron yield. The latter will not be discussed further in the course of this work but is mentioned for the sake of completeness. In transmission mode, the intensity of the beam is measured in ionization chambers (I_0, I_1, I_2) before and after the X-ray beam has passed the sample as shown in Figure 21.

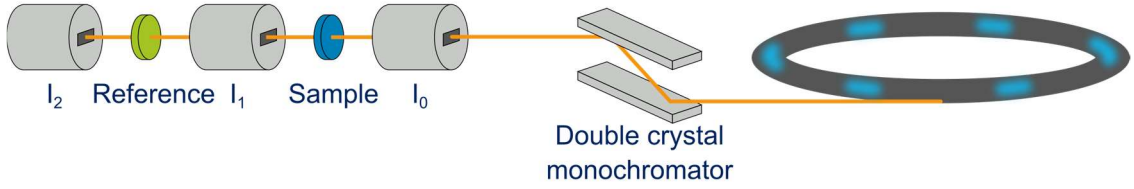

Figure 21: Schematic assembly of an XAS measurement in transmission geometry.

An ionization chamber is filled with gas, which is usually an inert gas like N_2, He, Ar, etc., and a pair of electrodes which are creating an electric field. By passing through the ionization chamber the X-ray beam is ionizing the gas. The generated charged particles are accelerated toward the anode and cathode inside the ionization chamber, respectively, generating a current that is proportional to the amount of ionized gas and thus to the intensity of the incident beam. The signal of the transmitted beam intensity is normalized to the incident beam intensity during the data reduction process.[96] By measuring a parameter that is proportional to the flux before and after the sample, logarithm and transformation of LAMBERT-BEER's law can be applied (cf. chapter 4.1). Since the thickness *d* is a parameter in the LAMBERT-BEER's law it is necessary that the sample is not too thick, homogeneous, and flat. Doing so, *d* is constant, and it is possible to measure a sufficiently good spectrum. Furthermore, the sample need relatively low concentration (0.1-10%), since the concentration is anticorrelated with the thickness of the sample. To ensure that the current spectral calibration is correct, a foil of the corresponding metal (cf. Figure 21, Reference) can be measured simultaneously to with the transmission measurement and any shifts in energy can be corrected.[123]

To overcome the issue of sample concentration and homogeneity, measurement in fluorescence mode can be carried out. For that, a fluorescence detector is placed at 90° in a horizontal plane towards the incident beam, whilst the sample is turned by 45° as presented in Figure 22.[96] The obtained fluorescence signal is normalized to the incident beam signal of the ionization chamber I_0. Again, since the core-hole relaxation process alters with the incoming energy and thus to the absorption, a spectrum similar to that obtained in the transmission mode is obtained.[123]

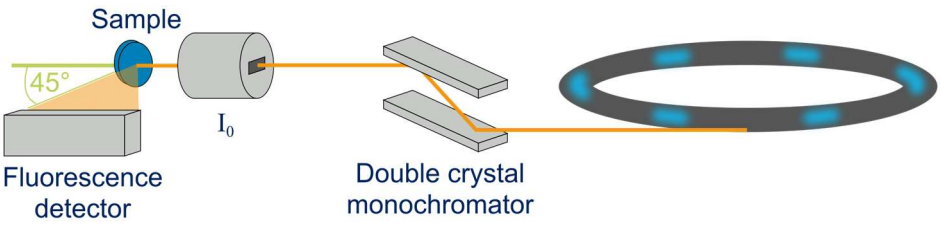

Figure 22: Schematic assembly of an XAS measurement in fluorescence mode.

The detection of the X-ray fluorescence is geometrically limited and there are additional accompanying physical effects to be included. Thus, the quality is usually not as high as that of a transmission measurement. The fluorescence detection is affected by self-absorption effects, is more susceptible to background noise (since all incident photons are recorded) and to inherent electronic noise of the detector. Nevertheless, the fluorescence geometry has the important advantage that a measurement can be made independent of the sample concentration. Furthermore, it opens the possibility of, for example, *in-situ* studies in modified cells that cannot be used in transmission geometry experiments.

6.2 Principle of an XES measurement

To measure all the before-mentioned methods in XES (cf. chapter 5) high energy-resolution analyzer crystals are needed. In principle, geometries for measuring XES can be distinguished between reflection detection according to BRAGG or transmission decay according to LAUE.[163] However, for photon energies that are below 20 000 eV, reflection geometries are usually used.[139] The principle of the XES spectrometers is based on the BRAGG equation:[139]

$$n\lambda = 2d \cdot sin(\theta) \qquad \textbf{Eq. 37}$$

Where n is the diffraction order, λ describes the X-ray photon wavelength, d is the lattice plane distance of a single crystal and θ is the angle between its surface and the incident beam. The BRAGG relation states that a photon with a given energy (wavelength) is diffracted by a single crystal only at a defined angle θ. In practice, the X-ray beam is scattered in an angular deviation close to the theoretical value θ. The angular width $\Delta\theta$ over which the BRAGG relation is satisfied is called the DARWIN width. $\Delta\theta$ depends on several factors, such as the quality and thickness of the crystal, of the lattice stress, and goes to zero for the case of working at an angle of 90°. Therefore, in practice, it is tried to work in the so-called backscatter geometry, which implies the angle of 90°. A contribution to the energy resolution can be estimated according to the derivation of the BRAGG equation.[174]

$$\frac{dE}{E} = d\theta \cdot \cot(\theta) \qquad \textbf{Eq. 38}$$

The spectrometers for measuring XES can be divided into two groups: the scanning and the dispersive geometries. The two different geometries will be described in more detail below.

6.2.1 The scanning spectrometers

The focusing or scanning geometry is based on a ROWLAND circle and mainly two solutions: JOHANN- and JOHANNSSON-types.[142,143] In this geometric setup, the radiation source is a fixed point. Whereas the sample, the analyzer crystals and the detector are always moving on the ROWLAND circle. The most common method is the JOHANN setup.[139] Here, the detector and the sample are lying on the circle with a radius of *R*. The reflecting surface of the crystal is formed in a parabolic way according to two times the radius of the circle. The radius of the bent crystal and the ROWLAND circle differ from each other, consequently, only one point of the bent crystal lies directly on the ROWLAND circle. Subsequently, this leads to the so-called JOHANN aberration, which is negligible when approximating the backscatter geometry (θ=90°). In the original JOHANN geometry, the analyzer crystal should be bent cylindrically along the ROWLAND circle.[142] As shown in Figure 23, multiple analyzing crystals can be installed on overlapping ROWLAND circles. The experimental setup is usually such that the sample is fixed, and both the crystals and the detector are moving along the ROWLAND circles. The JOHANSSON approach is very similar, but crystals have their radius bent to the radius *R* of the ROWLAND circle, which removes the JOHANN aberration.[143] However, JOHANSSON-type crystals are employed less frequently in practice owing to the difficulty and expense of producing them.[175]

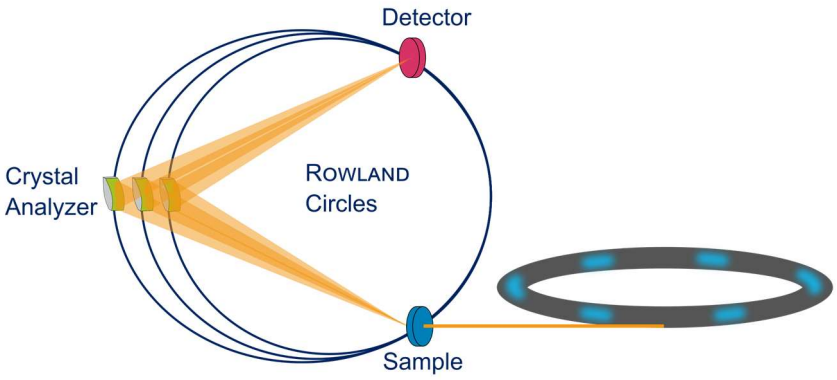

Figure 23: JOHANN-type X-ray emission spectrometer with three analyzer crystals.

The additional benefit is that geometries deviating from the backscattering angle can also be selected providing higher flexibility of the setup. A spectrometer of the JOHANSSON type is to

be preferred if lower energies of 1.4 to about 4.5 keV are to be measured. In such an energy region, small BRAGG angles are unavoidable and no crystal analyzers with angles greater than 70° are available.[139]

6.2.2 The dispersive spectrometer

As an alternative to the scanning approach, the dispersive geometry setup (cf. Figure 24) can be applied. Crystals over a range of BRAGG angles are combined with a position-sensitive detector,[139] and no scanning of the emission energy is necessary. Dispersive spectrometers are of great interest in the investigation of time-dependent measurements like catalysis, or excited-state investigations in a pump-probe experiment since it allows recording of a single-shot spectrum. The simplest dispersive spectrometer design uses a flat analyzing crystal that diffracts the incoming X-rays and energy-wise focuses them on the 2D detector. However, this setup does not allow high resolution with simultaneous detection of a large solid angle. A solution to this problem is provided by the VON HAMOS geometry,[144] which is based on a matrix of cylindrically bent crystal analyzers. It combines the properties of the flat crystal, especially high energy resolution, with the property of the bent crystal to be able to cover large solid angles. Following BRAGG's law, the X-rays scattered from the sample are diffracted and focused by the crystals and can then be recorded by the detector.

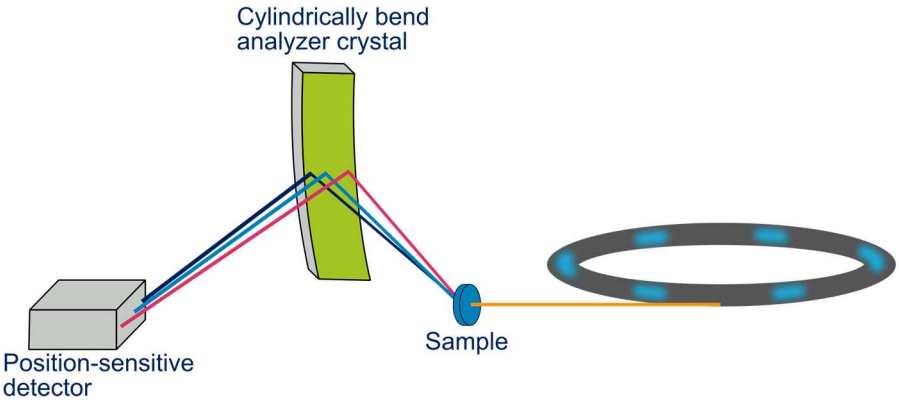

Figure 24: A VON HAMOS Spectrometer as an example of dispersive geometry.

7 Aim of this work

To develop catalysts for the methanation of CO_2 with high stability to hydrogen dropouts that occur due to weather conditions (cf. Figure 25), the approach of thermal decomposition of Ni-based MOFs is presented. Here, a synthesized Ni(BDC)(PNO) MOF, containing Ni(II) centers with benzene-1,4-dicarboxylate (BDC) and pyridine-*N*-oxide (PNO) substituents, is thermally decomposed in different atmospheres (inert, 5% and 10% H_2 in He) at varying temperatures (350 °C, 375 °C, 400 °C and 500 °C). A highly dispersed and undefined Ni@C pre-catalyst species with a broad particle size distribution is obtained. Within the subproject MOFCO$_2$DYN-X^2 of the DFG priority program SPP2080 DynaKat, the catalyst system based on this approach should be optimized and characterized. However, to specifically tailor these catalysts, a profound understanding of the pre-catalysts and the resulting catalysts is crucial. Due to the high complexity of the system, a multidimensional measurement procedure consisting of methods based on hard X-rays is necessary.

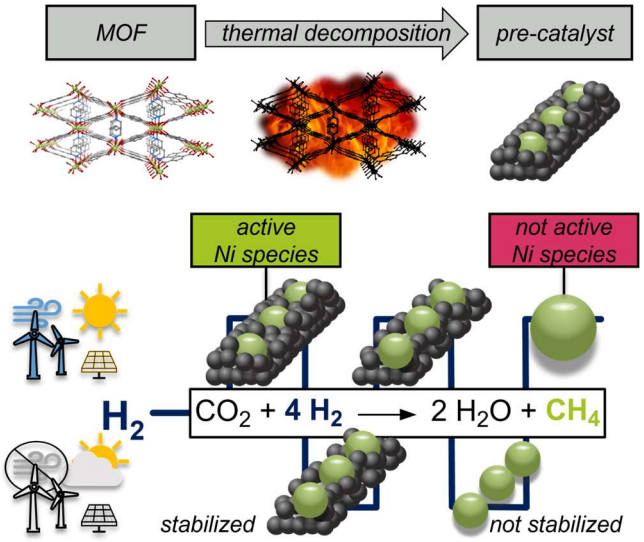

Figure 25: A schematic illustration of the synthesis route of the pre-catalyst *via* thermal decomposition (top). Scheme of weather-induced fluctuations in hydrogen production and the resulting deactivation of the catalyst for the methanation reaction of CO_2 (bottom).

The aim of this work is a thorough spectroscopic investigation of the novel Ni catalysts embedded in a carbon matrix using XAS and XES. For this purpose, a structure-activity correlation should first be determined. Therefore, the synthesized Ni-MOF was thermally decomposed in different temperatures and different gas atmospheres and investigated in detail to elucidate the structural properties of the resulting pre-catalysts by XAS. These results were subsequently to be correlated with the catalytic activity of these catalysts to optimize their preparation

in terms of structural and catalytic properties. Building on the findings obtained, an in-depth investigation based on XES was carried out, establishing a novel approach to the analysis of VtC spectra of highly undefined mixtures. Here, built on a linear combination of HERFD-XANES spectra, which was combined with a theoretical calculation based on the FEFF software package, a VtC analysis was performed. This allowed correlations between particle growth and the presence of Ni(II) in the compound to be determined through electronic interactions. Furthermore, a positive influence of NiO in the pre-catalyst sample was shown with respect to the catalytic activity. These results were complemented by evidence for a carbon layer around the Ni species by VtC analysis. To further extend the *ex-situ* analyses, *in-situ* studies were performed by XAS to investigate the activated catalyst and the catalytically active species under reaction conditions. Three different dropout scenarios were applied to realize a simulation of the hydrogen losses. It was found, as by XES, that in the samples showing high catalytic activity, a NiO layer is present in the pre-catalysts, which must be reduced in the first step. Furthermore, a clear correlation between the presence of a carbon matrix and the catalytic stability could be exhibited, insofar as that the catalyst deactivates as soon as the carbon layer is no longer present. In the two scenarios where hydrogen is only reduced but not switched off, the catalyst remains stable. However, if there is a complete loss of hydrogen, the catalyst deactivates after a few cycles.

8 Hard X-ray based techniques for structural investigations of CO_2 methanation catalysts prepared by MOF decomposition

In this chapter, the first characterization tests of the novel nickel catalyst system for the methanation of CO_2 are discussed. In particular, the focus was on the *ex-situ* characterization of the pre-catalysts. With the help of the analytical methods used, the first structure-activity correlations could be identified.

Participation in this publication

N. Prinz & M. Zobel – PDF analysis, TEM measurements

L. Schwensow & W. Kleist – catalyst preparation, catalytic studies, XRD measurements

A. Jentys – measuring of one sample in XAS

S. Wendholt & M. Bauer – XAS measurements, XANES analysis, LC-XANES, EXAFS analysis

Reproduced from:

Hard X-ray based techniques for structural investigations of CO_2 methanation catalysts prepared by MOF decomposition

Nils Prinz, Leif Schwensow, Sven Wendholt, Andreas Jentys, Matthias Bauer, Wolfgang Kleist and Mirijam Zobel, *Nanoscale,* **2020**, *12*, 15800-15813. (DOI: 10.1039/d0nr01750g)

With permission from the Royal Society from Chemistry.

Nanoscale

ROYAL SOCIETY OF CHEMISTRY

PAPER

View Article Online
View Journal | View Issue

Check for updates

Cite this: *Nanoscale*, 2020, **12**, 15800

Hard X-ray-based techniques for structural investigations of CO_2 methanation catalysts prepared by MOF decomposition†

Nils Prinz, ‡[a] Leif Schwensow, ‡[b] Sven Wendholt, ‡[c] Andreas Jentys, [d] Matthias Bauer, *[c] Wolfgang Kleist *[b] and Mirijam Zobel *[a]

Thermal decomposition of metal–organic framework (MOF) precursors is a recent method to create well-dispersed metal centers within active catalyst materials with enhanced stability, as required for dynamic operation conditions in light of challenges caused by the renewable energy supply. Here, we use a hard X-ray-based toolbox of pair distribution function (PDF) and X-ray absorption spectroscopy (XAS) analysis combined with X-ray diffraction and catalytic activity tests to investigate structure–activity correlations of methanation catalysts obtained by thermal decomposition of a Ni(BDC)(PNO) MOF precursor. Increasing the decomposition temperature from 350 to 500 °C resulted in Ni_{fcc} nanoparticles with increasing particle sizes, alongside a decrease in Ni^{2+} species and strain-induced peak broadening. For lower temperatures and inert atmosphere, Ni_3C and NiO phases co-existed. A graphitic shell stabilized the Ni particles. Compared to an inert atmosphere, reducing conditions led to larger particles and a faster decomposition of the MOF precursor. Catalytic studies revealed that the decomposition at an intermediate temperature of 375 °C in 5% H_2/He is the best set of parameters to obtain high specific surface areas while maintaining particle sizes that feature many active Ni centers for the formation of CH_4.

Received 1st March 2020,
Accepted 2nd July 2020

DOI: 10.1039/d0nr01750g

rsc.li/nanoscale

Introduction

The long-term storage of energy from renewable resources will be a key challenge for sustainable power supply within the next decades. In this scenario, excess energy from wind or solar sources can be utilized to operate electrochemical cells for water electrolysis, generating hydrogen in a sustainable way. This hydrogen can be subsequently used for the synthesis of valuable energy carriers. A promising approach within this "power to X" (P2X) concept is the methanation of CO_2 according to the Sabatier reaction (eqn (1)).[1,2]

$$CO_2 + 4H_2 \rightleftharpoons CH_4 + 2H_2O\ (g) \quad (1)$$

The formation of methane from CO_2 can be formally described by a combination of the reverse water gas shift reaction (eqn (2)) and the methanation of CO (eqn (3)).

$$CO_2 + H_2 \rightleftharpoons CO + H_2O\ (g) \quad (2)$$

$$CO + 3H_2 \rightleftharpoons CH_4 + H_2O\ (g) \quad (3)$$

Typical catalyst systems for this transformation are supported Ni species due to their high activity and methane selectivity at relatively mild conditions.[3] Since the catalytic performance depends strongly on the properties and the nature of the active Ni species and the support, various studies have been performed to enhance the catalytic performance and to study the reaction mechanisms.[4] Improvements were achieved by optimizing the properties of the active Ni sites and their dispersion at the surface of the support materials.[5–7] In many cases, the applied preparation routes lead to a surface or even bulk oxidation of the Ni particles at the end of the synthesis. Since metallic Ni species are required to catalyze the methanation reaction, these pre-catalysts need to be activated in a reducing atmosphere prior to the methanation reaction.

Due to the fluctuations in solar or wind energy, the hydrogen production will also be fluctuating, which represents a major challenge for the continuous operation of the methanation reactor, since the active catalyst is prone to deactivation by

[a]*Chemistry Department, University Bayreuth, Universitätsstr. 30, Bayreuth 95447, Germany. E-mail: mirijam.zobel@uni-bayreuth.de*
[b]*Faculty of Chemistry and Biochemistry, Ruhr University Bochum, Universitätsstr. 150, 44801 Bochum, Germany. E-mail: wolfgang.kleist@rub.de*
[c]*Faculty of Science and Center for Sustainable Systems Design (CSSD), Paderborn University, Warburger Str. 100, Paderborn 33098, Germany. E-mail: matthias.bauer@upb.de*
[d]*Department of Chemistry, Technical University of Munich, Lichtenbergstr. 4, 85748 Garching, Germany*

†Electronic supplementary information (ESI) available. See DOI: 10.1039/d0nr01750g

‡These authors contributed equally to this work.

surface oxidation or sintering under dynamic feed conditions. Operando studies revealed a severe deactivation of active Ni species during periods of a hydrogen dropout.[8,9] Consequently, for P2X reactions based on renewable energies, highly stable catalyst systems are required, which can tolerate fluctuating conditions at elevated temperatures without being deactivated under the resulting less reducing atmospheres during a hydrogen dropout.

In the present contribution, we have chosen the thermal decomposition of metal–organic framework (MOF) precursors as a promising approach for the synthesis of carbon-supported catalysts featuring unique properties.[10,11] The so-called MOF-mediated synthesis (MOFMS) describes the treatment of a metal–organic framework in a defined atmosphere at elevated temperatures.[12] During this process, the organic linkers of the MOF precursor are decomposed, oxidized or converted to carbonaceous species and the resulting materials typically feature high dispersions of metal nanoparticles, which are supported and stabilized by a carbon matrix.[13,14]

The easy synthesis, modifiability, versatility and high crystallinity make MOFs promising as precursor materials for the synthesis of catalytically relevant materials, which can feature high thermochemical resistance, improved longevity and hydrothermal stability.[15–17] Depending on the decomposition conditions and possible post-synthetic modifications, different morphologies, compositions and surface properties can be obtained.[12,18–20] This gives access to an exceptional freedom to tune and optimize the properties of catalysts synthesized by this rather new strategy. The decomposition of metal–organic frameworks has already been used to create catalytically active nanoparticles,[21,22] electrode materials,[23,24] nanoporous carbon materials[25] and hybrid supercapacitors.[26] To our knowledge, energy-related applications of such materials have rarely been studied. Previous studies primarily showcased the sustainability of Ni-MOF-derived carbon-confined nanoparticles for the methanation of CO_2 or focused solely on the investigation of the geometry and electronic properties of the decomposed materials.[27,28] However, the thermal decomposition and its multiple parameters impacting the final structure–activity correlations of the catalyst material have not been targeted at all.[27]

In the present work, we have chosen the metal–organic framework Ni(BDC)(PNO) as the precursor species, which features a well-defined crystal structure.[29] Ni(BDC)(PNO) contains Ni^{2+} centers, which are cross-linked using benzene-1,4-dicarboxylate (BDC) and pyridine-*N*-oxide (PNO) molecules. The crystal structure (Fig. 1) is very similar to MIL-53 and contains one-dimensional channels. The Ni coordination can be described by distorted octahedral NiO_6, but in contrast to the MIL-53 structure, the metal centers are not connected *via* OH groups parallel to the channels, but *via* PNO molecules, which leads to a blocking of the channels and a relatively low porosity of the framework.[30]

To retain a carbonaceous matrix around the Ni species in the catalysts, the decomposition should be performed under inert or slightly reducing conditions to avoid combustion of the organic material. Core methods for the characterization of the precursor and the obtained catalyst materials are based on hard X-rays. X-ray absorption spectroscopy (XAS) and pair distribution function (PDF) analysis are very well suited to study the short-, medium- and long-range order of materials that potentially contain a high fraction of amorphous structures.

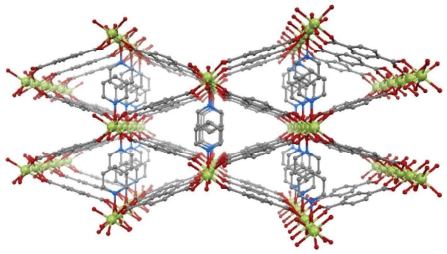

Fig. 1 Schematic representation of the crystal structure of Ni(BDC)(PNO) with nickel atoms in green, oxygen atoms in red, nitrogen atoms in blue and carbon atoms in grey. Hydrogen atoms are omitted.

Synchrotron PDF experiments have recently been used to study MOFs and heterogeneous catalysts. The PDF is a real-space representation of all interatomic distances in the sample and, thus, its particular strength is the access to disordered structures with only short- to medium-range order. In the PDF, small structural transformations can be followed that occur when reaction conditions are varied.[31,32] Here, the structure and size of small supported Ni species can be accessed. To obtain complementary information in an element-specific manner on the short-range order and oxidation state, XAS is a versatile tool. Both XANES (X-ray absorption near edge structure) and EXAFS (extended X-ray absorption fine structure) analysis are used for this purpose.[33–39] XANES provides qualitative information for analysis of the oxidation states and EXAFS delivers the local structure for the averaged local structure of Ni species, including type, number and distance of coordinating atoms[40]

PDF and XAS are complemented by PXRD, physisorption and catalytic activity tests to establish first of all a proof of principle for the feasibility of the chosen approach to decompose MOFs with the aim of obtaining active methanation catalysts. In particular, the combination of PXRD, PDF and XAS, which are sensitive to structures of different degrees of disorder, allows to establish a detailed and highly differentiated structure–activity correlation.

Experimental section and methods

Synthesis of Ni(BDC)(PNO)

For the synthesis of Ni(BDC)(PNO), 9.887 g (34.00 mmol) of $Ni(NO_3)_2{\cdot}6H_2O$, 5.684 g (34.00 mmol) of terephthalic acid and 3.804 g (40.00 mmol) of pyridine-*N*-oxide were dissolved in 200 mL of dimethylformamide (DMF) in a 500 mL Schott flask

using an ultrasonic bath. Subsequently, the reaction solution was heated to 120 °C for 18 h in an oven, and the resulting solid was filtered off from the hot mixture and washed with 1 × 100 mL of DMF, 2 × 60 mL of DMF and 1 × 60 mL of deionized water. The solid green material was dried over night at room temperature and subsequently for 3 days at 130 °C in air.

Formation of methanation catalysts *via* thermal decomposition of Ni(BDC)(PNO) precursor

The methanation catalysts were synthesized by placing 800 mg of Ni(BDC)(PNO) in a glass boat in a tube furnace. The catalyst precursor was treated for 10 min in He with a flow rate of 102 mL min^{-1} and subsequently for 10 min in 102 mL min^{-1} of He, 5% H_2/He or 10% H_2/He, respectively. The samples were heated in the reaction gas mixture to temperatures between 350 °C and 500 °C with a heating ramp of 5 K min^{-1} and held at the final temperature for 1 h. Subsequently, the samples were treated in 102 mL min^{-1} of He and cooled to room temperature.

Standard characterization methods

Powder X-ray diffraction was carried out at room temperature with a STOE STADI P Mythen2 4K diffractometer (Ge(111) monochromator; Ag $K\alpha_1$ radiation, λ = 0.5594 Å) using four Dectris MYTHEN2 R 1K detectors in Debye–Scherrer geometry. Samples were measured in 1 mm diameter Kapton capillaries for 12 h. The *Q*-range was 20.4 $Å^{-1}$. For more information on this dedicated diffractometer for pair distribution function analysis, see ref. 41. Inductively coupled plasma optical emission spectroscopy (ICP-OES) was performed with an iCAP 6500 Duo from Thermo Scientific *via* a six-point calibration. The software iTEVA9.8 was used for data processing. The thermal stability and the decomposition of Ni(BDC)(PNO) were investigated on a thermo balance Cahn TG-2131 in He atmosphere. 15 mg of the sample was heated from 40 °C to 1000 °C with a heating rate of 5 K min^{-1}. For temperature programmed reduction (TPR) analysis, 59.3 mg of the sample was heated with 2 K min^{-1} with a gas flow of 84.1 mL min^{-1} in an atmosphere of 4.6% H_2/Ar. The hydrogen consumption was determined using a Conthos 3 thermal conductivity detector.

X-ray absorption spectroscopy

X-ray absorption experiments at the Ni K-edge (8333 eV) were carried out at PETRA III beamlines P64 and P65 at DESY in Hamburg (Germany). The PETRA III storage ring at DESY operates at 6 GeV particle energy with a current of 100 mA in top-up mode keeping the flux stable with 1%. While using the 1st harmonic, the measurements have been carried out in transmission mode using a Ni foil for calibration of the beam. Simultaneously, the foil has been measured during the sample measurements as a reference. For beamline P65, an 11 period mini-undulator is the photon source which is providing a moderate photon flux density and the incident energy is selected using a water-cooled Si(111), double crystal monochromator. At beamline P64, the photon source is a 2 m-long undulator. Specific energies are selected using a Si(111) double crystal monochromator. All samples were measured as pellets diluted with cellulose. For every sample, a XANES and EXAFS analysis was carried out.

X-ray total scattering experiments

Total scattering data were acquired both on the laboratory diffractometer and at Petra III P21.1 beamline at the DESY facility in Hamburg with an X-ray energy of 102 keV (wavelength of 0.1215 Å). At the beamline, all samples were measured in Kapton capillaries with a diameter of 1 mm for 200 seconds. The powder diffraction patterns were collected using a Pilatus CdTe 2M detector, resulting in a *Q*-range of 0.5–22.4 $Å^{-1}$. Radial integration was done with the software xpdtools,[42] PDF calculation with PDFgetX3 [43] and PDF modelling with diffpy-cmi.[44]

Transmission electron microscopy

Transmission electron microscopy images were collected using a JEOL JEM-2200FS equipped with a Schottky field-emission gun operated at 200 kV and a magnetic in-column omega type energy filter. Images were acquired using a GatanOneView imaging filter with a CMOS camera. Samples were prepared by dipping a lacey carbon film coated on a copper grid (Electron Microscopy Sciences) into the sample powder. For determination of particle sizes, about 200 particles were counted for each sample.

CO_2 hydrogenation studies

For the CO_2 hydrogenation studies, 40 mg of the pre-catalysts was diluted with 160 mg SiC in a stainless-steel u-tube reactor coated with Silconert2000 and activated at 350 °C for 2 h with 2 K min^{-1} in H_2 atmosphere to generate the active methanation catalyst. The CO_2 hydrogenation was then performed with 30 mL min^{-1} of a stoichiometric gas composition of $CO_2 : H_2$ = 1 : 4 and 3 mL min^{-1} Ar as an internal standard. The temperature was increased with a ramp of 5 K min^{-1} and the methanation activity was tested at 250 °C, 275 °C, 300 °C, 325 °C, 350 °C, 375 °C, 400 °C and 425 °C. The products were separated with the help of a CP-Al_2O_3/KCl capillary, a PoraPLOT Q capillary and a MolSieve 5 Å and analyzed using GC-2010 systems from Shimadzu with a thermal conductivity detector and two flame ionization detectors. To determine the CO_2 conversion and the product yields, the peak areas of CO_2, CO and CH_4 were correlated to the gas feeds and to the peak area of Ar as an internal standard to exclude volume changes caused by the CO_2 methanation.

Results and discussion

Standard characterization of catalyst precursor and pre-catalyst

Powder X-ray diffraction analysis of Ni(BDC)(PNO) shown in Fig. 2 proves that the MOF precursor is obtained as a highly crystalline material with a structure that is closely related to MIL-53 and in accordance with the structure reported by Munn *et al.*[29]

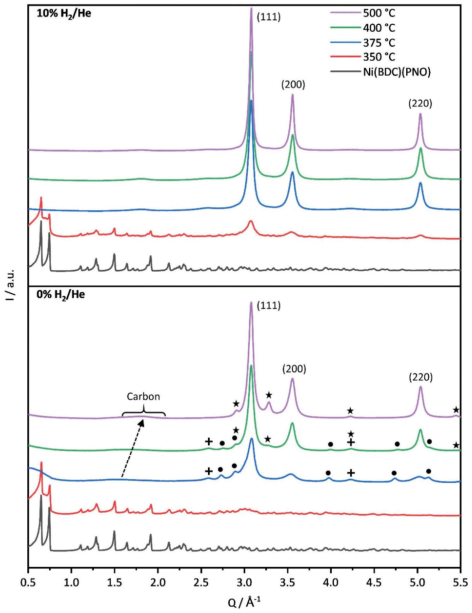

Fig. 2 PXRD patterns of Ni(BDC)(PNO) decomposed in 10% H_2/He (top panel) and in 0% H_2/He (bottom panel) at different temperatures. For 10% H_2/He, the MOF directly decomposes to Ni_{fcc} (indicated by Miller indices). For 0% H_2/He, Ni_3C (dots) and NiO (crosses) appear at intermediate temperatures of 375 and 400 °C, disappearing for 500 °C. A new phase (stars) starts to appear at 400 °C and is the only secondary phase at 500 °C, likely being interstitial-atom-free Ni_{hcp}. The decomposed organic linkers form a carbonaceous phase, which does not change in reducing atmosphere, but shifts in position in 0% H_2/He, indicating graphitization.

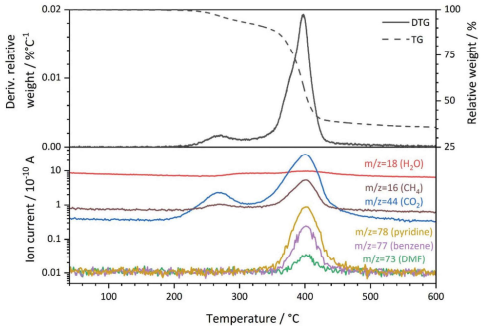

Fig. 3 Thermogravimetric analysis of Ni(BDC)(PNO) in He atmosphere. The corresponding weight loss and its first derivative (top) and the quadrupole mass spectrometry signals (bottom) of m/z = 16, 18, 44, 73, 77 and 78 are shown, which correspond to CH_4, H_2O, CO_2, DMF, benzene and pyridine, respectively.

ATR-IR spectroscopy (see ESI, Fig. S2†) reveals that only small amounts of free *N*,*N*-dimethylformamide (IR bands around 1100 cm^{-1} and 1670 cm^{-1}) and no significant amounts of free pyridine-*N*-oxide (IR band at 1243 cm^{-1}) or free terephthalic acid (IR bands at 2500 cm^{-1} – 2600 cm^{-1}) are present in the pores of Ni(BDC)(PNO).[45–47] Therefore, the linker molecules are mostly incorporated in the framework of Ni(BDC)(PNO), which results in carboxylate vibrations at 1380 cm^{-1} and 1571 cm^{-1} and N–O vibrations at 1213 cm^{-1}, respectively (see ESI†).[46,48] The BDC/PNO ratio could be determined to 1.05 : 1 *via* ^{1}H NMR spectroscopy (Fig. S3†), which is in good accordance with the expected ratio of 1 : 1. The specific surface area of 7 $m^2\ g^{-1}$ that was derived from N_2 physisorption experiments using the BET method (Table S2†) is low compared to other metal–organic frameworks, but can be explained by the pore blocking of PNO linker molecules (schematically shown in Fig. 1). The first derivative of the TG signal (DTG curve, Fig. 3) features two main maxima at 270 °C and 398 °C, respectively, with a shoulder at approximately 376 °C. Quadrupole mass spectroscopy (QMS) revealed that the removal of solvent molecules starts at temperatures around 220 °C (maximum rate at 270 °C), before the decomposition of the MOF lattice is initiated around 330° and reaches the highest decomposition rate at 398 °C. The small shoulder at 376 °C might indicate a second step during the decomposition process. CO_2, CH_4 and NO_2 also feature a shoulder at this temperature in the mass spectrum. Since DMF is not thermally decomposed at this temperature and should only be present in small amounts as revealed by ATR-IR spectroscopy, the nitrogen containing species will likely originate from PNO.

The main signal of the DTG curve can be attributed to the collapse of the framework, which is also supported by the observation of fragments from both organic linker molecules (pyridine-*N*-oxide at m/z = 78 and terephthalate at m/z = 77). No significant weight losses were observed below 200 °C and between 600 °C and 800 °C. The total weight loss of Ni(BDC)(PNO) during the thermal decomposition in He was approximately 64.2%.

Consequently, the decomposition of the Ni(BDC)(PNO) precursor was performed in the temperature range between 350 °C and 500 °C to study the potential influence of the decomposition process on the activity and structure of the resulting catalysts. To avoid a combustion of the organic linkers, which would be expected in oxygen-containing atmosphere, the MOF precursor was decomposed in inert or H_2-containing atmospheres, as this might result in a stabilization of the active Ni particles in a carbonaceous matrix.

The relative Ni content in the samples strongly depends on the decomposition parameters (Table S1†). Only 23–27 wt% of Ni are found in the samples that were decomposed at 350 °C. Generally, more reducing atmospheres result in higher Ni loadings at identical decomposition temperatures, which is explained by the formation of volatile hydrocarbons *via* the hydrogenation of carbonaceous species in the presence of H_2,

leading to higher weight losses. In contrast, the specific surface areas increase to over 100 $m^2\ g^{-1}$ from 350 °C to 375 °C for the hydrogen containing atmospheres compared to He atmosphere with 32 $m^2\ g^{-1}$. Noticeably, the specific surface areas decrease for all atmospheres from 375 °C to 400 °C, but increase only for the He and the 5% H_2/He atmosphere from 400 °C to 500 °C (Table S2†). The increase of the specific surface areas from 350 °C to 375 °C might be explained by a release of the pore-blocking pyridine-*N*-oxide molecules in Ni(BDC)(PNO) at lower temperatures. The collapse of the framework structure and the subsequent formation of porous carbonaceous species could then explain the decrease between 375 °C and 400 °C and the increase from 400 °C to 500 °C in He and 5% H_2/He.

First insights into the structures after the decomposition are provided by powder XRD measurements shown in Fig. 2. The decomposition of the Ni(BDC)(PNO) precursors in He reveals that a temperature of 350 °C is not sufficient to destroy the MOF lattice completely. The intensities of the Ni(BDC)(PNO) reflections decrease, but are still visible in the diffraction pattern. In addition, the formation of small fractions of metallic and oxidic Ni nanoparticles is observed. At higher decomposition temperatures, crystalline Ni_{fcc} particles form, for which crystallite sizes of 15.9 nm and 15.0 nm at 400 °C and 500 °C, respectively, are determined using Williamson–Hall plots (Table S4†). Additionally, Ni_3C and NiO appear as secondary phases denoted as dots and crosses. These secondary phases disappear at 500 °C. In their place, another hexagonal species with different lattice parameters evolves, likely interstitial-atom-free Ni_{hcp}.[49] Amorphous carbon is visible in the PXRDs as a broad hump at 1.5 $Å^{-1}$, which shifts to 1.8 $Å^{-1}$ and gets narrower with temperature. This points towards a graphitization of the amorphous carbon.[50,51]

Decomposition in 5% H_2/He (Fig. S4†) and 10% H_2/He at 350 °C led to significantly lower intensities of the Ni(BDC)(PNO) reflections compared to the decomposition in He atmosphere, which is in line with a more efficient, but still incomplete decomposition of the framework structure. Furthermore, broad reflections indicate the formation of Ni_{fcc} at 350 °C already, which points toward a faster formation of nanoparticles in the presence of hydrogen. For both, 5 and 10% H_2/He (Fig. 2), only Ni_{fcc} was observed after decomposition at 375 °C, 400 °C and 500 °C without contributions of other crystalline phases. Williamson–Hall analysis results in crystallite sizes of 18.8 nm, 15.9 nm and 21.9 nm in 5% H_2/He and 17.5 nm, 18.8 nm and 20.2 nm in 10% H_2/He, respectively (Table S4†). Further, Williamson-Hall analysis reveals a size anisotropy in the 200 crystal direction, as the 200 and 400 reflections lie above the linear regression of all other reflections (see Fig. S5†). The diameter in the 200 direction is smaller than in the other directions, approximately by 2.1–8.3 nm (respectively 10–45%) for the different samples (Table S4†). The exact origin of this anisotropy is subject of ongoing studies.

A significant amount of microstrain or defects such as stacking faults or dislocations exists in all samples, given by the slope of the linear regression in the Williamson Hall plots, decreasing with higher decomposition temperature. This contributes decisively to the Bragg peak broadening, resulting in an underestimation of particle sizes with other XRD methods like Scherrer analysis.

X-ray absorption spectroscopy

As can be seen in the PXRD data, a large fraction of X-ray amorphous structures are present in the catalysts obtained by decomposition of the Ni(BDC)(PNO) MOF. X-ray absorption spectroscopy (XAS) is a powerful tool to characterize such amorphous species due to its short range sensitivity.[40,52–56] The XANES (X-ray absorption near edge structure) region of a XAS spectrum provides information about the oxidation state by means of the absorption edge and about the local structure in a fingerprinting manner by the first oscillations after the edge step. The XANES data obtained for the different catalysts are shown in Fig. 4.

In particular, the pre-edge region at around 8335 eV and the first resonance after the edge step, the so-called white line, in the range of 8345–8355 eV represents a first diagnostic tool to identify the formed structures in the decomposed MOF samples.

With increasing degree of reduction, the pre-edge signal intensity increases and approximates that of the Ni^0 reference foil. Additionally, the white line intensity drops and splits into a doublet-like signal. Compared to the MOF precursor, treatment at 350 °C in He leads to a partial reduction of the Ni^{2+} centers, which is slightly more pronounced in the presence of 10% H_2/He. By means of linear combination XANES fit[57] using the MOF precursor and bulk nickel foil as references (Fig. 5), the individual fractions of Ni^0 are determined resulting in values between 19% (0% H_2/He) and 36% (10% H_2/He), respectively (full table, see Table S5†).

At 375 °C in He, the fraction of reduced Ni centers is increased. Still the white line is characteristic for Ni^{2+}, but

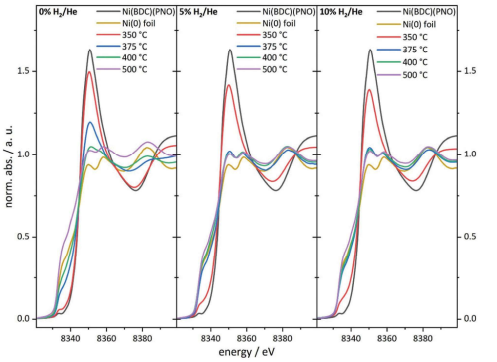

Fig. 4 Ni K-edge XANES spectra of the catalyst precursor decomposed in an atmosphere containing 0% (left), 5% (middle) and 10% of hydrogen (right) in helium.

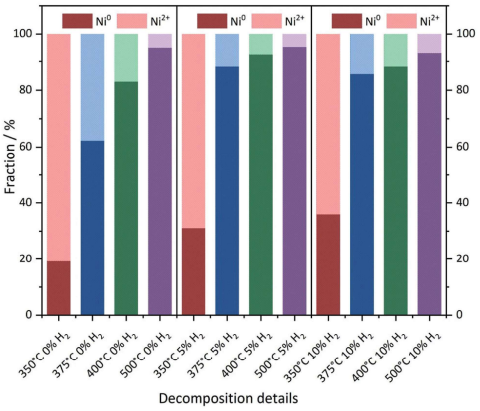

Fig. 5 Linear combination fitting of the XANES spectra. Ni foil and the Ni(BDC)(PNO) precursor were used as the Ni^0 and Ni^{2+} references, respectively.

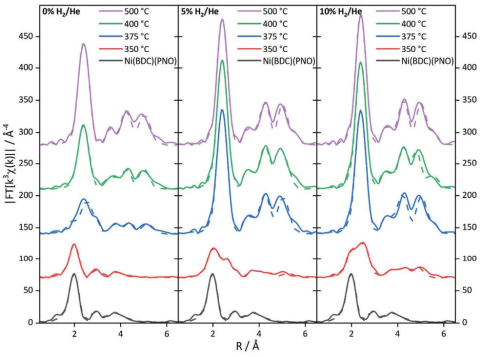

Fig. 6 Fourier-transformed experimental $k^3\chi(k)$ EXAFS functions of the MOF precursor decomposed in an atmosphere containing 0% (left), 5% (middle) and 10% (right) of hydrogen in helium. The solid line shows the experimental spectra, the dotted line shows the theoretical fit of the EXAFS analysis.

according to the LC-XANES fit, already 63% are present as Ni^0. Contrary, the XANES spectrum of the sample decomposed at 375 °C in 10% H_2/He exhibits a typical Ni^0 doublet white line. Interestingly, here still a fraction of 14% Ni^{2+} is present. At 400 °C in 10% H_2/He, the composition is only slightly changed and 88% Ni^0 is found. Although a comparable white line intensity is observed at 400 °C in He and the LC-XANES analysis yields 83% Ni^0, the white line shape indicates a much smaller Ni^0 particle size deduced from the smeared out fine structure.[58] After decomposition at 500 °C, the Ni^0 fraction increases to 95% under inert conditions, but interestingly only to 93% in 10% hydrogen atmosphere. The samples have also been decomposed in a 5% H_2/He atmosphere, representing intermediate conditions. For 350 °C, the amount of Ni^0 is around 31%, which is in accordance with the findings in inert and 10% H_2/He atmosphere. For higher temperatures, the amount of Ni^0 in the 5% H_2/He samples is similar to the samples, which were decomposed in 10% H_2/He atmosphere. For 375 °C, the 5% H_2/He sample shows a Ni^0 amount of 88% in comparison to 86% for 10% H_2. If the 400 °C samples are compared to each other, it is getting clear, that 92% of Ni^0 are present, making it a similar amount as in the sample which has been decomposed at 500 °C in 10% H_2/He atmosphere. In the comparable Ni@C-5%H_2-500 sample 95% of Ni^0 are observed. This fact also illustrates the weakness of the LC-XANES analysis. Although the Ni^{2+} reference is very well represented by the MOF precursor, the bulk Ni^0 metal foil might be less suited to model the small nanoparticles that are present after reduction. In order to account for slightly shifting edge positions due to particle size effects, alternative fits were carried out with floating edge positions. The according fit results are shown in Table S5,† and only small changes are observed. The fractions of the obtained oxidation states can therefore be used with high confidence.

To further substantiate these results, an EXAFS analysis was carried out. Although this delivers mainly structural parameters, also information about the particle size and the composition of the decomposed samples can be gained. Fig. 6 shows the Fourier-transformed EXAFS spectra of the investigated samples.

The EXAFS results for the samples decomposed in He are summarized in Fig. S6 and Table S6.† In agreement with the XANES and PXRD results, treatment at 350 °C leaves the MOF structure intact to a large extent. The first coordination shell contains still six light backscatters. The Ni–C shell at 3.02 Å shows an increased coordination number, which might be indicative of the decomposition process. In turn, the higher contributions are reduced in intensity due to the same reason. At 375 °C, the Fourier-transformed spectrum already shows the onset of a significant Ni^0 contribution with the formation of a Ni–Ni pair at 2.5 Å with 3.5 neighbors. Compared to the coordination number of twelve for bulk Ni^0, this corresponds to a particle size of only 10–20 atoms.[59,60] In contrast, the Ni–O coordination number in the first shell suggests a decomposition of the initial MOF structure by 50%. This is in rough agreement with the XANES analysis. Due to the very small particle size in the decomposed MOF sample, the bulk Ni foil is not fully suited as a reference in the LC-XANES fit and causes an error, potentially making the EXAFS data more reliable in this case. In turn, at 400 °C Ni^0 is dominating the spectrum and no remaining MOF shells can be found in the EXAFS analysis anymore. From the first Ni–Ni contribution with a coordination number of 6.9, a particle size of around 1.2 nm is deduced (see Table 1 for particle sizes).[59,60] Since the LC-XANES fit yields remaining 17% Ni^{2+}, it might be discussed, whether this is an artefact of the LC-XANES approach or the consequence of a large degree of disorder in the remaining Ni^{2+} structures shading their visibility in the EXAFS ana-

Table 1 Diameters of Ni NPs according to TEM, XRD, PDF and XAS. TEM errors are standard deviations from lognormal distributions and XRD errors stem from the standard deviation of the linear regression of the Williamson–Hall plots. XAS errors are deduced from the error in the determined coordination numbers

Crystallite/particle sizes with different methods in nm												
	0% H_2/He				5% H_2/He				10% H_2/He			
Temperature	TEM	XRD	PDF	XAS	TEM	XRD	PDF	XAS	TEM	XRD	PDF	XAS
350 °C	12.6 ± 3.1	—	2.1	<0.8	17.5 ± 4.0	—	5.7	1.0 ± 0.2	16.0 ± 3.1	—	6.2	0.9 ± 0.2
375 °C	12.1 ± 3.7	—	4.8	1.0 ± 0.2	22.0 ± 5.2	18.8 + 4.1–2.8	8.8	>6[a]	20.4 ± 4.7	17.5 + 1.9–1.6	9.1	>6[a]
400 °C	13.9 ± 4.8	15.9 + 4.6/–2.8	9.2	1.2 ± 0.3	19.6 ± 11.3[b]	15.9 + 1.6–1.3	9.7	>6[a]	19.2 ± 4.3	18.8 + 2.3–1.8	9.7	>6[a]
500 °C	16.5 ± 10.0[b]	15.0 + 1.4–1.2	9.3	1.5 ± 0.3	21.7 ± 4.7	21.9 + 3.1–2.4	10.5	3.0 ± 1.0	23.7 ± 6.7	20.2 + 0.8–0.7	13.7	>6[a]

[a] Upper limit to size estimation according to the text is 6 nm. Due to the found coordination numbers, particles seem to be larger than this limit. [b] Bimodal distribution, average over all particle sizes.

lysis. A similar situation is found for the sample decomposed at 500 °C. In the first shell 8.1 Ni–Ni backscatterers can be seen at 2.5 Å distance. If the method for size estimation is used for the first shell it leads to 75 atoms resulting in roughly 1.5 nm particle size. It is interesting to note that a Ni–C shell was necessary to achieve a satisfactory quality of fit at elevated decomposition temperatures. Although the bond distance is too long for a direct Ni–C contact, this contribution could be tentatively assigned to the formation of a carbon shell around the nickel particles.

The EXAFS structure parameters for 5% H_2/He are summarized in Table S7.† At 350 °C, a Ni–Ni coordination number of 2.7 is found at a distance of 2.5 Å. If this amount of nearly one fourth of the saturated fcc first shell is used for EXAFS size estimation, a particle size of 10 to 20 atoms, *i.e.* roughly 1 nm is obtained.[59,60] The full fcc Ni–Ni coordination number of 12 at around 2.5 Å is observed at 375 °C. The high coordination number is in agreement with the LC-XANES fit of 88% Ni^0 contribution in the sample. A very similar situation is found for decomposition at 400 °C. Since from a cluster size of roughly 6 nm the bulk coordination number of 12 is detected by EXAFS, the particle sizes in the 375 and 400 °C must be larger than this value.

Decomposition at 500 °C leads to a slightly reduced coordination number of 10.5 in the first shell at 2.47 Å. This corresponds to 87% of the bulk fcc value and a particle size of around 3 nm, thus a partial decomposition of the particles formed at 400 °C might be observed. However, due to the already large coordination numbers, the error is rather large.

The spectra of the samples decomposed in 10% H_2/He (Fig. 6) show a distinctly different behavior (for details of the parameters see Table S8†). Already at 350 °C, a Ni–Ni shell at 2.48 Å characteristic of Ni^0 is found. Additional Ni–Ni shells at 3.49 Å and 4.31 Å support this finding. The first three shells are indicating 8–10 atoms leading to particle sizes smaller than 0.8 nm. From the Ni–O coordination number a fraction of 80% precursor-like short range order can be concluded. Compared to the XANES analysis, this value is larger, and the small Ni^0 particles are identified again as a potential source of error in the LC-XANES fit. Above 375 °C, bulk-like Ni–Ni coordination numbers are found. These nickel structures dominate the spectra in such a way that minor contributions of light atoms cannot be identified anymore. Due to the large Ni–Ni coordination numbers a particle size larger than 6 nm can be concluded from the 375 °C upwards.

X-ray total scattering

PDF analysis complements the XAS analysis by providing not only insight into the local coordination environment, but also the medium- to long-range structure in the nanometer range, as well as information about the local disorder and crystallite sizes.[61,62]

In the PDFs, we can observe the MOF decomposition and the Ni^0 particle growth for increasing temperatures, see Fig. 7 (left) for the decomposition in He. The comparison of the

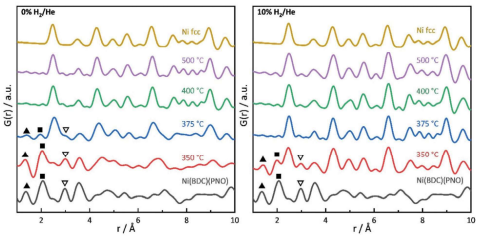

Fig. 7 PDFs of Ni(BDC)(PNO) and its decomposed products at different temperatures in comparison to a calculated Ni_{fcc} PDF. C–C (triangles), Ni–O (squares) and Ni–N distances (open triangles) are highlighted.

sample decomposed at 350 °C with the original MOF shows many remaining MOF peaks. For increasing temperatures, the interatomic C–C distance at 1.37 Å and the Ni–O distance at 2.0 Å decrease in peak height and are not distinguishable in the samples decomposed at 400 and 500 °C. Simultaneously, peaks appear and grow, which indicate a Ni_{fcc} structure and, thus, the formation of Ni^0 particles (see Fig. 7). At 375 °C, an additional hexagonal phase, likely Ni_3C can be observed *via* the broadening of the peaks at 2.65 and 4.60 Å and a shoulder at 7.00 Å (for a detailed overview of the difficulty to differentiate between Ni_3C and Ni_{hcp} see ref. 63).[64]

The fraction of this hcp phase decreases with increasing temperature and disappears at 500 °C. The contribution of this hcp phase in the 375 °C sample was investigated by the simultaneous refinement of three phases, consisting of Ni_{fcc}, Ni_3C and NiO. NiO was additionally included as a third phase, as it further improved the fit quality indicating a nickel oxide formation during decomposition under inert conditions (Fig. 8). The goodness-of-fit R_w improved significantly from R_w = 0.54 for a single-phase fit of Ni_{fcc} to R_w = 0.32 with the additional Ni_3C and NiO phases. For detailed refined final values see Table S9.† The relative fractions of the phases refined to 47% fcc, 38% Ni_3C and 15% NiO for the sample decomposed at 375 °C, while the percentage of Ni_{fcc} increased to 55% for the sample decomposed at 400 °C with co-existing Ni_3C (38%) and NiO (7%, Fig. S8†). Note, that the domain size of the hcp structure decreases from 5.4 nm at 375 °C to 1.4 nm at 400 °C, indicating the transformation of the hcp to the fcc structure.

In the range up to 10 Å, the samples decomposed at 400 and 500 °C differ only slightly (see Fig. 7, left). Stronger dampening of PDF peak heights in the 400 °C sample is visible in the high r-region indicating smaller crystalline domains (for longer range PDF see Fig. S10†). Overall, the dampening is consistently decreasing with temperature, which shows the growth of the crystallite domains.

In 5% and 10% H_2/He at 350 °C, there are PDF peaks reminiscent of the initial MOF structure out to around 10 Å (see Fig. 7 and Fig. S7†). This corresponds approximately to the unit cell dimension of the MOF in *b* and *c* direction, but is smaller than the *a* lattice parameter of 19.3 Å.[29] The interatomic distance at 3.56 Å in the MOF precursor originates from Ni–Ni pairs of Ni–O–Ni chains in the MOF, and it shortens to 3.53 Å at 350 °C and further to 3.51 Å at 400 °C. The latter distance of 3.51 Å can be ascribed to the second coordination shell of Ni atoms in Ni_{fcc}.[65] This indicates that the Ni–O–Ni chains of the initial *b*-axes in the MOF are destroyed rather fast with increasing temperature. Yet at 350 °C, the Ni–O distance still remains intense due to remaining NiO_6 octahedrons from the MOF lattice. The fact that the Ni–O and C–C distances vanish already at 375 °C in 5% H_2/He and 10% H_2/He can be explained by an accelerated framework decomposition, because of the reducing atmosphere.

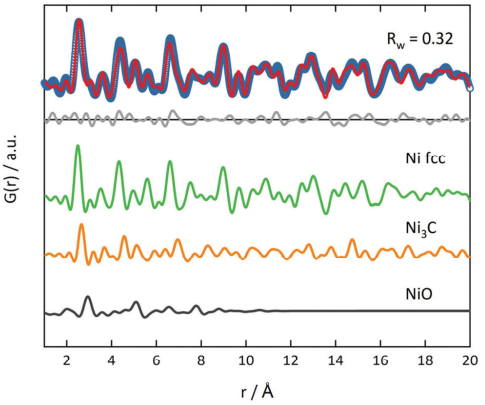

Fig. 8 PDF refinement of Ni(BDC)(PNO) decomposed at 375 °C in He with three phases (Ni_{fcc}, Ni_3C and NiO). Blue open circles represent the experimental PDF and red line the calculated PDF. The grey line in the offset shows the difference between experimental and calculated PDF.

The particle size in PDF is visible in the dampening of peaks with higher distances. PDF refinements were done for all samples and atmospheres to extract particle sizes. At 350 °C, spherical Ni_{fcc} nanoparticles with diameters of 2.1 nm, 5.7 nm and 6.2 nm form in 0% H_2/He, 5% H_2/He and 10% H_2/He (Table 1). Generally, smaller nanoparticles form under inert conditions. With higher temperatures, PDF refinements show larger crystallite domains, for instance under inert conditions refined particle diameters grow from 2.1 nm at 350 °C to 9.2 nm for 500 °C final decomposition temperature. For reducing conditions, the same trend exists, yet with overall larger domain sizes. The strain, confirmed by Williamson–Hall plots, can lead to PDF peak shifts, additional peak broadening and a faster decay of $G(r)$.[66,67] The particle sizes estimated here by the decay of PDF peak heights, therefore underestimate the true particle diameters. Additionally, the strain-induced peak broadening is reflected in larger thermal displacement parameters U_{iso} for lower decomposition temperatures (Tables S4 and S10†). The trend of U_{iso} values is in accordance with the Williamson-Hall analysis.

Transmission electron microscopy/comparison of particle sizes from different methods

TEM analysis shows lognormal particle size distributions for most samples (Fig. 9). The mean diameters extracted from fits of lognormal distributions agree well with particle diameters from the Williamson-Hall analysis of XRD data that larger particles form at higher temperatures under all investigated atmospheres (Fig. S12 and S13†). This can be explained by an Ostwald ripening of the nanoparticles, which leads to a growth of larger particles and a shrinking of small particles.[68,69]

In TEM, it becomes evident that most of the nanoparticles are still embedded in the framework matrix at lower temperatures. Furthermore, the confinement of the nanoparticles in the matrix is more pronounced for the samples decomposed in He, supporting the findings of XRD, XAS and PDF, which show a faster decomposition of the framework in reducing atmosphere. This in fact hinders the extraction of particle sizes at lower temperatures, as the small particles cannot be distinguished from the metal–organic framework matrix. Further TEM analysis of single particles proves the presence of a graphitic carbon shell around the Ni particles (Fig. 10). This

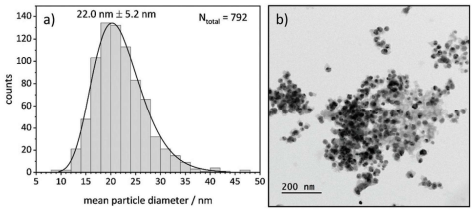

Fig. 9 (a) Particle size distribution of Ni(BDC)(PNO) decomposed at 375 °C in 5% H_2/He and (b) corresponding TEM image of the sample.

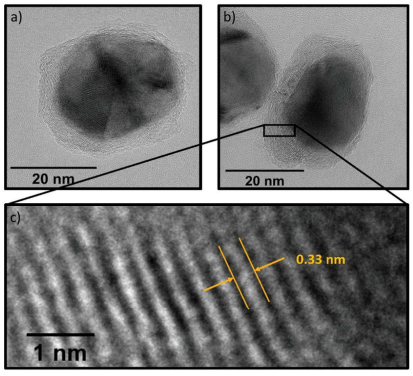

Fig. 10 (a) TEM of a polycrystalline particle after decomposition at 400 °C in 10% H_2 with graphitic shell. (b) TEM of a particle after decomposition at 500 °C in 10% H_2, no twinning is visible. (c) Zoom into carbon shell, revealing a layered carbon structure with 0.33 nm interlayer spacing.

is visible in the ordered structure of the carbon matrix, which can clearly be distinguished from the amorphous carbon background of the TEM grid. The distance between the layers is approximately 0.33 nm, which is in accordance with the plane separation between two graphene layers and furthermore supports the finding of graphitic carbon, as non-graphitic carbon layers have a larger interlayer spacing.[70] Based on the slight ellipsoidal shape of the particle in Fig. 10a/b, we evaluate the degree of particle anisotropy for the catalytically most active sample (375 °C in 5% H_2/He sample) by separately extracting particle lengths and widths from TEM images. On average, particle lengths exceed particle widths by 14.3%, indicating a slightly ellipsoidal shape (Fig. S11†). Overall, the trends in nickel particle sizes determined from TEM and XRD match very well, while PDF and XAS underestimate particle sizes. In general, XRD (and PDF) data is more sensitive to larger particles, while TEM is equally sensitive to differently sized particles above a certain size limit. PDF underestimates the particle diameters due to the strain-induced peak broadening as discussed above, yet it provides valuable insight into the MOF residuals and simultaneous detection of multiple phases like Ni_{fcc}, Ni_3C, Ni_{hcp} and NiO in refinements. On the contrary, XAS averages over all metal centers in the samples. It is thus also sensitive to very small clusters in the ensemble, which are not detected by TEM and XRD. Additionally, the error for size determination becomes very large for particles larger than 6–7 nm, which is therefore considered as a soft upper detection limit. Particles beyond that size do not change the coordination number anymore and thus XAS is blind for very large particles. The particle sizes determined by EXAFS analysis therefore due not contradict the other results.

Despite these different sensitivity ranges, all techniques indicate larger particles for higher decomposition temperatures. The carbonaceous matrix hides particularly small nanoparticles in the TEM images, so that the average diameters determined by TEM for samples 350–400 °C 0% H_2/He and 350 °C 5/10% H_2/He, likely overestimate the true average diameter. With TEM, we additionally observe that the sample decomposed at 500 °C in 0% H_2/He shows a bimodal size distribution with a fraction of particle diameters <10 nm and larger particles with diameters >10 nm (Fig. S12†). A similar behavior is also found for decomposition in 5% H_2/He, although the determined particle sizes at 500 °C are larger than under inert conditions. The largest particles are formed in 10% H_2/He atmosphere.

Since the trends are the same under all applied decomposition conditions, a general statement about the methodical combination of TEM, XRD, PDF and XAS is possible here. From the TEM images shown in Fig. 9, it is obvious that only a broad Ni^0 particle size distribution can be obtained with the proposed preparation method. This having said, it follows that the potential *in situ* methods PDF and XAS can only detect the average of these size distributions including the X-ray amorphous species in the catalyst. On the other hand, it can also be concluded that the applied method combination is currently necessary to collect all structural aspects of the catalysts pre-

pared by MOF decomposition: TEM and XRD are suitable for larger particles with long range order, XAS for very small ones including amorphous structures and remaining MOF structures, and PDF to connect both ranges. The equivalence of XAS and PDF concerning the short-range order is also reflected in the coordination numbers obtained for the different coordination shells in the nanoparticles as shown in the ESI.†

According to the previous discussion, more simple characterization efforts can only be applied after a preparation method has been identified that yields phase-pure structures or a narrow distribution of particle sizes. Therefore, also the catalytic results discussed in the next section can only be correlated to the average structures in the catalysts.

Catalytic studies

As a first step of the catalytic studies, TPR profiles are recorded to determine a suitable activation temperature for the reduction of oxidized surface Ni species in hydrogen atmosphere in the methanation reactor. Exemplarily, the result for the sample decomposed at 375 °C in 10% H_2/He is shown in Fig. 11. It reveals three distinct signals. The peak at 77 °C can be assigned to the desorption or decomposition of physisorbed species from the catalyst precursor.[71] The maximum at 349 °C corresponds to the reduction of amorphous NiO species in the catalyst to metallic Ni,[71] which starts already at temperatures below 300 °C. The maximum at 496 °C is assigned to the hydrogenation of carbonaceous species to methane or other volatile hydrocarbons in the presence of Ni,[72] which needs to be prevented during the activation process in order to retain the carbonaceous matrix around the Ni particles. This behavior is in accordance with the results of the ICP-OES measurements, since the Ni metal loading is increasing with rising decomposition temperature and hydrogen content. To minimize losses of the carbon matrix during the activation prior to methanation, the decomposed pre-catalysts were therefore reduced at 350 °C for 2 h in hydrogen atmosphere.

The catalytic data for methanation of CO_2 at atmospheric pressure are compared in Fig. 12 for the catalysts prepared at different decomposition temperatures and atmospheres. Beside the desired product methane, also CO and minor traces of ethane are detected as side products, but the latter one is neglected in the following due to its very low amount.

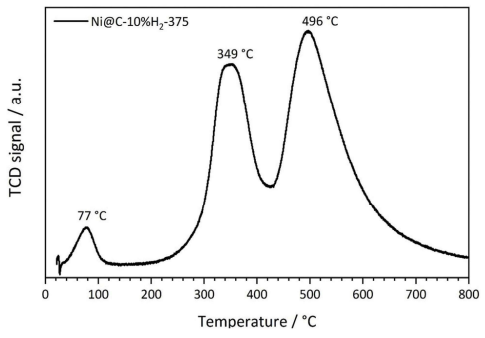

Fig. 11 Temperature-programmed reduction profile of Ni(BDC)(PNO) decomposed at 375 °C in 10% H_2/He.

Low CO_2 conversions are observed at 250 °C for all materials and they increase with rising reaction and decomposition temperature. The catalysts decomposed in 0% H_2/He show a good correlation between the decomposition temperature and the catalytic performance (Fig. 12a). Generally, higher decomposition temperatures lead to higher CO_2 conversions. The very low activity of Ni@C-0%H_2-350 is in accordance with the incomplete decomposition of the metal–organic framework precursor and, thus, a relatively high fraction of catalytically inactive Ni centers. The decrease in conversion above a reaction temperature of 350 °C for this sample can be explained by a further framework decomposition at reaction temperatures above the decomposition temperature, which does not yield highly active Ni sites. The Ni@C-0%H_2-500 catalyst features the highest CO_2 conversion of 67% with a methane selectivity of 91% at 425 °C. In comparison, the material decomposed at 400 °C shows both lower conversion (50%) and methane selectivity (81%). Remarkably, the decomposition at 375 °C leads to much lower CO_2 conversion (23%) and, more importantly, a low selectivity towards methane (23%), while large amounts of CO are formed. The very low CH_4 yield for Ni@C-0%H_2-375 can be explained by the additional presence of the hcp phase, which is inactive for the methanation reaction and instead favors the production of CO.[73]

Note that the methane yield (see Fig. 12b) increases with increasing decomposition temperature. In Fig. 12c, the productivity normalized to the relative Ni content of the samples is plotted to evaluate the performance of the catalysts with respect to the number of Ni centers. Considering the normalized molar product yields at a reaction temperature of 425 °C (Fig. 12c), the Ni@C-0%H_2-500 catalyst shows the highest productivity with a very high selectivity towards CH_4, followed by Ni@C-0%H_2-400 and Ni@C-0%H_2-375. The increasing activity of the catalysts with increasing decomposition temperature can be explained by the absence of Ni_{hcp}, Ni_3C and NiO and, consequently, the exclusive presence of catalytically active Ni_{fcc} in Ni@C-0%H_2-500. The results are also in accordance with the particle size investigations, since the decomposition in inert atmosphere does not lead to significant sintering at high temperatures (*cf.* Table 1), and the high specific surface area of 127 $m^2\ g^{-1}$ of Ni@C-0%H_2-500 (compare Table S2†), which both favor a high dispersion and, thus, an increasing amount of active Ni centers. For the catalysts that were decomposed in 5% H_2/He, the CO_2 conversions are very low at 250 °C (<1%), as shown in Fig. 12d, whereas an increase of the reaction temperature to 425 °C results in significantly higher conversions of CO_2 (37%–74%). In general, the methane yields are increasing at higher reaction temperature for all materials (Fig. 12e). Interestingly, the decomposition in 5% H_2/He does not give the same activity trend for the four catalysts of the series, which has been observed in inert atmosphere. While

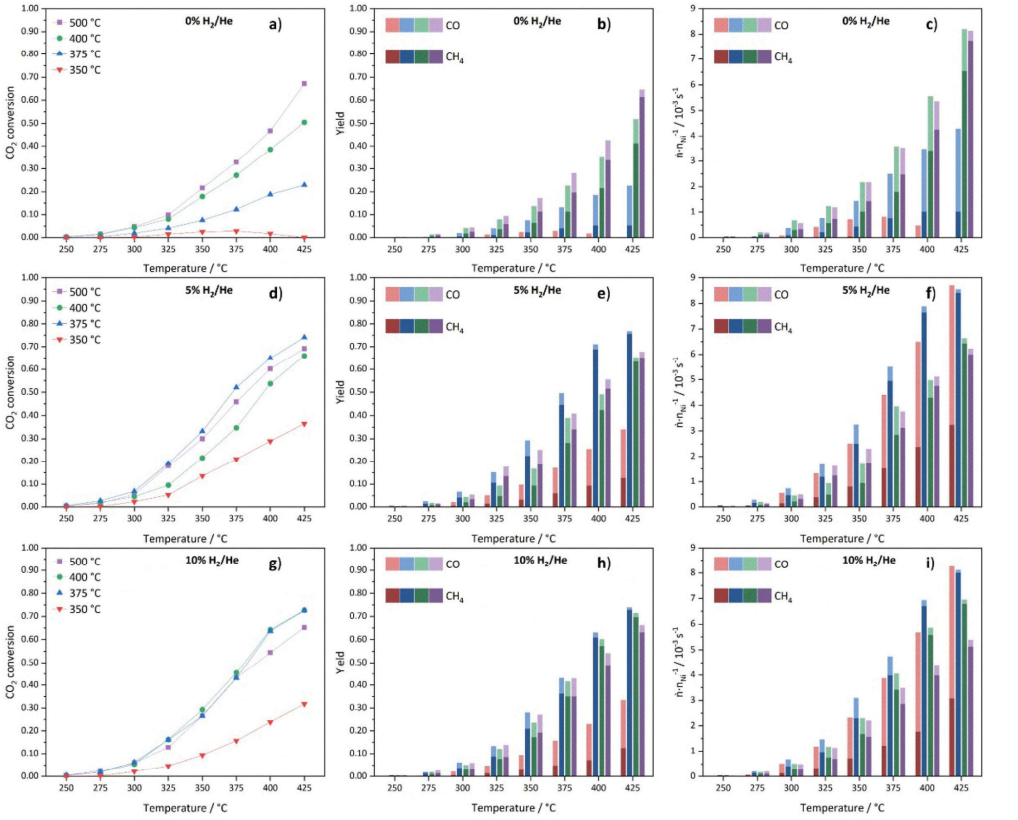

Fig. 12 CO_2 conversions (a, d and g), stacked CH_4 and CO yields (b, e and h) and stacked productivities of CH_4 and CO normalized to the molar Ni content (c, f and i) of Ni(BDC)(PNO) decomposed at temperatures of 350 °C (red), 375 °C (blue), 400 °C (green) and 500 °C (purple) in 0% (a–c), 5% (d–f) and 10% H_2/He (g–i) atmospheres.

Ni@C-5%H_2-350 still features the lowest activity and methane selectivity, Ni@C-5%H_2-375 turns out to be the most active sample, resulting in a CO_2 conversion of 74% and a methane selectivity close to 100% at a reaction temperature of 425 °C. Both samples decomposed at higher temperatures, Ni@C-5%H_2-400 (66% conversion at 425 °C) and Ni@C-5%H_2-500 (69% conversion at 425 °C), are less active. This activity trend correlates with the specific surface area of the three samples (*cf.* Table S2†), since Ni@C-5%H_2-375 (102 m^2 g^{-1}) exhibits a larger surface area than Ni@C-5%H_2-400 (56 m^2 g^{-1}) and Ni@C-5%H_2-500 (89 m^2 g^{-1}). The decrease of the specific surface area at higher decomposition temperatures can be explained by a partial gasification of the porous carbon support under these conditions, which results in a higher relative Ni content (*cf.* Table S1†). Furthermore, the particle sizes (*cf.* Table 1), show the same trend, as slightly smaller particles are obtained after decomposition at 375 °C in comparison to 400 °C and 500 °C. In addition, the observed strain or defects in the particles might be a possible reason for the different reactivity of the samples. Decomposition at high temperatures results in less defects in the particles, which might be leading to a different surface structure with a lower number of highly exposed Ni sites. The productivity of the catalysts normalized to the Ni content (Fig. 12f), is in accordance with these observations, since Ni@C-5%H_2-375 produces the largest amounts of methane, followed by Ni@C-5%H_2-400 and Ni@C-5%H_2-500. Remarkably, the Ni@C-5%H_2-350 catalyst shows a very high CO selectivity, while the methane yield is much lower than for all other catalysts of the series.

Consequently, the activity of the catalysts of this series seems to correlate with the dispersion and particle size of the Ni species in the carbon matrix, which gives also an explanation for the high methane selectivity of the Ni@C-5%H_2-375 catalyst.

Finally, the catalysts that are prepared in 10% H_2/He, have also been tested in the methanation reaction and also for this series low CO_2 conversions are obtained for all materials at 250 °C, which start to steadily increase with rising reaction temperature (shown in Fig. 12g). Like in the other atmospheres, the sample that was decomposed at 350 °C is significantly less active than the other three samples, which can be explained by the incomplete destruction of the MOF lattice and the high fraction of inactive Ni centers. Therefore, activity trends are only discussed for the other three samples of the series. The highest CO_2 conversions are achieved for the Ni@C-10%H_2-375 and Ni@C-10%H_2-400 samples with 73% at 425 °C. The sample that was decomposed at 375 °C features a slightly higher methane yield (73% *vs.* 69%), but both catalysts reach methane selectivities close to 100%. Similar to the materials that were decomposed in 5% He/H_2, smaller Ni nanoparticles seem to be beneficial for the methanation reaction, since the CO_2 conversion is decreased for Ni@C-10%H_2-500 (65%) with larger particle size. Also for this series, high decomposition temperatures lead to less defects in the Ni particles, which might be another explanation for the reduced catalytic activity of these catalysts. All three samples decomposed in 10% H_2/He at 375 °C, 400 °C and 500 °C feature very high methane selectivities above 95%. These observations can be understood considering the adsorption strength of intermediate CO_{ads} species, which increases with increasing particle sizes.[74] A longer residence time of the CO molecules at the surface of the Ni particles increases the probability to react to methane, but inhibits the adsorption of gaseous CO_2 molecules by blocking adsorption sites. As a consequence, larger Ni particles enhance the formation of CH_4, but decrease the CO_2 conversion. The determined specific surface areas (*cf.* Table S2†) follow the same trend as the catalytic activity. The most active catalyst material Ni@C-10%H_2-375 (111 m^2 g^{-1}) features a larger specific surface area than Ni@C-10%H_2-400 (77 m^2 g^{-1}) and Ni@C-10%H_2-500 (63 m^2 g^{-1}), which is again in line with the increasing relative Ni contents (*cf.* Table S1†) due to a partial gasification of the stabilizing carbon shell. The highest production rate of methane in relation to the Ni content (Fig. 12i) is also achieved with the Ni@C-10%H_2-375 catalyst.

In summary, the decomposition at an intermediate temperature of 375 °C and in an atmosphere with intermediate hydrogen content (5% H_2/He) seems to be the best set of parameters to obtain a high specific surface area of the carbon matrix and a relatively small particle size of Ni, which results in a high dispersion of highly active Ni_{fcc} centers.

In general, our observations are in accordance with the findings of Tayal *et al.*,[28] who also reported that higher decomposition temperatures lead to a more pronounced decomposition of Ni-MOF precursors and larger Ni particles. However, these authors have described the structure of their catalyst as a mixture of Ni nanoparticles and a residual MOF phase without considering the fact that organic linkers break and disintegrate at high decomposition temperatures. This disintegration of organic linkers, which has been confirmed at temperatures above 350 °C in the present work, results in the formation of a graphitic shell around the Ni nanoparticles, which seems to be beneficial for the catalytic performance and probably also for the long-term stability of our novel catalysts compared to systems that are prepared using conventional preparation methods. Our observations concerning the MOF decomposition and carbon layer formation are also in accordance with a study by Lin *et al.*[27] on a MOF-derived methanation catalyst. However, the present investigation represents one of the first systematic studies concerning the impact of a wide range of decomposition parameters on the final structures and the activity of Ni-based methanation catalysts that have been prepared *via* the controlled decomposition of MOF-based precursors. Such systematic studies are essential to establish structure–activity correlations for targeted catalyst preparation.

Conclusions

The present work has proven that the controlled thermal decomposition of metal–organic framework precursors is a promising synthesis route for the preparation of highly active Ni@C catalysts for the methanation of carbon dioxide. The decomposition of Ni(BDC)(PNO) was performed at four different temperatures (350, 375, 400 and 500 °C) in three different atmospheres (0%, 5% and 10% H_2 in He) and the resulting materials were studied using a wide variation of characterization techniques, including X-ray absorption spectroscopy (XAS) and pair distribution function (PDF) analysis to reveal structure–activity correlations. In combination with standard characterization methods, the two complementary hard X-ray-based techniques proved that a decomposition at 350 °C was not sufficient in all atmospheres to destroy the metal–organic framework completely, resulting in a very low catalytic activity of these three catalysts. Decomposition in inert atmosphere led to phase mixtures of highly active Ni_{fcc} and undesired Ni_3C and NiO impurities at medium temperatures (375 and 400 °C), which resulted in a lower activity than for the sample that was decomposed at 500 °C and contained only Ni_{fcc}. In contrast, for the decomposition in both reducing atmospheres the best catalytic performance was achieved with the catalysts that were decomposed at medium temperatures. This behavior can be explained by larger specific surface areas and the presence of a protective carbon shell around the Ni particles, which both favor the formation of smaller particles leading to a high dispersion of active Ni_{fcc}. In contrast, decomposition at 500 °C led to a partial gasification of the porous carbonaceous matrix, causing a reduced specific surface area and sintering of less strained Ni particles resulting in a lower catalytic activity. Ni@C-5%H_2-375 emerged as the best catalyst, resulting in a CO_2 conversion of 73% and a methane selectivity close to 100% at a reaction temperature of 425 °C. Consequently, medium decomposition temperatures and slightly reducing atmospheres appear to be ideal for the preparation of Ni@C catalysts *via* decomposition of the Ni(BDC)(PNO) precursor. Since the structures of the decomposed

catalysts are very complex and contain both crystalline and amorphous components, only the unique combination of TEM, XRD, XAS and PDF enabled the establishment of the structure–activity correlations that have been presented in this work. As long as the available preparation methods for MOF decomposition do not yield a narrower size distribution of Ni^0 particles, such an approach is mandatory to access the full width of possible active species.

Conflicts of interest

There are no conflicts to declare.

Acknowledgements

We acknowledge funding by the Deutsche Forschungsgemeinschaft (DFG, German Research Foundation) *via* SPP2080 (BA 4467/8-1, KL 2913/1-1, ZO 369/2-1). We thank Marco Schwarzmann and Oliver Scharold for TEM support and Ute Krämer and Petra Düchting for performing ICP-OES measurements. We further thank the Bavarian Polymer Institute (BPI) for access to the keylabs 'Electron and Optical Microscopy'. We gratefully acknowledge beamtime at P21.1, P64 and P65 at DESY Petra III and Ann-Christin Dippel, Wolfgang Caliebe and Edmund Welter for support, and Soham Banerjee for discussion.

Notes and references

1 S. Rönsch, J. Schneider, S. Matthischke, M. Schlüter, M. Götz, J. Lefebvre, P. Prabhakaran and S. Bajohr, *Fuel*, 2016, **166**, 276.
2 P. Sabatier and J. B. Senderens, *J. Chem. Soc.*, 1902, **82**, 333.
3 G. A. Mills and F. W. Steffgen, *Catal. Rev.: Sci. Eng.*, 1974, **8**, 159.
4 P. Frontera, A. Macario, M. Ferraro and P. Antonucci, *Catalysts*, 2017, **7**, 59.
5 T. A. Le, M. S. Kim, S. H. Lee, T. W. Kim and E. D. Park, *Catal. Today*, 2017, **293–294**, 89.
6 H. Muroyama, Y. Tsuda, T. Asakoshi, H. Masitah, T. Okanishi, T. Matsui and K. Eguchi, *J. Catal.*, 2016, **343**, 178.
7 S. Danaci, L. Protasova, J. Lefevere, L. Bedel, R. Guilet and P. Marty, *Catal. Today*, 2016, **273**, 234.
8 B. Mutz, P. Sprenger, W. Wang, D. Wang, W. Kleist and J.-D. Grunwaldt, *Appl. Catal., A*, 2018, **556**, 160.
9 B. Mutz, A. M. Gänzler, M. Nachtegaal, O. Müller, R. Frahm, W. Kleist and J.-D. Grunwaldt, *Catalysts*, 2017, **7**, 279.
10 H.-L. Jiang, B. Liu, Y.-Q. Lan, K. Kuratani, T. Akita, H. Shioyama, F. Zong and Q. Xu, *J. Am. Chem. Soc.*, 2011, **133**, 11854.
11 B. Liu, H. Shioyama, H. Jiang, X. Zhang and Q. Xu, *Carbon*, 2010, **48**, 456.
12 L. Oar-Arteta, T. Wezendonk, X. Sun, F. Kapteijn and J. Gascon, *Mater. Chem. Front.*, 2017, **1**, 1709.
13 B. Liu, H. Shioyama, T. Akita and Q. Xu, *J. Am. Chem. Soc.*, 2008, **130**, 5390.
14 T. Kundu, S. C. Sahoo and R. Banerjee, *Cryst. Growth Des.*, 2012, **12**, 2572.
15 A. H. van Pelt, O. A. Simakova, S. M. Schimming, J. L. Ewbank, G. S. Foo, E. A. Pidko, E. J. M. Hensen and C. Sievers, *Carbon*, 2014, **77**, 143.
16 M. T. Claure, S.-H. Chai, S. Dai, K. A. Unocic, F. M. Alamgir, P. K. Agrawal and C. W. Jones, *J. Catal.*, 2015, **324**, 88.
17 M. D. Porosoff, X. Yang, J. A. Boscoboinik and J. G. Chen, *Angew. Chem., Int. Ed.*, 2014, **53**, 6705.
18 Y. Kimitsuka, E. Hosono, S. Ueno, H. Zhou and S. Fujihara, *Inorg. Chem.*, 2013, **52**, 14028.
19 Z. Long, L. Wei, L. Shuang, W. Jifei, W. Huanlei and C. Jiaxin, *J. Mater. Chem. A*, 2015, **3**, 14210.
20 M. van de Voorde and B. Sels, *Nanotechnology in Catalysis*, Wiley-VCH Verlag GmbH & Co. KGaA, Weinheim, Germany, 2017.
21 J. M. Zamaro, N. C. Pérez, E. E. Miró, C. Casado, B. Seoane, C. Téllez and J. Coronas, *Chem. Eng. J.*, 2012, **195–196**, 180.
22 J. Li, B. Wang, Y. Qin, Q. Tao and L. Chen, *Catal. Sci. Technol.*, 2019, **9**, 3726.
23 Z. Guo, F. Wang, Y. Xia, J. Li, A. G. Tamirat, Y. Liu, L. Wang, Y. Wang and Y. Xia, *J. Mater. Chem. A*, 2018, **6**, 1443.
24 Y. Guo, X. Gao, C. Zhang, Y. Wu, X. Chang, T. Wang, X. Zheng, A. Du, B. Wang, J. Zheng, K. Ostrikov and X. Li, *J. Mater. Chem. A*, 2019, **7**, 8129.
25 W. Chaikittisilp, K. Ariga and Y. Yamauchi, *J. Mater. Chem. A*, 2013, **1**, 14.
26 J. Kim, C. Young, J. Lee, Y.-U. Heo, M.-S. Park, M. S. A. Hossain, Y. Yamauchi and J. H. Kim, *J. Mater. Chem. A*, 2017, **5**, 15065.
27 X. Lin, S. Wang, W. Tu, Z. Hu, Z. Ding, Y. Hou, R. Xu and W. Dai, *Catal. Sci. Technol.*, 2019, **9**, 731.
28 A. Tayal, Y. Chen, C. Song, S. Hiroi, L. S. R. Kumara, N. Palina, O. Seo, M. Mukoyoshi, H. Kobayashi, H. Kitagawa and O. Sakata, *Inorg. Chem.*, 2018, **57**, 10072.
29 A. S. Munn, G. J. Clarkson, F. Millange, Y. Dumont and R. I. Walton, *CrystEngComm*, 2013, **15**, 9679.
30 C. Serre, F. Millange, C. Thouvenot, M. Noguès, G. Marsolier, D. Louër and G. Férey, *J. Am. Chem. Soc.*, 2002, **124**, 13519.
31 A. E. Platero-Prats, A. Mavrandonakis, L. C. Gallington, Y. Liu, J. T. Hupp, O. K. Farha, C. J. Cramer and K. W. Chapman, *J. Am. Chem. Soc.*, 2016, **138**, 4178.
32 Y. Lei, H. Zhao, R. D. Rivas, S. Lee, B. Liu, J. Lu, E. Stach, R. E. Winans, K. W. Chapman, J. P. Greeley, J. T. Miller, P. J. Chupas and J. W. Elam, *J. Am. Chem. Soc.*, 2014, **136**, 9320.
33 M. Bauer and C. Gastl, *Phys. Chem. Chem. Phys.*, 2010, **12**, 5575.
34 M. Bauer, T. Kauf, J. Christoffers and H. Bertagnolli, *Phys. Chem. Chem. Phys.*, 2005, **7**, 2664.

35 A. J. Dent, *Top. Catal.*, 2002, **18**, 27.
36 C. C. Scarborough, S. Sproules, T. Weyhermüller, S. DeBeer and K. Wieghardt, *Inorg. Chem.*, 2011, **50**, 12446.
37 S. C. E. Stieber, C. Milsmann, J. M. Hoyt, Z. R. Turner, K. D. Finkelstein, K. Wieghardt, S. DeBeer and P. J. Chirik, *Inorg. Chem.*, 2012, **51**, 3770.
38 N. M. Martin, F. Hemmingsson, X. Wang, L. R. Merte, U. Hejral, J. Gustafson, M. Skoglundh, D. M. Meira, A.-C. Dippel, O. Gutowski, M. Bauer and P.-A. Carlsson, *Catal. Sci. Technol.*, 2018, **8**, 2686.
39 C. Nayak, P. Jain, C. P. Vinod, S. N. Jha and D. Bhattacharyya, *J. Synchrotron Radiat.*, 2019, **26**, 137.
40 M. Bauer and H. Bertagnolli, in *Methods in Physical Chemistry*, ed. R. Schäfer and P. C. Schmidt, Wiley-VCH, Weinheim, 2012, p. 231.
41 S. L. J. Thomae, N. Prinz, T. Hartmann, M. Teck, S. Correll and M. Zobel, *Rev. Sci. Instrum.*, 2019, **90**, 43905.
42 C. J. Wright and X. D. Zhou, *J. Synchrotron Radiat.*, 2017, **24**, 506.
43 P. Juhás, T. Davis, C. L. Farrow and S. J. L. Billinge, *J. Appl. Crystallogr.*, 2013, **46**, 560.
44 P. Juhás, C. L. Farrow, X. Yang, K. R. Knox and S. J. L. Billinge, *Acta Crystallogr., Sect. A: Found. Adv.*, 2015, **71**, 562.
45 A. Shastri, A. K. Das, S. Krishnakumar, P. J. Singh and B. N. R. Sekhar, *J. Chem. Phys.*, 2017, **147**, 224305.
46 J. V. Quagliano, J. Fujita, G. Franz, D. J. Phillips, J. A. Walmsley and S. Y. Tyree, *J. Am. Chem. Soc.*, 1961, **83**, 3770.
47 C. Volkringer, T. Loiseau, N. Guillou, G. Férey, E. Elkaïm and A. Vimont, *Dalton Trans.*, 2009, 2241.
48 F. G. Sherif, *Ind. Eng. Chem. Prod. Res. Dev.*, 1970, **9**, 408.
49 R.-T. Chiang, R.-K. Chiang and F.-S. Shieu, *RSC Adv.*, 2014, **4**, 19488.
50 Z. Q. Li, C. J. Lu, Z. P. Xia, Y. Zhou and Z. Luo, *Carbon*, 2007, **45**, 1686.
51 A. M. Molodets and A. A. Golyshev, *J. Exp. Theor. Phys.*, 2018, **126**, 772.
52 R. P. W. J. Struis, T. J. Schildhauer, I. Czekaj, M. Janousch, S. M. A. Biollaz and C. Ludwig, *Appl. Catal., A*, 2009, **362**, 121.
53 E. Keceli, M. Hemgesberg, R. Grünker, V. Bon, C. Wilhelm, T. Philippi, R. Schoch, Y. Sun, M. Bauer, S. Ernst, S. Kaskel and W. R. Thiel, *Microporous Mesoporous Mater.*, 2014, **194**, 115.
54 S. Schuster, E. Klemm and M. Bauer, *Chem. – Eur. J.*, 2012, **18**, 15831.
55 M. A. Gotthardt, R. Schoch, S. Wolf, M. Bauer and W. Kleist, *Dalton Trans.*, 2015, **44**, 2052.
56 M. A. Gotthardt, R. Schoch, T. S. Brunner, M. Bauer and W. Kleist, *ChemPlusChem*, 2015, **80**, 188.
57 M. Bauer, G. Heusel, S. Mangold and H. Bertagnolli, *J. Synchrotron Radiat.*, 2010, **17**, 273.
58 D. Bazin and J. J. Rehr, *J. Phys. Chem. B*, 2003, **107**, 12398.
59 A. Jentys, *Phys. Chem. Chem. Phys.*, 1999, **1**, 4059.
60 A. I. Frenkel, C. W. Hills and R. G. Nuzzo, *J. Phys. Chem. B*, 2001, **105**, 12689.
61 S. J. L. Billinge and I. Levin, *Science*, 2007, **316**, 561.
62 S. J. L. Billinge and M. G. Kanatzidis, *Chem. Commun.*, 2004, 749.
63 L. He, *J. Magn. Magn. Mater.*, 2010, **322**, 1991.
64 R. W. G. Wyckoff, *Crystal structures*, Wiley, New York, 1963, vol. 1.
65 K. Pirkkalainen and R. Serimaa, *J. Appl. Crystallogr.*, 2009, **42**, 442.
66 A. S. Masadeh, E. S. Božin, C. L. Farrow, G. Paglia, P. Juhas, S. J. L. Billinge, A. Karkamkar and M. G. Kanatzidis, *Phys. Rev. B: Condens. Matter Mater. Phys.*, 2007, **76**, 115413.
67 B. Gilbert, F. Huang, H. Zhang, G. A. Waychunas and J. F. Banfield, *Science*, 2004, **305**, 651.
68 C. J. Gommes, *Nanoscale*, 2019, **11**, 7386.
69 V. P. Zhdanov, E. M. Larsson and C. Langhammer, *Chem. Phys. Lett.*, 2012, **533**, 65.
70 G. E. Bacon, *Acta Crystallogr.*, 1951, **4**, 558.
71 J. Sá, Y. Kayser, C. J. Milne, D. L. A. Fernandes and J. Szlachetko, *Phys. Chem. Chem. Phys.*, 2014, **16**, 7692.
72 A. Tomita, Y. Ohtsuka and Y. Tamai, *Fuel*, 1983, **62**, 150.
73 Y. Guo, M. U. Azmat, X. Liu, J. Ren, Y. Wang and G. Lu, *J. Mater. Sci.*, 2011, **46**, 4606.
74 C. Vogt, E. Groeneveld, G. Kamsma, M. Nachtegaal, L. Lu, C. J. Kiely, P. H. Berben, F. Meirer and B. M. Weckhuysen, *Nat. Catal.*, 2018, **1**, 127.

Electronic Supplementary Material (ESI) for Nanoscale.

Supplementary Information

Hard X-ray-based techniques for structural investigations of CO_2 methanation catalysts prepared by MOF decomposition

Nils Prinz,[a,#] Leif Schwensow,[b,#] Sven Wendholt,[c,#] Andreas Jentys[d], Matthias Bauer,[c,*] Wolfgang Kleist[b,*] and Mirijam Zobel[a,*]

[a] *Chemistry Department, University Bayreuth, Universitätsstr. 30, Bayreuth 95447, Germany*

[b] *Faculty of Chemistry and Biochemistry, Ruhr University Bochum, Universitätsstr. 150, 44801 Bochum*

[c] *Chemistry Department, Paderborn University, Warburger Str. 100, Paderborn 33098, Germany*

[d] *Department of Chemistry, Technical University of Munich, Lichtenbergstr. 4, 85748 Garching*

[#]*Contributed equally to this work.*

Table of contents

General methods and approaches

XAS analysis

The XANES analysis, the LC-XANES fitting and the data preparation have been carried out with the program Athena of the demeter program package[1]. For data evaluation, the spectra background has to be removed in first instance and, therefore, a Victoreen-type polynomial was substracted.[1–4] The first inflection point was taken as energy $E_{(0)}$. To determine the smooth part of the spectrum, a piecewise polynomial was used. It was adjusted in a way to minimize the low-R components of the resulting Fourier transform. Afterwards the background-subtracted spectrum was divided by its smoothed part and the photon energy was converted to photoelectron wave number *k*. For the detailed EXAFS analysis, the resulting functions were weighted with k^3 and calculated with EXCURVE98, which works based on the EXAFS function and according to a formulation in terms of radial distribution functions:[4,5]

$$\chi(k) = \sum_j S_0^2(K) F_j(k) \int P_j(r_j) \frac{e^{\frac{-2r_j}{\lambda}}}{kr_j^2} \sin\left[2kr_j + \delta_j(k)\right] dr_j$$

The number of independent points N_{ind} was calculated according to information theory to determine the degree of overdeterminacy:[5]

$$N_{ind} = \frac{2\Delta k \Delta R}{\pi}$$

In this formula, Δk describes the range in *k*-space used for the data analysis and in ΔR the corresponding radial distance range in the Fourier filtering process is observable. For Δk the area from 3 to 14 in k-space has been used for analysis, leading to Δk of 11. In the R-space 1 to 6 was used, leading to ΔR of 5. So the number of independent parameters is 35, according to the given equation.
For the determination of the quality of the fit, two methods were used. The reduced χ^2_{red} considers the degree of overdeterminacy of the system and the number of fitted parameters p. Leading to the possibility to compare different models directly:[6]

$$\chi^2_{red} = \frac{\left(\frac{N_{ind}}{N}\right)}{N_{ind-p}} \sum_i \left(\frac{k_i^n}{\Sigma_j k_j^n \left| \chi_j^{exp}(k_j) \right|} \right)^2 \left[\chi^{exp}(k_j) - \chi^{theo}(k_j) \right]^2$$

With the R-factor, the percentage disagreement between experiment and adjusted function is shown. Thereby, it considers both systematic and random errors.[6]

$$R = \sum_i \frac{k_i^n}{\Sigma_j k_j^n \left| \chi^{exp}(k_j) \right|} \left| \chi^{exp}(k_j) - \chi^{theo}(k_j) \right| \cdot 100\%$$

PDF refinement procedures

The refinements were done with *DiffPy-CMI*, a python-based complex modelling software.[10] A Ni fcc crystallographic information file was used as the theoretical model for single-phase fits, and NiO and Ni hcp structures were used additionally for multi-phase fits. During the least squares refinements, we refined the lattice parameters *a* for the cubic, respectively *a* and *c* for the hexagonal structure, the atomic thermal motion parameter $B_{iso,i}$, correlated motion of nearest neighbors δ_2[11], the spherical crystallite diameter (based on an isotropic attenuated crystal model) and a scale factor. The goodness of fit is described by the least square residuum R_w:

$$R_w = \sqrt{\frac{\sum_n (G_{obs,n} - G_{calc,n})^2}{\sum_n G_{obs,n}^2}}$$

Radial distribution function and coordination numbers from PDF data

The radial distribution function (RDF) R(r) can be derived from the pair distribution function G(r).

$$R(r) = [G(r) + 4\pi\rho_0 r]r$$

The average number density ρ_0 is empirically extracted from the negative linear slope of the low r region in the PDF.[8] The coordination number N_C is defined as the number of atoms between distance r_1 and r_2 ($r_1 < r_2$), i.e. $N_C = \int_{r_1}^{r_2} R(r)dr$.[9] The integral of the peaks in the properly normalized R(r) yields the coordination number.

Although the PDF is not normalized on an absolute scale, the ratio of the coordination numbers is maintained by the ratio of peak areas. They can thus be normalized with the XAS coordination numbers. For this we set the N_C of the 1st peak equal to the EXAFS analysis and apply the necessary scaling factor to the other N_C.

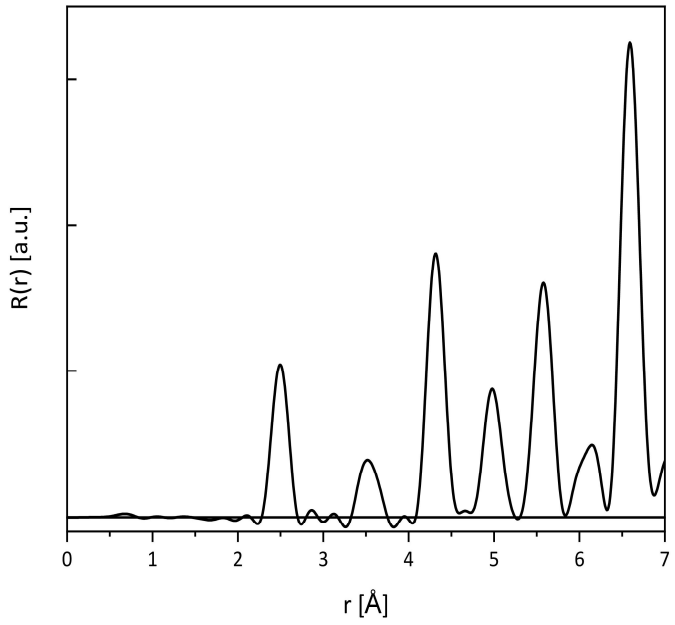

Fig.S1 Radial distribution function of Ni(BDC)(PNO) decomposed at 500 °C in 10% H_2/He.

Determination of conversion and selectivity using gas chromatography
The conversions of the methanation reaction were calculated using the following equation:

$$conversion\text{: X}(CO_2) = \left(1 - \frac{CO_{2,out}}{CO_{2,out} + CO_{out} + CH_{4,out} + C_2H_{6,out}}\right) \cdot 100\%$$

For conversions above 10%, Ar was used as an internal standard to correct for reaction-related volume contractions:

$$conversion\text{: X'}(CO_2) = \left(1 - \frac{CO_{2,out} \cdot Ar_{in}}{CO_{2,in} + Ar_{out}}\right) \cdot 100\%$$

The yields and selectivities were determined according to the following equations:

$$yield\text{: } Y(CH_4) = \left(\frac{CH_{4,out} \cdot Ar_{in}}{CO_{2,in} \cdot Ar_{out}}\right) \cdot 100\%$$

$$yield\text{: } Y(CO) = \left(\frac{CO_{out} \cdot Ar_{in}}{CO_{2,in} \cdot Ar_{out}}\right) \cdot 100\%$$

$$selectivity\text{:} S(CH_4) = \frac{Y(CH_4)}{X(CO_2)} \cdot 100\%$$

$$selectivity\text{:} S(CO) = \frac{Y(CO)}{X(CO_2)} \cdot 100\%$$

4

Material characterization and analysis

Samples were characterized using various methods including attenuated total reflectance infrared (ATR-IR) spectroscopy, ^{1}H nuclear magnetic resonance (NMR) spectroscopy, N_2 physisorption analysis, ion coupled plasma optical emission (ICP-OES) spectroscopy, powder X-ray diffraction (PXRD), X-ray absorption spectroscopy (XAS), pair distribution function (PDF) and transmission electron microscopy (TEM).

Attenuated total reflection infrared spectroscopy (ATR-IR)

ATR-IR spectroscopy was performed using undiluted powder samples at room temperature at a Nicolet 6799 FT-IR spectrometer with a Smart iTX Diamant-ATR detector from Thermo Fisher Scientific. The final spectrum was calculated by the mean of 100 scans for wavenumbers between 400 cm^{-1} and 4000 cm^{-1} with a resolution of 4 cm^{-1}.

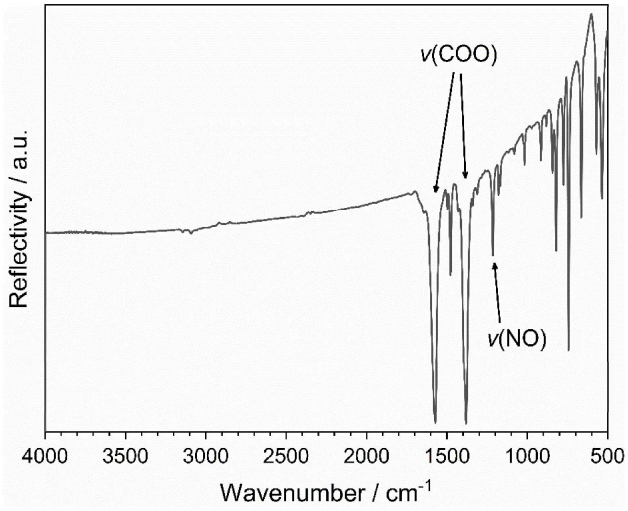

Fig. S2 ATR-IR spectrum of Ni(BDC)(PNO).

^{1}H nuclear magnetic resonance (NMR) spectroscopy

For ^{1}H-NMR spectroscopy, approximately 5 mg of MOF material was mixed with 70 µL DCl/D_2O and treated for 3 min in an ultrasonic bath. Subsequently, 140 µL NaOD/D_2O and 150 D_2O were added and placed in an ultrasonic bath for several minutes. The suspension was centrifuged at 10,000 min^{-1} and the liquid was transferred into a NMR tube. The residual solid was mixed with 50 µL NaOD/D_2O and 150 µL D_2O. After treatment in an ultrasonic bath and centrifugation, this liquid was added to the same NMR tube. The liquid phase ^{1}H NMR spectrum was recorded with a Bruker Ascend 400 MHz spectrometer and referenced to tetramethylsilane.

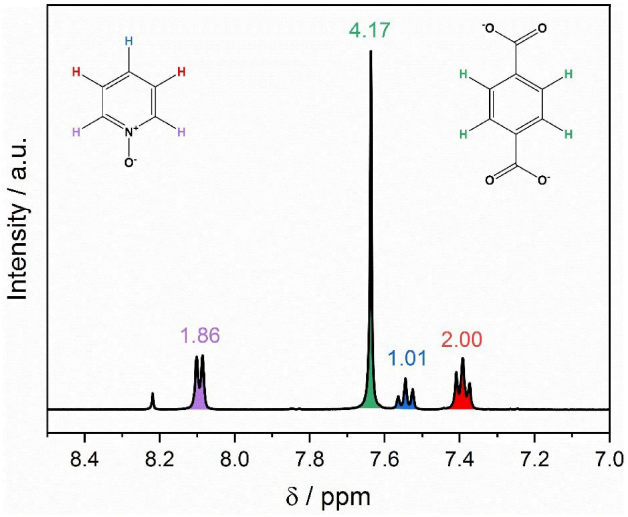

Fig. S3 ^{1}H nuclear magnetic resonance (NMR) spectrum of Ni(BDC)(PNO).

Ion coupled plasma optical emission spectroscopy (ICP-OES)

Prior to the ICP-OES analysis, 4-15 mg of the sample were burned in a crucible over a Bunsen burner. HCl was added and evaporated to form $NiCl_2$. Subsequently, the sample was dissolved in HNO_3 and transferred to a volumetric flask that was then filled with deionized water. Inductively coupled plasma optical emission spectroscopy (ICP-OES) of the solutions was performed with an iCAP 6500 Duo from Thermo Scientific via a six-point calibration. The software iTEVA9.8 was used for data processing.

Table S1 ICP-OES results for all decomposed samples.

Decomposition temperature	Ni content according to ICP-OES / wt%		
	0% H_2/He	**5%H_2/He**	**10%H_2/He**
350 °C	23	26	27
375 °C	35	60	61
400 °C	42	66	68
500 °C	53	72	82

Specific surface areas from N_2 physisorption

Specific surface areas were determined from nitrogen physisorption measurements using the BET method. The samples were dried for 20 h at 130 °C under vacuum and the measurements were performed with an Autosorb 6 setup from Quantachrome.

Table S2 BET surface analysis of all decomposed samples.

Decomposition temperature	Specific surface area according to BET / m^2/g		
	0% H_2/He	**5%H_2/He**	**10%H_2/He**
350 °C	5	48	44
375 °C	32	102	111
400 °C	23	56	77
500 °C	127	89	63

Powder X-ray diffraction (PXRD)

Powder X-ray diffraction was carried out at room temperature with a STOE STADI P Mythen2 4K diffractometer (Ge(111) monochromator; Ag Kα1 radiation, λ = 0.5594 Å) using four Dectris MYTHEN2 R 1K detector in Debye–Scherrer geometry. Samples were measured in 1 mm diameter Kapton capillaries for 12 h. The Q-range was 20.4 $Å^{-1}$.

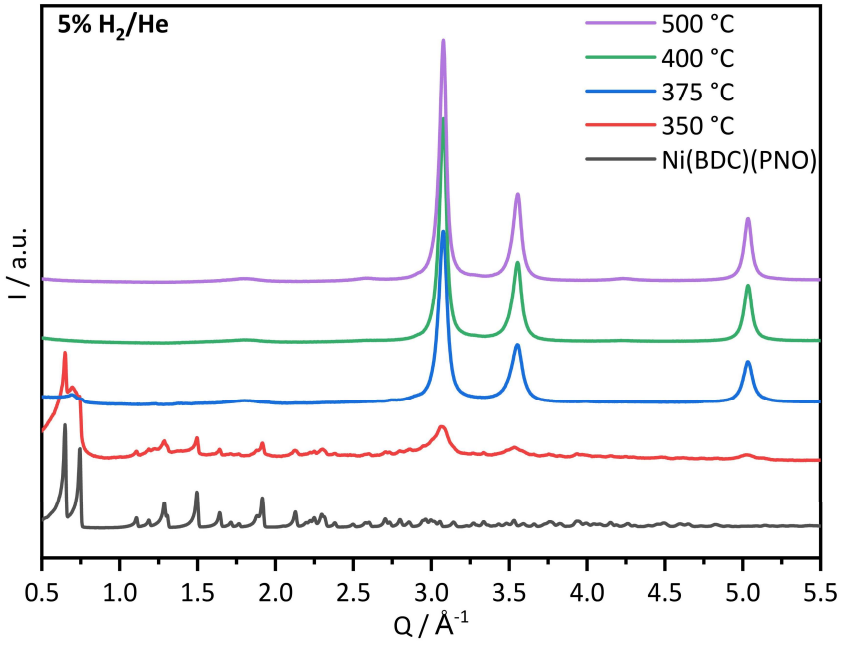

Fig. S4 PXRD of Ni(BDC)(PNO) decomposed at different temperatures in 5% H_2/He.

Particle size estimation with Scherrer equation

The Scherrer equation with the wave impulse vector Q was used to determine crystallite sizes:

$$D = \frac{K \cdot 2\pi}{FWHM(Q)}$$

$$K = 0.89\ (spherical\ shape\ constant)$$

The first three Bragg reflections of Ni fcc (111), (200) and (220) were used for a single peak fit with a pseudo Voigt function from which the FWHM was extracted.

Table S3: Particle sizes using Scherrer equation for different reflections.

Decomposition temperature	Reflection (hkl)	Particle size after decomposition in different atmospheres / nm		
		0% H_2/He	5% H_2/He	10% H_2/He
350 °C	(111)	-	6.0	7.2
	(200)	-	5.9	5.4
	(220)	-	4.5	7.0
375 °C	(111)	7.1	12.2	13.6
	(200)	3.0	8.2	9.6
	(220)	-	10.4	11.7
400 °C	(111)	11.5	15.8	14.6
	(200)	8.3	11.1	10.4
	(220)	11.3	13.6	12.9
500 °C	(111)	12.9	16.7	24.2
	(200)	8.6	12.1	19.7
	(220)	12.1	14.6	21.5

Williamson-Hall plots – evaluation of particle size and strain

XRD data was further analyzed with Williamson-Hall plots to separate particle size broadening from strain-induced broadening. The following equations provide the correlation of full width half maxima FWHM, scattering angle 2ϑ, Scherrer constant K (0.89 for spherical shape), employed wavelength λ (0.059 nm), particle diameter D and strain ε. For a plot of FWHM vs. sin(ϑ), particle size can thus be evaluated from the y-axis intercept and strain induced broadening from the slope of a straight line, if all data points (FWHM of all *hkl* reflexes) fall onto this line. The individual peak positions and FWHM have been determined from single peak fits using a pseudo-Voigt function. Instrumental broadening was accounted for with a LaB_6 standard measurement, by plotting the instrumental broadening $FWHM_{ins}$ against peak position 2ϑ. A 2nd order polynomial function was used to fit this instrumental broadening.

$$FWHM * \cos(\theta) = \frac{K * \lambda}{D} + 4 * \sin(\theta) * \varepsilon$$

$$D = \frac{K * \lambda}{y - intercept}$$

$$\varepsilon = slope$$

FWHM of all hkl reflections, except 200 and 400, fall onto a line for all samples, as shown for the 375 °C in 5 % H_2/He sample in Fig. S5. The following table provides the derived particle diameters and strain for all samples. As can be seen in Fig. S5, strain is homogeneous in different crystallographic directions of the particle, since the two straight lines in Fig. S5 have the same slope. However, particle size in the 200 direction is smaller (which was already estimated from Debye Scherrer neglecting ostrain broadening).

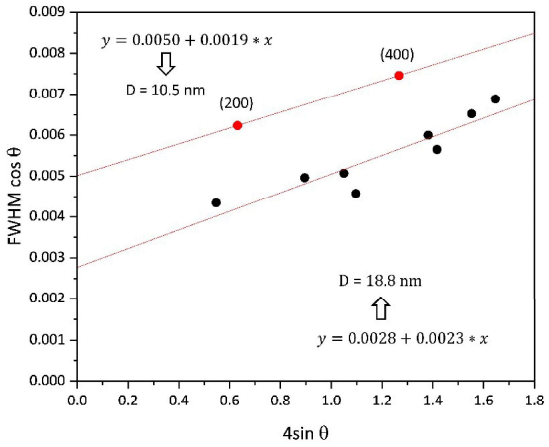

Fig. S5 Williamson-Hall plot of the sample decomposed at 375 °C in 5% H_2/He (catalytically most active sample). The red dots for the (200) and (400) reflection were not taken into account for the linear fit through the black data points.

Table S4: Particle sizes and strain extracted from Williamson-Hall plots. Different lower and upper error margins result for the particle diameters from the x^{-1} dependency of the diameter from the y-axis intercept, as shown in brackets.

	Particle size / nm		
Temperature	0 % H_2/He	5% H_2/He	10% H_2/He
375	-[a]	18.8 (+4.1 / -2.8)	17.5 (+1.9 / -1.6)
400	15.9 (+4.6 / –2.8)	15.9 (+1.6 / -1.3)	18.8 (+2.3 / -1.8)
500	15.0 (+1.4 /-1.2)	21.9 (+3.1 / -2.4)	20.2 (+0.8 / -0.7)
	Strain ε corresponding to Δd/d		
375	-[a]	0.0023 ±0.0004	0.0016 ±0.0003
400	0.0016 ±0.0005	0.0018 ±0.0002	0.0013 ±0.0003
500	0.0011 ±0.0002	0.0013 ±0.0002	0.0012 ±0.0001

[a] For 350 °C 0/5/10% H_2/He and 375 °C 0% H_2/He overlaps with phases that differs from fcc Ni were present. An accurate calculation of FWHM of a statistical amount of peaks was not possible.

XANES analysis

Table S5 Linear Combination fitting of the XANES spectra. Ni foil and Ni(BDC)(PNO) have been used as references for Ni^0 and Ni^{II}, respectively.

Sample	Fraction Ni^0 / %	Fraction Ni^{II} / %	Fraction Ni^0 (floating E_0) / %	Fraction Ni^{II} (floating E_0) / %
Ni@C-0%H_2-350	19.2 ± 0.8	80.8 ± 0.8	18.6 ± 0.6	81.4 ± 0.6
Ni@C-0%H_2-375	62.3 ± 0.6	37.7 ± 0.6	62.4 ± 0.6	37.6 ± 0.6
Ni@C-0%H_2-400	83.0 ± 0.7	17.0 ± 0.7	82.7 ± 0.7	17.3 ± 0.7
Ni@C-0%H_2-500	95.1 ± 3.0	4.9 ± 3.0	90.5 ± 2.3	9.5 ± 2.3
Ni@C-5%H_2-350	31. 1 ± 1.0	68.9 ± 1.0	30.4 ± 0.5	69.6 ± 0.5
Ni@C-5%H_2-375	88.2 ± 0.3	11.8 ± 0.3	88.1 ± 0.3	11.9 ± 0.3
Ni@C-5%H_2-400	92.4 ± 1.2	7.6 ± 1.2	91.2 ± 0.9	8.8 ± 0.9
Ni@C-5%H_2-500	95.4 ± 1.6	4.6 ± 1.6	93.8 ± 1.3	6.2 ± 1.3
Ni@C-10%H_2-350	36.0 ± 0.8	64.0 ± 0.8	35.6 ± 0.4	64.4 ± 0.4
Ni@C-10%H_2-375	85.7 ± 0.5	14.3 ± 0.5	85.4 ± 0.4	14.6 ± 0.4
Ni@C-10%H_2-400	88.2 ± 0.8	11.8 ± 0.8	87.7 ± 0.6	12.3 ± 0.6
Ni@C-10%H_2-500	92.9 ± 1.6	7.1 ± 1.6	91.4 ± 1.3	8.6 ± 1.3

EXAFS analysis

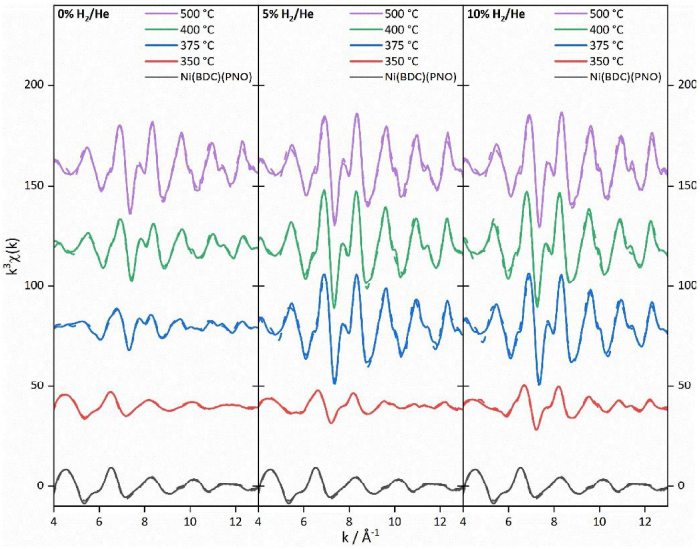

Fig. S6 Experimental $k^3\chi(k)$ EXAFS function of the MOF precursor decomposed in 0% (left), 5% hydrogen (middle) and 10% hydrogen in helium (right) atmosphere. The solid line shows the experimental spectra, the dotted line shows the theoretical fit of the EXAFS analysis.

Table S6 Structural parameter obtained by fitting the experimental EXAFS spectra of the sample, which have been decomposed in 0% H_2/He atmosphere in comparison to the catalyst precursor.

Sample	Abs-Bs[a]	N(Bs)[b]	R(Abs-Bs)[c] /Å	σ^d /Å^{-1}	R^e /%, χ_{red}^{2f}, E_f^g /eV, A_{fac}^h
Ni(BDC)(PNO)	Ni – O	6.1 ± 0.3	2.04 ± 0.02	0.084 ± 0.008	16.13
	Ni – C	6.6 ± 0.7	2.97 ± 0.03	0.110 ± 0.001	2.10×10^{-6}
	Ni – Ni	1.4 ± 0.3	3.52 ± 0.04	0.089 ± 0.009	7.243
	Ni – C	5.3 ± 1.1	3.98 ± 0.04	0.102 ± 0.010	1.048
	Ni – C	10.7 ± 2.2	4.49 ± 0.04	0.112 ± 0.011	
Ni@C-0%H_2-350	Ni – O	6.8 ± 0.4	2.05 ± 0.02	0.092 ± 0.009	16.82
	Ni – C	7.2 ± 1.4	3.02 ± 0.03	0.112 ± 0.011	1.74×10^{-6}
	Ni – Ni	1.1 ± 0.2	3.52 ± 0.04	0.112 ± 0.011	5.549
	Ni – C	6.6 ± 1.3	3.97 ± 0.04	0.110 ± 0.011	0.8000
	Ni – O	4.8 ± 1.0	4.44 ± 0.04	0.112 ± 0.011	
Ni@C-0%H_2-375	Ni – O	2.8 ± 0.3	1.99 ± 0.02	0.110 ± 0.011	35.00
	Ni – Ni	3.5 ± 0.4	2.50 ± 0.03	0.095 ± 0.010	7.6×10^{-6}
	Ni – C	2.4 ± 0.2	2.98 ± 0.03	0.032 ± 0.003	10.71
	Ni – Ni	1.6 ± 0.3	3.47 ± 0.03	0.110 ± 0.011	0.8581
	Ni – C	3.7 ± 0.7	3.85 ± 0.04	0.039 ± 0.04	
	Ni – Ni	3.4 ± 0.7	4.28 ± 0.04	0.087 ± 0.009	
	Ni – Ni	6.6 ± 1.3	5.10 ± 0.05	0.097 ± 0.010	
Ni@C-0%H_2-400	Ni – Ni	6.9 ± 0.7	2.49 ± 0.03	0.095 ± 0.010	22.74
	Ni – Ni	2.4 ± 0.5	3.41 ± 0.03	0.112 ± 0.011	2.67×10^{-6}
	Ni – C	3.7 ± 0.7	3.82 ± 0.04	0.022 ± 0.002	16.45
	Ni – Ni	7.4 ± 1.5	4.24 ± 0.04	0.095 ± 0.010	0.8148
	Ni – Ni	10.2 ± 2.1	5.06 ± 0.05	0.089 ± 0.009	
Ni@C-0%H_2-500	Ni – Ni	8.1 ± 0.8	2.47 ± 0.02	0.081 ± 0.008	21.46
	Ni – Ni	3.8 ± 0.8	3.49 ± 0.03	0.112 ± 0.011	3.03×10^{-6}
	Ni – C	3.8 ± 0.8	3.80 ± 0.04	0.032 ± 0.003	0.1029
	Ni – Ni	17.0 ± 3.4	4.28 ± 0.04	0.102 ± 0.010	0.8000
	Ni – Ni	19.6 ± 3.9	5.10 ± 0.05	0.095 ± 0.010	

[a] Abs: X-ray absorbing atom, and Bs: backscattering atom. [b] Number of backscattering atoms. [c] Distance of the absorbing atom from the backscattering atom. [d] Debye-Waller like factor. [e] Fit index. [f] Reduced χ^2. [g] Fermi energy, which accounts for the shift between theory and experiment. [h] Amplitude reduction factor.

Table S7 Structural parameter obtained by fitting the experimental EXAFS spectra of the sample, which have been decomposed in 5% H_2/He atmosphere in comparison to the catalyst precursor.

Sample	Abs-Bs[a]	*N*(Bs)[b]	*R*(Abs-Bs)[c] /Å	σ^d /Å^{-1}	R^e /%, $\chi_{red}{}^{2f}$, $E_f{}^g$ /eV, $A_{fac}{}^h$
Ni(BDC)(PNO)	Ni – O	6.1 ± 0.3	2.04 ± 0.02	0.084 ± 0.008	16.13
	Ni – C	6.6 ± 0.7	2.97 ± 0.03	0.110 ± 0.001	2.10×10^{-6}
	Ni – Ni	1.4 ± 0.3	3.52 ± 0.04	0.089 ± 0.009	7.243
	Ni – C	5.3 ± 1.1	3.98 ± 0.04	0.102 ± 0.010	1.048
	Ni – C	10.7 ± 2.2	4.49 ± 0.04	0.112 ± 0.011	
Ni@C-5%H_2-350	Ni – O	5.5 ± 0.6	2.05 ± 0.02	0.092 ± 0.009	16.21
	Ni – Ni	2.7 ± 0.3	2.51 ± 0.03	0.100 ± 0.010	2.95×10^{-6}
	Ni – C	1.9 ± 0.4	3.05 ± 0.03	0.039 ± 0.004	4.932
	Ni – Ni	0.3 ± 0.0	3.50 ± 0.04	0.039 ± 0.004	0.8000
	Ni – C	5.9 ± 1.2	3.97 ± 0.04	0.74 ± 0.007	
	Ni – Ni	2.4 ± 0.5	4.35 ± 0.04	0.100 ± 0.010	
	Ni – Ni	4.3 ± 0.8	5.18 ± 0.05	0.105 ± 0.011	
Ni@C-5%H_2-375	Ni – Ni	11.8 ± 1.2	2.47 ± 0.02	0.084 ± 0.008	23.68
	Ni – Ni	4.2 ± 0.8	3.45 ± 0.03	0.112 ± 0.011	2.29×10^{-6}
	Ni – C	6.7 ± 1.3	3.82 ± 0.04	0.045 ± 0.004	0.7178
	Ni – Ni	24.1 ± 4.8	4.28 ± 0.04	0.105 ± 0.011	12.89
	Ni – Ni	31.8 ± 6.2	5.10 ± 0.05	0.102 ± 0.010	
Ni@C-5%H_2-400	Ni – Ni	12.0 ± 1.2	2.48 ± 0.02	0.087 ± 0.009	16.45
	Ni – Ni	2.1 ± 0.4	3.46 ± 0.03	0.077 ± 0.008	1.62×10^{-6}
	Ni – C	5.8 ± 1.2	3.86 ± 0.04	0.032 ± 0.003	-0.0646
	Ni – Ni	12.8 ± 2.6	4.28 ± 0.04	0.084 ± 0.008	0.7353
	Ni – Ni	23.0 ± 4.6	4.76 ± 0.05	0.112 ± 0.011	
	Ni – Ni	35.6 ± 7.1	5.10 ± 0.05	0.112 ± 0.011	
Ni@C-5%H_2-500	Ni – Ni	10.5 ± 1.1	2.47 ± 0.02	0.081 ± 0.008	21.10
	Ni – Ni	3.6 ± 0.7	3.46 ± 0.03	0.100 ± 0.010	2.61×10^{-6}
	Ni – C	4.0 ± 0.8	3.82 ± 0.04	0.032 ± 0.003	1.102
	Ni – Ni	19.9 ± 4.0	4.28 ± 0.04	0.095 ± 0.010	0.6908
	Ni – Ni	23.3 ± 4.7	5.09 ± 0.05	0.087 ± 0.009	
	Ni - Ni	3.1 ± 0.6	5.53 ± 0.06	0.045 ± 0.005	

[a] Abs: X-ray absorbing atom, and Bs: backscattering atom. [b] Number of backscattering atoms. [c] Distance of the absorbing atom from the backscattering atom. [d] Debye-Waller like factor. [e] Fit index. [f] Reduced χ^2. [g] Fermi energy, which accounts for the shift between theory and experiment. [h] Amplitude reduction factor.

Table S8 Structural parameter obtained by fitting the experimental EXAFS spectra of the sample, which have been decomposed in 10% H_2/He atmosphere in comparison to the catalyst precursor.

Sample	Abs-Bs[a]	*N*(Bs)[b]	*R*(Abs-Bs)[c] /Å	σ^d /Å^{-1}	R^e /%, $\chi_{red}{}^{2f}$, $E_f{}^g$ /eV, $A_{fac}{}^h$
Ni(BDC)(PNO)	Ni – O	6.1 ± 0.3	2.04 ± 0.02	0.084 ± 0.008	16.13
	Ni – C	6.6 ± 0.7	2.97 ± 0.03	0.110 ± 0.001	2.10×10^{-6}
	Ni – Ni	1.4 ± 0.3	3.52 ± 0.04	0.089 ± 0.009	7.243
	Ni – C	5.3 ± 1.1	3.98 ± 0.04	0.102 ± 0.010	1.048ö
	Ni – C	10.5 ± 2.1	4.49 ± 0.04	0.112 ± 0.011	
Ni@C-10%H_2-350	Ni – O	5.6 ± 0.6	2.06 ± 0.02	0.097 ± 0.010	19.62
	Ni – Ni	3.5 ± 0.4	2.48 ± 0.03	0.089 ± 0.009	2.15×10^{-6}
	Ni – Ni	1.9 ± 0.4	3.49 ± 0.03	0.112 ± 0.011	4.879
	Ni – C	7.9 ± 1.6	3.94 ± 0.04	0.097 ± 0.010	0.7921
	Ni – Ni	2.0 ± 0.4	4.31 ± 0.04	0.071 ± 0.007	
	Ni – Ni	6.7 ± 1.3	4.80 ± 0.05	0.097 ± 0.010	
Ni@C-10%H_2-375	Ni – Ni	11.3 ± 1.1	2.47 ± 0.03	0.087 ± 0.009	22.68
	Ni – Ni	4.5 ± 0.9	3.46 ± 0.04	0.112 ± 0.011	2.55×10^{6}
	Ni – C	3.6 ± 0.7	3.84 ± 0.04	0.032 ± 0.003	12.95
	Ni – Ni	15.6 ± 3.1	4.26 ± 0.04	0.095 ± 0.010	0.7665
	Ni – Ni	25.1 ± 5,1	5.10 ± 0.05	0.095 ± 0.010	
	Ni – Ni	1.8 ± 0.36	5.54 ± 0.055	0.032 ± 0.003	
Ni@C-10%H_2-400	Ni – Ni	11.5 ± 1.2	2.48 ± 0.03	0.081 ± 0.008	18.93
	Ni – Ni	6.4 ± 1.3	3.49 ± 0.04	0.107 ± 0.011	2.14×10^{-6}
	Ni – C	4.9 ± 1.0	3.92 ± 0.04	0.045 ± 0.004	9.699
	Ni – Ni	17.2 ± 3.4	4.31 ± 0.04	0.087 ± 0.009	0.6490
	Ni – Ni	21.9 ± 4.4	4.78 ± 0.05	0.089 ± 0.009	
	Ni – Ni	21.2 ± 4.2	5.57 ± 0.06	0.112 ±0.011	
Ni@C-10%H_2-500	Ni – Ni	11.4 ± 1.1	2.47 ± 0.02	0.077 ± 0.008	21.05
	Ni – Ni	5.1 ± 1.0	3.46 ± 0.03	0.110 ± 0.011	2.52×10^{-6}
	Ni – C	5.9 ± 1.2	3.82 ± 0.04	0.032 ± 0.003	0.6036
	Ni – Ni	21.5 ± 4.3	4.28 ± 0.04	0.092 ± 0.009	0.6351
	Ni – Ni	26.1 ± 5.2	5.09 ± 0.05	0.087 ± 0.009	
	Ni – Ni	3.4 ± 0.7	5.54 ± 0.06	0.039 ± 0.004	

[a] Abs: X-ray absorbing atom, and Bs: backscattering atom. [b] Number of backscattering atoms. [c] Distance of the absorbing atom from the backscattering atom. [d] Debye-Waller like factor. [e] Fit index. [f] Reduced χ^2. [g] Fermi energy, which accounts for the shift between theory and experiment. [h] Amplitude reduction factor.

X-ray total scattering analysis

The following total scattering data was acquired on the laboratory diffractometer. All samples were measured in Kapton capillaries with a diameter of 1 mm for12 h. The powder diffraction patterns were collected in a Q-range of 0.3 – 20.4 $Å^{-1}$. PDF calculation was done with PDFgetX3[8] and PDF modelling with diffpy-cmi.[9]

Fig. S7 PDF of Ni(BDC)(PNO) decomposed at different temperatures in 10% H_2/He. As reference a calculated Ni fcc structure of particles with 10 nm size in diameter is shown

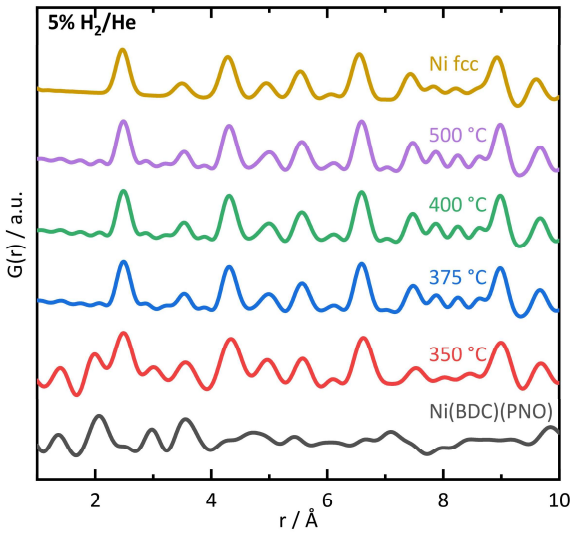

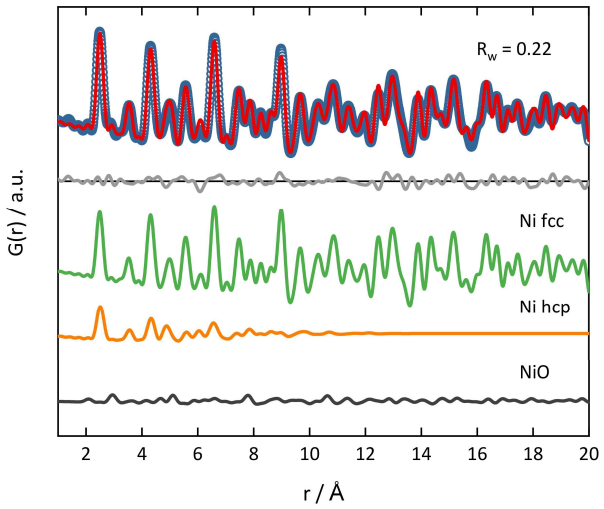

Fig. S8 PDF refinement of Ni(BDC)(PNO) decomposed at 400 °C in He. A small contribution of Ni hcp structure in the short range to the fit is still visible.

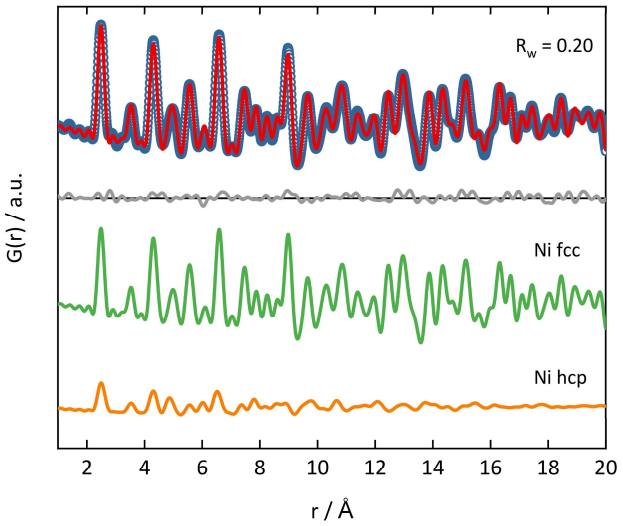

Fig. S9 PDF refinement of Ni(BDC)(PNO) decomposed at 500 °C in He. A small contribution of Ni hcp structure to the fit is still visible, but the overall ratio decreased from 375 °C to 500 °C.

For an overview of the robustness of the PDF modelling using Diffpy-CMI the refined values are exemplary showed for the sample decomposed at 375 °C in 0% H_2/He.

Table S9 Refined values from the Diffpy-CMI fit of the sample decomposed at 375 °C in 0% H_2/He.

Parameter	Refined value
B_{iso} Ni (fcc)	0.977 Å²
B_{iso} Ni (hcp)	0.367 Å²

B_{iso} Ni (NiO)	0.702 Å^2
B_{iso} O (NiO)	1.971 Å^2
a Ni fcc	4.17 Å
a NiO	3.53 Å
a Ni hcp	2.65 Å
c Ni hcp	4.34 Å
δ_2 Ni fcc	0.0
δ_2 Ni hcp	4.7
δ_2 NiO	6.9
Scale Ni fcc	0.30
Scale Ni hcp	0.15
Scale NiO	0.18
Particle size Ni fcc	48 Å
Particle size Ni hcp	55 Å
Particle size NiO	12 Å
R_w	0.32

Table S10 Change of the thermal displacement parameters U_{iso} extracted with Diffpy-CMI refinements

Temperature	U_{iso} 0%H_2/He	U_{iso} 5% H_2/He	U_{iso} 10%H_2/He
350°C	-	0.0121	0.0108
375°C	0.0124	0.0093	0.0086
400°C	0.0091	0.0084	0.0083
500°C	0.0081	0.0078	0.0083

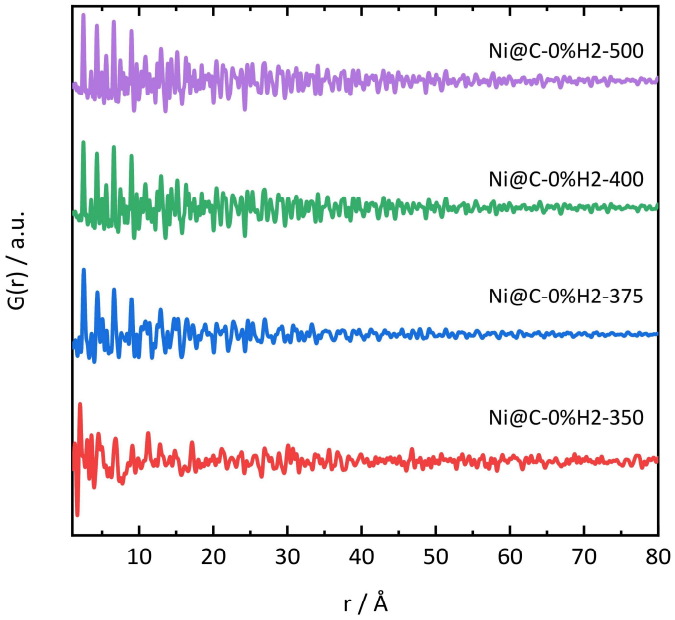

Fig. S10 PDF of Ni(BDC)(PNO) decomposed in 0% H_2/He over temperature in the range until 80 Å. The higher dampening in G(r) for smaller crystalline domain sizes is clearly visible.

Transmission electron microscopy

Transmission electron microscopy images were collected using a JEOL JEM-2200FS equipped with Schottky field-emission gun operated at 200 kV and a magnetic in-column omega type energy filter. Images were acquired using a GatanOneView imaging filter with a CMOS camera. Samples were prepared by dipping a lacey carbon film coated on a copper grid (Electron Microscopy Sciences) into the sample powder. For determination of particle sizes, about 200 particles were counted for each sample. For most samples a lognormal distribution could be fitted to the histograms. To determine the anisotropy of particles, a comparison of the width and length of particles for the most active sample decomposed at 375 °C under 5% H_2/He was carried out. This comparison shows, that particle lengths on average exceed particle widths, i.e. leading to a small particle anisotropy with axes differing by ca. (23.8-20.4)/23.8 = 14.3 %.

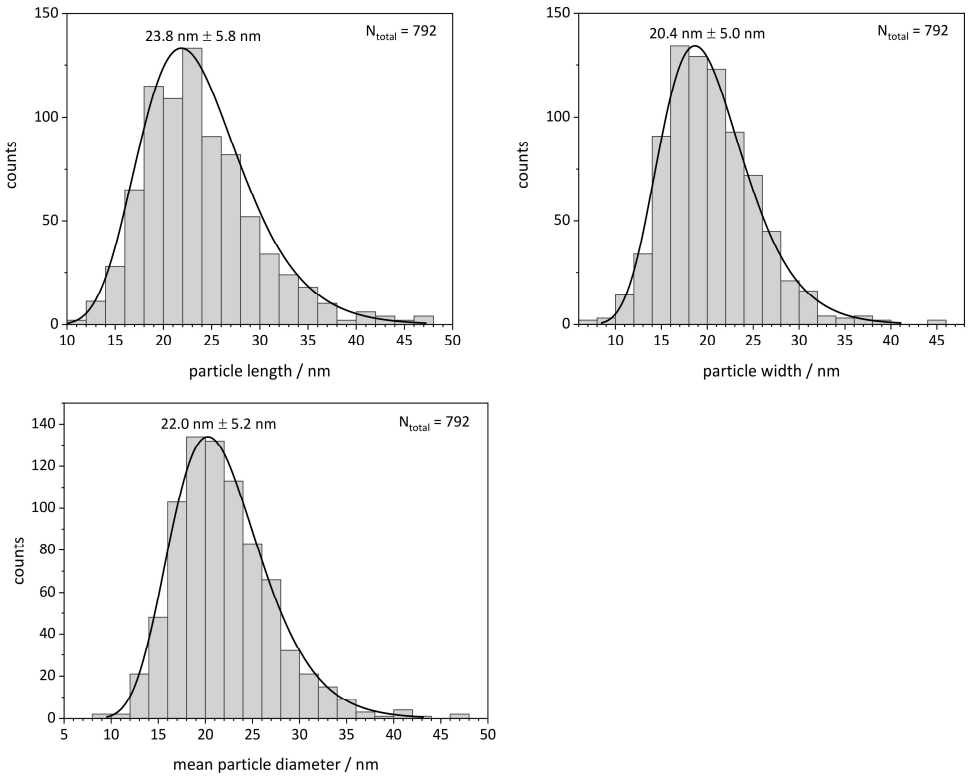

Fig. S11 Lognormal distributions for 375 °C 5% H_2/He using two orthogonal axes (length and width) for the particle sizes to investigate ellipsoidal contribution to the overall mean particle diameter. The lengths and widths are shown separately first (top row) and then averaged (bottom row).

TEM lognormal distributions 0% H_2/He

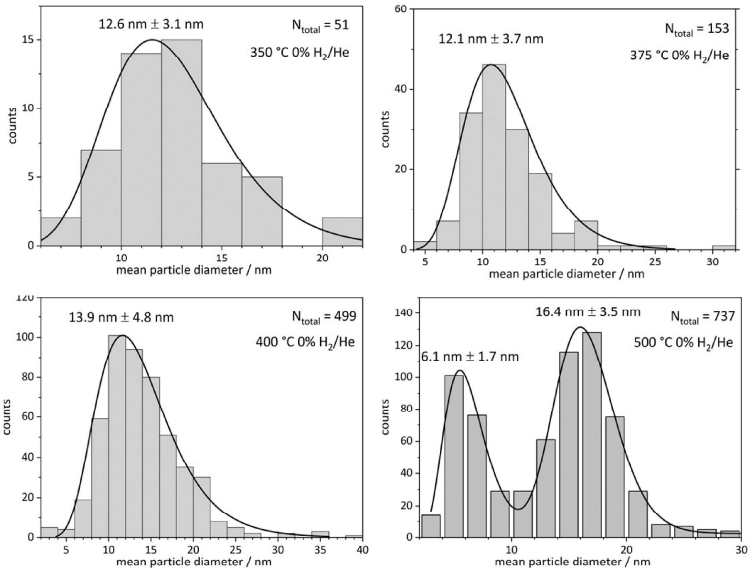

Fig. S12 Lognormal distribution of TEM particle sizes with mean diameter and standard deviation of the distribution for the samples decomposed under 0% H_2/He.

TEM lognormal distributions 10% H_2/He

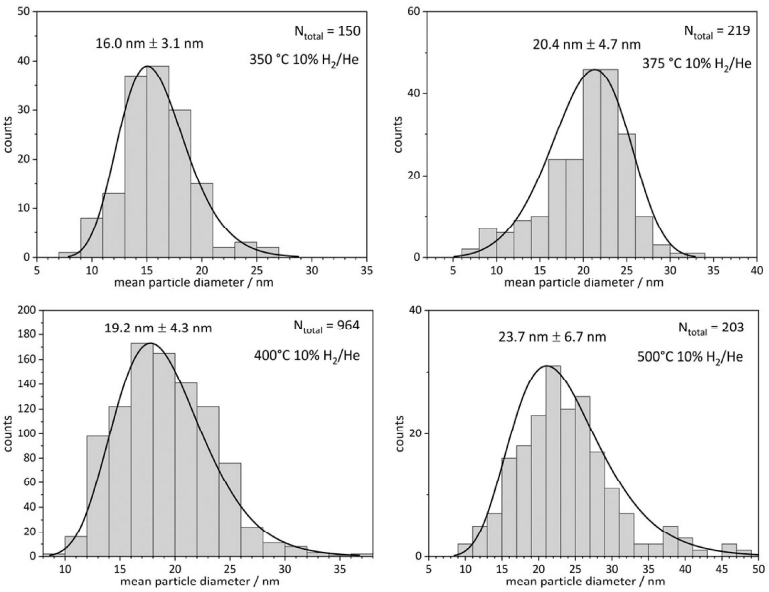

Fig. S13 Lognormal distribution (except 375 °C, which is a Weibull distribution) of TEM particle sizes with mean diameter and standard deviation of the distribution for the samples decomposed under 10% H_2/He.

Particle size estimation via EXAFS analysis

The method for particle size estimation is based on the following equation:[7]

$$N_i = \frac{aN_{at}}{b + N_{at}} + \frac{cN_{at}}{d + N_{at}}$$

N_i is the average number of neighbors in each coordination shell (i=1-5) as a function of atoms present in the cluster (N_{at}).[7]

Table S11: Parameters used to fit the coordination number (N_i) as a function of the number of atoms (N_{at}).

	N_1	N_2	N_3	N_4	N_5
a	8.981	3.922	13.204	6.830	10.609
b	9.640	7.368	39.134	55.369	37.582
c	3.026	2.192	11.593	5.684	14.265
d	1462.61	989.28	1292.24	1541.86	1020.82

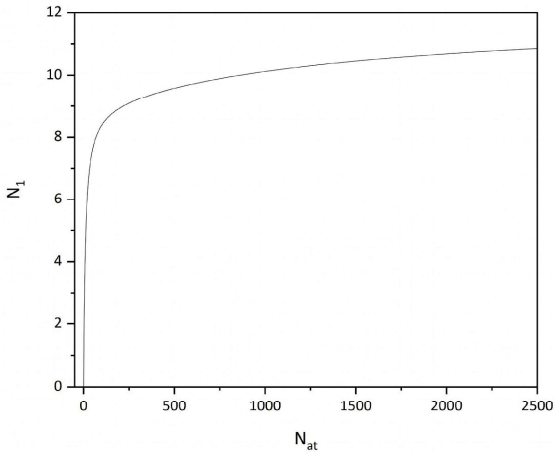

Fig. S14 Average coordination of the first coordination shell (N_1) as the number of atoms (N_{at}).

Comparison of coordination numbers from EXAFS and RDF analysis

Coordination numbers calculated from the radial distribution function derived from the experimental PDF are normalized with the 1st shell coordination number from EXAFS analysis. In contrast to EXAFS, coordination numbers beyond the third shell can be extracted, because of the smaller scattering and absorption cross sections and absence of multiple scattering of high energy X-rays compared to photoelectrons. The coordination numbers of the first three shells match well. The particle growth is also directly reflected in those increasing CN for distances beyond the XAS range, see for example at 6.6 Å.

Table S12 Coordination numbers from EXAFS and RDF analysis. Theoretical value for bulk Ni fcc in brackets.

Decomposition temperature	CN 1st shell at 2.5 Å (theor. CN 12)		CN 2nd shell at 3.5 Å (theor. CN 6)		CN 3rd shell at 4.3 Å (theor. CN 24)		CN 7th shell at 6.6 Å (theor. CN 48)
	PDF	XAS	PDF	XAS	PDF	XAS	PDF
0% H_2/He							
350 °C	-	-	-	-	-	-	-
375 °C	3.5	3.5	0.92	1.6	4.8	3.4	9.8
400 °C	6.9	6.9	3.6	2.4	12.0	7.4	21.4
500 °C	8.1	8.1	3.8	3.8	14.4	17.0	25.2
5 H_2/He							
350 °C	2.7	2.7	1.5	0.3	4.8	2.4	7.4
375 °C	11.8	11.8	5.6	4.2	21.3	24.1	37.9
400 °C	12.0	12.0	5.7	2.1	21.4	12.8	40.7
500 °C	10.5	10.5	5.4	3.6	19.3	19.9	35.3
10 H_2/He							
350 °C	3.5	3.5	1.7	1.9	6.1	2.0	11.2
375 °C	11.3	11.3	5.3	4.5	20.1	15.6	37.0
400 °C	11.5	11.5	5.6	6.4	20.7	17.2	39.6
500 °C	11.4	11.4	5.7	5.1	20.9	21.5	40.4

Note that the CN for 0% H_2/He 350 °C could not be derived, because of a large fraction of Ni(BDC)(PNO) in the sample.

References

1 B. Ravel and M. Newville, ATHENA, ARTEMIS, HEPHAESTUS: data analysis for X-ray absorption spectroscopy using IFEFFIT, *J. Synchrotron Radiat.*, 2005, **12**, 537–541. DOI: 10.1107/S0909049505012719.

2 T. S. Ertel, H. Bertagnolli, S. Hückmann, U. Kolb and D. Peter, XAFS Spectroscopy of Liquid and Amorphous Systems: Presentation and Verification of a Newly Developed Program Package, *Appl. Spectrosc.*, 1992, **46**, 690–698. DOI: 10.1366/0003702924125069.

3 M. Newville, IFEFFIT: interactive XAFS analysis and FEFF fitting, *J. Synchrotron Radiat.*, 2001, **8**, 322–324. DOI: 10.1107/s0909049500016964.

4 N. Binsted and S. S. Hasnain, State-of-the-Art Analysis of Whole X-ray Absorption Spectra, *J. Synchrotron Radiat.*, 1996, **3**, 185–196. DOI: 10.1107/S0909049596005651.

5 N. Binsted and F. Mosselmans, eds., *EXCURV98 Manual*, Daresbury, UK.

6 M. Bauer and H. Bertagnolli, The amplitude reduction factor and the cumulant expansion method: crucial factors in the structural analysis of alkoxide precursors in solution, *J. Phys. Chem. B*, 2007, **111**, 13756–13764. DOI: 10.1021/jp076386i.

7 A. Jentys, Estimation of mean size and shape of small metal particles by EXAFS, *Phys. Chem. Chem. Phys.*, 1999, **1**, 4059–4063. DOI: 10.1039/a904654b.

8 P. Juhás, T. Davis, C. L. Farrow and S. J. L. Billinge, PDFgetX3 : a rapid and highly automatable program for processing powder diffraction data into total scattering pair distribution functions, *J. Appl. Crystallogr.*, 2013, **46**, 560–566. DOI: 10.1107/S0021889813005190.

9 P. Juhás, C. L. Farrow, X. Yang, K. R. Knox and S. J. L. Billinge, Complex modeling: a strategy and software program for combining multiple information sources to solve ill posed structure and nanostructure inverse problems, *Acta Crystallogr., Sect. A: Found. Adv.*, 2015, **71**, 562–568. DOI: 10.1107/S2053273315014473.

9 High resolution X-ray absorption and emission spectroscopy for detailed analysis of new CO_2 methanation catalysts

Building on *the ex-situ* results, in-depth investigations of the pre-catalysts were carried out using XES, with particular focus on electronic interactions. To identify the highly undefined mixture of different Ni species, modeling by four references was carried out. Through a combination of HERFD-XANES, FEFF based calculations and VtC spectroscopy correlations between Ni(II) species in the nanoparticles and particle growth could be found.

Participation in this publication

M. Nowakowski – assistance in measurements, assistance in HERFD-XANES and VtC analysis

R. Schoch – assistance in manuscript preparation

S. Strübbe & M. Bauer – HERFD-XANES and VtC measurements, HERFD-XANES and VtC analysis, FEFF calculations

Reproduced from:

High resolution X-ray absorption and emission spectroscopy for detailed analysis of new CO_2 methanation catalysts

Sven Strübbe, Michał Nowakowski, Roland Schoch and Matthias Bauer, *ChemPhysChem*, *submitted.*

With permission from Wiley-VCH.

WILEY-VCH

RESEARCH ARTICLE

High resolution X-ray absorption and emission spectroscopy for detailed analysis of new CO_2 methanation catalysts

Sven Strübbe,[a] Michal Nowakowski,[a] Roland Schoch[a] and Matthias Bauer*[a]

[a] S. Strübbe, Dr. M. Nowakowski, Dr. R. Schoch, Prof. Dr. M. Bauer
Department of Chemistry and Center for Sustainable Systems Design (CSSD)
Paderborn University
Warburger Straße 100, 33098 Paderborn, Germany
E-mail: matthias.bauer@upb.de

Supporting information for this article is given via a link at the end of the document.

Abstract: A new approach for the characterization of CO_2 methanation catalysts prepared by thermal decomposition of a nickel MOF by hard X-ray photon-in/photon-out spectroscopy in form of high energy resolution fluorescence detected X-ray absorption near edge structure spectroscopy (HERFD-XANES) and valence-to-core X-ray emission (VtC-XES) is presented. In contrast to conventional X-ray absorption spectroscopy, the increased resolution of both methods allows a more precise phase determination of the final catalyst, which is influenced by the conditions during MOF decomposition.

Introduction

In the future, long-term storage of energy from renewable resources will be a major task for an efficient sustainable power supply. The excess energy from solar or wind sources can be used to empower electrochemical cells for water electrolysis and thus produce hydrogen in an environmentally friendly way. In a further step, this hydrogen can be used for the synthesis of known and already used carbon-based energy carriers. This is advantageous as it allows the continued use of the known energy infrastructure, both for storage and transportation. A potential approach as part of the power-to-X concept is the methanation of CO_2 based on the Sabatier reaction (Eq. 1).[1]

$$CO_2 + 4H_2 \rightleftharpoons CH_4 + 2\,H_2O\,(g) \qquad \text{Eq. 1}$$

It is a combination of the reverse water gas shift reaction (Eq. 2) and the reduction of CO towards methane (Eq. 3)

$$CO_2 + H_2 \rightleftharpoons CO + H_2O\,(g) \qquad \text{Eq. 2}$$
$$CO + 3H_2 \rightleftharpoons CH_4 + H_2O\,(g) \qquad \text{Eq. 3}$$

The most common catalysts for this approach are supported Ni compounds, which show high activity and methane selectivity under mild conditions.[2] Since the catalytic performance strongly depends on the nature of the active Ni species and the support material, several analytical methods have to be employed to understand the working principle of such catalysts and finally to improve the catalytic performance.[3] For this purpose, the structure of the active species has to be determined.[4] Metallic species are needed as catalysts for the reduction of CO_2 to methane, which is typically achieved by the activation of pre-catalysts in a reducing H_2 atmosphere. In a realistic scenario, due to the fluctuation in solar or wind energy, hydrogen supply by sustainable production methods fluctuates if consumed without intermediate storage. This presents a major challenge to the continuous operation of the methanation reaction of Eq. 1-3, as the Ni catalysts tend to deactivate under fluctuating hydrogen supply conditions due to surface oxidation or sintering. Previous operando studies have shown that a strong deactivation of the active Ni catalyst is observed during periods of hydrogen deficiency.[5] Thus, highly stable catalysts that can tolerate fluctuating conditions at different temperatures are crucial for the methanation of CO_2 by green hydrogen.

A possible approach to achieve this goal is the thermal decomposition of metal-organic frameworks (MOF) to yield carbon-supported catalysts.[6] The so-called MOF-mediated synthesis (MOFMS) describes the treatment of a metal-organic framework in a defined inert or reducing atmosphere at elevated temperatures.[7] During the preparation process, the organic linkers of the MOF precursor are decomposed, reduced, and finally converted to carbonaceous species. The resulting materials are typically characterized by metal nanoparticles, stabilized by a carbon matrix.[8] The ease of synthesis, modifiability, versatility, and high crystallinity make MOFs highly defined and promising precursors for the preparation of catalytically active materials.[9] By changing the decomposition conditions, morphologies and compositions of the final catalyst can be adjusted.[7,10] Although MOF decomposition as a synthetic route to active functional materials is quite new, it has already been used to create catalytically active nanoparticles,[11] nanoporous carbon materials,[12] electrode materials,[13] and hybrid supercapacitors.[14]

The potential of MOF decomposition to generate active CO_2 methanation catalysts was demonstrated in a previous study.[15] However, this initial attempt also proved that the manifold of parameters impacts the final structures which are formed to a large extent and the resulting species show a large particle size and phase distribution. Therefore, the establishment of a structure-activity correlation is a major challenge for such systems. The element specificity of X-ray absorption-based techniques, such as XANES (X-ray absorption near edge structure) and EXAFS (Extended X-ray absorption fine structure) offers unique tools to investigate these catalysts by determination of the qualitative electronic and geometric structure.[16] However, the sensitivity of both XANES and EXAFS is limited due to the core-hole lifetime broadening in XANES spectra and the similarity of scattering amplitudes of atomic neighbors in the periodic table

as backscatterers in EXAFS functions. High-energy-resolution fluorescence detected X-ray absorption near edge structure (HERFD-XANES) determination and Valence-to-Core X-ray emission spectroscopy (VtC-XES) offer the chance to reduce these limitations, while still using the benefits of hard X-rays such as nearly unlimited tolerance towards sample environment and element specificity.[17]

In this work, both methods are applied and established to investigate the composition of a real CO_2 methanation catalysts. The samples were investigated in a previous study utilizing conventional XAS, XRD, and PDF.[15] The metal-organic framework Ni(BDC)(PNO), which has a well-defined crystal structure[18] of Ni^{2+} centers that are cross-linked using benzene-1,4-dicarboxylate (BDC) and pyridine-*N*-oxide (PNO) molecules are used as a precursor for the catalyst preparation as well as a reference for the analysis. The crystal structure is very similar to MIL-53 containing one-dimensional channels formed by distorted octahedral NiO_6 Octahedrons. In addition to their coordinated BDC, every Ni center is coordinated by one PNO molecule which protrudes the channels, which allows to achieve a high porosity of the framework.[19] The desired carbonaceous matrix around the Ni-species is achieved by the organic linkers through decomposition under an inert or moderately reducing (10 % H_2) atmosphere.

Eight nickel pre-catalysts obtained by different decomposition conditions were studied. The Ni(BDC)(PNO) MOF was decomposed at 350, 375, 400, and 500 °C and in two different atmospheres: pure helium and 10% hydrogen in helium, respectively. Since the pre-catalyst samples represent a mixture of several nickel species, modeling of the samples in terms of different phases had to be performed. HERFD-XANES and VtC spectra of the obtained products were thus analyzed in terms of potential bulk Ni(0), Ni_3C, NiO, and MOF phases after careful calibration of the methods using the four mentioned references with the support of *ab initio* calculations based on the FMS (Full Multiple Scattering) approach.[20] A multistep approach has been chosen: First, FEFF calculations of the four reference spectra were performed for the unoccupied and occupied density of states (DOS) contributions. The parameters (cf. Table 1) were chosen to match the HERFD-XANES spectra in the individual features. In the next step, the experimental HERFD-XANES spectra of the pre-catalyst samples were fitted in a linear combination fit (LCF) using the four references Ni(0), Ni_3C, NiO, and Ni-MOF. Based on the fitted fractions in the LCF of the four references, the DOS contributions of the references, weighted by the fraction from the LCF, were multiplied to represent the DOS contributions of the samples in the VtC-XES.

Results and Discussion

Linear combination fitting of the HERFD-XANES spectra

For detailed analysis of the pre-catalyst samples, four different references have been used which are contributing to the phase composition during the thermal decomposition of Ni MOFs. In a previous study, only bulk Ni and the original MOF were used as Ni(0) and Ni(II) references, respectively, in a linear combination XANES (LC-XANES) fit to determine the oxidation state fractions in the samples.[15,21] Here, two more references were added: NiO to reproduce the first steps in decomposition progress, and Ni_3C to account for Ni carbon species that were identified in previous work by TEM.[15] Due to the normalized nature of HERFD-XANES, only these high-resolution data can be used in an LC fit procedure, while VtC-XES data has to be interpreted in light of the LC HERFD-XANES fit results (*vide infra*). The LC fit results of the four references to the experimental HERFD-XANES spectra for the activation process in different atmospheres of 0 and 10% H_2 at various temperatures from 350 to 500°C are shown in Figure 1. The LC fits are based on the derivatives of the XANES spectra. As an example spectrum for the LC fit, the sample decomposed at 375 °C in a 10% H_2 atmosphere is shown. The LC fit results and spectra of the other samples are given in the supplementary information (Figures S1-S8), as well as the detailed description of the VtC spectra of the reference samples (Figures S9-S12), and the comparison with FEFF calculation (Figures S13-S16). The numerical values of the LCF of the pre-catalysts are shown in Table S1 in the supplementary information.

Comparison of the two samples decomposed at 350 °C shows that the sample in the reductive atmosphere of 10% H_2 exhibits a more pronounced loss of MOF fractions towards the Ni_3C species. These results fit the Thermogravimetric analysis (TGA) results from previous work, where the decomposition of MOF was mainly induced between 360 and 365 °C.[15] If the temperature specified in the TGA is exceeded and the samples are decomposed at 375 °C, this trend continues even further. While the contribution of MOF continues to decrease, a significant proportion of Ni(0) is formed. At the same time, the fraction of Ni_3C increases significantly, so that these two references dominate the composition according to LCF. By further increasing the decomposition temperature to 400 °C, about half of the sample composition is represented by Ni_3C. Only when decomposing in a reductive atmosphere, no contribution by the MOF can be observed anymore. Whereas NiO is preserved in both samples. In the case of the 500 °C sample, it is observed that in an inert atmosphere, all four references continue to represent the LCF. In a 10% H_2 atmosphere, however, the sample consists of 60% Ni_3C and 40% Ni foil, which means that no traces of Ni(II) containing species can be found.

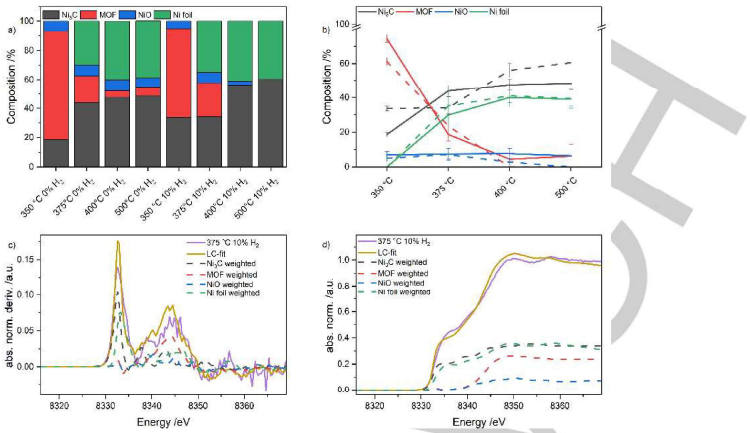

Figure 1: Linear combination fitting of the HERFD-XANES spectra. The four references, Ni_3C, MOF, NiO and Ni foil have been compared. In a) the percentage weightings of the LC-fit are shown. b) shows the trend of the references with increasing temperature. The solid line shows the sample that was decomposed at 0% H_2 in He, the dashed line shows 10% H_2 in He, respectively. The diagram is showing the mathematical error as well. In c) the LC-fit of the derivative functions for the 375 °C 10% H_2 are shown together with the weighted fractions. D) shows the corresponding normalized HERFD-XANES spectra. In c) and d) the solid lines show the samples and the LC-fit functions, the dotted lines are the weighted fractions of the references.

Valence-to-core and HERFD-XANES analysis

The linear combination fitting (LCF) of references with a combination of the FEFF calculations (see supplementary information, Figure S1-S12) for the references was used to analyze the decomposed samples further. The DOS functions of the four references were weighted by the values extracted from the LCF (Figure 1) to reconstruct the average electronic structure of the decomposed pre-catalyst samples. It has to be emphasized here, that this approach will include neither any long-range interactions in the mixture nor interface effects. For the sake of clarity, the occupied and unoccupied DOS functions have been plotted in Figure 2 and Figure 3 separately for each orbital contribution (sDOS, pDOS, and dDOS) and were compared to the experimental spectra of the samples. The energy axis is adjusted to show the spectra relative to the Fermi level (E_F) as 0 eV. Below the Fermi level, the signals are dominated by occupied state contributions, above the Fermi level mainly unoccupied states are representing the shape of the spectra. More detailed information on the individual contributions of each element at specific energies can be found in the supplementary information (Figure S13-S16).

Figure 2 shows the calculated p, d, and sDOS functions of the samples which have been decomposed in 0% H_2 in Helium atmosphere. All the main features of the experimental spectra are reproduced by the overlap of the corresponding calculated DOS functions. The overlap of occupied and unoccupied states is present for every sample, indicating that the whole set of pre-catalyst behaves as conductors.

For the pre-catalyst which was decomposed at 350 °C, the *unoccupied states* (dotted lines) are showing a pre-peak feature. If the decomposition temperature is increased to 375 °C the pre-peak is shifting to higher energies. The pre-peak is less resolved as it contains three contributions, i.e. Ni_3C, Ni(0), and MOF, and the reference pre-peaks are shifted by 1.5 eV to each other. At 400 °C decomposition temperature, the unoccupied states responsible for the pre-peak are shifting towards the range of +2 to +4 eV. Still, the references are used to fit the mixture of the 400 °C pre-catalyst are affected by a shift of pre-edges and white lines, thus affecting the resolution of the pre-peak. The pre-catalyst which was decomposed at 500 °C shows the pre-peak feature between +2 and +3 eV and is highly dominated by bulk Ni(0) species. Accordingly, the unoccupied DOS contributions show a clear trend and the spectra represent the high contribution of Ni_3C and Ni foil. Since the pre-peak originates from a p/d hybridization, these unoccupied DOS contributions are also responsible for the pre-peak here.

The DOS functions of the *occupied states* (solid line) are showing some specific features of high MOF contribution in the sample which was decomposed at 350 °C. These are mainly dominated by s and p contributions of O and N in the low energy range of around -20 eV. Since in the LCF the MOF contributions decrease sharply, the O and N contributions also decrease sharply at higher temperatures, especially at the decomposition temperature of 400 and 500 °C. This fits the slight increase of intensity in this energy region of the VtC spectrum. When the ratio between the maximum peak around -2 eV and the signal for the N and O contributions around -20 eV is compared, it increases in favor of the signal at -2 eV with increasing temperature. Another feature that contributes to the spectral shape is the C sDOS and O pDOS overlap in the region of -10 eV (cf. ESI). The pre-catalyst sample which has been decomposed at 350 °C has two C sDOS features at -10.4 eV and -8.7 eV which are mainly overlapping with O pDOS features. With increasing temperature, the signal at -8.7 eV is vanishing and a C sDOS contribution around -11.5 eV becomes visible. Simultaneously a small pDOS contribution of Ni appears

in this energy range. These diminishing contributions can be attributed to the C and O contributions of the MOF. Accordingly, the loss of the MOF can also be represented electronically in this energy region of the VtC spectrum. The overlap between the strong C sDOS contribution and the O pDOS contribution around -10 eV is also increasing with a higher amount of Ni pDOS contribution, hence with higher temperatures. Here, the C sDOS feature can be attributed to the Ni_3C contributions. Thus, the building up of a carbon shell is indicated.

The VtC spectrum of the sample which was decomposed at 350 °C is showing two main features, one around -6 eV and one around -2 eV. They are generated by the overlap of absorbing Ni dDOS contributions with C, N, and O pDOS. The lower intensity between these features can be attributed to the decrease of the shape of N pDOS functions from the MOF and the C pDOS functions from the Ni_3C since these two references mainly dominate the spectrum. Even though around -4 eV and -9 eV Ni sDOS functions are slightly overlapping with C, N, and O pDOS functions, the mentioned p/d overlap is representing the VtC shape of the measured pre-catalyst more accurately.

With increasing temperature, the shape of the VtC spectrum of the pre-catalysts approaches the VtC shape of the bulk Ni(0). Overall, the individual contributions show that an approximation of the electronic states of the sample is possible. The high fractions of all references in the sample cause a broad, poorly defined spectrum of the 350°C 0% H_2 sample. In particular, the contributions of the MOF provide a strong broadening of the spectrum in the sample.

The VtC signal of the 375 °C pre-catalyst is mainly reflected by the Ni and C pDOS / Ni dDOS overlap around -2 eV. Contrary, for 350 °C the spectrum is represented mainly by the O pDOS contributions in this energy range. This fits the assumption that the carbon containing species in the sample are changing from species with higher MOF contributions to species that are showing more Ni_3C behavior and higher Ni(0) contributions. At the same time, the dDOS functions of neighbour Ni atoms overlap with Ni, and O pDOS functions around -3 and -4 eV are decreasing. Nevertheless, the shape of the spectrum is influenced by the contribution of Ni sDOS overlap with O pDOS around -6 eV. The overlaps at lower energies, which strongly affect the shape of the 350 °C spectrum, are still present but decrease. Since fewer references are needed to model the spectrum and the DOS functions are less distributed, the spectra become more defined as the temperature increases. Thus, the high fractions of Ni_3C and Ni foil are reproduced.

This trend continues as the temperature is increased to 400 °C. In particular, the fraction of MOF decreases significantly, whereas the fraction represented by NiO remains relatively constant. However, when further increased to 500°C, there is hardly any change in the composition of the HERFD-XANES spectra by the references, so these two samples can be similarly reflected by DOS functions. For the lower-energy range from -20 to -10 eV, there is still slight overlap of the sDOS and pDOS contributions, but only the contribution around -10 eV visibly influences the spectral shape. The VtC spectrum increases in intensity and at the same time two features can be observed in the signal maximum. These are at about -4 and -2 eV. The signal at -4 eV can be explained in particular by the contributions of Ni pDOS with Ni dDOS overlap. Contrary, the signal at -2 eV is due to the C pDOS / Ni dDOS combination.

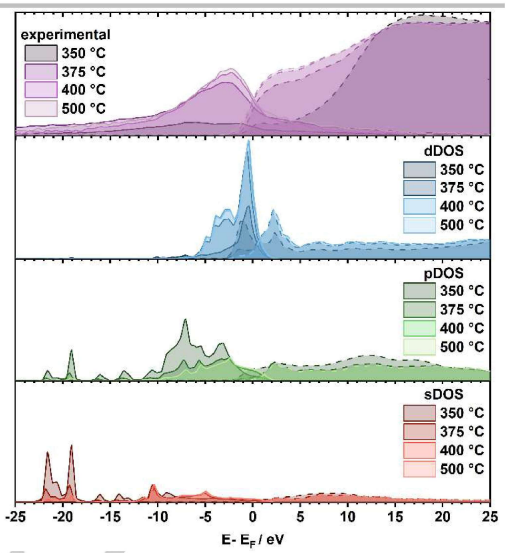

Figure 2: Experimental VtC-XES and HERFD-XANES spectra samples decomposed in without H_2 in He atmosphere. Dashed lines in each color indicate unoccupied states and solid lines in the same colors indicate the same but occupied electronic states. In each layer different states are shown. From top to bottom: 1) Experimental VtC-XES and HERFD XANES, 2) calculated dDOS functions, 3) calculated pDOS functions, 4) calculated sDOS functions.

In Figure 3 the calculated DOS functions of the samples which have been decomposed in the presence of 10% H_2 in a Helium atmosphere are shown (a detailed discussion of the individual spectra can be found in the supplementary information). All the main features of the experimental spectra are reproduced by the calculated DOS functions. Every sample is showing an overlap of occupied and *unoccupied states*, indicating again a conducting behavior of all samples. The pre-peak of the pre-catalyst decomposed at 350 °C in 10% H_2 in He atmosphere is only weakly separated from the white line since it is a linear combination of the four reference spectra. In particular, the high content of Ni_3C and MOF dominates the pre-peak signal (for a more detailed description see supplementary information).

Below the Fermi level mainly the occupied states are present, representing the VtC-spectra of the corresponding pre-catalyst samples. Analogous to the set of samples decomposed in an inert pure helium atmosphere, the pre-catalyst treated at 350 °C shows a high contribution of MOF and Ni_3C DOS functions. Around -20 eV the O sDOS functions overlap with the C pDOS functions. With increasing temperature, this contribution to the VtC spectrum decreases. While it is still present at 375 °C, it is not observable at 400 °C anymore. This is in agreement with the HERFD-XANES LC-fit, which shows no MOF contributions anymore. Another clear feature, which shows the decreasing MOF contribution in the VtC is the overlap of the C and N sDOS functions around -11 eV with the O and N pDOS functions. While the overlap is still clearly visible at 375 °C decomposition temperature, it disappears from 400 °C upwards. This also explains why the maximum of the VtC spectrum at 400 °C appears much more defined and less noisy than at 375 °C. At this point, a large fraction of the pre-catalyst is already in the form of

Ni(0) in a carbon containing matrix, which is represented by the Ni_3C contribution. The C sDOS function at around -10 eV also shows overlap with the dDOS function of the absorbing Ni atom (Ni_{abs}). This feature dominated mainly by C sDOS / O pDOS contributions for the 375 °C sample, and no overlap is visible at this energy above 400 °C. However, for the pre-catalyst decomposed at 375 °C, there is an sDOS feature that occurs approximately around -11 eV and can be attributed to C contributions. Contrary, an overlap with pDOS functions attributed to Ni is pronounced in the VtC spectra at 400 °C and 500 °C.

Looking at the energy range near the Fermi level, the 350 °C sample decomposed in a 10% H_2 atmosphere shows two main features around -5 eV and -2 eV, similar to the VtC spectrum of the corresponding pre-catalyst decomposed in inert atmosphere. In this case, however, the feature around -2 eV is already more intense than the feature at -5 eV at 350°C. Since this feature is dominated by the Ni dDOS functions, this shows the strong contribution of the Ni_3C. Whereas in an inert atmosphere, the higher C, N, and O contents of the MOF have increased the feature at -5 eV. A slight decrease in the intensity of the pDOS features. The enhanced feature at lower energies is dominated by a p/d overlap that can be attributed to O and C pDOS and Ni dDOS features.

At higher temperatures, this O and C pDOS and Ni dDOS signal decreases, and the VtC spectrum becomes sharper and more similar to the spectrum of bulk Ni(0), with the most intense feature around -2 eV. Still this contribution is present in the sample decomposed at 375 °C, as the most intense feature still splits. At 400 °C, this feature contributes only in a minor way to the spectrum, but still, the most intense feature has a wide maximum. On the other side, this O and C pDOS / Ni dDOS overlap is negligible for 500 °C. The entire signal for 400 and 500 °C is dominated by the C pDOS / Ni dDOS contribution, leading to the high intensity feature around -2 eV for the entire set of samples which have been decomposed in 10% H_2. This feature is mixed with the Ni pDOS / Ni dDOS overlap feature around -2 eV, which also leads to the high intensity of the VtC feature.

Thus, the change in the shape of the spectra fits the description by the weighted DOS features reflecting a decreasing MOF and NiO contribution with higher temperatures and an increasing contribution of Ni(0) and Ni_3C species. In particular, the presence of carbonaceous species in the spectra is visible up to 500 °C. It is one of the dominant contributions to the p-density and additionally mixes with the d-density of the Ni species. At the same time, the shape of the spectrum becomes sharper as the temperature increases, indicating a reduced number of phases and species contributing to the spectral average.

Comparing the results of the electronic structure studies with the catalytic studies published in previously,[15] the presence of a carbonaceous environment of Ni(0) particles and traces of NiO are supported by the results here. The presence of oxidic species is noticeable since the samples are treated under reducing conditions. In contrast to MOF decomposition in a reducing atmosphere which starts at 365 °C, the inertly decomposed sample at 375 °C show larger contributions around -10 eV and -20 eV from the N, O, and C contributions of the MOF. For the example of 400°C decomposition temperature, this leads to higher contributions of MOF and NiO without H_2 compared to the corresponding sample in a 10% H_2 atmosphere. The VtC spectrum becomes sharper with hydrogen, indicating a higher Ni(0) character as shown by the LC HERFD-XANES analysis and the corresponding overlaps of the DOS functions. The desired carbon matrix begins to build up as hydrogen is added to the atmosphere, as represented by larger contributions of Ni_3C and corresponding C-DOS contributions. The oxidic and carbonaceous species might lead to non-Ni_{fcc} containing (represented by Ni foil) defects in the surface, resulting in higher catalytic activity. The catalytic performance in the methanation of CO_2 has been studied in previous work.[15] CO can be formed as a by-product in the Sabatier reaction (Eq. 2 and Eq. 3). *In-situ* studies have shown that the catalysts have high selectivity towards CO, especially in the absence of hydrogen, leading to the hypothesis that the carbonaceous matrix is used as a reducing reagent at higher temperatures when no other reducing compounds can be provided. Since only methane is the desired product, this side reaction must be suppressed.

The sample used for further catalytic studies was the sample decomposed at 400 °C in a 10% hydrogen atmosphere. In contrast, the sample decomposed at 500 °C in 10% H_2 showed lower selectivity towards methane. It is known from previous work that the samples decomposed at 500 °C have the largest particle size with a tremendous size distribution.[15] Especially when comparing these two samples, the differences in the NiO content are remarkable. This suggests that an oxide layer inhibits particle growth during decomposition, resulting in more active catalysts that show the required particle size distribution to provide an appropriate balance between high activity and selectivity while remaining stable in dynamic catalytic conditions. Consequently, it could be beneficial if the sample still contains some Ni(II) species in the form of NiO or MOF. They could lead to impurities of the Ni(0) in the particle surface structure during the decomposition process, resulting in slower and more controlled particle growth.

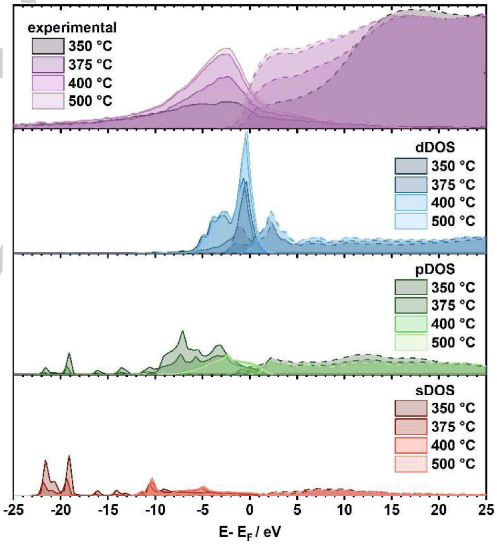

Figure 3: Experimental VtC-XES and HERFD-XANES spectra samples decomposed in 10% H_2 in He atmosphere. Dashed lines in each color indicate unoccupied states and solid lines in the same colors indicate the same but occupied electronic states. In each layer different states are shown. From top to bottom: 1) Experimental VtC-XES and HERFD XANES, 2) calculated dDOS functions, 3) calculated pDOS functions, 4) calculated sDOS functions.

At the same time, the NiO layer must be degraded in the pre-catalyst activation process and is therefore necessary for the catalysts to be active.

Conclusion

A novel methodical approach is proposed for analyzing the phase composition and electronic structure of catalysts prepared by thermal MOF decomposition using high-resolution hard X-ray absorption and emission spectroscopy. It takes advantage of the increased resolution of HERFD-XANES and VtC-XES concerning details of the electronic interactions, which in turn reflects the geometric structure. Taken together, both methods are sensitive in a complementary way to the unoccupied and occupied densities of states, allowing comparison with theoretical ab-initio calculations. The chosen approach combines the well-established method of linear combination fitting using experimental HERFD-XANES spectra with a thorough comparison of HERFD-XANES and VtC-XES with FEFF calculations.

With this method, the spectra of samples obtained by decomposition of a Ni(BDC)(PNO) MOF at different temperatures and with or without hydrogen were analyzed with respect to i) the phase composition in terms of remaining Ni-MOF, Ni(0), Ni_3C, and NiO; and ii) more detailed insights into the electronic structure of the obtained pre-catalysts were obtained.

With respect to i), an increasing fraction of Ni(0) and Ni_3C with increasing temperature and reducing atmosphere could be identified. Furthermore, a minor fraction of NiO species is visible even at higher temperatures, which correlates to the particle size and thus the selectivity of the catalytic samples.

Regarding ii), additional information about the potential conduction behavior could be obtained and most of the samples do not show any band gap. The presence of a carbon shell was demonstrated by the overlap of the d-states of the Ni absorber with the p-states of C as mimicked by the Ni_3C reference. Even an electronic interaction of the carbon in the second shell distance with the absorbing metal centers could be identified. This result reinforces the assumption that a carbon matrix is present around relatively large nickel particles as origin of stable catalytic stability. This stabilization results in the formation of more dispersed highly distributed catalytic centers during the activation process, leading to higher selectivity toward methane. An important piece of information obtained by the proposed methodic approach is the absence of oxidic contributions in the pre-catalyst samples showing the lowest selectivity towards methane (500 °C samples). Accordingly, the presence of carbonaceous, as well as oxidic species, seems to be necessary for selectivity towards methane formation. Because this creates impurities in the Ni_{fcc} layer, this could inhibit particle growth.

Experimental Section

Synthesis of Ni(BDC)(PNO) and formation of methanation pre-catalysts *via* thermal decomposition of Ni(BDC)(PNO) precursor

The MOF precursor and the catalysts are described in detail by Prinz, Schwensow, Wendholt *et al.* in a previous work.[15] The methanation catalysts were synthesized by placing 800 mg of Ni(BDC)(PNO) in a glass boat in a tube furnace. The catalyst precursor is treated for 10 min in He with a flow rate of 102 mL min^{-1} and subsequently for 10 min in 102 mL min^{-1} of He or 10% H_2/He, respectively. The samples were heated in the reaction gas mixture to temperatures between 350 °C and 500 °C with a heating ramp of 5 K min^{-1} and held at the final temperature for 1 h. Subsequently, the samples were treated in 102 mL min^{-1} of He and cooled down. The Ni(0) reference was provided as foil, the NiO reference was purchased from Sigma-Aldrich and the Ni_3C reference was synthesized according to literature procedures.[22]

X-ray emission spectroscopy measurements

HERFD XANES and VtC-XES experiments of the references and decomposed Ni-samples were performed at P64 beamline, Petra III at DESY (Hamburg, Germany).[23,24] The measurements were carried out using the first harmonic of a 2-m-long U33 undulator. The incident energy was selected using the (311) reflection of the Si double-crystal monochromator and the energy calibration was performed using the first inflection point of the Ni-foil XANES spectrum (8333 eV). VtC-XES and HERFD spectra were recorded at an excitation energy of 8500 eV in the range of 8190-8370 eV, with the energy-dispersive von Hamos setup, using eight Si(444) analyzing crystals.[24] Radiation damage studies were carried out for 30 minutes with 30 s step size measuring XANES spectra. Within these time frames, no radiation damage could be detected.

FEFF calculations

For an in-depth understanding of the contributions of atomic orbitals to the experimental spectral features, *ab initio* calculations utilizing FEFF 9.6 software[25] in a frame of the Full Multiple Scattering (FMS) theory were performed. All computations were performed using Self Consistency Field (SCF) for muffin-tin atomic potentials followed by the FMS calculation. An individual set of parameters was chosen for each reference (s. Table 1). The structures of Ni(0) and NiO were taken from the WebAtoms database.[26] In the case of Ni_3C,[27] the structure was taken from the Materials Project database. For the MOF structure, a crystal structure of Co(BDC)(PNO) was modified by changing the Co metals to Ni. Due to EXAFS and PDF analysis in previous work, it is known that the bond distances are comparable.[15] The data were adjusted in energy for the Fermi level (E_F) position of the respective FEFF calculation to match the condition E_F = 0 eV. The calculated DOS functions were multiplied by an erf() step function (Eq. 4), with the Fermi energy as a parameter given by the calculations to differentiate the occupied and unoccupied contributions.[28]

$$I_{step} = H\left[\frac{1}{2}+\frac{1}{2}erf\left(\frac{E-P}{\frac{\Gamma_G}{c^*}}\right)\right] \quad \text{Eq. 4}$$

Where P is the position of the inflection point of the step, H is the height of the function immediately above the step (here, normalized to 1), Γ_G is the core-hole lifetime in Ni 1 s level (1.39 eV)[29] and $c^* = 2\sqrt{ln2}$.

Table 1: Individual set of parameters for FEFF calculations of the reference samples. The parameters were set so that the calculated spectrum was in agreement with the measured HERFD-XANES spectrum.

Reference	SCF radius /Å	FMS radius /Å	Electron core-hole exchange-correlation potential	Background function	Core-hole screening
Ni-foil	5.0	5.0	Hedin-Lundqvist[30]	Ground state	Final State Rule[31]
Ni_3C	7.0	7.0	Hedin-Lundqvist	Ground state	RPA[32]
NiO	5.0	5.0	Partially nonlocal	Ground state	No
MOF	5.0	5.0	Hedin-Lundqvist	Ground state	Final State Rule

Conflicts of interest

There are no conflicts of interest to declare.

Acknowledgements

We acknowledge funding by the Deutsche Forschungsgemeinschaft (DFG, German Research Foundation) *via* SPP2080 (BA 4467/8-1 and BA 4467/8-2). We thank Wolfgang Kleist and Leif Rohrbach (RPTU Kaiserslautern-Landau) for providing the chemical samples. We gratefully acknowledge beamtime at P64 at DESY Petra III and Wolfgang Caliebe and Aleksandr Kalinko for their support.

Keywords: CO_2 methanation • X-ray emission spectroscopy • HERFD-XANES • Valence-to-core • FEFF-Calculations

References

[1] a) S. Rönsch, J. Schneider, S. Matthischke, M. Schlüter, M. Götz, J. Lefebvre, P. Prabhakaran, S. Bajohr, *Fuel* **2016**, *166*, 276; b) P. Sabatier, J. B. Senderens, *J. Chem. Soc.* **1902**, *82*, 333.

[2] G. A. Mills, F. W. Steffgen, *Catal. Rev.: Sci. Eng.* **1974**, *8*, 159.

[3] P. Frontera, A. Macario, M. Ferraro, P. Antonucci, *Catalysts* **2017**, *7*, 59.

[4] a) S. Danaci, L. Protasova, J. Lefevere, L. Bedel, R. Guilet, P. Marty, *Catal. Today* **2016**, *273*, 234; b) H. Muroyama, Y. Tsuda, T. Asakoshi, H. Masitah, T. Okanishi, T. Matsui, K. Eguchi, *J. Catal.* **2016**, *343*, 178; c) T. A. Le, M. S. Kim, S. H. Lee, T. W. Kim, E. D. Park, *Catal. Today* **2017**, *293-294*, 89.

[5] a) B. Mutz, P. Sprenger, W. Wang, Di Wang, W. Kleist, J.-D. Grunwaldt, *Appl. Catal., A* **2018**, *556*, 160; b) B. Mutz, A. Gänzler, M. Nachtegaal, O. Müller, R. Frahm, W. Kleist, J.-D. Grunwaldt, *Catalysts* **2017**, *7*, 279.

[6] a) H.-L. Jiang, B. Liu, Y.-Q. Lan, K. Kuratani, T. Akita, H. Shioyama, F. Zong, Q. Xu, *J. Am. Chem. Soc.* **2011**, *133*, 11854; b) B. Liu, H. Shioyama, H. Jiang, X. Zhang, Q. Xu, *Carbon* **2010**, *48*, 456.

[7] L. Oar-Arteta, T. Wezendonk, X. Sun, F. Kapteijn, J. Gascon, *Mater. Chem. Front.* **2017**, *1*, 1709.

[8] a) B. Liu, H. Shioyama, T. Akita, Q. Xu, *J. Am. Chem. Soc.* **2008**, *130*, 5390; b) T. Kundu, S. C. Sahoo, R. Banerjee, *Cryst. Growth Des.* **2012**, *12*, 2572.

[9] a) A. H. van Pelt, O. A. Simakova, S. M. Schimming, J. L. Ewbank, G. S. Foo, E. A. Pidko, E. J. Hensen, C. Sievers, *Carbon* **2014**, *77*, 143; b) M. Taborga Claure, S.-H. Chai, S. Dai, K. A. Unocic, F. M. Alamgir, P. K. Agrawal, C. W. Jones, *J. Catal.* **2015**, *324*, 88; c) M. D. Porosoff, X. Yang, J. A. Boscoboinik, J. G. Chen, *Angew. Chem., Int. Ed.* **2014**, *53*, 6705.

[10] a) Y. Kimitsuka, E. Hosono, S. Ueno, H. Zhou, S. Fujihara, *Inorg. Chem.* **2013**, *52*, 14028; b) Z. Long, L. Wei, L. Shuang, W. Jifei, W. Huanlei, C. Jiaxin, *J. Mater. Chem. A* **2015**, *3*, 14210; c) M. van de Voorde, B. Sels, *Nanotechnology in Catalysis*, Wiley-VCH, Weinheim, Germany, **2017**.

[11] a) J. M. Zamaro, N. C. Pérez, E. E. Miró, C. Casado, B. Seoane, C. Téllez, J. Coronas, *Chem. Eng. J. (Amsterdam, Neth.)* **2012**, *195-196*, 180; b) J. Li, B. Wang, Y. Qin, Q. Tao, L. Chen, *Catal. Sci. Technol.* **2019**, *9*, 3726.

[12] W. Chaikittisilp, K. Ariga, Y. Yamauchi, *J. Mater. Chem. A* **2013**, *1*, 14.

[13] a) Z. Guo, F. Wang, Y. Xia, J. Li, A. G. Tamirat, Y. Liu, L. Wang, Y. Wang, Y. Xia, *J. Mater. Chem. A* **2018**, *6*, 1443; b) Y. Guo, X. Gao, C. Zhang, Y. Wu, X. Chang, T. Wang, X. Zheng, A. Du, B. Wang, J. Zheng et al., *J. Mater. Chem. A* **2019**, *7*, 8129.

[14] J. Kim, C. Young, J. Lee, Y.-U. Heo, M.-S. Park, M. S. A. Hossain, Y. Yamauchi, J. H. Kim, *J. Mater. Chem. A* **2017**, *5*, 15065.

[15] N. Prinz, L. Schwensow, S. Wendholt, A. Jentys, M. Bauer, W. Kleist, M. Zobel, *Nanoscale* **2020**, 15800.

[16] M. Bauer, H. Bertagnolli in *Methods in Physical Chemistry* (Eds.: R. Schäfer, P. C. Schmidt), Wiley-VCH, Weinheim, **2012**, pp. 231–269.

[17] a) S. C. E. Stieber, C. Milsmann, J. M. Hoyt, Z. R. Turner, K. D. Finkelstein, K. Wieghardt, S. DeBeer, P. J. Chirik, *Inorg. Chem.* **2012**, *51*, 3770; b) M. Bauer, C. Gastl, *Phys. Chem. Chem. Phys.* **2010**, *12*, 5575; c) C. Nayak, P. Jain, C. P. Vinod, S. N. Jha, D. Bhattacharyya, *J. Synchrotron Radiat.* **2019**, *26*; d) C. C. Scarborough, S. Sproules, T. Weyhermüller, S. DeBeer, K. Wieghardt, *Inorg. Chem.* **2011**, *50*, 12446; e) U. Bergmann, P. Glatzel, *Photosynth. Res.* **2009**, *102*, 255; f) E. Gallo, P. Glatzel, *Adv. Mater. (Weinheim, Ger.)* **2014**, 7730.

[18] A. S. Munn, G. J. Clarkson, F. Millange, Y. Dumont, R. I. Walton, *CrystEngComm* **2013**, *15*, 9679.

[19] C. Serre, F. Millange, C. Thouvenot, M. Noguès, G. Marsolier, D. Louër, G. Férey, *J. Am. Chem. Soc.* **2002**, *124*, 13519.

[20] J. J. Rehr, Albers, *Phys. Rev. B Condens. Matter* **1990**, *41*, 8139.

[21] a) M. Bauer, G. Heusel, S. Mangold, H. Bertagnolli, *J. Synchrotron Radiat.* **2010**, *17*, 273; b) M. Wilke, F. Farges, P.-E. Petit, G. E. Brown, F. Martin, *Am. Mineral.* **2001**, *86*, 714.

[22] M. Xing, J. Mohapatra, F. Zeng, J. Ping Liu, *AIP Adv.* **2018**, *8*, 56308.

[23] W. A. Caliebe, V. Murzin, A. Kalinko, M. Görlitz in *AIP Conference Proceedings*, Author(s), **2019**, p. 60031.

[24] A. Kalinko, W. A. Caliebe, R. Schoch, M. Bauer, *J. Synchrotron Radiat.* **2020**, *27*, 31.

[25] J. J. Rehr, J. J. Kas, F. D. Vila, M. P. Prange, K. Jorissen, *Phys. Chem. Chem. Phys.* **2010**, *12*, 5503.

[26] Ni, "WebAtoms. The Atoms.inp archive", can be found under https://millenia.cars.aps.anl.gov/atomsdb/.

[27] Ni3C, mp-7586, *Materials Data on Ni_3C by Materials Project*, Ernest Orlando Lawrence Berkeley National Laboratory (LBNL), United States: N. p., **2020**.

[28] J. Stöhr in *NEXAFS Spectroscopy* (Eds.: H. Lotsch, G. Ertl, R. Gomer), Springer, Berlin, **1996**, pp. 211–238.

[29] J. L. Campbell, T. Papp, *At. Data Nucl. Data Tables* **2001**, *77*, 1.

[30] M. Roy, S. J. Gurman, *J. Synchrotron Radiat.* **2001**, *8*, 1095.

[31] C. Lamberti, J. A. van Bokhoven (Eds.) *X-ray absorption and X-ray emission spectroscopy. Theory and applications*, John Wiley & Sons, Inc, Chichester, West Sussex, **2015**.
[32] J. J. Rehr, J. J. Kas, M. P. Prange, A. P. Sorini, Y. Takimoto, F. D. Vila, *C. R. Phys.* **2009**, *10*, 548.

Supplementary Information

High resolution X-ray absorption and emission spectroscopy for detailed analysis of new CO_2 methanation catalysts

Sven Strübbe[a], Michal Nowakowski[a] Roland Schoch[a] and Matthias Bauer*[a]

[a] S. Strübbe, Dr. M. Nowakowski, Dr. R. Schoch, Prof. Dr. M. Bauer
Department of Chemistry and Center for Sustainable System Designs
Paderborn University
Warburger Straße 100, 33098 Paderborn, Germany
E-mail: matthias.bauer@upb.de

Table of contents

Linear combinations of the pre-catalyst samples

***Table S1**: Values of linear combination fitting of the pre-catalyst samples.*

Sample	Fraction Ni_3C /%	Fraction MOF /%	Fraction NiO /%	Fraction Ni foil /%
350 °C 0% H_2	18.7 ± 1.3	74.4 ± 2.2	6.9 ± 1.8	0.0 ± 0.0
375 °C 0% H_2	43.9 ± 3.4	18.7 ± 3.8	7.5 ± 3.1	29.9 ± 6.0
400 °C 0% H_2	47.7 ± 3.3	4.4 ± 3.5	7.7 ± 2.9	40.1 ± 5.6
500 °C 0% H_2	48.5 ± 3.7	6.2 ± 6.7	6.4 ± 3.2	39.0 ± 3.9
350 °C 10% H_2	33.7 ± 1.4	61.2 ± 2.3	5.1 ± 1.9	0.0 ± 0.0
375 °C 10% H_2	34.2 ± 3.8	23.6 ± 4.3	7.1 ± 3.5	35.1 ± 6.7
400 °C 10% H_2	56.1 ± 3.7	0.0 ± 0.0	2.8 ± 2.0	41.1 ± 4.2
500 °C 10% H_2	60.6 ± 5.6	0.0 ± 0.0	0.0 ± 0.0	39.4 ± 5.6

For the LC-fitting of the precatalysts with by the four references, the derivatives of the spectra were fitted with the derived spectra of the precatalysts. The figures show the spectrum of the precatalyst, the LC fit and the weighted portions of the reference spectra. The reference spectra are shown as dashed lines.

Inert atmosphere

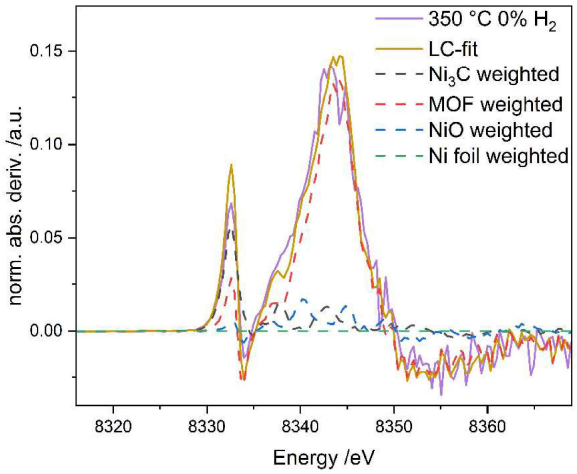

***Figure S1**: The LC-fit of the derivative functions for the 350 °C 0% H_2 are shown together with the weighted fractions. The solid lines show the samples and the LC-fit functions, the dotted lines are the weighted fractions of the references.*

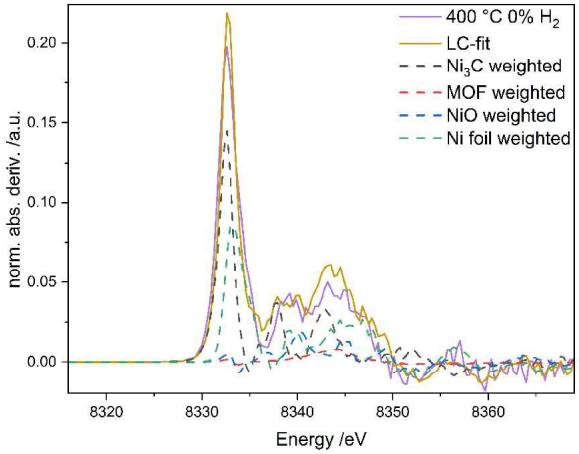

***Figure S4**: The LC-fit of the derivative functions for the 400 °C 0% H_2 are shown together with the weighted fractions. The solid lines show the samples and the LC-fit functions, the dotted lines are the weighted fractions of the references.*

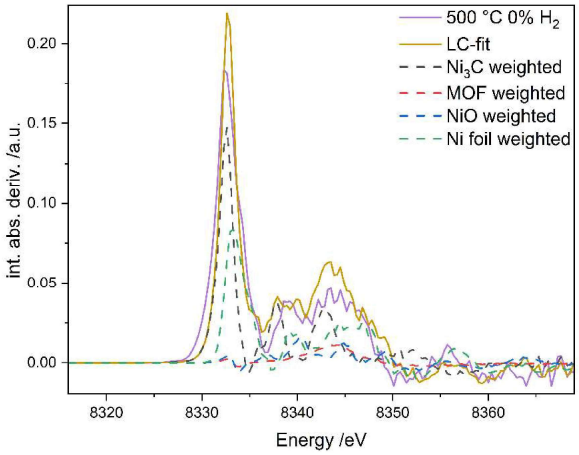

***Figure S3**: The LC-fit of the derivative functions for the 500 °C 0% H_2 are shown together with the weighted fractions. The solid lines show the samples and the LC-fit functions, the dotted lines are the weighted fractions of the references.*

Reductive atmosphere

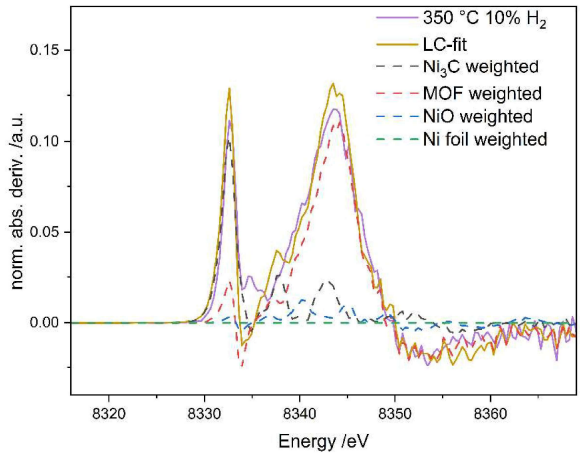

***Figure S5**: The LC-fit of the derivative functions for the 350 °C 10% H_2 are shown together with the weighted fractions. The solid lines show the samples and the LC-fit functions, the dotted lines are the weighted fractions of the references.*

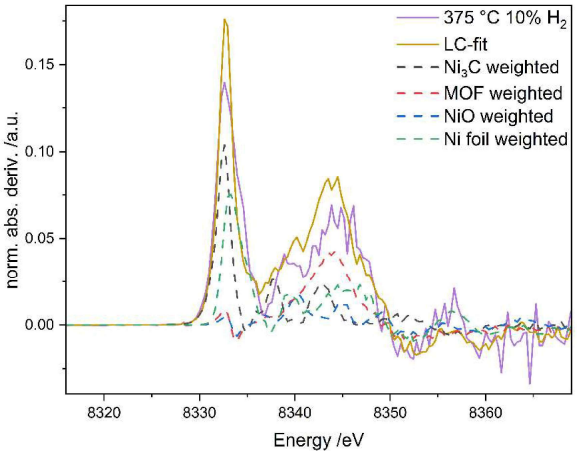

***Figure S6**: The LC-fit of the derivative functions for the 375 °C 10% H_2 are shown together with the weighted fractions. The solid lines show the samples and the LC-fit functions, the dotted lines are the weighted fractions of the references.*

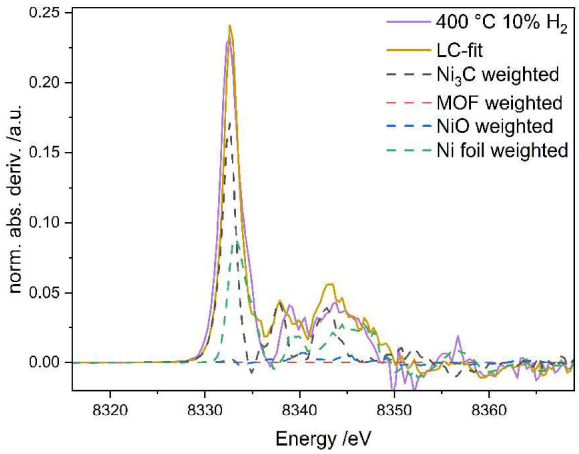

***Figure S8**: The LC-fit of the derivative functions for the 400 °C 10% H_2 are shown together with the weighted fractions. The solid lines show the samples and the LC-fit functions, the dotted lines are the weighted fractions of the references.*

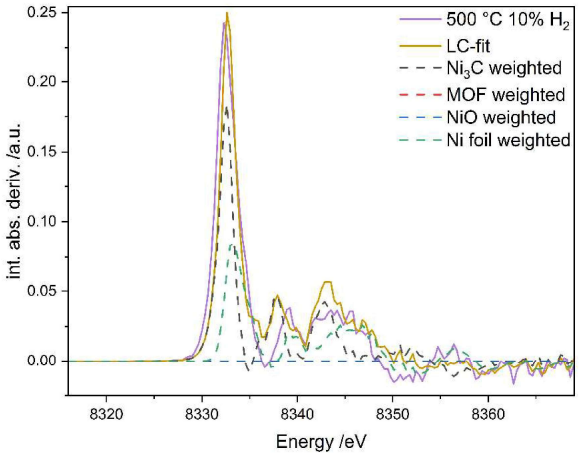

***Figure S7**: The LC-fit of the derivative functions for the 500 °C 10% H_2 are shown together with the weighted fractions. The solid lines show the samples and the LC-fit functions, the dotted lines are the weighted fractions of the references.*

Detailed description of the references

Ni foil

In Figure S9 the unoccupied and occupied DOS functions of Ni-foil calculated with FEFF are shown and compared to the corresponding experimental HERFD-XANES and VtC-XES spectra. The Ni(0) sample shows an overlap of occupied and unoccupied states as expected for conducting material. The pre-peak of the HERFD-XANES spectrum at +3.0 eV is reproduced by overlapped unoccupied d-states of the metal center and the unoccupied p-states of the neighboring Ni atoms. This reflects the p-d-hybridization, an interaction characteristic for pre-peaks in XANES spectra.[1] Below the Fermi level, the main VtC-XES feature between -2 and -5 eV emerges because of the mixed occupied d-states of the metal atom and p-states of the neighbored Ni atoms. From -5 eV to -10 eV there is no d-state contribution visible, but s-p-mixing of occupied Ni-center s-states, with a small addition of occupied Ni-ligand p-states, are contributing to the shape of the VtC feature. The maximum of the sDOS function is at -5 eV.

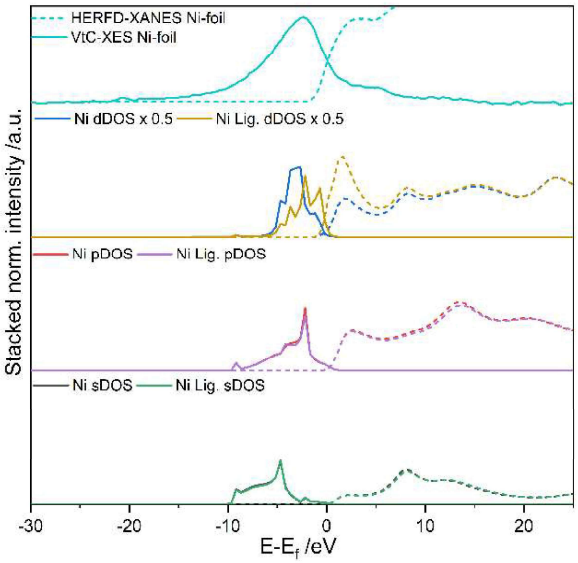

***Figure S9**: Ni-foil reference: Comparison of measured data with calculated FEFF DOS functions. Dashed lines in each colour indicates unoccupied states and solid lines in the same colours corresponding occupied electronic states. The unoccupied DOS contributions were scaled by a factor of 5/3 in respect to occupied DOS functions.*

Ni_3C

The rationale for CO_2 methanation catalyst preparation by MOF decomposition is the expected carbon shell formation, which is supposed to prevent the sintering of the active Ni particles. Thus Ni_3C as a reference is reasonable for the investigation of the decomposed precatalysts. The occupied and unoccupied dDOS functions are presented in Figure S10 and are compared to the experimental VtC-XES and HERFD-XANES spectra of the Ni_3C. A partial overlap of occupied and unoccupied states is also visible for Ni_3C.[2] At +1.6 eV hybridized unoccupied Ni-center dDOS and ligand C pDOS functions contribute to the pre-peak in the HERFD-XANES spectrum. At -1.9 eV a peak in VtC-XES is reproduced by the mixture of occupied d-states of the Ni metal center, occupied p-states of the C ligands, and second shell Ni neighbors. The feature at -4.2 eV is composed of the dominant mixture of occupied Ni pDOS contributions and C ligands. At -12.5 eV there is a Kβ" feature due to the C 2s → Ni 1s transitions.[3] This crossover peak in the VtC-XES spectrum is characteristic of the type of coordinating ligand.[4]

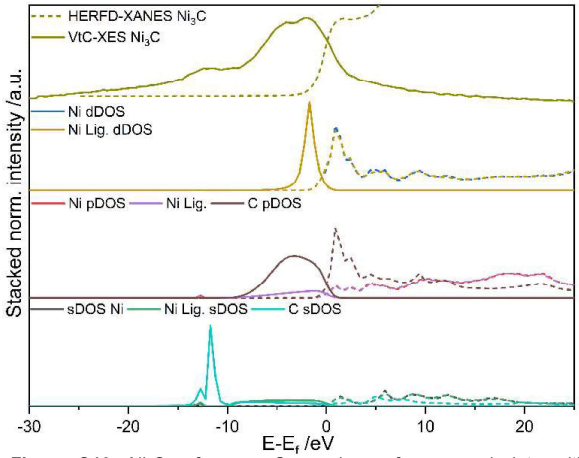

***Figure S10**: Ni_3C reference: Comparison of measured data with calculated FEFF DOS functions. Dashed lines in each colour indicates unoccupied states and solid lines in the same colours corresponding occupied electronic states. The unoccupied DOS contributions were scaled by a factor of 5/3 in respect to occupied DOS functions.*

NiO

Figure S11 shows the experimental VtC-XES and HERFD-XANES spectra of NiO in comparison to the FEFF calculations. A bandgap of 2.6 eV, close to the literature value of 2.414 eV NiO[5] is present. The difference is attributed to the experimental resolution of the X-Ray experiment. In the conduction band, at +1.5 eV a sharp pre-peak is present due to the unoccupied Ni d-states and O ligand p-states mixing. The VtC features at -2.1 - -7.5 eV is the result of the mixing of occupied Ni- dDOS with O p-DOS functions at varying rates and small contributions of the Ni p-states (-7.5 eV). The occupied Ni dDOS function is split into two sublevels at -19 eV and – 5 eV. Since NiO can be considered a Mott insulator,[6] it can be considered a locally partially ionic compound with local octahedral geometry distorted by the Jahn-Teller effect. At -19 eV an O 2s crossover peak is visible.

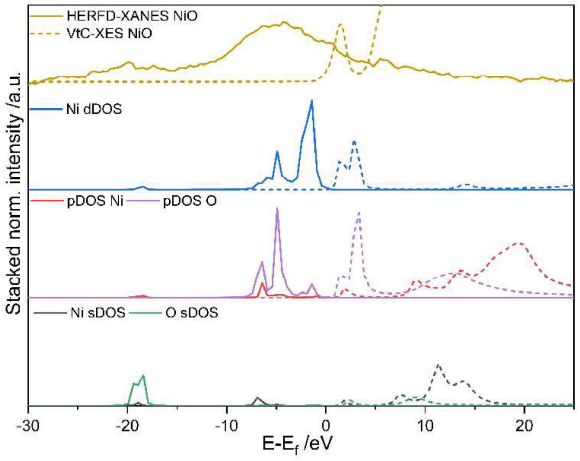

***Figure S11**: NiO reference: Comparison of measured data with calculated FEFF DOS functions. Dashed lines in each colour indicates unoccupied states and solid lines in the same colours indicates the same but occupied electronic states. The DOS contributions have been increased by factor of 5 for unoccupied electronic states.*

MOF

The Ni(BDC)(PNO) MOF was used as a reference in the previous work.[7] The experimental spectra with computed occupied and unoccupied DOS functions are shown in Figure S12. An overlap of unoccupied and occupied DOS functions are visible, indicating conducting properties of the Ni(BDC)(PNO). Reports have shown that MOFs[8] and MIL-53-based MOFs in particular[9] are behaving like semiconductors to a conductor. The pre-peak at +0.4 eV emerges due to the p-d-hybridization of unoccupied Ni d-states with O and N p-states. At 0.4 - -20 eV, the $K\beta_{2,5}$ lines are reproduced by a dominant occupied Ni dDOS and C, N, and O ligand pDOS mixed states. Interestingly, while at 0.4 – -4 eV the dominant p-states originate from the O ligand, for energies from -4 to -8 eV, N and C pDOS contributions from the second coordination shell are present. Therefore, the two maxima of the $K\beta_{2,5}$ line at 0 and -6 eV are emerging due to the different range interactions. A very broad ligand Kβ" peak in the VtC-spectrum is reproduced by transitions from O and N 2s states at -18 and -21 eV respectively. Interestingly, the N 2s DOS has comparable intensity to the O 2s contribution, despite that N is a second shell atom. The simultaneous presence of C 2p and 2s states at energies from -19 to -17.5 eV is proof of strong delocalization of the orbitals from the 2nd atomic shell over the absorbing atom.[10]

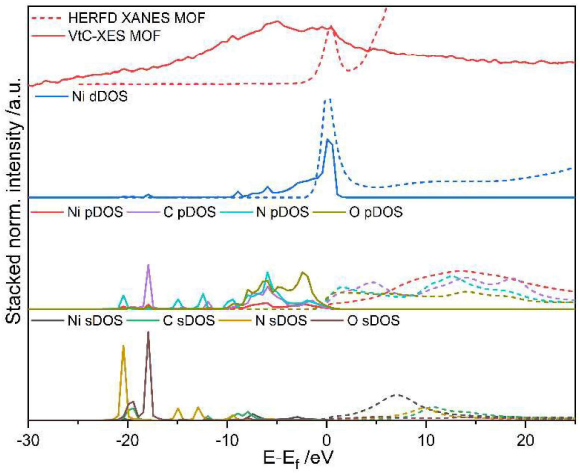

***Figure S12**: MOF reference: Comparison of measured data with calculated FEFF DOS functions. Dashed lines in each colour indicates unoccupied states and solid lines in the same colours indicates the same but occupied electronic states. The unoccupied DOS contributions were rescaled by a factor of 10/3 in respect to occupied electronic states.*

Detailed description of the pre-catalyst samples

In Figure S13 the calculated DOS functions are fractioned by the percentage value of the corresponding LC fit references of the 350 °C samples in both atmospheres in comparison to experimental spectra. All main features of the experimental spectra are well reproduced. Since both samples were mainly composed of MOF (74% for 0% H_2, and 61% for 10% H_2) a strong overlap of unoccupied and occupied d-states similar to the MOF (Figure S12) can be seen, providing no bandgap. Thus, the decomposed MOF pre-catalysts exhibit a conducting behavior. Without hydrogen, a pre-peak is visible at +0.9 eV which is an effect of the overlap of unoccupied Ni d-states with the unoccupied C and O p-states from the MOF and Ni_3C. The pre-edge peaks of the Ni_3C and Ni-MOF references are separated by 2 eV and the sample spectrum is a linear combination of both, with a 7 % yield of NiO. This explains, why the pre-peak for the 350 °C sample in 0 % H_2 is less resolved from the white line than for the references (MOF and NiO, Figure S11 and Figure S12). It also clarifies the large yield of unoccupied Ni

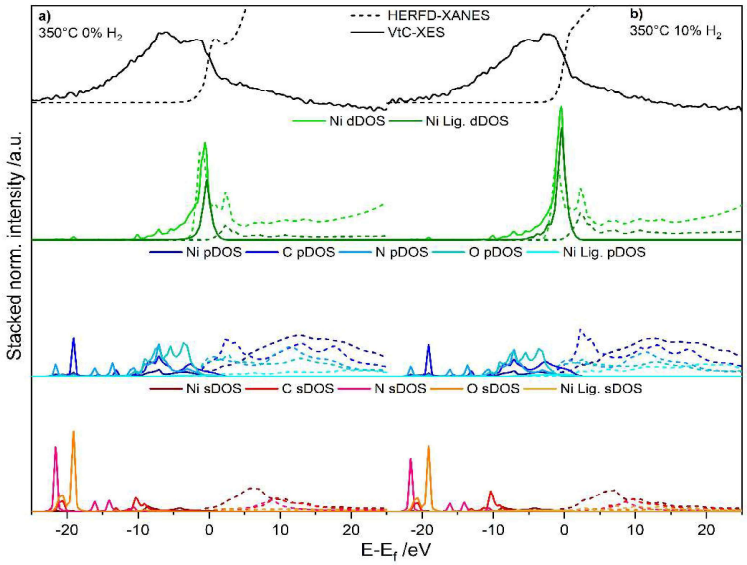

***Figure S13**: Experimental VtC-XES and HERFD-XANES spectra of the 350 °C samples in 0% (a)) and 10% (b)) H_2 atmosphere. Dashed lines in each colour indicates unoccupied states and solid lines in the same colours indicates the same but occupied electronic states. Intensity of the DOS functions have been increased. Composition a): Ni_3C: 19%, MOF: 74%; NiO: 7%, Ni-foil: 0%. Composition b): Ni_3C: 34%, MOF: 61%, NiO: 5%, Ni-foil: 0%.*

d-states with low intensities of unoccupied p-states of the Ni and O neighbors in Ni_3C and MOF, respectively.

For the 350 °C sample in 10 % H_2, (Figure S13 b)) the intense overlap of unoccupied and occupied d-states is indicating conduction properties, which is reasonable since MOF and Ni_3C contributed 95% of DOS functions. The pre-edge peak results from the linear combination of reference spectra and is very weakly separated from the white line. It is composed of mixed Ni metal center d-states with the O (from MOF) and C p-states mainly from Ni_3C. An almost complete lack of separation between the pre-edge and the white line can be attributed to a higher fraction of Ni_3C.

Below the Fermi level, the spectra are dominated by occupied states. XES spectra of samples decomposed at 350 °C (Figure S13 a-b) are showing two distinct features of occupied states at -1.5 eV and -6.4 eV. The feature at -1.5 eV is composed of Ni dDOS, mainly mixed with O

pDOS, and C pDOS. The C pDOS are the main contributor to this peak. Note that the main Ni dDOS feature (for the absorber) at -0.6 eV in the sample decomposed at 350 °C in 0 % H_2 and -0.4 eV in sample decomposed at 350 °C in 10 % H_2 are centered on the minima of the occupied ligand pDOS functions, therefore their contribution to XES spectra is limited. The XES feature at -6.4 eV is reproduced by transitions from p-states of O, C, and N ligands and by residual Ni dDOS contribution. Interestingly, similarly to MOF, the N ligand is in the 2nd coordination shell. Additionally, in the sample decomposed in 10 % of H_2, the feature at -1.5 eV is more intense than the feature at -6.4 eV, contrary to the XES spectrum of the sample decomposed in 0 % of H_2. The sample decomposed at 10 % of H_2, consists of more Ni_3C, and this translates to a higher C pDOS contribution to feature at -1.5 eV. The crossover peak region starts at -10 eV, where a small contribution from C 2s states is present in both samples and simultaneously the broad p- and d- state contributions disappear.

At -18 eV and -21 eV there are sDOS contributions, indicating transitions from O and N 2s states from the MOF. Moreover, at -18 eV, the 2p DOS form C in the MOF is present.

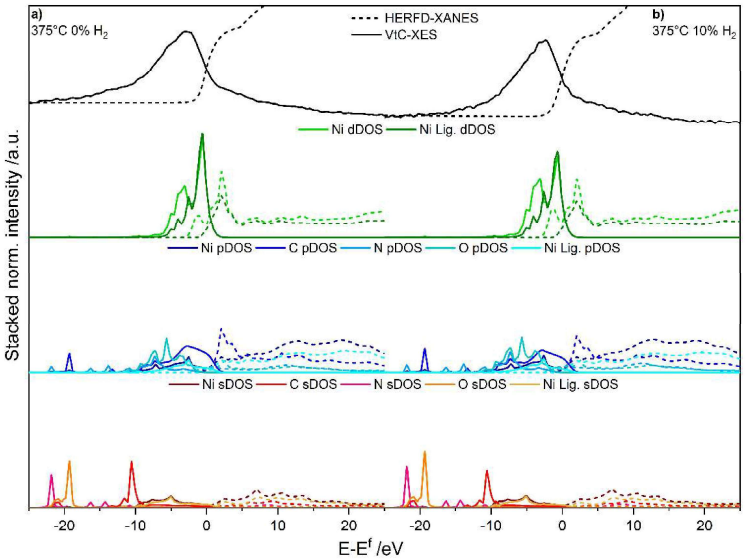

***Figure S14**: Experimental VtC-XES and HERFD-XANES spectra of the 375 °C samples in 0% (a)) and 10% (b)) H_2 atmosphere. Dashed lines in each colour indicates unoccupied states and solid lines in the same colours indicates the same but occupied electronic states. Intensity of the DOS functions have been increased. Composition a): Ni_3C: 44%, MOF: 19%; NiO: 7%, Ni-foil: 30%. Composition b): Ni_3C: 34%, MOF: 24%, NiO: 7%, Ni-foil: 35%.*

The samples which have been decomposed at 375 °C without and with H_2 are shown Figure S14 All the main features of the experimental spectra are reproduced by the calculated DOS functions. The contribution of MOF (19% in 0% H_2, 24% in 10% H_2) is significantly decreased in comparison to the samples shown in Figure S13, and the overlap of unoccupied and occupied d-states between -3 eV and +1.7 eV is less intense than in the respective 350°C sample or in the MOF (Figure S12). Though a bandgap is still missing, due to the high percentage of MOF, Ni_3C, and Ni-foil (94%) this result is expected. In the absence of H_2, the pre-peak is visible in the range from +1 to +3 eV due to three contributions. The overlap of the unoccupied Ni d-states with the C p-states of the Ni_3C contributes 44 % to this sample pre-edge. The hybridization of Ni d-states with Ni ligand p-states from Ni-foil is adding 30 % to the

pre-peak intensity from the bulk Ni. Finally, the mixing of unoccupied Ni d-states with O p-states from MOF at +2.5 eV yields 19% of the pre-peak in the sample. Since the pre-peaks in the dominating references are shifted by 1.5 eV this results in a less resolved pre-peak in the mixture (Figure S14 a)). For the sample decomposed at 10% H_2 the conducting behavior is similar. An overlap of unoccupied and occupied dDOS functions can be seen from -2 eV to +3 eV. The missing bandgap can be explained by high fractions of Ni_3C, MOF, and Ni-foil. Again, the pre-peak is a result of the linear combination of the samples and is weakly separated from the white line. It can be theoretically resolved into the mixed unoccupied Ni absorber d-states with unoccupied C p-states of Ni_3C, O p-states of the MOF, and Ni p-states from both, Ni_3C, and Ni-foil. Below the Fermi level, the DOS functions are dominated by occupied states. In the energy range from -1.5 eV to +0.8 eV the VtC spectra are represented by an overlap of occupied Ni dDOS functions with C p-states from Ni_3C and Ni p-states from Ni_3C and Ni-foil. Experimental VtC-spectra of both samples decomposed at 375 °C (Figure S15 a-b) are showing one main feature at -2.5 eV. This feature mainly consists of the mixing of occupied Ni center d-states with the occupied C p-states of Ni_3C. In both samples, the Ni_3C fraction is very high (44% without H_2, 34% with 10% H_2). On the same energy position as the maximum of the C pDOS function, the maximum of the Ni ligand p-state function is observed. The Ni pDOS functions are represented by 74% for the sample decomposed without H_2, and 69% with 10% H_2, respectively. Due to this contribution, the main VtC feature is enhanced. These two contributions (C-Ni p-d overlap and Ni-Ni p-d overlap) are resulting in the two features, that are visible at the VtC main feature in Figure S15 b) at -2.4 and -2.8 eV. In the sample decomposed with 0% Hydrogen, these two features are less resolved and are occurring as one feature. Whereas the mixing of Ni d-states with O pDOS functions had a high contribution to the shape of VtC in Figure S14 this contribution is weaker in the samples decomposed at 375 °C. Therefore, the intensity of the C p-states is increased and contributes significantly to the VtC spectrum. The broad O pDOS functions overlap with the Ni absorber dDOS functions from -2 eV to -7 eV. Interestingly, the N p-states which are the 2nd coordination sphere atoms of the MOF, are overlapping weaker with the dDOS functions of the Ni absorber. The main feature of the N p-states is at -7.1 eV. Here the Ni dDOS functions are showing only low yields. From -10 eV, the crossover peak region is starting. As in the samples decomposed at 350 °C (Figure S13) the p- and d-state contributions disappear, while C 2s states from Ni_3C are visible. The MOF yields to the O and N 2s states at -18 and -21 eV, respectively. Furthermore, the C 2p states of the MOF are present at -18 eV overlapping with the 2s states of O.

In Figure S15 the samples, the results of the samples that were decomposed at 400 °C in 0% H_2 (a)) and 10% H_2 (b)) are shown in comparison with weighted DOS functions. All main features of the experimental spectra can be translated from the DOS functions. Because in both samples unoccupied and occupied DOS functions from the main fractions Ni_3C (48% for 0% H_2 sample, 56% for 10% H_2 sample) and Ni(0) (40% and 41%, respectively) overlap, there is no bandgap. The pre-peak, which is visible between +2 and +4 eV is the result of the hybridization of unoccupied Ni d-states with unoccupied C p-states from Ni_3C and Ni p-states from both dominant references. The pre-edge peaks of the references are separated in energy, and as previously, it affects the separation of the experimental pre-edges and white lines. Contrary to the samples decomposed at 350 °C (Figure S13) and 375 °C (Figure S14) the pre-peak contribution of the MOF reference plays now only a minor role in the 400 °C samples. It is only represented by a 4% fraction in the sample that was decomposed without H_2 and is not present in the 10% H_2 sample.

Below the Fermi level, the occupied states dominate DOS contributions to the spectrum shape. In both samples, intense Ni dDOS functions are visible in the range from 0 to -6 eV. The main feature of the sample which was decomposed at 400 °C in a 0% H_2 atmosphere is at -2.3 eV, while for the other sample, the maximum is -2.4 eV. For those samples, the importance of O pDOS is decreasing significantly. Instead, maxima of the C p-states from Ni_3C are mixed with the occupied d-states of Ni atoms. The minor contribution of O pDOS from the MOF (4%) and NiO (8%) is visible at -6 eV for the sample decomposed in pure He. These features are further decreased in the sample decomposed with 10% H_2 since NiO is only contributing with 3%. The crossover peak region starts at -10 eV, where a contribution of C 2s states from Ni_3C is present for both samples. Although in Figure S15 a) the 2s DOS features of N and O still can be seen at -21 and -18 eV, respectively, they are negligible. Contrary to other samples, the 2p DOS functions of MOF C are not present in either of the samples.

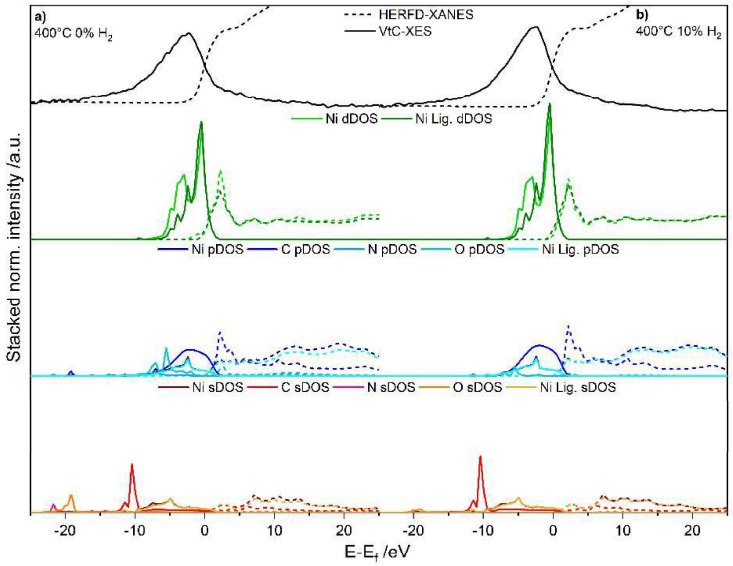

***Figure S15**: Experimental VtC-XES and HERFD-XANES spectra of the 400 °C samples in 0% (a)) and 10% (b)) H_2 atmosphere. Dashed lines in each colour indicates unoccupied states and solid lines in the same colours indicates the same but occupied electronic states. Intensity of the DOS functions have been increased. Composition a): Ni_3C: 48%, MOF: 4%; NiO: 8%, Ni-foil: 40%. Composition b): Ni_3C: 56%, MOF: 0%, NiO: 3%, Ni-foil: 41%.*

Finally, two samples decomposed at 500°C were investigated. Figure S16 shows the results. For the sample decomposed in the inert atmosphere the unoccupied and occupied d-states of the Ni_3C (49%), Ni(0) (30%), and MOF (6%) constituents are overlapping. The sample decomposed in 10% H_2 shows a mixing of unoccupied and occupied d-states as well. However, the DOS functions originate from only Ni_3C (61%) and Ni-foil (39%) in this case. Nevertheless, there is no bandgap visible for both sample.

In Figure S16 a)-b) pre-peak features between +2 and +3 eV are present. These features consist of unoccupied dDOS functions of the Ni absorber which are overlapping with unoccupied p-states of Ni ligands of Ni_3C and Ni(0) and dominantly with the pDOS functions of Ni_3C carbon. Few contributions to the experimental pre-edge features of the samples decomposed at 500 °C cause they are less resolved from the white line. The high temperature in the reducing atmosphere is leading to only Ni(0) species as pre-catalyst. Below the Fermi level, the spectra are dominated by occupied states.

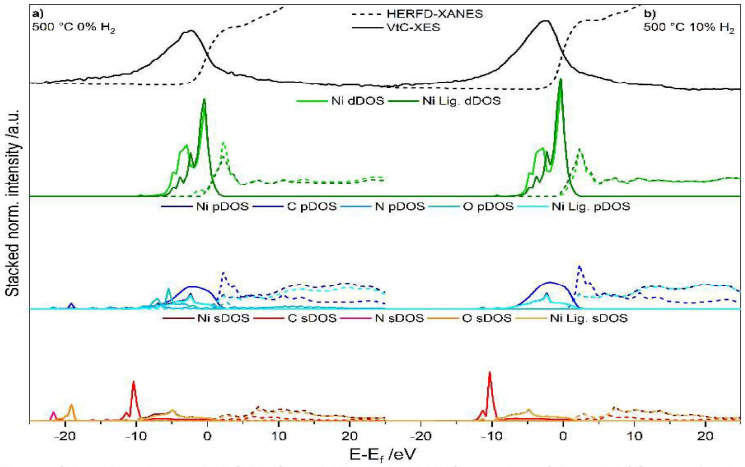

***Figure S16**: Experimental VtC-XES and HERFD-XANES spectra of the 500 °C samples in 0% (a)) and 10% (b)) H_2 atmosphere. Dashed lines in each colour indicates unoccupied states and solid lines in the same colours indicates the same but occupied electronic states The unoccupied DOS contributions were rescaled by a factor of 5/3 in respect to occupied electronic states.Composition a): Ni_3C: 49%, MOF: 6%; NiO: 6%, Ni-foil: 30%. Composition b): Ni_3C: 61%, MOF: 0%, NiO: 0%, Ni-foil: 39%.*

Both 0% H_2 and 10% H_2 samples show mixing of the most intense feature of occupied Ni absorber dDOS function at -0.4 eV and -0.3 eV, respectively, with occupied Ni_3C C pDOS functions and occupied Ni p-states of the neighboring Ni atoms. The sample that was decomposed without hydrogen exhibits the main VtC- feature at -2.4 eV. It is reproduced by mixed occupied Ni absorber d-states with occupied C p-states from Ni_3C. Additionally, Ni ligand p-states from both dominant references are present. As in Figure S15 a) the VtC-spectra in Figure S16 a) is less resolved and shows features of reduced intensity in comparison with Figure S15 b) and Figure S16 b), respectively. Again this can be seen in the 2nd main feature at -3.4 eV which is represented by an overlap of O p-states of MOF and NiO with Ni d-states since the two Oxygen-containing references are still present with a 12% contribution. This is in contrast to the sample in Figure S16 b), which only consists of Ni_3C and Ni(0) and is showing only the mixing of Ni p-states and C p-states with Ni d-states at -2.2 eV, consequently. The 0% Hydrogen sample is characterized by a broad overlap of occupied Ni absorber d-states with C p-states and Ni ligand p-states from -5.6 eV to +1.1 eV, leading to a broad VtC feature. Simultaneously, it is accentuated by the overlap of Ni metal center d-states with the O p-states leading to a broadened shape of the VtC spectrum. If this is compared to the sample that was decomposed in 10% hydrogen, it can be seen, that the 10% H_2 spectrum appears to be sharper. This spectrum mainly originates from the p-d-overlap of Carbon and Nickel and is enhanced by the Ni-Ni p-d-mixing of Ni(0) and Ni_3C. At -10 eV the crossover peak region starts, where the broad pDOS and dDOS contributions disappear for both samples. Simultaneously, a contribution of C 2s-states can be seen, which results in a small shoulder in the VtC spectra

for both samples. Additionally, in the 0% sample, O and N 2s states from the MOF are still present at -18 and -21 eV, respectively, indicating transitions from O and N 2 s states. Moreover, at -18 eV, the C 2 p-state from MOF is visible.

References

[1] a) J. K. Kesavan, I. Luisetto, S. Tuti, C. Meneghini, C. Battocchio, G. Iucci, *J. Mater. Sci.* **2017**, *52*, 10331–10340; b) M. Hunault, V. Vercamer, M. W. Haverkort, M.-A. Arrio, C. Brouder, G. Calas, A. Juhin, *J. Phys.: Conf. Ser.* **2016**, *712*, 12005; c) D. A. Muller, D. J. Singh, J. Silcox, *Phys. Rev. B Condens. Matter* **1998**, *57*, 8181–8202;

[2] a) Ni3C, mp-7586, *Materials Data on Ni3C by Materials Project*, LBNL Materials Project; Lawrence Berkeley National Laboratory (LBNL), Berkeley, CA (United States), **2020**; b) P. K. Tyagi et al., *Thin Solid Films* **2004**, *469-470*, 127–130;

[3] a) J. Kelling, P. Zahn, J. Schuster, S. Gemming, *Phys. Rev. B* **2017**, *95*; b) L. Yue, R. Sabiryanov, E. M. Kirkpatrick, D. L. Leslie-Pelecky, *Phys. Rev. B Condens. Matter* **2000**, *62*, 8969–8975;

[4] a) R. P. W. J. Struis, D. Bachelin, C. Ludwig, A. Wokaun, *J. Phys. Chem. C* **2009**, *113*, 2443–2451; b) F. Davodi, E. Mühlhausen, D. Settipani, E.-L. Rautama, A.-P. Honkanen, S. Huotari, G. Marzun, P. Taskinen, T. Kallio, *J. Colloid Interface Sci.* **2019**, *556*, 180–192;

[5] NiO, mp-19009, *Materials Data on NiO by Materials Project*, LBNL Materials Project; Lawrence Berkeley National Laboratory (LBNL), Berkeley, CA (United States), **2017**.

[6] S. Hüfner, *Adv. Phys.* **1994**, *43*, 183–356.

[7] N. Prinz, L. Schwensow, S. Wendholt, A. Jentys, M. Bauer, W. Kleist, M. Zobel, *Nanoscale* **2020**, 15800–15813.

[8] a) H. Zhang, G. Liu, L. Shi, H. Liu, T. Wang, J. Ye, *Nano Energy* **2016**, *22*, 149–168; b) T. Zhang, W. Lin, *Chem. Soc. Rev.* **2014**, *43*, 5982–5993; c) C.-C. Wang, X.-D. Du, J. Li, X.-X. Guo, P. Wang, J. Zhang, *Appl. Catal., B* **2016**, *193*, 198–216;

[9] a) P. Freund, I. Senkovska, S. Kaskel, *ACS Appl. Mater. Interfaces* **2017**, *9*, 43782–43789; b) Y. Han, C. Bai, L. Zhang, J. Wu, H. Meng, J. Xu, Y. Xu, Z. Liang, X. Zhang, *New J. Chem.* **2018**, *42*, 3799–3807; c) H. Jiang, X.-C. Liu, Y. Wu, Y. Shu, X. Gong, F.-S. Ke, H. Deng, *Angew. Chem.* **2018**, *130*, 3980–3985; d) F. Wu, X. Guo, Q. Wang, S. Lu, J. Wang, Y. Hu, G. Hao, Q. Li, M.-Q. Yang, W. Jiang, *J. Mater. Chem. A* **2020**, *8*, 14574–14582;

[10] a) G. E. Cutsail, N. L. Gagnon, A. D. Spaeth, W. B. Tolman, S. DeBeer, *Angew. Chem., Int. Ed.* **2019**, *58*, 9114–9119; b) T.-T. Lu, T.-C. Weng, W.-F. Liaw, *Angew. Chem.* **2014**, *126*, 11746–11750;

10 Investigation of MOF-derived Ni@C catalysts in the methanation of CO_2 under dynamic gas feed conditions using *in-situ* XAS and PDF

In this chapter, *in-situ* investigations of the catalytic system were performed. Hydrogen losses were simulated in three different scenarios. Both, the activation of the pre-catalyst to the active catalyst species, and the methanation combined with different dropout scenarios, were investigated. The presence of a NiO layer and the stabilizing influence of the carbonaceous matrix around the nickel were thus proven.

Participation in this publication

L. Rohrbach & W. Kleist – catalyst preparation, catalytic studies

N. Prinz & M. Zobel – PDF analysis, PXRD measurements, TEM measurements

C. Wilhelm – assistance in the analysis of catalytic data

P. Müller – assistance XAS *in-situ* measurements

M. Nowakowski – scientific input for the XAS analysis

A. Schökel – PDF beamtime support

S. Strübbe & M. Bauer – *in-situ* XAS measurements, XANES analysis, EXAFS analysis

Reproduced from

Investigation of MOF-derive Ni@C catalysts in the methanation of CO_2 under dynamic gas feed conditions using *in-situ* XAS and PDF

Leif Rohrbach, Sven Strübbe, Nils Prinz, Christian Wilhelm, Patrick Müller, Michał Nowakowski, Alexander Schökel, Mirijam Zobel, Matthias Bauer and Wolfgang Kleist *ChemCatChem*, *in revision.*

With permission from Wiley-VCH.

WILEY-VCH

RESEARCH ARTICLE

Investigation of MOF-derived Ni@C catalysts in the methanation of CO_2 under dynamic gas feed conditions using *in-situ* XAS and PDF

Leif Rohrbach[a],#, Sven Strübbe[b],#, Nils Prinz[c],#, Christian Wilhelm[a], Patrick Müller[b], Michal Nowakowski[b], Alexander Schökel[d], Mirijam Zobel*[c], Matthias Bauer*[b], Wolfgang Kleist*[a]

[a] *L. Rohrbach, Dr. C. Wilhelm, Prof. Dr. W. Kleist*
Department of Chemistry
RPTU Kaiserslautern-Landau
67663 Kaiserslautern (Germany)
E-mail: wolfgang.kleist@rptu.de

[b] *S. Strübbe, Dr. P. Müller, Dr. M. Nowakowski, Prof. Dr. M. Bauer*
Department of Chemistry and Center for Sustainable Systems Design
Paderborn University
33098 Paderborn (Germany)
E-mail: bauerm@mail.uni-paderborn.de

[c] *N. Prinz, Prof. Dr. M. Zobel*
Institute of Crystallography
RWTH Aachen University
52066 Aachen (Germany)
E-mail: zobel@ifk.rwth-aachen.de

[d] Dr. *A. Schökel*
Deutsches Elektronen Synchrotron DESY
22607 Hamburg (Germany)

# These authors contributed equally to this work.

Supporting information for this article is available on the WWW under https://doi.org/DOI

Abstract: The production of methane from renewable resources is one promising pathway to a sustainable energy supply if atmospheric CO_2 and H_2 from electrocatalytic water splitting are combined. In light of intermittent renewable energy supply, catalysts are required that can tolerate hydrogen fluctuations. Thus, the catalytic performance under different dynamic scenarios is investigated and structural changes are monitored by a combination of *in-situ* X-ray absorption spectroscopy and pair distribution function analysis. The Ni@C catalyst, which consists of Ni nanoparticles surrounded by graphitic shells derived from a metal-organic framework, deactivates only under full H_2 dropout conditions due to the consumption of the stabilizing carbon shell and subsequent sintering of the nanoparticles. Concerning potential industrial applications, the stoichiometric reduction of CO_2 during a hydrogen dropout is beneficial to achieve high methane selectivities. A structure-insensitive reaction via a consecutive reaction pathway is confirmed, in which the catalytic performance is limited by the modified residence time.

Introduction

The combustion of fossil energy carriers accounts for a large fraction of the global emissions of carbon dioxide, a well-known greenhouse gas. While the global energy demand is predicted to rise in the coming decades, fossil energy reserves are limited, thus, requiring novel sustainable sources. The methanation of carbon dioxide can be employed within the "power to X" (P2X) concept, which consists of an initial hydrogen production step (e.g. via water splitting) followed by the hydrogenation of carbon dioxide according to the Sabatier reaction.[1] Formally, the CO_2 methanation reaction (Eqn. (3)) can be described by a reverse water gas shift reaction (Eqn. (1)) followed by the subsequent methanation of carbon monoxide (Eqn. (2)).[2,3]

$$CO_2 + H_2 \rightleftharpoons CO + H_2O \quad (1)$$
$$CO + 3\,H_2 \rightleftharpoons CH_4 + H_2O \quad (2)$$
$$CO_2 + 4\,H_2 \rightleftharpoons CH_4 + 2\,H_2O \quad (3)$$

For the catalytic methanation of CO_2, metallic nickel is commonly used as the active phase due to its high activity at a relatively low cost.[4] Since the catalytic performance depends strongly on the properties of the nickel phase and the support, various studies have been performed to enhance the catalytic performance and to study the reaction mechanism.[5,6] Many efforts focused on the immobilization and stabilization of metal nanoparticles on support materials to avoid deactivation processes like high-temperature sintering.[7] Especially for dynamic gas feed conditions, which might occur due to fluctuations in hydrogen supply, novel catalysts tolerating such conditions are required.[8]

However, most studies on the production of methane by heterogeneous CO_2 hydrogenation are focused on constant hydrogen gas feed conditions.[9] Only a few experiments considered the effects of fluctuations in the H_2 supply and tried to track the changes in the catalyst using *in-situ* characterization methods.[10–12] In case of an energy shortage (clouded sky, calm air), the production of green hydrogen via electrocatalysis is hindered and, consequently, the H_2 feed for methanation is strongly affected. Hence, it is crucial to identify suitable operation scenarios in the case of hydrogen shortage that allows better long-term stability and activity of methanation catalysts. Recently, dynamic *in-situ* X-ray absorption spectroscopy (XAS) studies revealed a fast deactivation of the active Ni species on Al_2O_3 support during complete H_2 dropouts, which prevents the application of such catalysts under fluctuating conditions in continuous operation.[12] Similar degradation effects can occur as a consequence of varying gas compositions, possibly leading to undesired side reactions. In this context, superior Ni-based catalysts are needed that feature an enhanced stability against deactivation under fluctuating conditions.

The spatial confinement of Ni nanoparticles facilitated by suitable support systems represents a promising approach for the development of improved catalysts.[13] The thermal decomposition of metal-organic framework (MOF) precursors can offer a useful toolbox to design such improved functional nanomaterials.[14,15] Previously, we could show that this approach can yield Ni nanoparticles encapsulated by carbonaceous support, which showed high activity in the methanation of CO_2 under static

conditions.[16] To structurally characterize this complex system, a combination of sophisticated analytical tools is required. For instance, pair distribution function (PDF) analysis from high-energy X-ray scattering data and XAS[17–19] proved to be highly sensitive to identify ordered and disordered structures across length scales from short-range order on the Ångström level to crystalline structures in the nanometer to micrometer regime. Hereby, structural changes can readily be tracked and precise structure-activity correlations could be developed.[16,20]

While previous studies on fluctuating conditions in CO_2 methanation concentrated on cycles of a complete hydrogen dropout, the present study focuses on three different dropout scenarios to simulate more realistic conditions, namely (i) a full H_2 dropout (FD), (ii) a partial H_2 dropout, i.e. the reduction of the H_2 flow to 50% (PD), and (iii) a simultaneous reduction of both the H_2 and the CO_2 flow to 50%, according to a stoichiometric dropout (SD). Considering the H_2 production from fluctuating renewable energies, adjusting the CO_2 feed to keep the H_2/CO_2 ratio constant might be easier to accomplish than reactivating a deactivated catalyst.[21] Consequently, a dynamic adjustment of the gas feed composition can be a promising approach to prevent catalyst deactivation and open new possibilities in terms of the reaction engineering of P2X processes. To develop a structure-activity correlation of the catalyst during the different dropout scenarios, an in-depth characterization of the catalysts using a combination of *in-situ* XAS, and *in-situ* PDF analysis, complemented by TEM and PXRD was performed.

Results and Discussion

Dynamic catalytic studies

Previously, we have reported the influence of the decomposition conditions of the Ni(BDC)(PNO) MOF on the nature of the resulting Ni@C catalyst. In the following, the Ni@C-10%H_2-400 catalyst will be applied under dynamic operation conditions, which featured a high catalytic activity regarding both CO_2 conversion (73%) and methane selectivity (96%).[16] Structural characterization showed that the catalyst consists of Ni_{fcc} nanoparticles encapsulated in a carbonaceous matrix without any additional Ni phases.[16]

In the first part of the present work, three different dropout scenarios for dynamic catalytic studies were applied for 24 h, which corresponds to 24 cycles of 30 min methanation conditions (H_2/CO_2 = 4:1) and 30 min dropout conditions each (see Experimental Scheme 1). Additionally, a reference run under static methanation conditions has been carried out for 24 h to exclude effects that were not related to the dropouts. For more complementary data not shown here, see SI Figure S1-2. Under static methanation conditions, Ni@C remains active in the methanation of CO_2 and deactivates only gradually within 24 h operation time as shown in Figure 1a. Both the CO_2 consumption rate and the CH_4 production rate increase slightly until 3 h time on stream. In the full H_2 dropout scenario (see Figure 1b), a more pronounced increase in the CO_2 consumption rate (black) is observed after the first full H_2 dropout in comparison to static conditions. The formation of CO (blue) is also significantly reduced compared to the initial value. After three full H_2 dropouts, the catalyst starts to deactivate rapidly until only a minor amount of CH_4 is formed after cycle eight. In comparison to previously reported results, where the deactivation of the alumina- supported Ni catalyst already

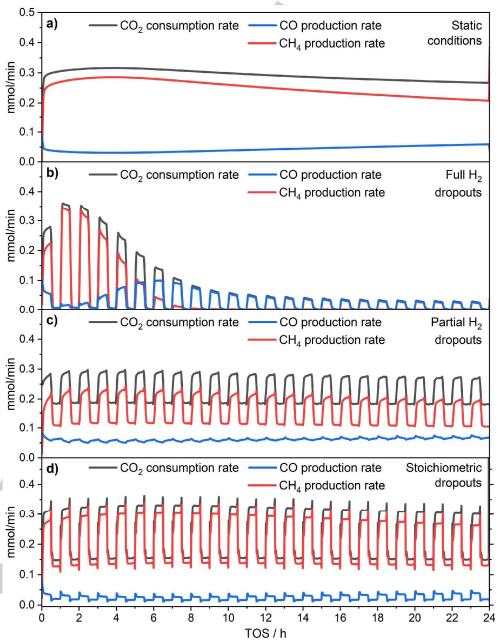

Figure 1. Methanation of CO_2 catalyzed by Ni@C during static (a) and the three dynamic operation conditions, switching every 30 min between methanation (66 mLmin^{-1} $N_2/H_2/CO_2$ = 0.5/4/1) and dropout conditions with full H_2 dropouts (b), partial H_2 dropouts (c) and stoichiometric dropouts (d). The reaction was carried out at 425 °C at 1 atm.

started after the first H_2 dropout and within a few minutes,[12] Ni@C appears to be more stable within the first 3 h. However, with proceeding deactivation, an increasing amount of CO is formed under methanation conditions and CO becomes the main product after cycle five. No methane is formed during the dropout periods. However, a small conversion of CO_2 to CO is observed (0.01 mmolmin^{-1}), which already provides some information about the deactivation process. Since hydrogen is not available during the full H_2 dropouts, an alternative electron source for the reduction of CO_2 to CO needs to be considered. Carbon can act as a reducing reagent according to the Boudouard equilibrium (Eqn. 4):

$$CO_2 + C \rightleftharpoons 2\ CO \qquad (4)$$

With increasing reaction time in Figure 1b, the CO yield drops, which is in agreement with the carbon consumption under full H_2 dropout conditions. In turn, this could eventually lead to deactivation if the consumed carbon originates from the protective carbon shell around the Ni nanoparticles, which then sinter as a consequence.

The increase in methane production after the first and second H_2 dropout, the deactivation mechanism itself, and the increased conversion of CO_2 to CO with the proceeding deactivation

progress is discussed in detail in the section on the Structure-activity correlation below.

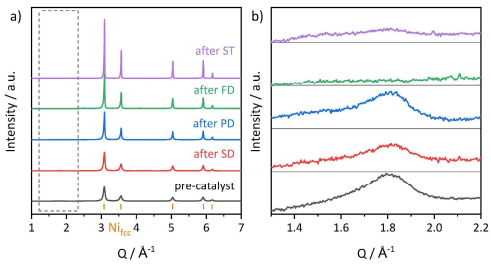

Figure 2. a) Background-corrected PXRD patterns of the spent Ni@C catalyst after the different scenarios static conditions (ST), full H_2 dropouts (FD), partial H_2 dropouts (PD) and stoichiometric dropouts (SD) compared with the pre-catalyst. The calculated powder pattern of Ni_{fcc} (orange) matches the observed Bragg reflections. b) Magnification of the region between 1.3-2.3Å^{-1} is shown to showcase the broad hump originating from the residual carbon in the sample.

During partial and stochiometric dropouts (Figure 1c-d), the catalyst remains active with only a small reduction of CO_2 conversion. Interestingly, the methanation rate increases during the first stochiometric dropouts, similar to the methanation under static conditions. During these stoichiometric dropouts, the CO_2 consumption, CH_4 production, and CO production rates are in agreement with the reduction of the absolute amounts of the reactant gases.

To summarize the results of the three dropout scenarios, it is evident that the presence of at least a certain amount of hydrogen is necessary to maintain the stabilizing carbonaceous matrix. Deactivation of the Ni@C catalyst was only observed for the full H_2 dropout scenario, while the catalyst activity remained unaltered under both partial and stoichiometric dropout conditions. In comparison to the methanation under static conditions, the catalyst remained slightly more stable for the partial and stoichiometric dropout scenarios, with the downside of less overall CH_4 production in the 24 h TOS.

***Ex-situ* characterization of the spent catalysts with X-ray scattering and TEM**

PXRD measurements of the spent Ni@C catalyst after 24 h TOS of the scenarios described above show that the samples consist of Ni_{fcc} and different amounts of carbon (Figure 2). No reflections of NiO are observed. The integrated intensity of the broad humps between 1.5 and 2.0 Å^{-1} reflects, qualitatively, the carbon content in the sample, in the form of carbon shells around the nanoparticles.[16] The amount of carbon in the sample is the highest for the pre-catalyst and decreases in the following order for the post mortem catalysts: PD > SD > ST > FD. The fast deactivation of the catalyst in the full H_2 dropout scenario can be explained by the disintegration of the stabilizing carbon shell and, thus, the fast sintering of the nanoparticles. The domain sizes of the nanoparticles correlate strongly with the amount of residual carbon visible in the PXRD: the lower the carbon signal, the sharper the Bragg reflections and, hence, the larger the domain sizes of Ni_{fcc}. The correlation between the carbon species and stabilized small particles is therefore obvious.

TEM images of the spent catalysts were analyzed and compared with the TEM analysis of the pre-catalyst from previous work.[16] In the spent catalysts after partial H_2 dropout, stoichiometric dropout, and static conditions, the carbon shells around the nanoparticles persist (see SI Figure S7), which is in line with the PXRD results. For the full H_2 dropout scenario, the carbon shells disintegrate and there are no nanoparticles visible. This underlines our assumption that the reaction of the carbon shell with CO_2 via the Boudouard-equilibrium leads to sintering of the nanoparticles and, ultimately, the deactivation of the catalyst. We expected different particle sizes after the different dropout conditions. Yet, the lognormal particle size distributions determined from TEM images yield very similar particle diameters of 22-24 nm for all scenarios, except for the full H_2 dropout scenario, where no nanoparticles are visible (see SI Figure S8). Further insight into the structural features of the nanoparticles of the spent catalysts was achieved by PDF refinements using a spherical attenuated crystal model. PDF refinements with a single domain size or with bulk Ni_{fcc} result in a residual structural signal in the difference curves (Figure 3a and b). This is due to erroneous peak widths and heights. By combining a Ni_{fcc} phase of finite domain size with a bulk Ni_{fcc} phase, a better fit quality with a goodness of fit value R_w = 0.12 for static conditions is achieved (Figure 3c). With a second phase, also a second isotropic displacement parameter is introduced, which influences the PDF shape in the range 1-10 Å by matching the peak widths better (see Figure S9). As expected, the U_{iso} of the nanoparticle phase is higher (see SI Table S1), which is the result of higher disorder compared to a crystalline bulk material. The peak heights are influenced by the shape function. For the partial and the stoichiometric dropouts, similar results are

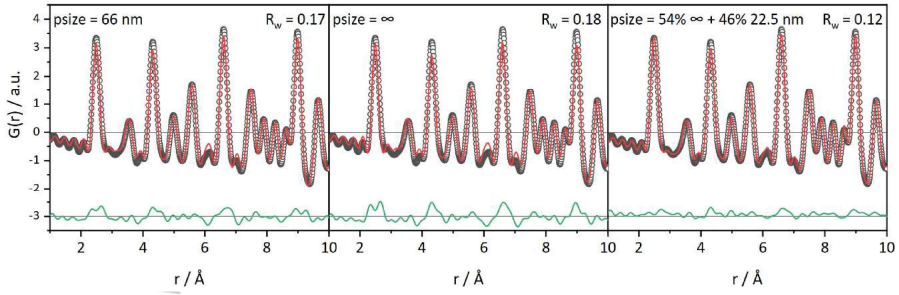

Figure 3. PDF refinements of Ni@C after catalysis under static conditions, showing the experimental data (black circles), the calculated fit (red line) and the difference between them in offset (green line). Both the refinement with a single domain size (66 nm) (left), and with an infinite crystal (middle) showed residual structural signals in the difference curve. The biphasic refinement with a finite domain size alongside a bulk phase is shown on the right side.

Table 1. Comparison of TEM, Williamson-Hall (WH) analysis, and PDF particle sizes for different dropout conditions of Ni@C.

Ni@C	TEM particle size	PDF domain size	Phase fraction of Ni particles compared to bulk Ni from PDF
pre-catalyst	19 ± 4 nm	8 nm	90 at%
after ST	23 ± 7 nm	23 nm	46 at%
after FD	- [a]	bulk	0 at% [b]
after PD	24 ± 8 nm	9 nm	83 at%
after SD	26 ± 8 nm	9 nm	59 at%

[a] Too few particles to yield a meaningful size distribution.
[b] A two-phase refinement of finite-size nanoparticle and bulk Ni did not result in a better fit quality than a one-phase refinement of bulk Ni. Although small fractions particles < 50 nm could co-exist, these are below the detection limit.

obtained by this refinement strategy (see Table 1 for an overview of particle diameters from TEM and PDF analysis, as well as the ratio of bulk and nanoscale phase as determined from PDF fits).
At first glance, the refinement of a Ni_{fcc} bulk phase is in contradiction with the TEM results. Yet, this contradiction can be resolved by awareness of the TEM grid preparation loosing the Ni bulk phase from the sample to the grid: the grid is dipped into a dispersion of the sample and due to gravity effects, the large crystalline particles (refined as bulk Ni_{fcc}) may have already sedimented, leaving only the smaller particles on the carbon grid. In contrast, for PXRD/PDF measurements, the entire sample was filled into the capillary as a powder. The samples are in general very polydisperse after the dropout scenarios. Such polydispersity leads to the assumption, that the carbon shells might have different thicknesses around different particles. Thin shells lead to fast sintering to bulk Ni_{fcc}, whereas thick shells stabilize the nanoparticles for a longer time.
The Ni nanoparticles show increased sintering under static conditions, visible in the larger size of 23 nm and the smaller phase fraction of nanoparticular Ni (see Table 1). During static conditions, a larger volume of reaction gases interacts with the catalyst and, hence, more heat is generated by the exothermic methanation reaction, resulting in increased sintering. This is reflected in the lower catalytic performance after 24 h TOS. The PDF determined domain size after the partial and stoichiometric dropouts is 9 nm, presenting an underestimation compared to TEM. We already know that the Ni@C pre-catalyst particles contain a significant amount of internal stress, strain, or disorder due to the synthesis procedure.[16]

***In-situ* PDF experiments**

Batch refinements of the *in-situ* PDF data yields domain sizes of the active Ni_{fcc} nanoparticles (Figure 4a), molar contents of Ni_{fcc} and NiO phases (Figure 4b), as well as lattice parameters (Figure 5) and isotropic displacement parameters U_{iso}. During the activation, the Ni_{fcc} domain size increases only slightly, which underlines the stability of the nanoparticles at elevated temperatures of 350 °C if surrounded by a carbon shell (Figure 4a). Upon reaching the reaction temperature of 425 °C, the domain size grows rapidly from around 9 nm to 11 nm during the first methanation cycle. Subsequently, in cycles 2-4, slower, steady growth is observed. It is important to keep in mind that these diameters are not corrected for possible internal strain. Hence, on the one hand, the true particle diameters might be larger and on the other hand, the effect of nominal growth could just stem from a release of the internal strain of the catalyst particle.
Although the pre-catalyst already consist of a high degree of Ni, there is still a fraction of NiO visible, mainly in the highest PDF peak of the NiO structure at 3.0 Å (see Figure 4b). This peak is diminishing during the heating to activation especially between 90 and 110 °C. The peak is completely gone at 350 °C, where the fraction of NiO approach 0%. We used two-phase PDF refinement with Ni_{fcc} and NiO to support this finding. The refined NiO phase of the initial catalyst state makes up for 15 mol% and has very broad peaks, which can be explained by the disorder of the NiO shell (see Figure S12). A high degree of reduction to Ni is already achieved at a very low temperature of 80 °C. This temperature is significantly lower than for commercial Ni catalysts, which are activated at temperatures around 450 °C.[27] The relatively short activation time can be explained by the high Ni(0) fraction already present in the Ni@C pre-catalyst. There are only small amounts of surface NiO surrounding the Ni_{fcc} particles, which need to be reduced prior to catalysis. Overall, the PDF showed a remarkable sensitivity toward the NiO phase fraction to track the reduction process, and the results are well in line with XAS results (vide infra).

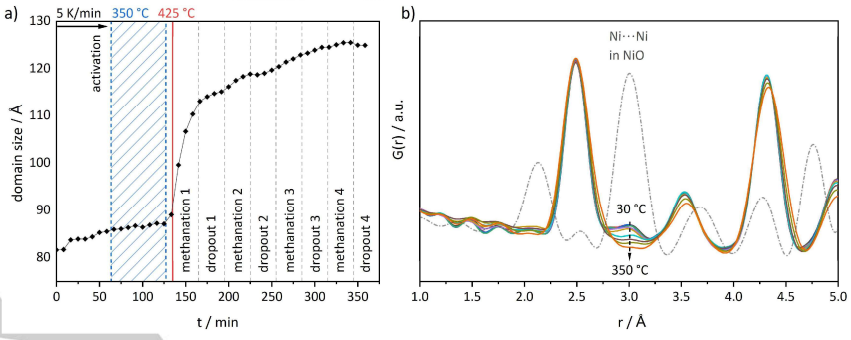

Figure 4. a) Domain sizes of the Ni phase from in situ PDF refinements of Ni@C during activation and full dropouts. Heating to activation with a ramp of 5 K/min and holding at 350 °C for 60 min for activation (blue hatched area). Then the sample was heated to 425 °C with 10 K/min and the first methanation was started (methanation 1). b) Molar content of Ni and NiO from *in-situ* PDF refinements during the activation process. Some temperatures are highlighted with dashed lines. The temperature was held constant after reaching 350 °C. No further changes are observed after 80 minutes.

During the FD experiments, no oxidation of Ni to NiO is observed even after four full H_2 dropout cycles, as the PDF does not show any Ni-O or Ni-Ni distances stemming from NiO (see SI Figure S13), and sequential PDF refinements did not improve when a NiO phase was added. Nevertheless, deactivation can be observed during the first four FD cycles (see Figure 5). Therefore, we propose that the deactivation mechanism is due to sintering, i.e., overall lower active surface. This is triggered by the loss of the carbon shells, which was observed via *ex-situ* PXRD after catalysis (Figure 2), TEM (SI Figure S7), and to some extent during the *in-situ* experiments (SI Figure S11).

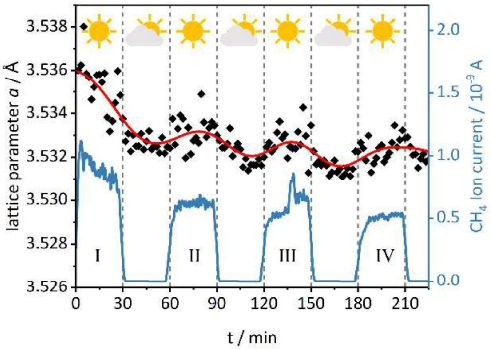

Figure 5. Lattice parameter (black diamonds) extracted from PDF refinements during the full H_2 dropout experiment. The oscillation was highlighted by an FFT smoothing (red line). Catalytic cycles are numbered with roman numerals The online MS analysis tracked the CH_4 formation (blue line).

During the dynamic dropout experiments, the lattice parameter expands in course of methanation and contracts under full H_2 dropouts (see Figure 5). The largest oscillation is found during the first cycle with a change in the lattice parameter *a* of around -0.1 % from 3.536 to 3.533 Å. The first Ni-Ni distance similarly contracts by roughly 0.2 % from 2.50 during methanation 1 to 2.49 Å during dropout 1. Compared to a study on very small (1-3 nm) Pt nanoparticles from Chapman *et al.*,[29] which showed a ~2.2 % expansion of the first Pt-Pt bond distance upon H_2 adsorption at room temperature, the changes observed here are rather small, yet our particles are significantly larger and more crystalline. To rule out temperature fluctuations as the origin of the lattice parameter change, the linear thermal expansion coefficient α = $1.24 \cdot 10^{-5}$ K^{-1} was extracted from the linear regression of the lattice parameter in the temperature range 30-330 °C (SI Figure S14). Translating the lattice parameter change of -0.003 Å to a temperature difference would require the sample to cool down by 70 K, which was not observed during the experiments. Consequently, we assume that these changes in the lattice parameter are induced by the dynamic conditions. This slight lattice expansion could, for instance, originate from the diffusion of H_2 into the subsurface of Ni, which is well known for metals,[30] but has not been observed for Ni-based methanation systems before. Alternatively, restructuring of the nanoparticle surfaces during the methanation reaction could occur due to the adsorption of gas molecules onto the metal surface. Thus, further adsorption studies are needed to fully understand this behavior.

***In-situ* X-ray absorption spectroscopy**

Since the initially employed catalyst contains amorphous Ni structures at the surface,[16] XAS is a powerful tool due to its short-range sensitivity.[31–36] By analysis of the XANES (X-ray absorption near edge structure) region of an XAS spectrum information about the oxidation state through the absorption edge can be gained. Also, near-edge resonances provide averaged electronic information about the absorbing Ni centers in a fingerprinting manner. The XANES spectra recorded during the activation with hydrogen are shown in Figure 6. The spectra of the initial state at 25 °C and final state at 350 °C are shown for comparison. To investigate the activation process from the pre-catalyst to the catalytic active species, the pre-edge region, and the first resonance after the edge step (white line) in the range of 8330-8360 eV are of particular interest. XANES spectra show that the first resonance at 8350 eV in the white line starts to decrease from 85 °C on, while the second resonance around 8360 eV increases. These changes are completed between 175 °C and 205 °C, which is in agreement with the PDF analysis presented in the preceding section. The changes in the edge shape of the white line indicate the presence of mixed species. In general, the form of metallic Ni is dominating, but a small fraction of oxidized species is deduced at lower temperatures. With increasing temperature, a reduction was observed resulting in a larger fraction of metallic species. This is reflected in the shape of the oscillations. The first oscillation is due to the unoccupied p-states being filled, while the second can be accounted for by the first EXAFS oscillation. In agreement, a closer look at the pre-edge region revealed a shift to lower energies from 8337 eV at 105 °C to 8333 eV, which is characteristic for the reduction to Ni(0).

The EXAFS analysis was carried out on the pre-catalyst sample at 25 °C in He. Then, the activated sample was probed at 350 °C in an H_2 atmosphere, as well as during reaction conditions and the different dropout scenarios. A small variation in the self-absorption effect is expected due to the sample geometry and preparation effects. The effect was taken into account during the fit of the pre-catalyst sample.

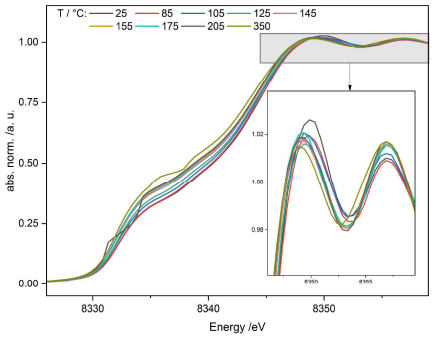

Figure 6. XANES spectra of the activation process in the temperature where the loss of the oxidic layer is happening. The starting point and the final point are added for comparison.

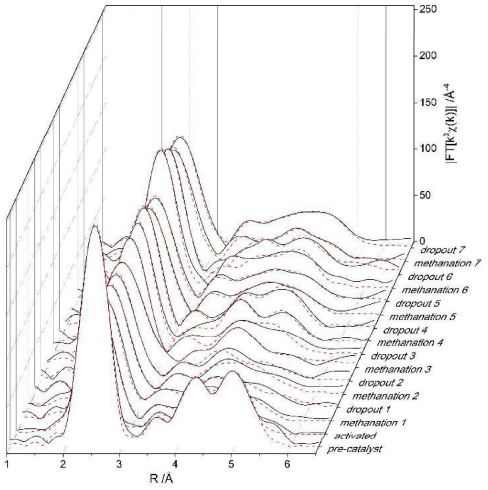

Figure 7. Fourier-transformed experimental k3χ(k) EXAFS functions of the different steps in the *in-situ* experiment in the full H_2 dropout scenario. The solid black lines show the experimental spectra, and the dotted red lines show the theoretical fit of the EXAFS analysis.

Since the particle size according to PDF analysis is exceeding 6 nm, no calculation of particle sizes was performed from EXAFS data.[37,38] In Figure 7 to Figure 9 the Fourier-transformed EXAFS spectra of the *in-situ* measurements are shown. The EXAFS results of the three different dropout scenarios are summarized in Figures S15 to S32 and Tables S2 to S4. All pre-catalyst samples are showing a Ni-O pair in the first coordination shell around 2.0 Å.

Full H_2 dropout scenario: The pre-catalyst shows clear evidence for bulk Ni(0) species above the EXAFS size detection limit (Ni-Ni coordination number in the first shell around 12) visible in the characteristic signal pattern around 3-5.5 Å. For the pre-catalyst sample, a number of 12.8 Ni-Ni scattering paths at 2.47 Å is in agreement to bulk Ni_{fcc}. Further insight can be gained from fits to the next coordination shell where six atoms should be present at around 3.5 Å. Only 1.8 Ni-atoms were visible at a range of 3.43 Å. Since in general large particles are present, this could be an indication of an increased disorder, other morphologies than spherical particles, and/or a considerable fraction of very small particles, due to the broad particle size distribution which was measured in a previous work.[16] Furthermore, this is explained by the Debye-Waller factor. This reduces the coordination number due to the high structural and static disorder in the system. Another possible reason for the low coordination number of 1.8 Ni in the third coordination shell can be the higher contribution of 7.9 Ni-C pairs at 3.88 Å. This shell shows a significant correlation with the Ni-Ni shell, since in a fit without a Ni-C shell the number of Ni atoms in the third shell increases. However, this feature could not be observed in the PDF analysis because the PDF does not respond to the weakly scattering carbon. Nevertheless, this carbonaceous surrounding has already been determined in the *ex situ* analysis of the pre-catalyst. However, a Ni-O pair with a backscatterer at 2.02 Å is detected in the nearest neighbor environment of the pre-catalyst, indicating the presence of a small fraction of oxidic species, which is in agreement with the XANES data. In general, for all probed scenarios the Ni-O coordination sphere disappears after the activation. For the activated species, the first shell consists of 12.2 Ni-Ni pairs at 2.47 Å. At 3.45 Å, 2.1 Ni-Ni backscatterers are found while the carbonaceous species at 3.84 Å are still present with 4.8 Ni-C pairs. Also, the last three Ni-Ni coordination shells are comparable to the pre-catalyst species, even though the coordination number decreased overall. This might be due to heating and gas adsorption. The coordination sphere at 4.27 Å provides 6.4 Ni-Ni pairs. As in the non-activated species, the shell around 4.75 Å still had to be included in the fit to get reliable results, which resulted in a coordination number of 15.3 Ni at 4.73 Å. In a higher coordination shell, 16.9 Ni-Ni backscatterers at 5.11 Å can be seen.

The EXAFS analysis of the full H_2 dropout scenario agrees with the catalytic data, since the carbonaceous species cannot be detected anymore after the second methanation cycle, and the features of the metallic Ni become sharper. For further information, see Table S2 in the SI.

Stoichiometric dropout scenario: For the second shell for the pre-catalyst sample (Figure 8), the characteristic bulk type value of 11.9 Ni-Ni backscatterers at 2.47 Å was found. In the third shell, 5.1 Ni-Ni backscatterers could be seen at 3.47 Å, which is in agreement with the Ni_{fcc} structure where 6 Ni atoms are present. Carbonaceous species were visible with a number of 9.3 Ni-C pairs at a distance of 3.83 Å. As in the full H_2 dropout scenario, the higher shells showed results that were similar to those of the pre-catalyst, indicative of bulk Ni.[16] In the activated sample, the first shell presented 11.8 Ni-Ni pairs at 2.47 Å, which perfectly fits the Ni_{fcc} structure. Although only 2.0 Ni-Ni backscatterers could be seen in the second shell at 3.43 Å distance, this shell was highly influenced by the 5.0 Ni-C pairs at 3.85 Å. Higher nickel shells showed significantly lower coordination numbers than in the pre-catalyst, which might be the case due to heating and gas adsorption in *in-situ* analysis.

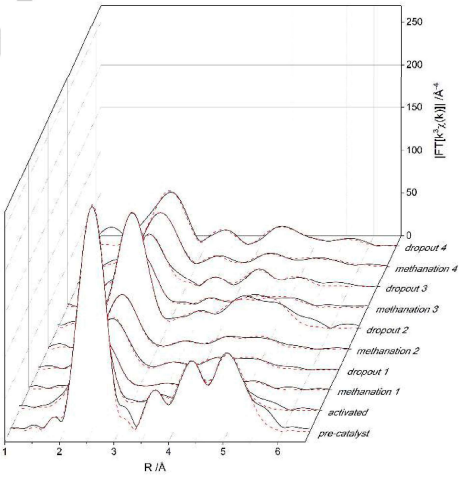

Figure 8. Fourier-transformed experimental k3χ(k) EXAFS functions of the different steps in the *in-situ* experiment in the stoichiometric dropout scenario. The solid black lines show the experimental spectra, and the dotted red lines show the theoretical fit of the EXAFS analysis.

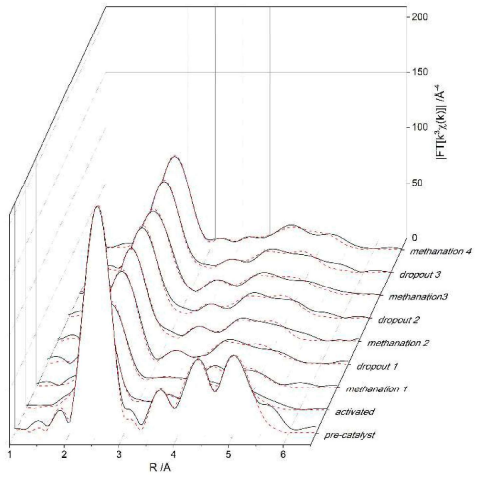

Figure 9. Fourier-transformed experimental k3χ(k) EXAFS functions of the different steps in the *in-situ* experiment in the partial H_2 dropout scenario The solid black lines show the experimental spectra, the dotted red lines show the theoretical fit of the EXAFS analysis.

The main difference between the full and the stoichiometric dropout scenario is the presence of the carbonaceous species around 3.8 Å for every cycle in the stoichiometric dropout scenario. In the fourth methanation cycle of the SD scenario, the spectra quality was decreasing, thus, no reliable fit of a carbon shell was possible (see SI, Table S3). Nevertheless, the catalytic behavior, which shows no decrease in catalytic activity, suggests that the carbon layer is still present. Except for the second dropout in the SD scenario, the Ni-Ni coordination numbers decreased to roughly 6 in the first coordination shell (Table S3, SI). Since no particle size decrease could be detected by PDF and PXRD, and instead an increase in particle size was found, these results are attributed to self-absorption effects. In fact, significant sintering to macroscopic particles would indeed increase self-absorption. These effects can however not be corrected properly due to the non-defined nature of the formed species.

Partial H_2 dropout scenario: Looking at the second shell of the pre-catalyst, it became clear that this value was slightly lower than in the compared scenarios with 9.0 Ni atoms at 2.47 Å. As mentioned before this is caused by varying but undefined self-absorption effects.

In the partial H_2 dropout scenario, 4.3 Ni-Ni pairs at 3.46 Å and 7.9 Ni-C pairs at 3.83 Å, could be seen. For the activated state, the loss of the oxygen layer is again the most notable difference. The first shell consisted of 10.1 Ni-Ni backscatterers at 2.47 Å and 1.1 Ni-Ni at 3.43 Å along with 3.5 Ni-C pairs at 3.85 Å in the second shell. The three Ni-Ni shells show a small decrease in coordination number in comparison to the non-activated state, possibly due to initial sintering at the beginning of the experiment. The coordination numbers for higher shells are slightly deviating from bulk Ni_{fcc}. Still, they are reasonable due to the high amount of bulk nickel in the sample, which is influenced by carbonaceous species and structure effects in the higher coordination spheres of nanoparticles.[39,40]. No loss of Ni-C species during the dropouts could be observed, similar to the stoichiometric dropout scenario.

The results of the three dropout scenarios show comparable behavior until the first dropout. After the activation process, the main difference between the EXAFS analyses concerned the loss of the Ni-O coordination sphere around 2.0 Å. Comparing the catalytic cycles during the process, it is clear that the chemical species do not change in the partial H_2 dropout scenario, thus maintaining the active catalyst state.

The carbon species were present for all four cycles in the PD and SD scenarios, which is in agreement with the catalytic data. The catalyst still showed high activity in later methanation cycles after several dropouts. This pattern suggested that the carbonaceous layer is indeed the stabilization factor of the catalyst and that it is necessary to prevent the Ni species from sintering during the catalytic reaction.

Structure-activity correlation

Further catalytic studies were carried out on the full H_2 dropout scenario to address (i) why an increased methanation activity was observed during the first few cycles and (ii) why the selectivities towards methane and CO changed significantly with proceeding deactivation.

The short-term increase in the CH_4 formation directly after the first two full H_2 dropouts in the FD scenario (compare Figure 1b, cycles 2 and 3) was not observed in the *in-situ* synchrotron studies. This may stem from experimental differences like different reactor setups, catalyst loadings, applied gas flows, and residence times. The increase in methane productivity could either originate from temporal activation effects or from permanent changes in the catalyst. A short-term effect might be

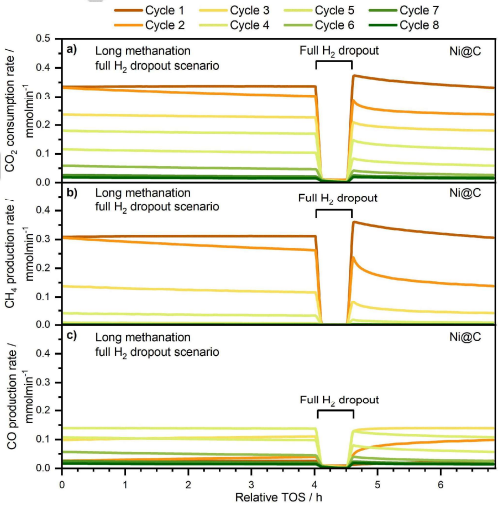

Figure 10. Methanation of CO_2 catalyzed by Ni@C according to the long methanation full H_2 dropout scenario. a) CO_2 consumption rate. b) CH_4 production rate. c) CO production rate. The first 4 h under methanation conditions were omitted (shown in SI Figure S3). During each cycle (Cycle 1-8), a full H_2 dropout was applied after 4 h relative to the start of the cycle (0 h). The catalytic activity was tested again under methanation conditions afterward. In total, the catalytic activity was studied for 380 min between each dropout under constant CO_2 methanation conditions. 40 mg catalyst was diluted with 160 mg.

the coverage of the catalyst surface with intermediate species that are formed, e.g., by the reaction of CO_2 with carbon from the catalyst via a route involving the Boudouard-equilibrium. These intermediate species could then react to methane after the addition of hydrogen to the gas feed. However, this process would not be sufficient to explain the extent of the increase in the CH_4 production that had been observed in the first cycles of the FD experiment: The additionally produced 2.4 mmol CH_4 with respect to the CH_4 production before the dropout in cycle 1 was already significantly higher than the maximum that could originate from the carbon matrix of the catalyst (1.1 mmol).

To answer the first of the two remaining questions and to elucidate the reason for the increase in CH_4 productivity after the first dropouts, the duration of the methanation period between each full H_2 dropout was elongated to 6.33 h in a modified full H_2 dropout scenario ("long methanation full H_2 dropout"). Eight cycles were investigated in this scenario to gain insight into the most relevant section of the deactivation process (cycles 1-8 in Figure 10). The catalyst was held for 4 h under methanation conditions prior to the cycles until a stable activity was achieved (compare SI Figure S3). As a result, the catalytic performance before the first full H_2 dropout is stable in cycle 1 (see Figure 10). In agreement with the previous full H_2 dropout scenario, the activity drops during the first dropout (compare Figure 10a-c with Figure 1a). After switching back to methanation conditions in the "long methanation full dropout scenario", the previously discussed jump in the catalytic activity is observed in cycle 1. As shown above, by various techniques, the carbon shell is consumed to a larger extent under full H_2 dropout conditions, thus, leading to the conclusion that in this early stage of the process more active metal sites are accessible.

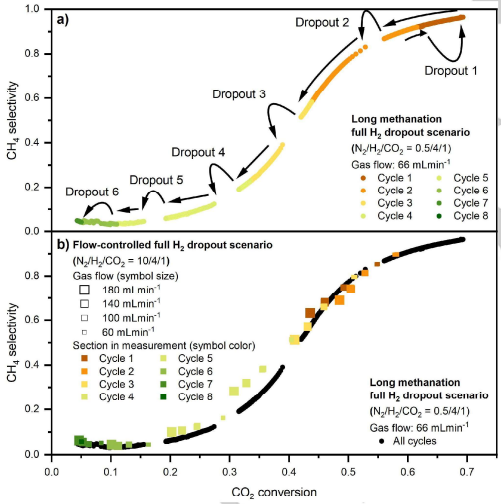

Figure 11. CH_4 selectivity plotted over the CO_2 conversion. Data points corresponding to the dropout conditions and the gas-switching process are omitted for increased visibility. Data points at low CO_2 conversions (< 4%) are omitted due to increased inaccuracy of the measurement. a) Long methanation full H_2 dropout scenario. The black arrows indicate the temporal chronology of the data points. The dropout labels correspond to the appropriate cycle number. b) CH_4 selectivities of the temperature- and flow-controlled FD scenario with 60 mLmin^{-1}, 100 mLmin^{-1}, 140 mLmin^{-1} and 180 mLmin^{-1} ($N_2/H_2/CO_2$ = 10/4/1). 425 °. For improved comparison, the data from the long methanation FD scenario (a) are shown in black (66 mLmin^{-1} with $N_2/H_2/CO_2$ = 0.5/4/1). Both scenarios were subdivided into 8 dropout cycles as described above. 40 mg catalyst were diluted with 160 mg SiC. Reaction temperature: 425 °C.under constant CO_2 methanation conditions. 40 mg catalyst was diluted with 160 mg.

After the first full H_2 dropout (cycle 1), the catalytic activity decreases steadily under constant methanation conditions, which results in a lower methane production rate (0.26 mmolmin^{-1}) compared to the production rate before the dropout (0.31 mmolmin^{-1}). This can be explained by the removal of stabilizing carbon under full H_2 dropout conditions, which then causes irreversible sintering and, consequently, a lower amount of accessible active sites.

To obtain further mechanistic insight and to answer the second of the remaining mechanistic questions, the CH_4 selectivity of the "long methanation full H_2 dropout scenario" is plotted versus the CO_2 conversion in Figure 11a. The progress of the catalyst deactivation can be tracked by the black arrows, following the sequence of consecutive dropouts. During deactivation, the selectivity to CH_4 decreases following a sigmoidal curve. The most common explanation in heterogeneous catalysis for this behavior would be that the reaction is structure-sensitive and the CH_4/CO ratio changes during the catalyst deactivation due to the sintering of the nickel particles, which leads to a different ratio of exposed facets that are responsible for the methane and carbon monoxide formation, respectively. To investigate if this is true also in the present case, we performed an additional series of catalytic experiments in each cycle with varying gas feed rates of 180, 140, 100, and 60 mLmin^{-1} with $N_2/H_2/CO_2$ = 10/4/1, thus, varying the residence times of the substrates over the catalyst ("flow-controlled full H_2 dropout scenario" SI Figure S4). For each cycle, the catalyst was treated under methanation conditions until a steady state of the catalyst was reached before the variation of the residence time was applied (described in SI, chapter *Complementary results to the TFFD scenario*). Consequently, the state of deactivation of the catalyst particles is the same for all flow variation experiments within the same cycle. If the reaction would be structure-sensitive, a different degree of conversion would be expected for the different flow rates (due to the different residence times), but the selectivity to CH_4 and CO should be the same or at least very similar. However, the trend of the CH_4 selectivity in the "flow-controlled FD scenario" is in very good agreement with the sigmoidal curve that was observed in the "long methanation full H_2 dropout" scenario (compare black circles in Figure 11b). Therefore, we can rule out a structure-sensitive reaction for the formation of the two products methane and carbon monoxide on our catalyst. Instead, the observed sigmoidal trends are explained by a consecutive reaction pathway, where CO_2 is first reduced to CO, which is subsequently converted to methane. Such a structure-insensitive mechanism for the methanation of CO_2 in the presence of Ni/Al_2O_3 catalysts with high Ni loadings has recently been proposed by Beierlein *et al.*[41] In particular, they proposed a linear correlation between the production of CH_4 and the accessible Ni surface area. Their findings are in good agreement with our experiments, since both the increased total gas flow feed ("flow-controlled full H_2 dropout" scenario), which results in a shorter contact time of the reactants with the catalyst surface, and the progressing deactivation process in the "long methanation full H_2 dropout" scenario led to data pairs on a sigmoidal curve for the CH_4 selectivity. Accordingly, the modified residence time, which describes the residence time of CO_2 per active Ni surface site is expected to be the common limiting property for the methanation of CO_2 in both cases.

Conclusion

In light of variable H_2 feedstocks from fluctuating supply of renewable energy, we have investigated the impact of different dropout scenarios on Ni nanoparticles embedded in carbon shells as a catalyst for the methanation of CO_2. We gained insight into the activation process showing that our Ni@C pre-catalyst already consisted of a high degree of Ni(0). Only mild conditions were needed to quickly reduce surface NiO to metallic Ni as identified by both *in-situ* XAS and PDF experiments, which was necessary to gain the active catalytic species. For the dynamic dropout scenarios, the presence of at least a certain amount of hydrogen in the gas feed during dropouts was necessary for the long-term stability of the Ni@C catalyst. The catalyst remained active under static conditions, partial H_2 and stoichiometric dropout conditions, but deactivated under full H_2 dropout conditions, since the carbon shell was consumed and the Ni nanoparticles sintered. A detailed EXAFS analysis of the individual catalytic and dropout cycles within the different dropout scenarios confirmed the correlation between the decreased catalytic activity and the loss of stabilizing carbonaceous species. Additionally, we noticed that the lattice parameter in PDF refinements oscillated with the gas switches during the full H_2 dropout experiment, but it remains unclear whether this stems from the diffusion of H_2 into metallic Ni(0) or other adsorption effects.

By applying additional flow variations to the full H_2 dropout scenario, a consecutive reaction mechanism via CO could be identified as the main reaction pathway for the methanation of CO_2 in presence of the Ni@C catalyst. Moreover, the spike in the CH_4 production rate after the initial full H_2 dropouts could be explained by an increase in the active catalyst surface by partial consumption of the carbon shell. Vice versa, the shift in the product selectivity from CH_4 to CO with proceeding deactivation was based on a decrease in the active catalyst surface by sintering. Since this deactivation could also be simulated by flow variations, the ratio of the active catalyst surface and the gas flow was identified to be decisive for the catalyst performance. Additionally, the Ni@C catalyst followed a structure-insensitive reaction pathway during the complete sintering process in the full H_2 dropout scenario.

Considering harsher conditions like increased quantities of oxygen traces in non-purified CO_2 in industrial plants, the consumption of the carbon shell instead of a possible catalyst deactivation under dropout conditions might be beneficial for long-term operation in real industrial applications. However, the protective carbon shell should be combined with a stable support to prevent the sintering of Ni nanoparticles after the carbon shell has worked off.

Experimental Section

Catalysts preparation

The Ni@C catalyst was prepared according to a previously reported method by decomposition of a Ni(BDC)(PNO) MOF at 400 °C in 10% H_2/He atmosphere.[16]

Catalytic tests with dropout scenarios

The principal sequences of the reaction cycles are shown in Scheme 1. First, the temperature is raised to 350 °C and is referred to as 'heating to activation' in the following sections. As soon as the temperature is reached, activation is used as the description. Then the setup is put under a helium atmosphere whilst it is cooling down and rests at 250 °C for 30 minutes before it is heated up again in a helium atmosphere. The catalysis section is the part where the variation of the different dropout scenarios takes place. From left to right in Scheme 1, the full H_2 dropout (FD), the partial H_2 dropout (PD), and finally the stoichiometric dropout (SD) are presented with the respective dynamic gas feed during methanation (m1-5) and dropouts (d1-4). In the full H_2 dropout, hydrogen is completely switched off during the dropout simulation. The 20% partial gas atmosphere of CO_2 is still present. During the partial H_2 dropout (PD) scenario, the hydrogen concentration is reduced by a factor of two, which corresponds to milder deactivation conditions compared to full H_2 dropouts. In the third, stoichiometric dropout (SD) scenario, H_2 and CO_2 are both reduced to 50% of the initial value to keep the H_2/CO_2 ratio of 4:1 constant. During the dropouts, a constant gas stream is ensured by helium balancing. The concentration of helium in the gas feed is not shown in Scheme 1, where only the hydrogen and carbon dioxide contents are provided.

Characterization methods

Dynamic CO_2 hydrogenation studies

For the CO_2 hydrogenation studies, 40 mg of the Ni@C pre-catalyst was diluted with 160 mg SiC in a stainless-steel u-tube reactor coated with Silconert2000 and activated at 350 °C for 2 h with 2 $Kmin^{-1}$ in an H_2 atmosphere to generate the active methanation catalyst. Subsequently, the catalyst was heated to the reaction temperature of 425 °C in an N_2 atmosphere. The CO_2 hydrogenation was then performed with 60 $mLmin^{-1}$ of stoichiometric gas composition of CO_2/H_2 = 1:4 and 6 $mLmin^{-1}$ N_2. For the dropout scenarios, the gas feeds of H_2 and CO_2 were adjusted according to Scheme 1 and the total gas flow was held constant at 66 $mLmin^{-1}$ by balancing with He. The total product gas flow was measured to exclude effects resulting from volume changes due to the reaction stoichiometry. Since changes in the product gas composition need to be measured in a reasonable time, the products were analyzed using an X-STREAM Enhanced XEGP from Emerson with three IR detector channels for CO_2, CH_4, and CO as well as a TCD detector for H_2 for quantitative analysis. To prevent the condensation of water within the analyzer, a Peltier sample gas cooler TC-MINI 61111 from Buehler

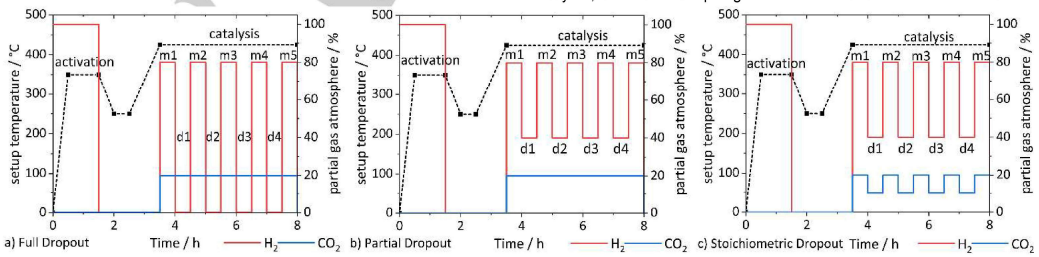

Scheme 1. Scheme of the dynamic catalytic reaction to simulate three dropout scenarios. From left to right: a) Full H_2 dropout, b) partial H_2 dropout, c) stoichiometric dropout. The difference of the gas atmosphere of hydrogen and carbon dioxide to 100% is filled up by helium.

Technologies was used to cool the products to 5 °C. Additionally, a ThermoStar quadrupole mass spectrometer (QMS) from Pfeiffer was used to identify possible side products. Note that very careful data treatment and evaluation are necessary when absolute values of different measurements and detection methods should be compared.

X-ray absorption spectroscopy

X-ray absorption experiments at the Ni K-edge (8333 eV) were carried out at PETRA III beamline P65 at DESY in Hamburg (Germany). The PETRA III storage ring at DESY operates at 6 GeV particle energy with a current of 120 mA in top-up mode keeping the current stable at 1%. Measurements have been carried out in fluorescence mode using a Ni foil for calibration of the beam with the first inflection point of Ni K edge at 8333 eV. For beamline P65, an 11-period mini-undulator is the photon source and the incident energy is selected using a water-cooled Si (111) double crystal monochromator with a beam size of 1.0 × 0.2 mm beam spot size. The performed *in-situ* experiments were carried out using quartz capillaries (WJM Glas, Berlin, Germany) of 1.5 mm diameter. The sample for full H_2 dropout simulation was diluted with SiC. A hot-air blower provided by the beamline was used for sample heating. A custom-built gas dosing system of mass flow controllers (Bronkhorst) was used to control the gas flow with an overall gas flow of 20 - 25 mLmin^{-1} while using a catalyst amount of 7-10 mg catalyst. Simultaneously, an online gas analysis was performed with a HIDEN mass spectrometer provided by beamline. Data analysis is explained in the supplementary information.

Powder X-ray diffraction

Powder X-ray diffraction (PXRD) was carried out at room temperature with an STOE STADI P Mythen2 4K diffractometer (Ge(111) monochromator; Ag $K\alpha_1$ radiation, λ = 0.5594 Å) using four Dectris MYTHEN2 R 1K detectors in Debye–Scherrer geometry, suited for PDF analysis.[22] Samples were measured in 1 mm diameter Kapton capillaries for 12 h. The Q-range was 0.4 – 20.4 Å^{-1}.

Synchrotron X-ray total scattering experiments

Synchrotron total scattering data were acquired at the P02.1 beamline at the DESY facility PETRA III in Hamburg with an X-ray energy of 59.7 keV (λ = 0.2075 Å). At the beamline, all experiments were carried out in a quartz capillary reactor (outer diameter 1.2 mm, wall thickness 0.05 mm) with a ceramic oven for heating. A custom-built gas dosing system of mass flow controllers (Bronkhorst) was used to control the gas flow with an overall gas flow of 20 - 25 mLmin^{-1} while using a catalyst amount of 7-10 mg. Online gas analysis was performed with a ThermoStar quadrupole mass spectrometer (QMS) from Pfeiffer. Data was measured continuously with 10 seconds for each detector image. The PXRD patterns were collected using a Pilatus CdTe 2M detector over a Q-range of 0.5 – 22.4 Å^{-1}. Radial integration was done with the software xpdtools,[23] PDF calculations with PDFgetX3[24] and PDF modeling with DiffPy-CMI.[25] For measurement and processing details see the Supporting Information.

Transmission electron microscopy

Transmission electron microscopy images were collected using a JEOL JEM-2200FS equipped with a Schottky field-emission gun operated at 200 kV and a magnetic in-column omega-type energy filter. Images were acquired using a GatanOneView imaging filter with a CMOS camera. Samples were prepared by dripping a dispersion of the sample in trichloromethane after sonication on a lacey carbon film coated on a copper grid (Electron Microscopy Science). For the determination of particle sizes, about 300 particles were counted for each sample.

Author contributions

L.R. synthesized the samples and did the catalytic tests. N.P. conducted the PXRD, TEM and PDF study of the spent catalysts, as well as the in-situ PXRD and PDF study. S.S conducted the in-situ XAS study. C.W. helped with the analysis of the catalytic data. A.S. provided essential support during beamtime and experimental setup during Covid-19 restricted beamtime access times. P.M assisted with the measurements of *in-situ* XAS beamtime. M.N. provided scientific input for the XAS analysis. M.B., M.Z. and W.K. conceptually laid out and led the project. All authors contributed to data analysis and discussion. N.P., L.R., S.S. wrote the original manuscript, A.S., M.N., M.Z., M.B. and W.K. revised it.

Concflict of interests

There are no conflicts to declare.

Acknowledgements

We acknowledge funding by the Deutsche Forschungsgemeinschaft (DFG, German Research Foundation) in frame of the priority program SPP2080 (BA 4467/8-1 and BA 4467/8-2, KL 2913/1-1 and KL 2913/1-2, ZO 369/2-1 and ZO 369/2-2). We thank Marco Schwarzmann for TEM support and the Bavarian Polymer Institute (BPI) for access to the keylab Electron and Optical Microscopy. We acknowledge DESY (Hamburg, Germany), a member of the Helmholtz Association HGF, for the provision of experimental facilities. Parts of this research were carried out at PETRA III using beamlines P65 and P02.1. Beamtime was allocated for the proposals H-20010169 and I-20200212.

Keywords: CO_2 methanation • Power-to-X • Dynamic operation conditions • X-ray absorption spectroscopy • Pair distribution function

References

[1] G. Centi, S. Perathoner, *Greenhouse Gases: Sci. Technol.* **2011**, *1*, 21–35.
[2] S. Rönsch, J. Schneider, S. Matthischke, M. Schlüter, M. Götz, J. Lefebvre, P. Prabhakaran, S. Bajohr, *Fuel* **2016**, *166*, 276–296.
[3] P. Sabatier, J. B. Senderens, *J. Chem. Soc., Abstr.* **1902**, *82*, A333.
[4] G. A. Mills, F. W. Steffgen, *Catal. Rev.: Sci. Eng.* **1974**, *8*, 159–210.
[5] C. Vogt, E. Groeneveld, G. Kamsma, M. Nachtegaal, L. Lu, C. J. Kiely, P. H. Berben, F. Meirer, B. M. Weckhuysen, *Nat. Catal.* **2018**, *1*, 127–134.
[6] G. Garbarino, P. Riani, L. Magistri, G. Busca, *Int. J. Hydrogen Energy* **2014**, *39*, 11557–11565.
[7] P. Frontera, A. Macario, M. Ferraro, P. Antonucci, *Catalysts* **2017**, *7*, 59.
[8] K. F. Kalz, R. Kraehnert, M. Dvoyashkin, R. Dittmeyer, R. Gläser, U. Krewer, K. Reuter, J.-D. Grunwaldt, *ChemCatChem* **2017**, *9*, 17–29.
[9] K. Ghaib, F.-Z. Ben-Fares, *Renewable Sustainable Energy Rev.* **2018**, *81*, 433–446.
[10] B. Mutz, A. Gänzler, M. Nachtegaal, O. Müller, R. Frahm, W. Kleist, J.-D. Grunwaldt, *Catalysts* **2017**, *7*, 279.
[11] M.-A. Serrer, K. F. Kalz, E. Saraçi, H. Lichtenberg, J.-D. Grunwaldt, *ChemCatChem* **2019**, *11*, 5018–5021.
[12] B. Mutz, P. Sprenger, W. Wang, Di Wang, W. Kleist, J.-D. Grunwaldt, *Appl. Catal., A* **2018**, *556*, 160–171.
[13] K. J. Lee, J. H. Lee, S. Jeoung, H. R. Moon, *Acc. Chem. Res.* **2017**, *50*, 2684–2692.
[14] L. Oar-Arteta, T. Wezendonk, X. Sun, F. Kapteijn, J. Gascon, *Mater. Chem. Front.* **2017**, *1*, 1709–1745.
[15] J. Bitzer, W. Kleist, *Chemistry* **2019**, *25*, 1866–1882.

[16] N. Prinz, L. Schwensow, S. Wendholt, A. Jentys, M. Bauer, W. Kleist, M. Zobel, *Nanoscale* **2020**, *12*, 15800–15813.
[17] N. M. Martin et al., *Catal. Sci. Technol.* **2018**, *8*, 2686–2696.
[18] C. Nayak, P. Jain, C. P. Vinod, S. N. Jha, D. Bhattacharyya, *J. Synchrotron Radiat.* **2019**, *26*, 137–144.
[19] M. Bauer, C. Gastl, *Phys. Chem. Chem. Phys.* **2010**, *12*, 5575.
[20] M. Newton, *Catalysts* **2017**, *7*, 58.
[21] B. Kreitz, G. D. Wehinger, T. Turek, *Chem. Eng. Sci.* **2019**, *195*, 541–552.
[22] S. L. J. Thomae, N. Prinz, T. Hartmann, M. Teck, S. Correll, M. Zobel, *Rev. Sci. Instrum.* **2019**, *90*, 43905.
[23] C. J. Wright, X. D. Zhou, *J. Synchrotron Radiat.* **2017**, *24*, 506–508.
[24] P. Juhás, T. Davis, C. L. Farrow, S. J. L. Billinge, *J. Appl. Crystallogr.* **2013**, *46*, 560–566.
[25] P. Juhás, C. L. Farrow, X. Yang, K. R. Knox, S. J. L. Billinge, *Acta Crystallogr., Sect. A: Found. Adv.* **2015**, *71*, 562–568.
[26] J. Beyer, N. Roth, B. Brummerstedt Iversen, *Acta Crystallogr., Sect. A: Found. Adv.* **2022**, *78*, 10–20.
[27] S. Weber et al., *ChemCatChem* **2022**, *14*.
[28] D. S. Lee, D. J. Min, *Met. Mater. Int.* **2019**, *25*, 982–990.
[29] Y. Lei et al., *J. Am. Chem. Soc.* **2014**, *136*, 9320–9326.
[30] M. Shirazi, A. Bogaerts, E. C. Neyts, *Phys. Chem. Chem. Phys.* **2017**, *19*, 19150–19158.
[31] M. Bauer, H. Bertagnolli in *Methods in Physical Chemistry*. 2nd ed. ed. (Eds.: R. Schäfer, P. C. Schmidt), Wiley-VCH, Weinheim, **2012**.
[32] R. P.W.J. Struis, T. J. Schildhauer, I. Czekaj, M. Janousch, S. M.A. Biollaz, C. Ludwig, *Appl. Catal., A* **2009**, *362*, 121–128.
[33] E. Keceli et al., *Microporous Mesoporous Mater.* **2014**, *194*, 115–125.
[34] S. Schuster, E. Klemm, M. Bauer, *Chemistry* **2012**, *18*, 15831–15837.
[35] M. A. Gotthardt, R. Schoch, T. S. Brunner, M. Bauer, W. Kleist, *ChemPlusChem* **2015**, *80*, 188–195.
[36] M. A. Gotthardt, R. Schoch, S. Wolf, M. Bauer, W. Kleist, *Dalton Trans.* **2015**, *44*, 2052–2056.
[37] A. Jentys, *Phys. Chem. Chem. Phys.* **1999**, *1*, 4059–4063.
[38] A. I. Frenkel, C. W. Hills, R. G. Nuzzo, *J. Phys. Chem. B* **2001**, *105*, 12689–12703.
[39] A. Anspoks, A. Kalinko, R. Kalendarev, A. Kuzmin, *Phys. Rev. B* **2012**, *86*.
[40] A. Anspoks, A. Kuzmin, A. Kalinko, J. Timoshenko, *Solid State Commun.* **2010**, *150*, 2270–2274.
[41] D. Beierlein, D. Häussermann, M. Pfeifer, T. Schwarz, K. Stöwe, Y. Traa, E. Klemm, *Appl. Catal., B* **2019**, *247*, 200–219.

Supplementary Information

Investigation of MOF-derived Ni@C catalysts in the methanation of CO_2 under dynamic gas feed conditions using *in-situ* XAS and PDF

Leif Rohrbach[a],#, Sven Strübbe[b],#, Nils Prinz[c],#, Christian Wilhelm[a], Patrick Müller[b], Michal Nowakowski[b], Alexander Schökel[d], Mirijam Zobel*[c], Matthias Bauer*[b], Wolfgang Kleist*[a]

[a] *L. Rohrbach, Dr. C. Wilhelm, Prof. Dr. W. Kleist*
Department of Chemistry
RPTU Kaiserslautern-Landau
67663 Kaiserslautern (Germany)
E-mail: wolfgang.kleist@rptu.de
[b] *S. Strübbe, Dr. P. Müller, Dr. M. Nowakowski, Prof. Dr. M. Bauer*
Department of Chemistry and Center for Sustainable Systems Design
Paderborn University
33098 Paderborn (Germany)
E-mail: bauerm@mail.uni-paderborn.de
[c] *N. Prinz, Prof. Dr. M. Zobel*
Institute of Crystallography
RWTH Aachen University
52066 Aachen (Germany)
E-mail: zobel@ifk.rwth-aachen.de
[d] *Dr. A. Schökel*
Deutsches Elektronen Synchrotron DESY
22607 Hamburg (Germany)

Table of contents

General methods and approaches

XAS Analysis

The XANES analysis and the data preparation have been carried out with the program Athena of the demeter program package.[1] For data evaluation, the spectra background has to be removed in the first instance and, therefore, a Victoreen-type polynomial was subtracted.[1–4] The first inflection point was taken as energy $E_{(0)}$. To determine the smooth part of the spectrum, a piecewise polynomial was used. It was adjusted in a way to minimize the low-R components of the resulting Fourier transform. Afterward, the background-subtracted spectrum was divided by its smoothed part and the photon energy was converted to photoelectron wave number *k*. For the detailed EXAFS analysis, the resulting functions were weighted with k^3 and calculated with EXCURVE98, which works based on the EXAFS function and according to a formulation in terms of radial distribution functions:[2,5]

$$\chi(k) = \sum_j S_0^2(K) F_j(k) \int P_j(r_j) \frac{e^{\frac{-2r_j}{\lambda}}}{k r_j^2} \sin\left[2kr_j + \delta_j(k)\right] \mathrm{d}r_j$$

The number of independent points N_{ind} was calculated according to information theory to determine the degree of overdeterminacy:[5]

$$N_{ind} = \frac{2\Delta k \Delta R}{\pi}$$

In this formula, Δk describes the range in *k*-space used for the data analysis and in ΔR the corresponding radial distance range in the Fourier filtering process is observable. For Δk the area from 3 to 14 in k-space has been used for analysis, leading to Δk of 11. In the R-space 1 to 6 was used, leading to ΔR of 5. So the number of independent parameters is 35, according to the given equation.
For the determination of the quality of the fit, two methods were used. The reduced χ^2_{red} considers the degree of overdeterminacy of the system and the number of fitted parameters p. This leads to the possibility to compare different models directly:[6]

$$\chi^2_{red} = \frac{\left(\frac{N_{ind}}{N}\right)}{N_{ind-p}} \sum_i \left(\frac{k_i^n}{\Sigma_j k_j^n \left| \chi_j^{\exp}(k_j) \right|} \right)^2 \left[\chi^{exp}(k_j) - \chi^{theo}(k_j) \right]^2$$

With the R-factor, the percentage disagreement between the experiment and the adjusted function is shown. Thereby, it considers both systematic and random errors.[6]

PDF refinement procedures

The refinements were done with *DiffPy-CMI*, a python-based complex modelling software.[7] The instrumental contributions Q_{damp} and Q_{broad} to the PDF were determined by the refinement of these parameters in a LaB_6 standard measurement. For the measurements carried out on the STOE STADI P Mythen 2 4K Q_{damp} was 0.011 and Q_{broad} was 0.010. For the measurements carried out at beamline P02.1 at DESY Q_{damp} was 0.026 and Q_{broad} was 0.000. A Ni fcc crystallographic information file was used as the theoretical model for single-phase fits, and NiO was used additionally for two-phase fits. During the least squares refinements, we refined the lattice parameters *a* for the cubic cell the atomic thermal motion parameter B_{iso_j}, the correlated motion of nearest neighbors δ_2,[8] the spherical crystallite diameter (based on an isotropic attenuated crystal model) and a scale factor.
The shape function to describe the domain size dampening effect on the PDF was:

$$sphericalCF(r, psize) = 1 - \frac{\frac{3}{2}r + \frac{1}{2}r^3}{psize}$$

The goodness of fit is described by the least square residual R_w:

$$R_w = \sqrt{\frac{\sum_n (G_{obs,n} - G_{calc,n})^2}{\sum_n G_{obs,n}^2}}$$

In situ measurements were refined using a python based serial approach. The first PDF is refined until no larger Rw change than 0.001 appears. The results are written into the start parameter of the next refinement and the procedure is repeated until the end of the dataset (up to 1000 datasets were refined).

Powder X-ray diffraction (PXRD)

Powder X-ray diffraction was carried out at room temperature with a STOE STADI P Mythen2 4K diffractometer (Ge(111) monochromator; Ag Kα1 radiation, λ = 0.5594 Å) using four Dectris MYTHEN2 R 1K detector in Debye–Scherrer geometry. Samples were measured in 1 mm diameter Borosilicate glass capillaries for 12 h. The Q-range was 20.4 $Å^{-1}$.

Complementary results to the dynamic catalytic scenarios

In Figure S1, the products of the dynamic scenarios were investigated. a)-d) showed the selectivities for methane and carbon monoxide formation. Ethane as the only identifiable side product was formed in insignificant amounts (compare Figure S1 e) - h)), which can be identified by the full H_2 dropout scenario. Since the quadrupole mass spectrometry (QMS) signals for methane (m/z = 15 (CH_3^+) and m/z =16 (CH_4^+)) correlated with fragments of CO_2 (O^+) and ethane (CH_3^+) only the combined evaluation can lead to a profound analysis of the product formation. The intensities of the QMS signals for methane (m/z = 16 and m/z = 15) were more than 3 orders of magnitude larger than ethane (m/z = 30)

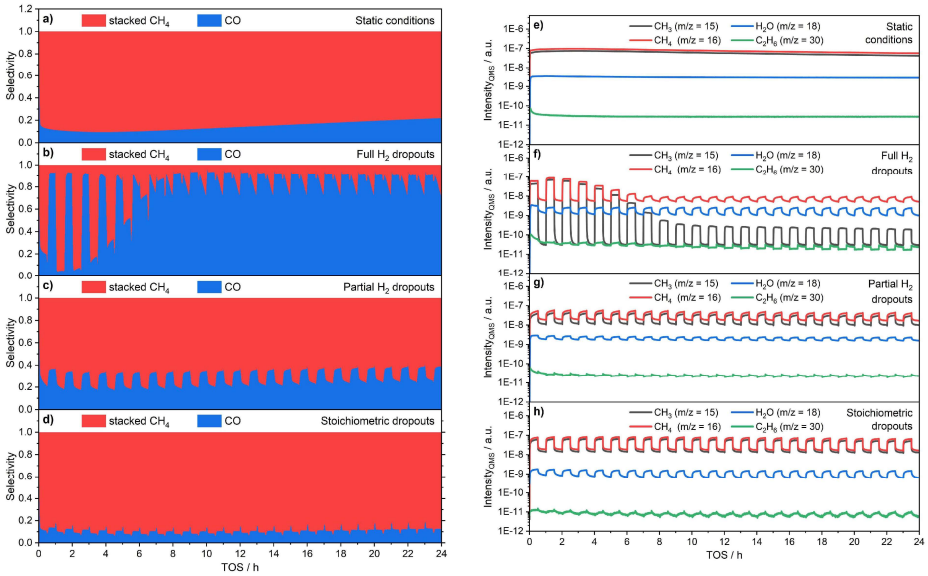

Figure S1: Selectivities (a-d) identified by IR detection and products identified by QMS analysis (e-h) of the different dynamic scenarios. a) and e) Static conditions. b) and f) Full H_2 dropouts. c) and g) Partial H_2 dropout. d) and h) Stoichiometric dropouts. Volume contraction due to the reaction stoichiometry was not accounted in the QMS analysis.

for the catalyst at the highest activity at the beginning. After deactivation in the full H_2 dropout scenario, where no significant conversion of CO_2 was observed (compare main text, Figure 2), the methane signal (m/z = 15) was only 1 order of magnitude larger than for ethane (m/z = 30). Accordingly, ethane was only a minor side product during the dynamic studies. CO could not be evaluated since N_2, which was also present in the gas feed, corresponded to the same mass per charge (m/z = 28).

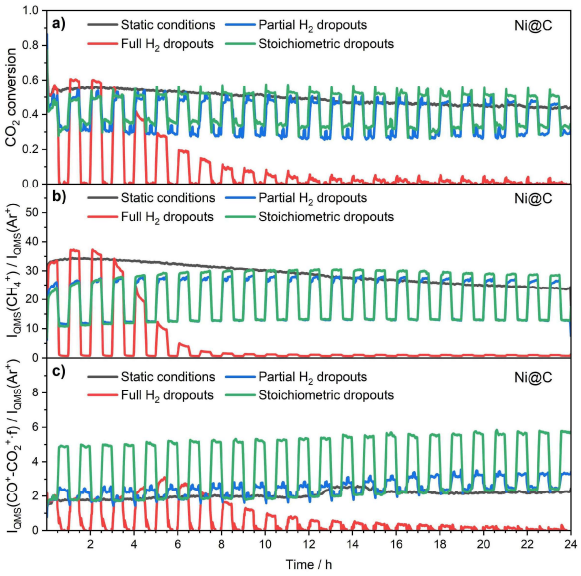

Figure S2: Methanation of CO_2 catalyzed by Ni@C-10%H_2/He during different dynamic operation conditions, switching every 30 min between methanation conditions (H_2/CO_2 = 4/1) and full H_2 dropout conditions (red), partial H_2 dropout conditions (blue) and stoichiometric dropout conditions (green). Black corresponds to methanation conditions without dropouts. a) CO_2 conversions. b) Ratio of the ion currents of m/z = 16 (I_{CH_4}+) / m/z = 40 (I_{Ar}+) and c) ratio of the ion currents of m/z = 28 (I_{CO}+) / m/z = 40 (I_{Ar}+) excluding fragments originating from CO_2. The ion currents are determined by quadrupole mass spectrometry. Volume changes that result from the reaction progress are excluded by normalizing to Ar. The reaction was carried out at 425 °C at 1 atm.

Complementary results to the LFD scenario

The long methanation full H_2 dropout measurement was subdivided into 8 cycle segments to allow a direct comparison of the catalytic performance between the different cycles. For an improved comparison of the activity before and after the dropout, the full H_2 dropout for each cycle was set to 4 h relative TOS. Accordingly, each cycle described a sequence of 4 h under methanation conditions, 0.5 h under full H_2 dropout conditions, and 2.33 h under methanation conditions. At the start of the long methanation full H_2 dropout scenario, the catalyst was held for 8 h under static CO_2 methanation conditions until a stable constant catalytic performance was observed before the first full H_2 dropout was applied. Thus, the segment before the first cycle started consisted of 4 h under standard methanation conditions and was labeled as Reference. All segments of the long methanation full H_2 dropout scenario were shown in Figure S3.

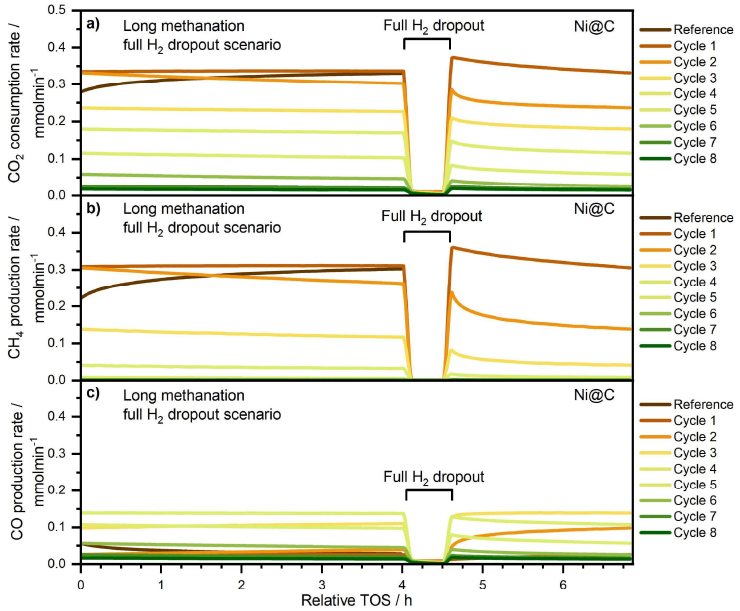

Figure S3: Methanation of CO_2 catalyzed by Ni@C according to the long methanation full H_2 dropout scenario. a) CO_2 consumption rate. b) CH_4 production rate. c) CO production rate. The measurement was subdivided into a reference measurement and 8 dropout cycles. The reference measurement was performed before the dropout cycles. During each cycle (Cycle 1-8), a full H_2 dropout was applied after 4 h relative to the start of the cycle (0 h). The catalytic activity was tested again under methanation condition afterward. In total, the catalytic activity was studied for 380 min between each dropout under constant CO_2 methanation conditions. 40 mg catalyst were diluted with 160 mg SiC. Reaction temperature: 425 °C.

Complementary results to the TFFD scenario

To analyze the influence of the residence time on the CO_2 conversion and product selectivity, a (temperature-) and flow-controlled full H_2 dropout (TFFD) scenario was developed. The temperature variations, which were applied for kinetic investigation, are not part of this work and only data points taken at a reaction temperature of 425 °C were considered in the evaluation. However, to fully understand the applied conditions and the catalyst state, the complete scenario was schematically shown in Figure S4 a)-c). The catalyst was tested at 325 °C, 350 °C, 375 °C, 400 °C and 425 °C and the residence time varied by controlling the total gas feeds (180 $mLmin^{-1}$, 140 $mLmin^{-1}$, 100 $mLmin^{-1}$ and 60 $mLmin^{-1}$) at a constant gas ratio ($N_2/H_2/CO_2$ = 10/4/1). Additionally, the methanation conditions, which were studied in the other scenarios, were also applied and were marked as standard methanation conditions (66 $mLmin^{-1}$ $N_2/H_2/CO_2$ = 0.5/4/1). During the flow series in the TFFD scenario, a different fraction of N_2 was used in the gas feed compared to standard methanation conditions to cover the widest possible

range of flow variations at a constant gas ratio while keeping a certain amount of total gas flow, which was necessary to minimize the error of the analytic setup.
For the development of Figure S6, only the data points at 425 °C were extracted from Figure S5 and compared between the different sections prior to the dropouts. The other data points cannot be compared with the full H_2 dropout scenario or the long methanation full H_2 dropout scenario since the reaction temperature was different.

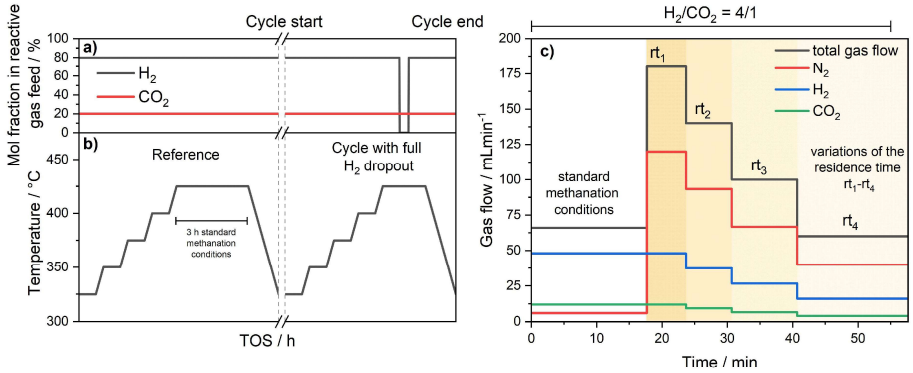

Figure S4**:** Schematic gas feeds and applied temperatures in the temperature- and flow-controlled full H_2 dropout scenario. **a)** Schematic gas feeds. **b)** Reaction temperatures. **c)** Gas flow variations in the gas feed, which were applied at each temperature step in **b)**. Additionally, the flow series in **c)** was applied directly after the full H_2 dropout (compare **a)**) The scenario can be divided into 9 sections: 1 reference study and 8 cycles. In each catalytic section, the temperature was varied between at 325 °C, 350 °C, 375 °C, 400 °C and 425 °C. The reference studies were performed before the cycles. During the reference measurement, the catalyst was held for 3 h under standard methanation conditions to address initial changes in the catalyst. In the 8 cycle loops, which started with the "cycle start" and ended with the "cycle end", a full H_2 dropout (30 min) and another flow series (c)) was performed at 425 °C subsequently to the temperature series.

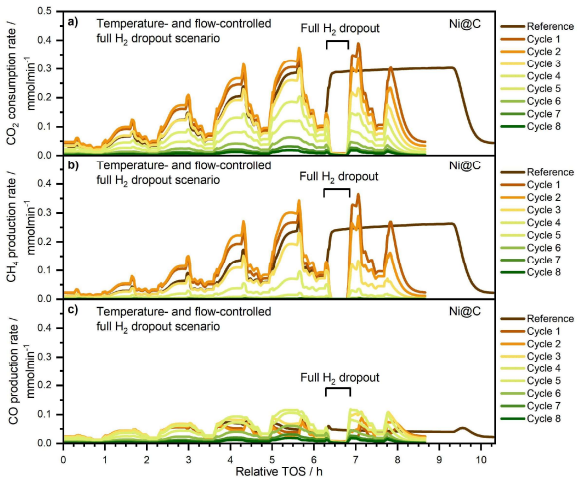

Figure S5: Methanation of CO_2 catalyzed by Ni@C according to the temperature- and flow-controlled methanation full H_2 dropout scenario. a) CO_2 consumption rate. b) CH_4 production rate. c) CO production rate. The measurement was subdivided into a reference measurement and 8 dropout cycles. The reference measurement was performed before the dropout cycles. During each cycle (Cycle 1-8), a full H_2 dropout was applied after 6.33 h relative to the start of the cycle (0 h). The catalytic activity was tested again under methanation condition afterward. In total, the catalytic activity was studied for 8.17 h between each dropout at varying temperatures and flow conditions. 40 mg catalyst were diluted with 160 mg SiC. Reaction temperature: 425 °C.

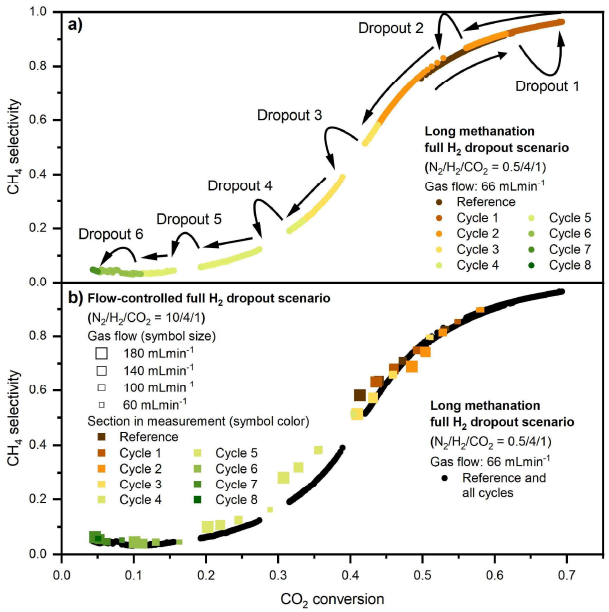

Figure S6: CH_4 selectivity plotted over the CO_2 conversion. Data points corresponding to the dropout conditions and the gas switching process are omitted for increased visibility. Data points at low CO_2 conversions (< 4%) are omitted due to increasing inaccuracy of the measurement. a) Long methanation full H_2 dropout scenario. The black arrows indicate the temporal chronology of the data points. The dropout labels correspond to the appropriate cycle number. b) CH_4 selectivities of the temperature- and flow-controlled FD scenario with for 60 $mLmin^{-1}$, 100 $mLmin^{-1}$, 140 $mLmin^{-1}$ and 180 $mLmin^{-1}$ ($N_2/H_2/CO_2$ = 10/4/1). 425 °. For improved comparison, the data from the long methanation FD scenario (a)) are shown in black (66 $mLmin^{-1}$ with $N_2/H_2/CO_2$ = 0.5/4/1). Both scenarios were subdivided into a reference measurement and 8 dropout cycles as described above. 40 mg catalyst were diluted with 160 mg SiC. Reaction temperature: 425 °C.

Catalytic studies with GC and quadrupole mass spectrum

The validation of the transferability for catalytic results from previous studies with a gas chromatography set-up[9] to this new multichannel IR set-up was covered by measuring the conversions and yields under static conditions for the same catalysts with both set-ups in combination with the same QMS system. The gas chromatography system consisted of a GC-2010 system from Shimadzu with a thermal conductivity detector and two flame ionization detectors. The products were separated with the help of a CP-Al_2O_3/KCl capillary, a PoraPLOT Q capillary, and a MolSieve 5Å. To evaluate the CO_2 conversion, the CH_4 and the CO production from the QMS signal, the ion currents of m/z = 44 u·e^{-1} ($I_{CO_2^+}$), m/z = 16 u·e^{-1} ($I_{CH_4^+}$) and m/z = 28 u·e^{-1} (I_{CO^+}) were, respectively, normalized to m/z = 40 u·e^{-1} (I_{Ar^+}) to exclude volume changes. The CO_2 conversion was calculated according to equation 4.

$$\mathrm{CO_2\ conversion} = \frac{\frac{I_{CO_2^+,0}}{I_{Ar^+,0}} - \frac{I_{CO_2^+}}{I_{Ar^+}}}{\frac{I_{CO_2^+,0}}{I_{Ar^+,0}}} \tag{4}$$

For the determination of the ion current I_{CO} that truly results from the formation of CO *via* the hydrogenation of CO_2, the contribution of m/z = 28 ion fragments that originate from the defragmentation of CO_2 needed to be excluded. This issue has been addressed by using equations 5 and 6.

$$I_{CO} = I_{CO^+} - I_{CO_2^+} \cdot f_1 \qquad \text{with} \quad f_1 = \frac{I_{CO^+,0}}{I_{CO_2^+,0}} \tag{5}$$

$$\leftrightarrow \qquad I_{CO} = \left(\frac{I_{CO^+}}{I_{CO^+,0}} - \frac{I_{CO_2^+}}{I_{CO_2^+,0}}\right) \cdot I_{CO^+,0} \tag{6}$$

$I_{CO^+,0}$ and $I_{CO_2^+,0}$ correspond to the ion currents that are measured under methanation conditions without any CO_2 conversion. Although the analysis with QMS could only be used for a semi-quantitative evaluation, the same scale and trend for the catalytic activity was observed for the set-up with the GC and the set-up with the multichannel IR, where water was removed from the product stream by a cold trap. The analysis of the QMS signals for catalysis under static conditions, the full H_2 dropout scenario, the stoichiometric dropout scenario, and the partial H_2 dropout scenario was in good accordance with the results from the more gas chromatography set-up and the multichannel IR set-up (compare Figure S2). Accordingly, the transferability of the catalytic results from our previous study could be validated.[9] Note that a quantitative comparison of the I_{CO} between the different scenarios could not be achieved since even slight deviations in the $I_{CO_2^+}$ signal influenced the absolute values of I_{CO} significantly. In particular for the stoichiometric scenario, where the CO_2 feed was reduced during a dropout, the absolute I_{CO} values became unreliable. However, the comparison of the activities under the same conditions within the same scenario was possible.

Material characterization and analysis

TEM analysis of the spent catalysts

Transmission electron microscopy images were collected using a JEOL JEM-2200FS equipped with Schottky field-emission gun operated at 200 kV and a magnetic in-column omega type energy filter. Images were acquired using a GatanOneView imaging filter with a CMOS camera. Samples were prepared by dripping a sonicated dispersion of the sample in Chloroforme on a lacey carbon film coated on a copper grid (Electron Microscopy Sciences). For determination of particle sizes, about 300 particles were counted for each sample except after FD, where not enough particles were present to yield a statistically meaningful distribution. A lognormal distribution could be fitted to the histograms.

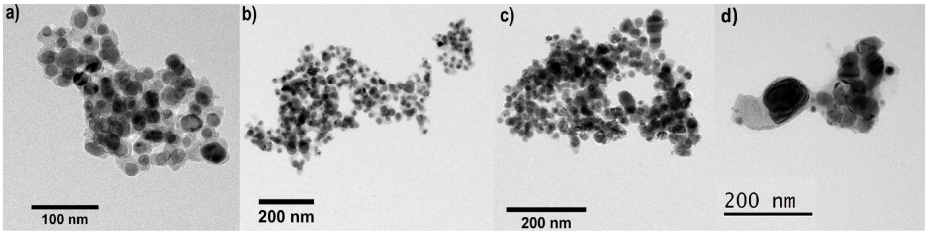

Figure S7: TEM images of a) Ni@C-10%H_2 after ST b) after PD c) after SD and d) after FD.

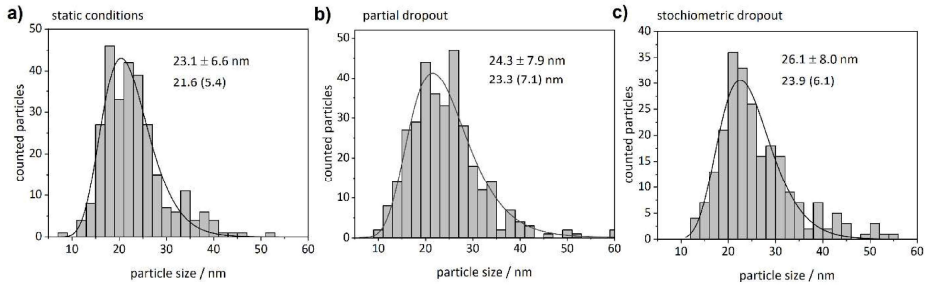

Figure S8: Lognormal particle size distributions for Ni@C-10%H_2. Average particle size ± standard deviation and particle size of the lognormal curve, as well as its width in parantheses.

X-ray total scattering analysis

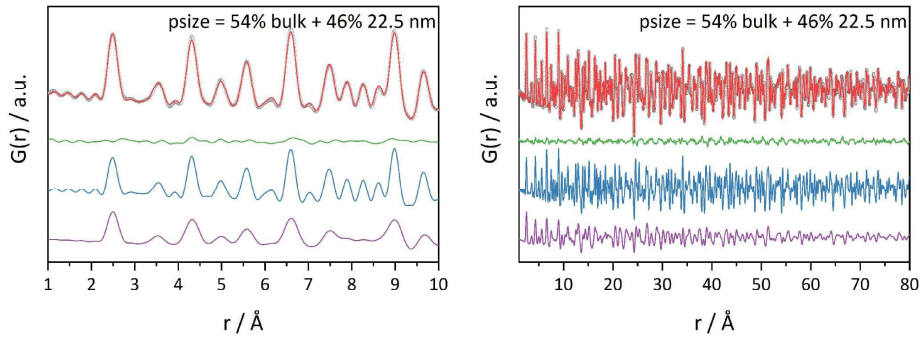

Figure S9: Two phase PDF refinement with a bulk Ni (blue line) and nanoparticle Ni (violet line) phase. The observed PDF (black circles) and the fitted PDF (red line) together with the difference between them (green line) is shown.

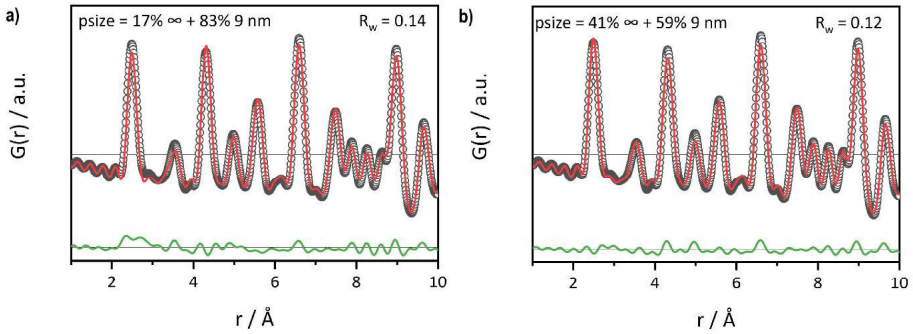

Figure S10 a): PDF refinement of Ni@C-400-10H_2 after PD. Black circles represent the experimental data, the red curve represents the calculated fit and the green curve in offset is the difference between experimental and calculated. b): PDF refinement of Ni@C-400-10H_2 after SD (stoichiometric dropout).

Table S1: Refined parameters of the PDF refinements of the spent catalysts after ST, PD and SD.

Sample	**particle phase**				**bulk phase**			R_w
	Lattice parameter *a* [Å]	displacemenet parameter B_{iso} [Å²]	Domain size [nm]	Correlated motion factor δ_2	Lattice parameter *a* [Å]	displacemenet parameter B_{iso} [Å²]	Correlated motion factor δ_2	
ST	3.531	1.2	22	0.9	3.524	0.3	3.3	0.12
PD	3.527	0.9	9	1.6	3.524	0.3	3.9	0.14
SD	3.533	1.2	9	3.0	3.525	0.4	2.5	0.12

***In-situ* XRD and PDF experiments**

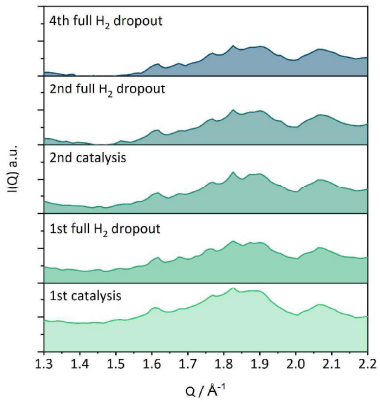

Figure S11: PXRD patterns of Ni@C FD showcasing the slow decay of the carbon signal.

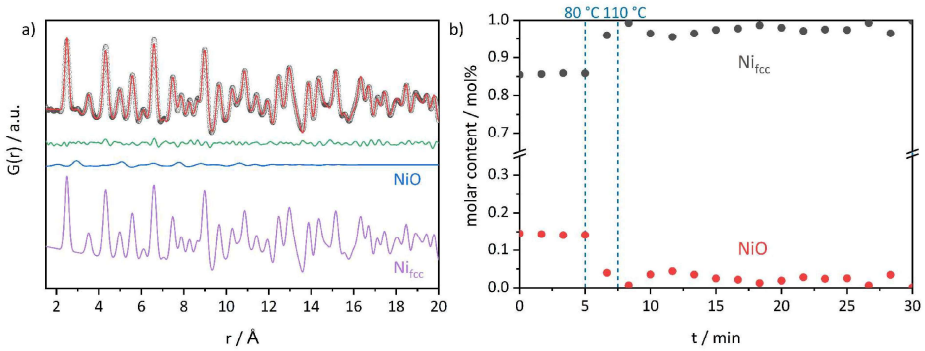

Figure S12: a) Two phase refinement of the precatalyst, with measured (black circles), calculate (red line), difference (green line), NiO phase (blue line) and Ni_{fcc} phase (violet line). b) calculated molar content from the two phase refinements during the heating to activation. The major reduction takes place between 80 and 110 °C.

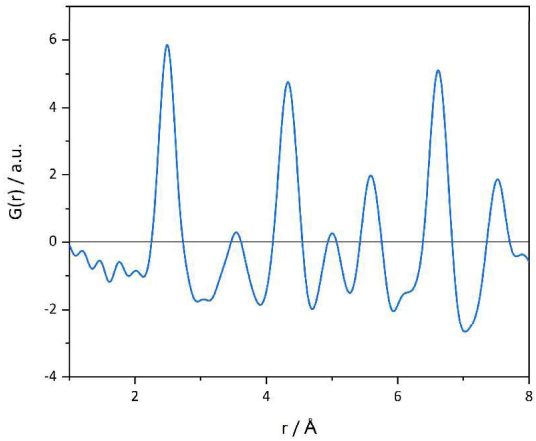

Figure S13: Exemplary PDF during the *in-situ* dynamic catalysis after four cycles of catalysis and four FD. No Ni-O distance (expected at ca. 2.0 Å) is visible.

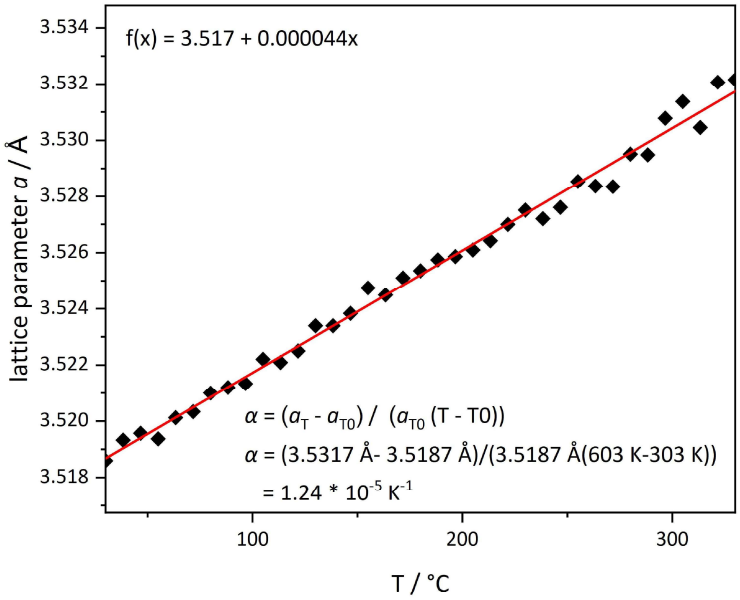

Figure S14: Linear regression from the refined lattice parameters during heat ramp of 5 K/min from 30-330 °C

EXAFS Analysis

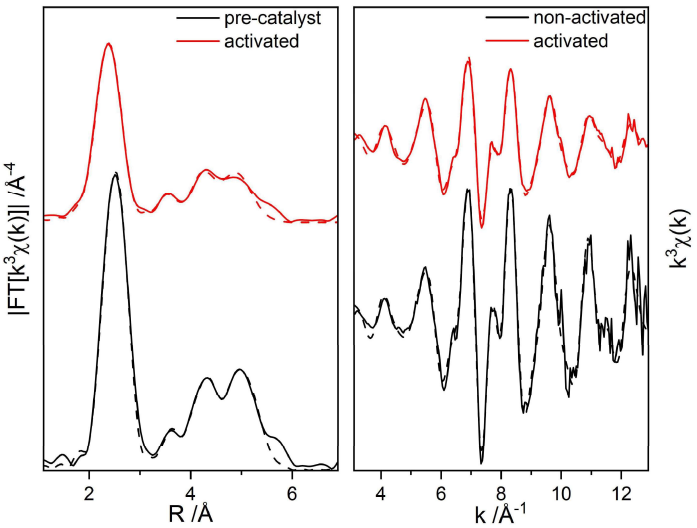

Figure S15: EXAFS spectra of the Full Dropout (FD) scenario. On the left side Fourier-transformed experimental k3χ(k) EXAFS functions are shown. On the right side Experimental $k^3\chi(k)$ EXAFS functions are shown. The solid line shows the experimental spectra, the dotted line shows the theoretical fit of the EXAFS analysis.

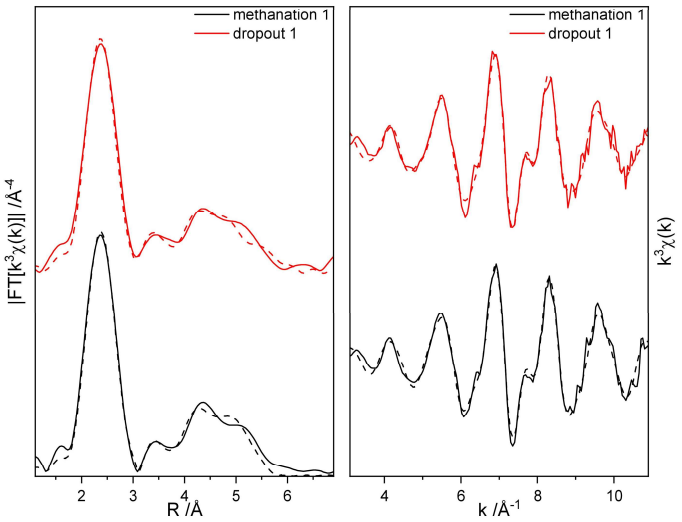

Figure S16: EXAFS spectra of the Full Dropout (FD) scenario. On the left side Fourier-transformed experimental k3χ(k) EXAFS functions are shown. On the right side Experimental $k^3\chi(k)$ EXAFS functions are shown. The solid line shows the experimental spectra, the dotted line shows the theoretical fit of the EXAFS analysis.

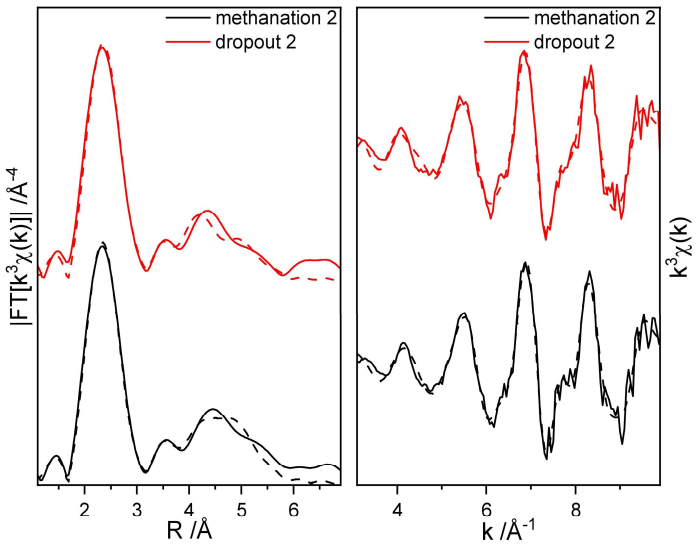

Figure S17: EXAFS spectra of the Full Dropout (FD) scenario. On the left side Fourier-transformed experimental k3χ(k) EXAFS functions are shown. On the right side Experimental $k^3\chi(k)$ EXAFS functions are shown. The solid line shows the experimental spectra, the dotted line shows the theoretical fit of the EXAFS analysis.

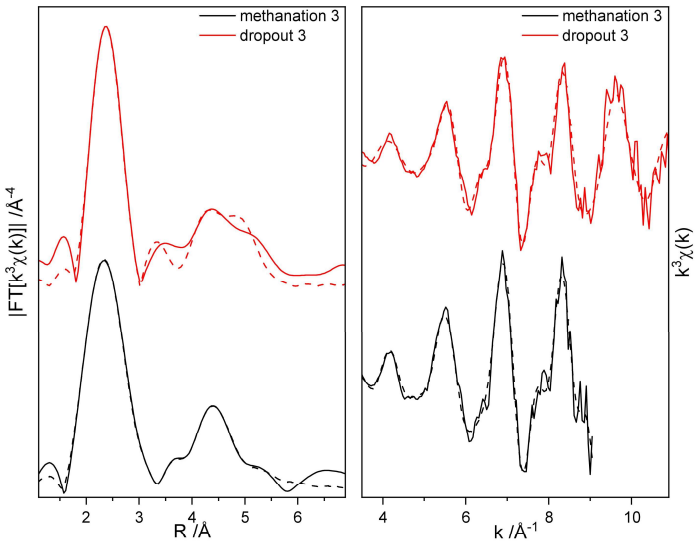

Figure S18: EXAFS spectra of the Full Dropout (FD) scenario. On the left side Fourier-transformed experimental k3χ(k) EXAFS functions are shown. On the right side Experimental $k^3\chi(k)$ EXAFS functions are shown. The solid line shows the experimental spectra, the dotted line shows the theoretical fit of the EXAFS analysis.

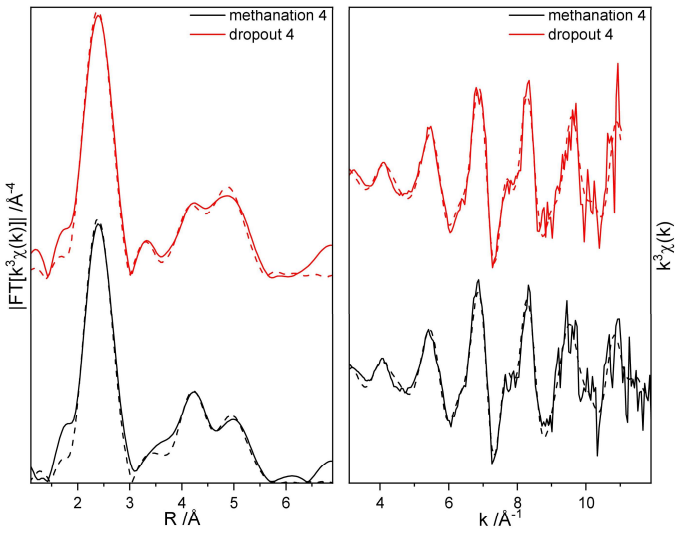

Figure S19: EXAFS spectra of the Full Dropout (FD) scenario. On the left side Fourier-transformed experimental k3χ(k) EXAFS functions are shown. On the right side Experimental $k^3\chi(k)$ EXAFS functions are shown. The solid line shows the experimental spectra, the dotted line shows the theoretical fit of the EXAFS analysis.

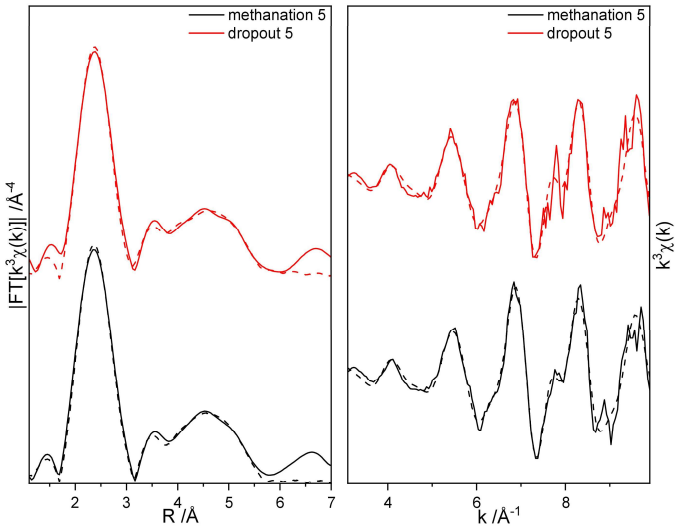

Figure S20: EXAFS spectra of the Full Dropout (FD) scenario. On the left side Fourier-transformed experimental k3χ(k) EXAFS functions are shown. On the right side Experimental $k^3\chi(k)$ EXAFS functions are shown. The solid line shows the experimental spectra, the dotted line shows the theoretical fit of the EXAFS analysis.

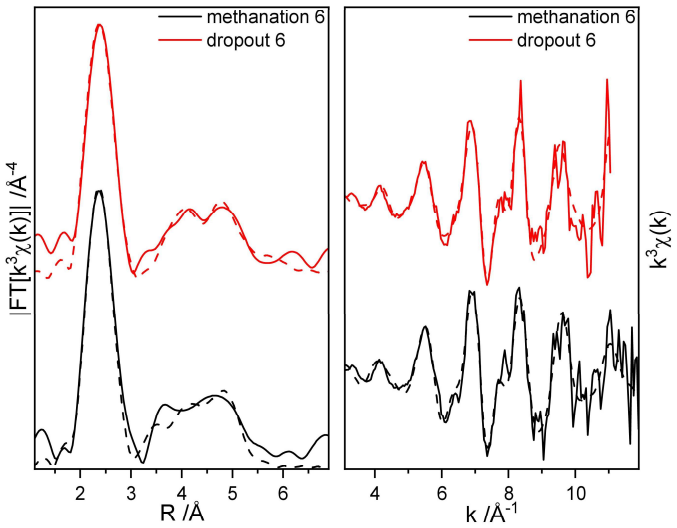

Figure S21: EXAFS spectra of the Full Dropout (FD) scenario. On the left side Fourier-transformed experimental k3χ(k) EXAFS functions are shown. On the right side Experimental $k^3\chi(k)$ EXAFS functions are shown. The solid line shows the experimental spectra, the dotted line shows the theoretical fit of the EXAFS analysis.

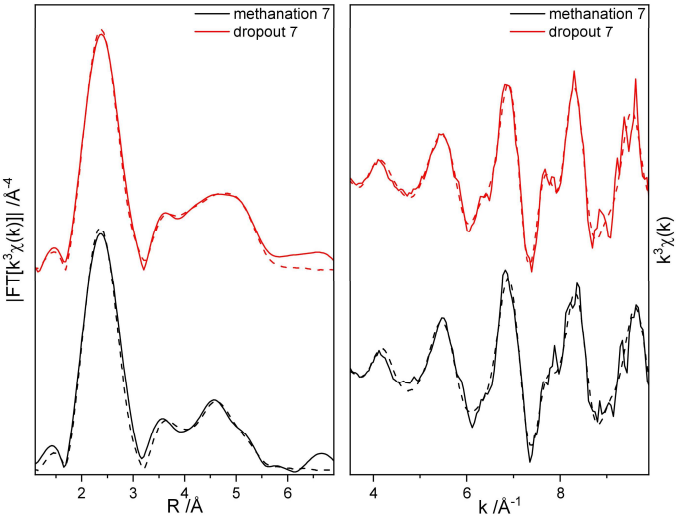

Figure S22: EXAFS spectra of the Full Dropout (FD) scenario. On the left side Fourier-transformed experimental k3χ(k) EXAFS functions are shown. On the right side Experimental $k^3\chi(k)$ EXAFS functions are shown. The solid line shows the experimental spectra, the dotted line shows the theoretical fit of the EXAFS analysis.

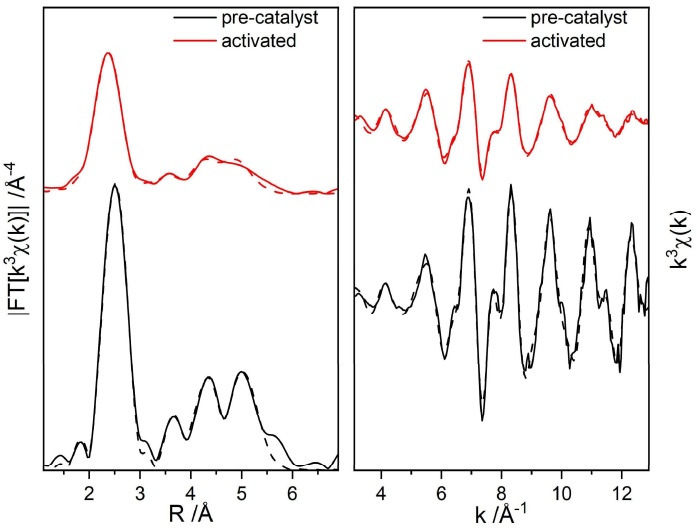

Figure S23: EXAFS spectra of the partial dropout (PD) scenario. On the left side Fourier-transformed experimental k3χ(k) EXAFS functions are shown. On the right side Experimental $k^3\chi(k)$ EXAFS functions are shown. The solid line shows the experimental spectra, the dotted line shows the theoretical fit of the EXAFS analysis.

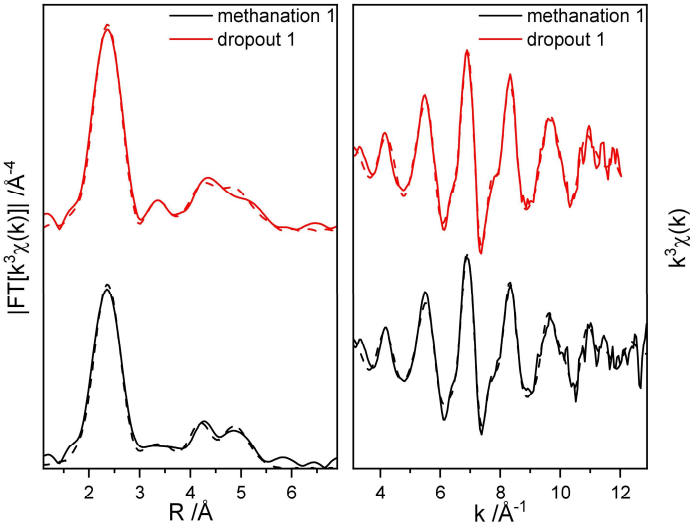

Figure S24: EXAFS spectra of the partial dropout (PD) scenario. On the left side Fourier-transformed experimental k3χ(k) EXAFS functions are shown. On the right side Experimental $k^3\chi(k)$ EXAFS functions are shown. The solid line shows the experimental spectra, the dotted line shows the theoretical fit of the EXAFS analysis.

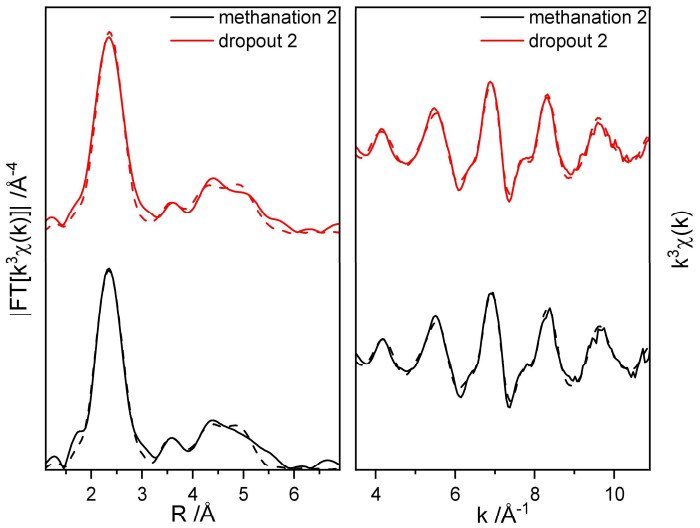

Figure S25: EXAFS spectra of the partial dropout (PD) scenario. On the left side Fourier-transformed experimental k3χ(k) EXAFS functions are shown. On the right side Experimental $k^3\chi(k)$ EXAFS functions are shown. The solid line shows the experimental spectra, the dotted line shows the theoretical fit of the EXAFS analysis.

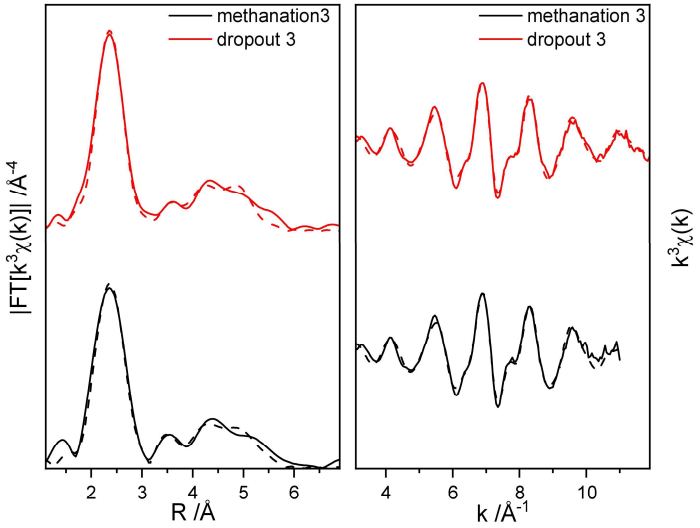

Figure S26: EXAFS spectra of the partial dropout (PD) scenario. On the left side Fourier-transformed experimental k3χ(k) EXAFS functions are shown. On the right side Experimental $k^3\chi(k)$ EXAFS functions are shown. The solid line shows the experimental spectra, the dotted line shows the theoretical fit of the EXAFS analysis.

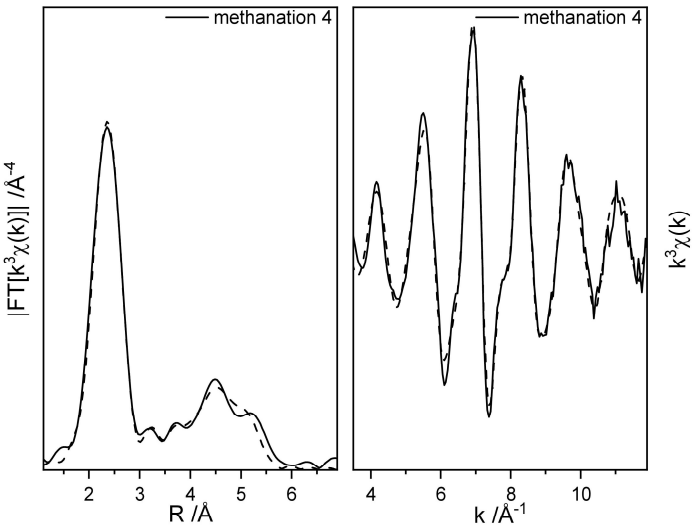

Figure S27: EXAFS spectra of the partial dropout (PD) scenario. On the left side Fourier-transformed experimental k3χ(k) EXAFS functions are shown. On the right side Experimental $k^3\chi(k)$ EXAFS functions are shown. The solid line shows the experimental spectra, the dotted line shows the theoretical fit of the EXAFS analysis.

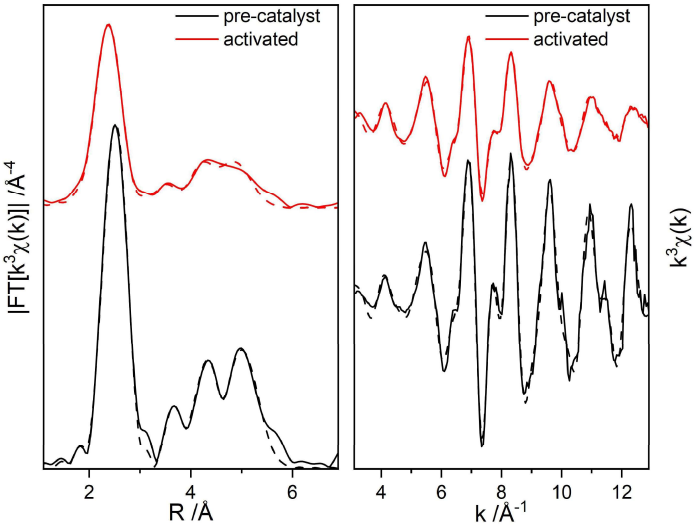

Figure S28: EXAFS spectra of the stoichiometric dropout (SD) scenario. On the left side Fourier-transformed experimental k3χ(k) EXAFS functions are shown. On the right side Experimental $k^3\chi(k)$ EXAFS functions are shown. The solid line shows the experimental spectra, the dotted line shows the theoretical fit of the EXAFS analysis.

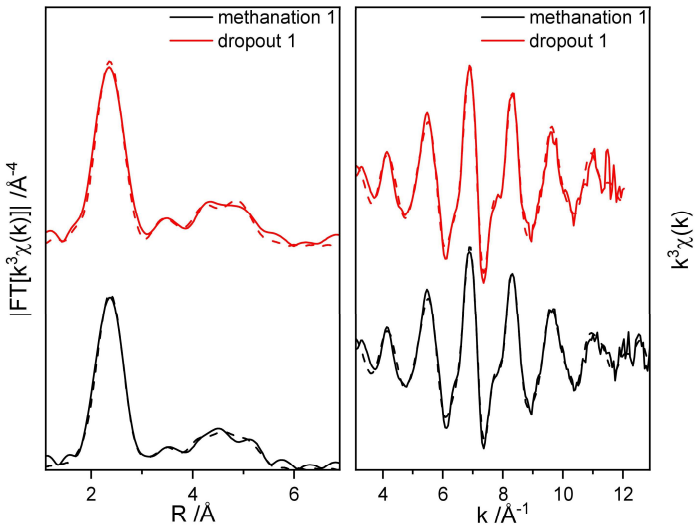

Figure S29: EXAFS spectra of the stoichiometric dropout (SD) scenario. On the left side Fourier-transformed experimental k3χ(k) EXAFS functions are shown. On the right side Experimental $k^3\chi(k)$ EXAFS functions are shown. The solid line shows the experimental spectra, the dotted line shows the theoretical fit of the EXAFS analysis.

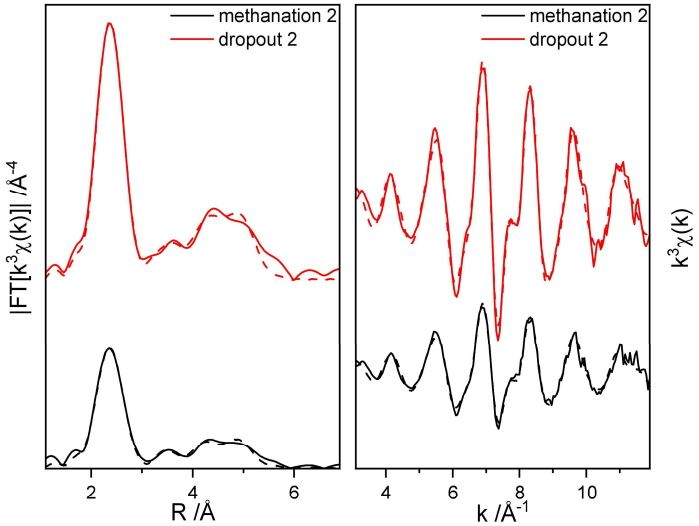

Figure S30: EXAFS spectra of the stoichiometric dropout (SD) scenario. On the left side Fourier-transformed experimental k3χ(k) EXAFS functions are shown. On the right side Experimental $k^3\chi(k)$ EXAFS functions are shown. The solid line shows the experimental spectra, the dotted line shows the theoretical fit of the EXAFS analysis.

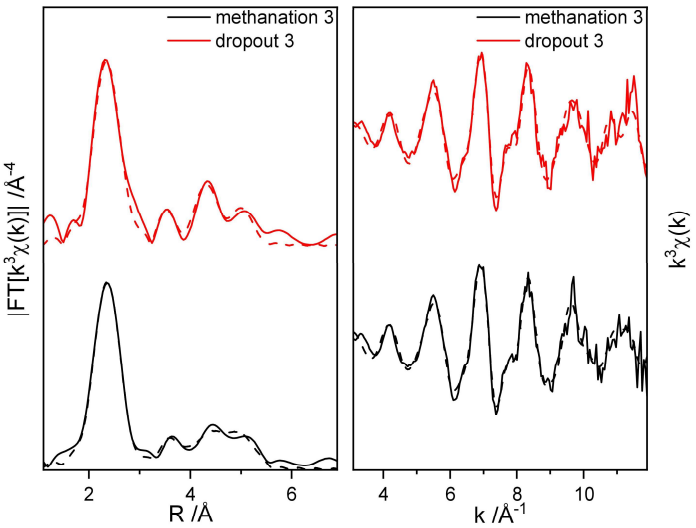

Figure S31: EXAFS spectra of the stoichiometric dropout (SD) scenario. On the left side Fourier-transformed experimental k3χ(k) EXAFS functions are shown. On the right side Experimental $k^3\chi(k)$ EXAFS functions are shown. The solid line shows the experimental spectra, the dotted line shows the theoretical fit of the EXAFS analysis.

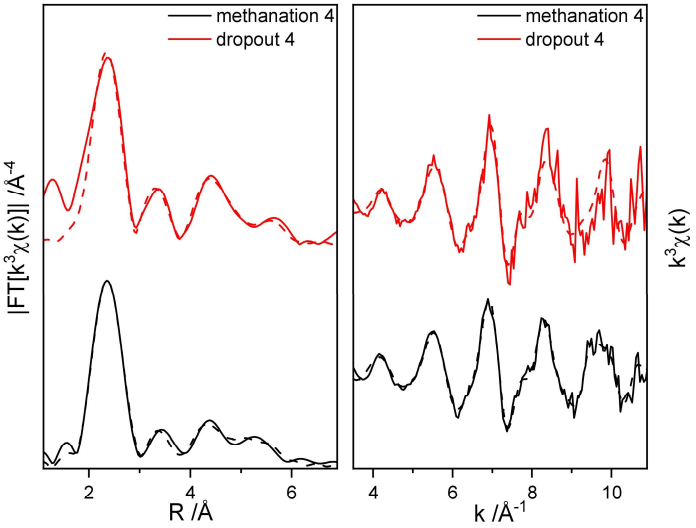

Figure S32: EXAFS spectra of the stoichiometric dropout (SD) scenario. On the left side Fourier-transformed experimental k3χ(k) EXAFS functions are shown. On the right side Experimental $k^3\chi(k)$ EXAFS functions are shown. The solid line shows the experimental spectra, the dotted line shows the theoretical fit of the EXAFS analysis.

Table S2: Structural parameters obtained by fitting the experimental EXAFS spectra of the *in-situ* measurement of the Full Dropout (FD) scenario.

Sample	Abs-Bs[a]	*N*(Bs)[b]	*R*(Abs-Bs)[c] /Å	$\sigma^{2\,d}$ /Å²	R^e /%, χ_{red}^{2f}, E_f^g /eV, A_{fac}^h
FD pre-catalyst	Ni – O	1.0 ± 0.1	2.02 ± 0.02	0.013 ± 0.0013	22.84
	Ni – Ni	12.8 ± 1.3	2.47 ± 0.02	0.007 ± 0.0007	7.52×10^{-6}

	Ni – Ni	1.8 ± 0.4	3.43 ± 0.03	0.005 ± 0.0005	-0.1071
	Ni – C	7.9 ± 1.6	3.88 ± 0.04	0.001 ± 0.0001	0.8000
	Ni – Ni	11.0 ± 2.2	4.27 ± 0.04	0.005 ± 0.0005	
	Ni – Ni	29.1 ± 5.8	4.75 ± 0.05	0.013 ± 0.0013	
	Ni – Ni	32.7 ± 6.5	5.09 ± 0.05	0.011 ± 0.0011	
FD activated	Ni – Ni	12.2 ± 1.2	2.47 ± 0.02	0.010 ± 0.0010	16.12
	Ni – Ni	2.1 ± 0.4	3.45 ± 0.03	0.012 ± 0.0012	2.18×10^{-6}
	Ni – C	4.8 ± 1.0	3.84 ± 0.04	0.002 ± 0.0002	1.272
	Ni – Ni	6.4 ± 1.3	4.27 ± 0.04	0.007 ± 0.0007	0.8000
	Ni – Ni	15.3 ± 3.1	4.73 ± 0.05	0.013 ± 0.0013	
	Ni – Ni	16.9± 3.4	5.11 ± 0.05	0.013 ± 0.0013	
FD methanation 1	Ni – Ni	11.4 ± 1.1	2.47 ± 0.02	0.011 ± 0.0011	19.15
	Ni – Ni	0.7 ± 0.1	3.50 ± 0.04	0.009 ± 0.0009	7.35×10^{-6}
	Ni – C	5.4 ± 1.1	3.83 ± 0.04	0.001 ± 0.0001	1.199
	Ni – Ni	4.1 ± 0.8	4.28 ± 0.04	0.005 ± 0.0005	0.8000
	Ni – Ni	4.3 ± 0.8	4.69 ± 0.05	0.004 ± 0.0004	
	Ni – Ni	6.5 ± 1.3	5.14 ± 0.05	0.005 ± 0.0005	
FD dropout 1	Ni – Ni	12.8 ± 1.3	2.47 ± 0.02	0.013 ± 0.0013	21.98
	Ni – Ni	2.1± 0.4	3.43 ± 0.03	0.010 ± 0.0010	10.91×10^{-6}
	Ni – C	4.1 ± 0.8	3.87 ± 0.04	0.001 ± 0.0001	1.190
	Ni – Ni	2.2 ± 0.4	4.25 ± 0.04	0.001 ± 0.0001	0.8000
	Ni – Ni	11.3 ± 2.3	4.72 ± 0.05	0.008 ± 0.0008	
	Ni – Ni	5.2± 1.0	5.53 ± 0.05	0.005 ± 0.0005	
FD methanation 2	Ni – Ni	12.0 ± 1.2	2.47 ± 0.02	0.011 ± 0.0011	24.34
	Ni – Ni	1.0 ± 0.2	3.42 ± 0.03	0.002 ± 0.0002	30.84×10^{-6}
	Ni – C	5.1 ± 1.0	3.84 ± 0.04	0.013 ± 0.0013	1.383
	Ni – Ni	3.6 ± 0.7	4.27 ± 0.04	0.002 ± 0.0002	0.8000
	Ni – Ni	6.3 ± 1.3	4.71 ± 0.05	0.007 ± 0.0007	
	Ni – Ni	4.6 ± 0.9	5.16 ± 0.05	0.001 ± 0.0001	
FD dropout 2	Ni – Ni	11.8 ± 1.2	2.47 ± 0.02	0.011 ± 0.0011	24.75
	Ni – Ni	0.8 ± 0.2	3.42 ± 0.03	0.001 ± 0.0001	16.06×10^{-6}
	Ni – C	3.5 ± 0.7	3.95 ± 0.04	0.008 ± 0.0008	0.3737
	Ni – Ni	11.1 ± 2.2	4.28 ± 0.04	0.008 ± 0.0008	0.8000
	Ni – Ni	8.8 ± 1.8	5.15 ± 0.05	0.007 ± 0.0007	
FD methanation 3	Ni – Ni	12.2 ± 1.2	2.46 ± 0.02	0.010 ± 0.0010	20.15
	Ni – Ni	7.2 ± 1.4	3.87 ± 0.04	0.002 ± 0.0002	33.52×10^{-6}
	Ni – Ni	10.1 ± 2.0	4.14 ± 0.04	0.002 ± 0.0002	1.691
	Ni – Ni	16.9 ± 3.4	4.77 ± 0.05	0.001 ± 0.0001	0.8000
	Ni – Ni	11.0 ± 2.2	5.03 ± 0.05	0.001 ± 0.0001	
FD dropout 3	Ni – Ni	8.5 ± 0.8	2.46 ± 0.02	0.008 ± 0.0008	29.34
	Ni – Ni	4.1 ± 0.8	3.44 ± 0.03	0.013 ± 0.0013	15.22×10^{-6}
	Ni – Ni	4.7 ± 1.0	4.22 ± 0.04	0.005 ± 0.0005	2.919
	Ni – Ni	5.0 ± 1.0	4.69 ± 0.05	0.001 ± 0.0001	0.8000
	Ni – Ni	3.9 ± 0.8	5.15 ± 0.05	0.001 ± 0.0001	

FD methanation 4	Ni – Ni	10.3 ± 1	2.49 ± 0.02	0.010 ± 0.0010	37.32
	Ni – Ni	2.3 ± 0.5	3.50 ± 0.04	0.009 ± 0.0009	13.73×10^{-6}
	Ni – Ni	10.0 ± 2.0	4.28 ± 0.04	0.007 ± 0.0007	-1.124
	Ni – Ni	2.5 ± 0.5	4.74 ± 0.05	0.001 ± 0.0001	0.8000
	Ni – Ni	4.4 ± 0.9	5.15 ± 0.05	0.003 ± 0.0003	
Fd dropout 4	Ni – Ni	10.3 ± 1.0	2.48 ± 0.02	0.010 ± 0.0010	32.93
	Ni – Ni	1.7 ± 0.4	3.44 ± 0.03	0.006 ± 0.0006	23.51×10^{-6}
	Ni – Ni	4.6 ± 0.9	4.27 ± 0.04	0.002 ± 0.0002	-0.0400
	Ni – Ni	5.1 ± 1.0	4.75 ± 0.05	0.001 ± 0.0001	0.8000
	Ni – Ni	5.9 ± 1.2	5.12 ± 0.05	0.006 ± 0.0006	
FD methanation 5	Ni – Ni	10.4 ± 1.0	2.48 ± 0.02	0.009 ± 0.0009	23.85
	Ni – Ni	4.0± 0.8	3.45 ± 0.03	0.012 ± 0.0012	32.35×10^{-6}
	Ni – Ni	7.0± 1.4	4.26 ± 0.04	0.007 ± 0.0007	-0.3638
	Ni – Ni	20.0± 4.0	4.78 ± 0.05	0.013 ± 0.0013	0.8000
	Ni – Ni	20.2 ± 4.0	5.08 ± 0.05	0.013 ± 0.0013	
FD dropout 5	Ni – Ni	9.9 ± 2.0	2.48 ± 0.02	0.009 ± 0.0009	26.67
	Ni – Ni	1.2 ± 0.2	3.48 ± 0.03	0.001 ± 0.0001	24.38×10^{-6}
	Ni – Ni	4.8 ± 1.0	4.26 ± 0.04	0.002 ± 0.0002	-0.9863
	Ni – Ni	8.4 ± 1.7	4.77 ± 0.05	0.003 ± 0.0003	0.8000
	Ni – Ni	16.2 ± 3.2	5.05 ± 0.05	0.013 ± 0.0013	
FD methanation 6	Ni – Ni	11.0 ± 1.1	2.46 ± 0.02	0.009 ± 0.0009	41.41
	Ni – Ni	1.3 ± 0.1	3.48 ± 0.03	0.001 ± 0.0001	21.92×10^{-6}
	Ni – Ni	13.1 ± 2.6	4.24 ± 0.04	0.011 ± 0.0011	1.591
	Ni – Ni	5.2 ± 1.1	4.72 ± 0.05	0.003 ± 0.0003	0.8000
	Ni – Ni	10.4 ± 2.1	5.13 ± 0.05	0.010 ± 0.0010	
FD dropout 6	Ni – Ni	8.6 ± 0.9	2.47 ± 0.02	0.008 ± 0.0008	36.98
	Ni – Ni	7.3 ± 1.4	3.91 ± 0.03	0.013 ± 0.0013	45.15×10^{-6}
	Ni – Ni	3.8 ± 0.8	4.22 ± 0.04	0.001 ± 0.0001	1.414
	Ni – Ni	7.0 ± 1.4	4.72 ± 0.05	0.001 ± 0.0001	0.8000
	Ni – Ni	1.8 ± 0.4	5.30 ± 0.05	0.003 ± 0.0003	
	Ni – Ni	5.5 ± 1.1	5.50 ± 0.06	0.001 ± 0.0001	
FD methanation 7	Ni – Ni	13.0 ± 1.3	2.47 ± 0.02	0.011 ± 0.0011	23.15
	Ni – Ni	10.0 ± 2.0	3.88 ± 0.04	0.013 ± 0.0013	17.17×10^{-6}
	Ni – Ni	8.5 ± 1.7	4.19 ± 0.04	0.013 ± 0.0013	1.174
	Ni – Ni	19.8 ± 4.0	4.75 ± 0.05	0.010 ± 0.0010	0.8000
	Ni – Ni	14.2 ± 2.8	5.02 ± 0.05	0.013 ± 0.0013	
FD dropout 7	Ni – Ni	11.1 ± 1.1	2.48 ± 0.02	0.009 ± 0.0009	22.62
	Ni – Ni	12.3 ± 2.5	3.92 ± 0.04	0.013 ± 0.0013	17.66×10^{-6}
	Ni – Ni	15.7 ± 3.1	4.23 ± 0.04	0.013 ± 0.0013	0.7019
	Ni – Ni	16.0 ± 3.2	4.77 ± 0.05	0.012 ± 0.0012	0.8000
	Ni – Ni	14.1 ± 2.8	5.10 ± 0.05	0.007 ± 0.0007	

[a] Abs: X-ray absorbing atom, and Bs: backscattering atom. [b] Number of backscattering atoms. [c] Distance of the absorbing atom from the backscattering atom. [d] Debye-Waller like factor. [e] Fit index. [f] Reduced χ^2. [g] Fermi energy, which accounts for the shift between theory and experiment. [h] Amplitude reduction factor.

Table S3: Structural parameters obtained by fitting the experimental EXAFS spectra of the *in-situ* measurement of the stoichiometric dropout (SD) scenario.

Sample	Abs-Bs[a]	*N*(Bs)[b]	*R*(Abs-Bs)[c] /Å	σ^{2} [d] /Å^2	R^e /%, χ_{red}^{2f}, E_f[g] /eV, A_{fac}[h]
SD pre-catalyst	Ni – O	1.0 ± 0.1	2.00 ± 0.02	0.013 ± 0.0013	18.95
	Ni – Ni	11.9 ± 1.2	2.47 ± 0.02	0.006 ± 0.0006	4.39×10^{-6}
	Ni – Ni	5.1 ± 1.0	3.47 ± 0.03	0.012 ± 0.0012	0.3138
	Ni – C	9.3 ± 1.9	3.83 ± 0.04	0.001 ± 0.0001	0.8000
	Ni – Ni	11.2 ± 2.2	4.27 ± 0.04	0.005 ± 0.0005	
	Ni – Ni	28.3 ± 5.7	4.76 ± 0.05	0.013 ± 0.0013	
	Ni – Ni	35.1 ± 7.0	5.09 ± 0.05	0.010 ± 0.0010	
SD activated	Ni – Ni	11.8 ± 1.2	2.47 ± 0.02	0.011 ± 0.0011	14.64
	Ni – Ni	2.0 ± 0.4	3.43 ± 0.03	0.013 ± 0.0013	1.84×10^{-6}
	Ni – C	5.0 ± 1.0	3.85 ± 0.04	0.003 ± 0.0003	1.327
	Ni – Ni	6.7 ± 1.4	4.27 ± 0.04	0.009 ± 0.0009	0.8000
	Ni – Ni	14.0 ± 2.8	4.72 ± 0.05	0.013 ± 0.0013	
	Ni – Ni	14.2 ± 2.8	5.11 ± 0.05	0.013 ± 0.0013	
SD methanation 1	Ni – Ni	6.5 ± 0.7	2.47 ± 0.02	0.013 ± 0.0013	19.61
	Ni – Ni	0.6 ± 0.1	3.42 ± 0.03	0.011 ± 0.0011	3.73×10^{-6}
	Ni – C	2.3 ± 0.5	3.85 ± 0.04	0.003 ± 0.0003	1.596
	Ni – Ni	1.8 ± 0.4	4.25 ± 0.04	0.007 ± 0.0007	0.8000
	Ni – Ni	3.3 ± 0.7	4.70 ± 0.05	0.007 ± 0.0007	
	Ni – Ni	1.5 ± 0.3	5.14 ± 0.05	0.003 ± 0.0003	
SD dropout 1	Ni – Ni	6.8 ± 0.7	2.47 ± 0.02	0.013 ± 0.0013	20.75
	Ni – Ni	1.4 ± 0.3	3.46 ± 0.03	0.012 ± 0.0012	5.88×10^{-6}
	Ni – C	4.6 ± 0.9	3.80 ± 0.04	0.011 ± 0.0011	1.904
	Ni – Ni	1.9 ± 0.4	4.26 ± 0.04	0.006 ± 0.0006	0.8000
	Ni – Ni	4.0 ± 0.8	4.73 ± 0.05	0.009 ± 0.0009	
	Ni – Ni	5.2 ± 1.0	5.13 ± 0.05	0.013 ± 0.0013	
SD methanation 2	Ni – Ni	6.5 ± 0.7	2.47 ± 0.02	0.012 ± 0.0012	20.20
	Ni – Ni	1.2 ± 0.2	3.48 ± 0.03	0.013 ± 0.0013	5.23×10^{-6}
	Ni – C	3.2 ± 0.6	3.81 ± 0.04	0.004 ± 0.0004	2.177
	Ni – Ni	1.4 ± 0.3	4.26 ± 0.04	0.003 ± 0.0003	0.8000
	Ni – Ni	4.4 ± 0.9	4.72 ± 0.05	0.009 ± 0.0009	
	Ni – Ni	5.1 ± 1	5.12 ± 0.05	0.013 ± 0.0013	
SD dropout 2	Ni – Ni	12.0 ± 1.2	2.47 ± 0.02	0.011 ± 0.0011	17.49
	Ni – Ni	1.7 ± 0.3	3.43 ± 0.03	0.013 ± 0.0013	3.74×10^{-6}
	Ni – C	5.3 ± 1.1	3.84 ± 0.04	0.001 ± 0.0001	1.661
	Ni – Ni	5.2 ± 1.0	4.27 ± 0.04	0.007 ± 0.0007	0.8000
	Ni – Ni	11.8 ± 2.4	4.72 ± 0.05	0.011 ± 0.0011	
	Ni – Ni	14.2 ± 2.8	5.12 ± 0.05	0.013 ± 0.0013	
SD methanation 3	Ni – Ni	6.5 ± 0.7	2.46 ± 0.02	0.012 ± 0.0012	28.66
	Ni – Ni	0.4 ± 0.1	3.50 ± 0.04	0.012 ± 0.0012	10.00×10^{-6}
	Ni – C	3.3 ± 0.7	3.84 ± 0.04	0.001 ± 0.0001	2.505
	Ni – Ni	2.3 ± 0.5	4.27 ± 0.04	0.010 ± 0.0010	0.8000
	Ni – Ni	4.8 ± 1.0	4.70 ± 0.05	0.011 ± 0.0011	
	Ni – Ni	1.3 ± 0.3	5.12 ± 0.05	0.002 ± 0.0002	

SD dropout 3	Ni – Ni	6.7 ± 0.7	2.46 ± 0.02	0.013 ± 0.0013	32.64
	Ni – Ni	0.9 ± 0.2	3.52 ± 0.03	0.006 ± 0.0006	16.07×10^{-6}
	Ni – C	4.2 ± 0.8	3.77 ± 0.04	0.001 ± 0.0001	2.651
	Ni – Ni	1.3 ± 0.3	4.27 ± 0.04	0.001 ± 0.0001	0.8000
	Ni – Ni	4.5 ± 0.9	4.70 ± 0.05	0.011 ± 0.0011	
	Ni – Ni	3.1 ± 0.6	5.12 ± 0.05	0.008 ± 0.0008	
SD methanation 4	Ni – Ni	6.5 ± 0.7	2.46 ± 0.02	0.012 ± 0.0012	24.25
	Ni – Ni	2.1 ± 0.4	3.41 ± 0.03	0.012 ± 0.0012	13.94×10^{-6}
	Ni – Ni	1.9 ± 0.4	4.23 ± 0.04	0.005 ± 0.0005	2.239
	Ni – Ni	2.0 ± 0.4	4.70 ± 0.05	0.001 ± 0.0001	0.8000
	Ni – Ni	1.4 ± 0.3	5.20 ± 0.05	0.001 ± 0.0001	
	Ni – Ni	1.5 ± 0.3	5.50 ± 0.06	0.001 ± 0.0001	
SD dropout 4	Ni – Ni	7.1 ± 0.7	2.45 ± 0.02	0.013 ± 0.0013	45.91
	Ni – Ni	0.9 ± 0.2	3.38 ± 0.03	0.001 ± 0.0001	42.95×10^{-6}
	Ni – Ni	1.3 ± 0.3	4.23 ± 0.04	0.001 ± 0.0001	3.911
	Ni – Ni	4.9 ± 1.0	4.68 ± 0.05	0.007 ± 0.0007	0.8000
	Ni – Ni	6.9 ± 1.2	5.55 ± 0.06	0.011 ± 0.0011	

[a] Abs: X-ray absorbing atom, and Bs: backscattering atom. [b] Number of backscattering atoms. [c] Distance of the absorbing atom from the backscattering atom. [d] Debye-Waller like factor. [e] Fit index. [f] Reduced χ^2. [g] Fermi energy, which accounts for the shift between theory and experiment. [h] Amplitude reduction factor.

Table S4: Structural parameters obtained by fitting the experimental EXAFS spectra of the *in-situ* measurements of the partial dropout (PD) scenario.

Sample	Abs-Bs[a]	N(Bs)[b]	R(Abs-Bs)[c] /Å	$\sigma^{2\,d}$ /Å^2	R^e /%, $\chi_{red}{}^{2f}$, $E_f{}^g$ /eV, $A_{fac}{}^h$
FD pre-catalyst	Ni – O	0.6 ± 0.1	1.91 ± 0.02	0.001 ± 0.0001	21.62
	Ni – Ni	9.0 ± 0.9	2.47 ± 0.02	0.006 ± 0.0006	5.68×10^{-6}
	Ni – Ni	4.3 ± 0.8	3.46 ± 0.03	0.013 ± 0.0013	0.8152
	Ni – C	7.9 ± 1.4	3.83 ± 0.04	0.001 ± 0.0001	0.8000
	Ni – Ni	5.7 ± 1.1	4.27 ± 0.04	0.003 ± 0.0003	
	Ni – Ni	20.1 ± 4.0	4.74 ± 0.05	0.013 ± 0.0013	
	Ni – Ni	19.4 ± 3.9	5.09 ± 0.05	0.008 ± 0.0008	
PD activated	Ni – Ni	10.1 ± 1.0	2.47 ± 0.02	0.012 ± 0.0012	15.23
	Ni – Ni	1.1 ± 0.2	3.43 ± 0.03	0.013 ± 0.0013	2.00×10^{-6}
	Ni – C	3.5 ± 0.7	3.85 ± 0.04	0.001 ± 0.0001	1.873
	Ni – Ni	3.6 ± 0.7	4.27 ± 0.04	0.007 ± 0.0007	0.8000
	Ni – Ni	9.9 ± 2.0	4.72 ± 0.05	0.013 ± 0.0013	
	Ni – Ni	9.2 ± 1.8	5.12 ± 0.05	0.013 ± 0.0013	
PD methanation 1	Ni – Ni	8.5 ± 0.9	2.46 ± 0.02	0.013 ± 0.0013	25.49
	Ni – Ni	1.2 ± 0.2	3.39 ± 0.03	0.011 ± 0.0011	8.03×10^{-6}
	Ni – C	2.7 ± 0.6	3.85 ± 0.04	0.003 ± 0.0003	2.462
	Ni – Ni	2.5 ± 0.5	4.25 ± 0.04	0.006 ± 0.0006	0.8000
	Ni – Ni	7.4 ± 1.5	4.74 ± 0.05	0.013 ± 0.0013	
	Ni – Ni	3.8 ± 0.8	5.11 ± 0.05	0.009 ± 0.0009	
PD dropout 1	Ni – Ni	10.2 ± 1.0	2.46 ± 0.02	0.013 ± 0.0013	19.58
	Ni – Ni	3.2 ± 0.6	3.43 ± 0.03	0.013 ± 0.0013	4.17×10^{-6}

	Ni – C	6.3 ± 1.3	3.69 ± 0.04	0.013 ± 0.0013	2.400
	Ni – Ni	1.8 ± 0.4	4.25 ± 0.04	0.002 ± 0.0002	0.8000
	Ni – Ni	2.9 ± 0.6	4.70 ± 0.05	0.003 ± 0.0003	
	Ni – Ni	3.2 ± 0.6	5.15 ± 0.05	0.005 ± 0.0005	
PD methanation 2	Ni – Ni	9.1 ± 0.9	2.46 ± 0.02	0.013 ± 0.0013	22.29
	Ni – Ni	1.0 ± 0.2	3.54 ± 0.03	0.013 ± 0.0013	6.21×10^{-6}
	Ni – C	5.2 ± 1.0	3.81 ± 0.04	0.001 ± 0.0001	2.705
	Ni – Ni	1.1 ± 0.2	4.25 ± 0.04	0.001 ± 0.0001	0.8000
	Ni – Ni	9.9 ± 2.0	4.72 ± 0.05	0.013 ± 0.0013	
	Ni – Ni	5.3 ± 1.1	5.13 ± 0.05	0.013 ± 0.0013	
PD dropout 2	Ni – Ni	9.2 ± 1.8	2.46 ± 0.02	0.013 ± 0.0013	23.09
	Ni – Ni	0.9 ± 0.2	3.52 ± 0.03	0.012 ± 0.0012	5.41×10^{-6}
	Ni – C	4.7 ± 0.9	3.84 ± 0.04	0.003 ± 0.0003	1.903
	Ni – Ni	3.4 ± 0.7	4.27 ± 0.04	0.008 ± 0.0008	0.8000
	Ni – Ni	8.3 ± 1.7	4.73 ± 0.05	0.013 ± 0.0013	
	Ni – Ni	7.7 ± 1.5	5.12 ± 0.05	0.012 ± 0.0012	
PD methanation 3	Ni – Ni	9.0 ± 0.9	2.47 ± 0.02	0.013 ± 0.0013	20.96
	Ni – Ni	0.7 ± 0.1	3.52 ± 0.04	0.012 ± 0.0012	10.02×10^{-6}
	Ni – C	4.8 ± 1.0	3.84 ± 0.04	0.001 ± 0.0001	1.158
	Ni – Ni	3.5 ± 0.7	4.26 ± 0.04	0.009 ± 0.0009	0.8000
	Ni – Ni	2.7 ± 0.5	4.70 ± 0.05	0.002 ± 0.0002	
	Ni – Ni	2.2 ± 0.4	5.17 ± 0.05	0.001 ± 0.0001	
PD dropout 3	Ni – Ni	9.3 ± 0.9	2.47 ± 0.02	0.013 ± 0.0013	19.40
	Ni – Ni	1.0 ± 0.2	3.57 ± 0.03	0.013 ± 0.0013	4.48×10^{-6}
	Ni – C	4.8 ± 1.0	3.82 ± 0.04	0.001 ± 0.0001	1.226
	Ni – Ni	2.2 ± 0.4	4.26 ± 0.04	0.004 ± 0.0004	0.8000
	Ni – Ni	4.4 ± 0.9	4.73 ± 0.05	0.007 ± 0.0007	
	Ni – Ni	6.7 ± 1.3	5.15 ± 0.05	0.012 ± 0.0012	
PD methanation 4	Ni – Ni	9.5 ± 1.0	2.46 ± 0.02	0.013 ± 0.0013	15.80
	Ni – Ni	0.4 ± 0.8	3.36 ± 0.03	0.004 ± 0.0004	3.63×10^{-6}
	Ni – C	3.7 ± 0.7	3.85 ± 0.04	0.001 ± 0.0001	2.617
	Ni – Ni	1.6 ± 0.3	4.25 ± 0.04	0.004 ± 0.0004	0.8000
	Ni – Ni	4.6 ± 0.9	4.70 ± 0.05	0.006 ± 0.0006	
	Ni – Ni	2.4 ± 0.5	5.15 ± 0.05	0.003 ± 0.0003	

[a] Abs: X-ray absorbing atom, and Bs: backscattering atom. [b] Number of backscattering atoms. [c] Distance of the absorbing atom from the backscattering atom. [d] Debye-Waller-like factor. [e] Fit index. [f] Reduced χ^2. [g] Fermi energy, which accounts for the shift between theory and experiment. [h] Amplitude reduction factor.

References

1. B. Ravel and M. Newville, *Journal of synchrotron radiation*, 2005, **12**, 537.
2. N. Binsted and S. S. Hasnain, *Journal of synchrotron radiation*, 1996, **3**, 185.
3. M. Newville, *Journal of synchrotron radiation*, 2001, **8**, 322.
4. T. S. Ertel, H. Bertagnolli, S. Hückmann, U. Kolb and D. Peter, *Appl Spectrosc*, 1992, **46**, 690.
5. N. Binsted and F. Mosselmans, eds., *EXCURV98 Manual*, Daresbury, UK.
6. M. Bauer and H. Bertagnolli, *J. Phys. Chem. B*, 2007, **111**, 13756.

7. P. Juhás, C. L. Farrow, X. Yang, K. R. Knox and S. J. L. Billinge, *Acta Crystallogr., Sect. A: Found. Adv.*, 2015, **71**, 562.
8. I.-K. Jeong, R. H. Heffner, M. J. Graf and S. J. L. Billinge, *Phys. Rev. B*, 2003, **67**. 10.1103/PhysRevB.67.104301.
9. N. Prinz, L. Schwensow, S. Wendholt, A. Jentys, M. Bauer, W. Kleist and M. Zobel, *Nanoscale*, 2020, **12**, 15800.

11 Conclusion and Outlook

The aim of this work was the spectroscopic investigation of novel nickel catalysts for the methanation of CO_2. The basis for the heterogeneous Ni catalysts in a carbon matrix is the thermal decomposition of simple, MIL-53-based, metal-organic framework compounds. By applying X-ray absorption and emission spectroscopies, substantiated by theoretical calculations, electronic contributions to the characterization and understanding of the highly amorphous structures of the carbon-supported Ni species were made possible. Using X-ray spectroscopy, cornerstones for further improvement of the catalysts in the future were formed. The optimal decomposition conditions could be narrowed down to moderate temperatures in a slightly reductive atmosphere. Furthermore, the activation temperature could be reduced potentially and the clear correlation between hydrogen dropouts and loss of the carbon layer could be demonstrated.

In first instance XANES, LCF of the XANES spectra, and EXAFS investigations of the pre-catalysts obtained by thermal decomposition were successfully performed. Through detailed analysis of the absorption edge region in XANES, it was found that in the absence of hydrogen as a reducing agent, higher temperatures are required to observe a significant reduction of the Ni(II) species. At the same time, the results obtained under hydrogen atmosphere prove that already very small amounts of hydrogen are sufficient to achieve rapid reduction as soon as 375 °C or higher are reached. Utilizing LC-XANES, it was further proven that even at high decomposition temperatures traces of Ni(II) species are still present in the pre-catalyst in unreduced form. Similar to XANES, EXAFS analysis confirmed that, for example, fractions of the MOF were still present in the decompositions at 350 °C. With higher temperatures, the Ni(II) fraction diminishes and the compound composition becomes closer to the coordination environment of Ni(0). It was also demonstrated that carbon backscatterers were present even at higher decomposition temperatures and thus the embedding of the catalyst species in a carbon matrix was successful.

In subsequent studies, the samples of the same composition were analyzed by XES for a more precise determination of the sample composing species. A new approach based on the linear combination of HERFD-XANES and subsequent DOS calculations in the VtC region of the spectra was successfully established. Within the analysis, it was shown that the backscatterer could be identified as carbon from previous results. Furthermore, a Ni-*d*-state/C-*p*-state overlap demonstrated a carbon shell around Ni phases. Also, a Ni-C interaction that does not take place in the first coordination sphere, but in a more distant coordination sphere. For the sample at 500 °C, with the lowest selectivity to methane, no oxide layer is represented by XES data.

A possible explanation for this is that the interactions with the light atoms decrease with increasing particle size and this worsens the stabilization of the catalyst.

With the detailed knowledge about the pre-catalysts, *in-situ* XAS measurements under dynamic conditions were then investigated to provide information on the stability of the catalyst under different degrees of hydrogen deficiency. This was the first time that an investigation of the activated catalyst could be carried out. A detailed *in-sit*u XANES analysis of the activation process from the pre-catalyst to the catalyst showed that main structural differences occur at about 80 to 200 °C. At higher temperatures, the structure of the pre-catalyst sample is affected slightly. Furthermore, EXAFS analysis of the individual steps within the dynamic catalytic cycle showed a clear correlation between carbon matrix and catalyst activation. In the full dropout scenario, no carbon was observed from the third catalytic cycle onward. At the same time, a loss of catalyst activity can be observed, especially in the full dropout scenario. For the partial and the stoichiometric dropout scenarios, neither the loss of activity nor that of the carbon layer was observed.

With the methodical combination of the hard X-ray based techniques XAS and XES, it was possible to model and describe the highly undefined and amorphous structures of Ni-catalysts based on thermal MOF decomposition. These findings have been supported by FEFF *ab-initio* calculations and have been widened to *in-situ* investigation, while H_2 dropouts have been simulated in different conditions.

Future works should first deal with XES *in-situ* measurements of the active catalyst species. The analysis will provide information about the electronic structure around the nickel atoms and, at the same time, a change in the direct ligand environment should be observable during the methanation process. Second, a catalyst doping study should be conducted (cf. chapter 2.2) to stabilize the catalyst without losing activity for methanation. Iron, for example, could be used for this purpose. Third, the weighting of VtC fractions based on HERFD-XANES-LCF in combination with theoretical calculations should be further deepened to model XES spectra with their help. Within the scope of this work, a proof-of-principle could be performed for this approach. The method is of particular importance for highly amorphous structures or strongly varying mixtures of substances where no clear calculations can be carried out for individual molecules and modeling of possible components is required.

12 Methods and Analysis tools

The methodical parts are described in the corresponding publications as well. In this chapter, an overview of the whole variance of used methods is presented (chapter 7[130], chapter 8, chapter 10).

12.1 Measurement

12.1.1 Used Beamlines

The full set of measurements was carried out at PETRA III beamlines P64 and P65 at Deutsches Elektronen-Synchrotron (DESY) in Hamburg (Germany). At DESY, the PETRA III storage ring operates at 6 GeV particle energy. The current of the ring is 120 mA in top-up mode to stabilize the current at a 1% deviation.

12.1.1.1 Beamline P64 (DESY)

The photon source at beamline P64 is a 2 m long U33 undulator yielding flux of ~ 10^{12} s^{-1}. The specific energies are selected using liquid nitrogen-cooled Si(111) and Si(311) double crystal monochromator (DCM). It covers an energy range from 4 keV to 44 keV.[176,177]

12.1.1.2 Beamline P65 (DESY)

At beamline P65, an 11-period mini-undulator is the photon source. It provides a photon flux of >10^{11} – 10^{12} s^{-1} and the incident energy is selected using Si(111) and Si(311) water-cooled DCM. The covered energy range is 4 keV to 44 keV.[178]

12.1.2 *Ex-situ* measurements

12.1.2.1 X-ray absorption spectroscopy measurements

X-ray absorption experiments were carried out at the Ni-*K*-edge (8333 eV). To calibrate the spectra energy, Ni-foil was measured and the first inflection point of the XANES spectrum was taken as E_0. The whole sample set was measured as pellets diluted with cellulose. XANES and EXAFS analyses were carried out on every sample.

12.1.2.2 X-ray emission spectroscopy measurements

The incident energy was selected using the (311) reflection of the Si DCM and the energy calibration was performed using the first inflection point of the Ni-foil XANES spectrum (8333 eV). XES and HERFD spectra were recorded at an excitation energy of 8500 eV in the range of 8190-8370 eV with the energy-dispersive VON HAMOS setup using eight Si(444) and Si(531) analyzing crystals for *Kα* and *Kβ*, respectively.[177] Radiation damage studies were carried out for 30 minutes with 30 s step size measuring XANES spectra. Within these time frames, no radiation damage could be detected.

12.1.3 *In-situ* measurements

The *in-situ* XAS measurements were performed at PETRA III beamline P65 at DESY. For the performed *in-situ* experiments, quartz capillaries (WJM Glas, Berlin, Germany) of 1.5 mm diameter were used. To heat the sample a hot-air blower provided by DESY was used. For the control of an overall gas flow of 20 to 25 mL/min, a custom-built gas dosing system of mass flow controllers (Bronkhorst) was used. The amount of catalyst varied between 7 and 10 mg. To perform an online gas analysis and to overview the reaction, a HIDEN mass spectrometer (ExQ) provided by beamline was installed. In this case, the capillary cell was installed horizontally for the XAS measurements. (cf. Figure 26)

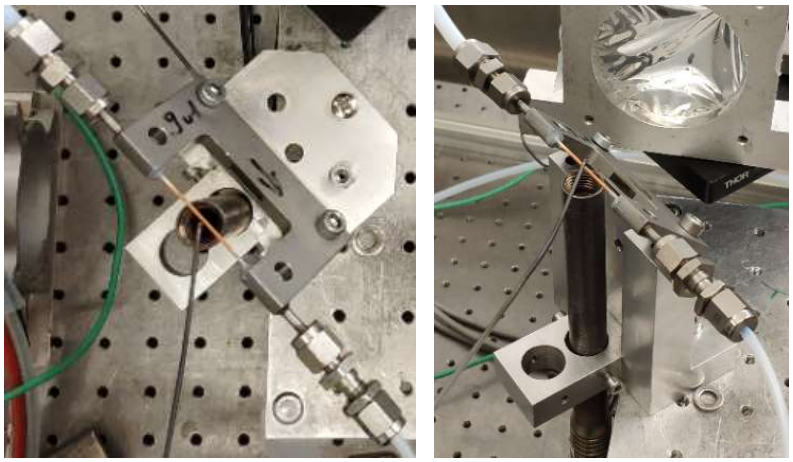

Figure 26: Example of the measurement while using *in-situ* XAS setup at beamline P65 at DESY.

12.2 XAS Analysis

This information is taken from the publications: “Hard X-ray based techniques for structural investigations of CO_2 methanation catalysts prepared by MOF decomposition” published in “Nanoscale” in 2020 (chapter 7)[130] and “Investigation of MOF-derived Ni@C catalysts in the methanation of CO_2 under dynamic gas feed conditions using *in-situ* XAS and PDF” published in “ChemCatChem” in 2023 (chapter 10).

The Athena program package was used for the analysis of the XANES spectra and the data preparation for EXAFS analysis.[179] At the first step of the data evaluation, E_0 was determined by choosing the local first maximum of the derivate. Then the pre- and post-edge regions were defined. After that, the spectra background was removed. For this purpose, a Victoreen-type polynomial was subtracted.[179,180,181] Next, the smooth part of the spectrum was modelled by a piecewise polynomial, to minimize the low-*R* components of the resulting FOURIER transform. Subsequently, the background-subtracted spectrum was divided by its smoothed part and the photon energy was converted to photoelectron wave number *k*. For the detailed EXAFS analysis, the resulting functions were weighted with k^3 and calculated with EXCURV98, which works based on the EXAFS function (cf. Eq. 39) formulated in terms of radial distribution functions:[181,182]

$$\chi(k) = \sum_j S_0^2(K) F_j(k) \int P_j(r_j) \frac{e^{\frac{-2r_j}{\lambda}}}{kr_j^2} \sin\left[2kr_j + \delta_j(k)\right] dr_j \qquad \textbf{Eq. 39}$$

The number of independent points N_{ind} was calculated according to information theory (cf. Eq. 40). The number of the fitted parameter must be less than N_{ind}.[182]

$$N_{ind} = \frac{2\Delta k \Delta R}{\pi} \qquad \textbf{Eq. 40}$$

In this formula, Δk describes the range in *k*-space used for the data analysis, and in ΔR the corresponding radial distance range in the FOURIER filtering process that is observable. For Δk the area from 3 to 10 or 14 in k-space has been used for analysis, leading to Δk of 8 or 11, respectively. In the *R*-space 1 to 6 were used, leading to a ΔR of 5. Thus, the number of independent parameters varied from 25 to 35, respectively.

For the determination of the quality of the fit, two methods were used. The reduced χ^2_{red} (cf. Eq. 41) considers the degree of overdeterminacy of the system and the number of fitted parameters *p*, and allows the comparison of different models directly:[183]

$$\chi^2_{red} = \frac{\left(\frac{N_{ind}}{N}\right)}{N_{ind-p}} \sum_i \left(\frac{k_i^n}{\Sigma_j k_j^n \left| \chi_j^{\exp}(k_j) \right|} \right)^2 \left[\chi^{exp}(k_j) - \chi^{theo}(k_j) \right]^2 \quad \textbf{Eq. 41}$$

With the *R*-factor (cf. Eq. 42), the percentage disagreement between the experiment and the adjusted function is shown. Therefore, it considers both systematic and random errors.[183]

$$R = \sum_i \frac{1}{\sigma_i} [\chi^{exp}(k_i) - \chi^{theo}(k_i)]^2 \quad \textbf{Eq. 42}$$

12.3 FEFF calculations for XES analysis

This information is taken from the publication: “High resolution X-ray absorption and emission spectroscopy for detailed analysis of CO_2 methanation catalysts” published in “ChemPhysChem” in 2023 (chapter 8).

Based on the Full Multiple Scattering (FMS) theory *ab initio* calculations were performed utilizing FEFF 9.6 software.[184] The FMS calculations were performed after Self Consistency Field (SCF) optimization for the muffin-tin atomic potentials was performed for all calculations. For each reference, an individual set of parameters was chosen and adjusted so that the calculated spectrum is as close as possible to the measured HERFD-XANES spectrum (s. Table 1).

Table 1: Individual set of parameters for FEFF calculations of the reference samples. The parameters were set so that the calculated spectrum was in agreement with the measured HERFD-XANES spectrum.

Reference	SCF radius /Å	FMS radius /Å	Electron core-hole exchange-correlation potential	Background function	Core-hole screening
Ni-foil	5.0	5.0	Hedin-Lundqvist[185]	Ground state	Final State Rule[186]
Ni_3C	7.0	7.0	Hedin-Lundqvist	Ground state	RPA[187]
NiO	5.0	5.0	Partially nonlocal	Ground state	No
MOF	5.0	5.0	Hedin-Lundqvist	Ground state	Final State Rule

The structure of Ni foil and NiO were necessary for the calculation. These were taken from the WebAtoms database.[188] The structure for Ni_3C was obtained from the Materials Project database.[189] By modifying a crystal structure of Co(BDC)(PNO) by replacing the Co metals with Ni, the required MOF structure could be obtained, which was then used for the subsequent calculation. However, although the values do not match exactly, based on EXAFS and PDF

analysis, the bond distances are comparable enough to be considered suitable within the margin of error.[130] The entire reference data set was adjusted in energy to fit the experimental data and corrected for the FERMI shift of the respective FEFF calculation to match the condition of the FERMI level equal to 0 eV. For the determination of the occupied and unoccupied electronic states, calculated DOS functions were multiplied by an *erf* step function, with the FERMI energy as a parameter given by the calculations.[190]

$$I_{step} = H\left[\frac{1}{2} + \frac{1}{2}erf\left(\frac{E-P}{\frac{\Gamma_G}{c^*}}\right)\right] \qquad \textbf{Eq. 43}$$

Where *P* is the position of the inflection point of the step, *H* is the height of the function immediately above the step (here: normalized to 1), Γ_G is the core-hole lifetime in Ni 1 *s* level (1.39 eV)[191] and c* is:

$$c^* = 2\sqrt{ln2} \qquad \textbf{Eq. 44}$$

13 References

[1] a) United Nations Security Council, *Climate Change 'Biggest Threat Modern Humans Have Ever Faced'. World-Renowned Naturalist Tells Security Council, Calls for Greater Global Cooperation*. SC/14445, **2021**; b) World Health Organization, *COP26 special report on climate change and health: the health argument for climate action.*, Geneva, **2021**.

[2] a) R. Schlögl, *Angew. Chem., Int. Ed.* **2019**, *58*, 343; b) R. Scholz, M. Beckmann, C. Pieper, M. Muster, R. Weber, *Renewable Sustainable Energy Rev.* **2014**, *35*, 109.

[3] BDEW, Statistisches Bundesamt, BMWK, AGEB, Statistik der Kohlenwirtschaft, ZSW, "Bruttostromerzeugung in Deutschland nach Energieträger in den Jahren 2000 bis 2021", can be found under https://de.statista.com/statistik/daten/studie/156695/umfrage/brutto-stromerzeugung-in-deutschland-nach-energietraegern-seit-2007/, **2021**.

[4] S. Schiebahn, T. Grube, M. Robinius, V. Tietze, B. Kumar, D. Stolten, *Int. J. Hydrogen Energy* **2015**, *40*, 4285.

[5] R. Schlögl, *Angew. Chem., Int. Ed.* **2015**, *54*, 4436.

[6] a) M. Robinius, A. Otto, P. Heuser, L. Welder, K. Syranidis, D. Ryberg, T. Grube, P. Markewitz, R. Peters, D. Stolten, *Energies (Basel, Switz.)* **2017**, *10*, 956; b) M. Sterner, *Bioenergy and renewable power methane in integrated 100% renewable energy systems*. *Limiting global warming by transforming energy systems*. Zugl.: Kassel, Univ., Diss., 2009, Kassel Univ. Press, Kassel, **2009**.

[7] P. Sabatier, J. B. Senderens, *J. Chem. Soc.* **1902**, *82*, 333.

[8] S. Rönsch, J. Schneider, S. Matthischke, M. Schlüter, M. Götz, J. Lefebvre, P. Prabhakaran, S. Bajohr, *Fuel* **2016**, *166*, 276.

[9] M. Sterner, I. Stadler, *Energiespeicher - Bedarf, Technologien, Integration*, Springer, Berlin, **2014**.

[10] Q. Lai, Y. Sun, T. Wang, P. Modi, C. Cazorla, U. B. Demirci, J. R. Ares Fernandez, F. Leardini, K.-F. Aguey-Zinsou, *Adv. Sustainable Syst.* **2019**, *3*, 1900043.

[11] K. Müller, W. Arlt, *Energy Technol.* **2013**, *1*, 501.

[12] G. A. Mills, F. W. Steffgen, *Catal. Rev.: Sci. Eng.* **1974**, *8*, 159.

[13] a) B. Mutz, A. Gänzler, M. Nachtegaal, O. Müller, R. Frahm, W. Kleist, J.-D. Grunwaldt, *Catalysts* **2017**, *7*, 279; b) B. Mutz, P. Sprenger, W. Wang, Di Wang, W. Kleist, J.-D. Grunwaldt, *Appl. Catal., A* **2018**, *556*, 160.

[14] K. F. Kalz, R. Kraehnert, M. Dvoyashkin, R. Dittmeyer, R. Gläser, U. Krewer, K. Reuter, J.-D. Grunwaldt, *ChemCatChem* **2017**, *9*, 17.

[15] P. Frontera, A. Macario, M. Ferraro, P. Antonucci, *Catalysts* **2017**, *7*, 59.

[16] K. J. Lee, J. H. Lee, S. Jeoung, H. R. Moon, *Acc. Chem. Res.* **2017**, *50*, 2684.

[17] L. Oar-Arteta, T. Wezendonk, X. Sun, F. Kapteijn, J. Gascon, *Mater. Chem. Front.* **2017**, *1*, 1709.

[18] J. Bitzer, W. Kleist, *Chem. - Eur. J.* **2019**, *25*, 1866.

[19] a) Y. Kimitsuka, E. Hosono, S. Ueno, H. Zhou, S. Fujihara, *Inorg. Chem.* **2013**, *52*, 14028; b) M. van de Voorde, B. Sels, *Nanotechnology in Catalysis*, Wiley-VCH, Weinheim, **2017**; c) J. M. Zamaro, N. C. Pérez, E. E. Miró, C. Casado, B. Seoane, C. Téllez, J. Coronas, *Chem. Eng. J. (Amsterdam, Neth.)* **2012**, *195-196*, 180; d) J. Li, B. Wang, Y. Qin, Q. Tao, L. Chen, *Catal. Sci. Technol.* **2019**, *9*, 3726.

[20] a) M. Bauer, H. Bertagnolli in *Methods in Physical Chemistry* (Eds.: R. Schäfer, P. C. Schmidt), Wiley-VCH, Weinheim, **2012**, pp. 231–270; b) R. P. Struis, T. J. Schildhauer, I. Czekaj, M. Janousch, S. M. Biollaz, C. Ludwig, *Appl. Catal., A* **2009**, *362*, 121; c) S. Schuster, E. Klemm, M. Bauer, *Chem. - Eur. J.* **2012**, *18*, 15831.

[21] a) M. Bauer, C. Gastl, *Phys. Chem. Chem. Phys.* **2010**, *12*, 5575; b) M. Bauer, T. Kauf, J. Christoffers, H. Bertagnolli, *Phys. Chem. Chem. Phys.* **2005**, *7*, 2664; c) A. J. Dent, *Top. Catal.* **2002**, *18*, 27; d) C. C. Scarborough, S. Sproules, T. Weyhermüller, S. DeBeer, K. Wieghardt, *Inorg. Chem.* **2011**, *50*, 12446; e) S. C. E. Stieber, C. Milsmann, J. M. Hoyt, Z. R. Turner, K. D. Finkelstein, K. Wieghardt, S. DeBeer, P. J. Chirik, *Inorg. Chem.* **2012**, *51*, 3770.

[22] a) G. B. Kauffman, *Platinum Met. Rev.* **1999**, *43*, 122; b) R. Hoffmann, *Am. Sci.* **1998**, *86*, 326.

[23] A. Behr, P. Neubert, *Applied homogeneous catalysis*, Wiley-VCH, Weinheim, **2012**.

[24] W. Ostwald, *Z. Phys. Chem. (Berlin, Ger.)* **1894**, *15U*, 699.

[25] W. Ostwald, *Nature* **1902**, *65*, 522.

[26] H. Hildebrand, *The Nobel Prize in Chemistry 1909 - Award ceremony speech*, **1909**.

[27] F. Haber, G. van Oordt, *Z. Anorg. Chem.* **1905**, *44*, 341.

[28] J. M. Thomas, W. J. Thomas, *Principles and practice of heterogeneous catalysis*, Wiley-VCH; Ciando, Weinheim, München, **2015**.

[29] F. Haber, DE235421C, **1908**.

[30] a) M. Baerns, A. Behr, A. Brehm, *Technische Chemie*, Wiley-VCH, Weinheim, **2006**; b) A. Mittasch, *Ber. Dtsch. Chem. Ges. B* **1926**, *59*, 13; c) G. Ertl, H. Knözinger, F. Schüth, J. Weitkamp (Eds.) *Handbook of Heterogeneous Catalysis*, Wiley-VCH, Weinheim, **2008**.

[31] M. Appl in *Ullmann's Encyclopedia of Industrial Chemistry*, Wiley-VCH, Weinheim, **2000**.

[32] a) G. Ertl, *Catal. Rev.: Sci. Eng.* **1980**, *21*, 201; b) A. F. Holleman, E. Wiberg, N. Wiberg, *Anorganische Chemie*, De Gruyter, Berlin, Boston, **2017**.

[33] A. F. Holleman, N. Wiberg, E. Wiberg, *Lehrbuch der Anorganischen Chemie*, De Gruyter, Berlin, **2007**.

[34] a) A. Hermann, *Phys. Bl.* **1965**, *21*, 168; b) V. Smil, "Nitrogen cycle and world food production", can be found under http://vaclavsmil.com/wp-content/uploads/docs/smil-article-worldagriculture.pdf, **2012**.

[35] J. Hagen, *Industrial catalysis*. *A practical approach*, Wiley-VCH, Weinheim, **2008**.

[36] B. Cornils, W. A. Herrmann, M. Rasch, *Angew. Chem.* **1994**, *106*, 2219.

[37] R. F. Heck, D. S. Breslow, *J. Am. Chem. Soc.* **1961**, *83*, 4023.

[38] O. Roelen, DE849548C, **1938**.

[39] a) G. Natta, *Angew. Chem.* **1964**, *76*, 553; b) K. Ziegler, E. Holzkamp, H. Breil, H. Martin, *Angew. Chem.* **1955**, *67*, 541.

[40] M. D. Lechner, *Makromolekulare Chemie*. *Ein Lehrbuch für Chemiker, Physiker, Materialwissenschaftler und Verfahrenstechniker*, Birkhäuser, Basel, **2010**.

[41] a) J. Heveling, *J. Chem. Educ.* **2012**, *89*, 1530; b) M. Schmal, *Heterogeneous Catalysis and its Industrial Applications*, Springer, Berlin, **2016**.

[42] a) P. T. Anastas (Ed.) *Green chemistry*, Wiley-VCH, Chichester, **2012**; b) A. Behr, D. W. Agar, J. Jörissen, *Einführung in die Technische Chemie*, Spektrum Akademischer Verlag, Heidelberg, **2009**.

[43] M. Röper, *Chem. Unserer Zeit* **2006**, *40*, 126.

[44] W. Wang, S. Wang, X. Ma, J. Gong, *Chem. Soc. Rev.* **2011**, *40*, 3703.

[45] J. Gao, Q. Liu, F. Gu, B. Liu, Z. Zhong, F. Su, *RSC Adv.* **2015**, *5*, 22759.

[46] J. Gao, Y. Wang, Y. Ping, D. Hu, G. Xu, F. Gu, F. Su, *RSC Adv.* **2012**, *2*, 2358.

[47] S.-I. Fujita, N. Takezawa, *Chem. Eng. J. (Amsterdam, Neth.)* **1997**, *68*, 63.

[48] S. Fujita, H. Terunuma, M. Nakamura, N. Takezawa, *Ind. Eng. Chem. Res.* **1991**, *30*, 1146.

[49] I. A. Fisher, A. T. Bell, *J. Catal.* **1996**, *162*, 54.

[50] a) J.-N. Park, E. W. McFarland, *J. Catal.* **2009**, *266*, 92; b) H. Y. Kim, H. M. Lee, J.-N. Park, *J. Phys. Chem. C* **2010**, *114*, 7128.

[51] a) T. Franken, A. Heel, *J. CO2 Util.* **2020**, *39*, 101175; b) Z. Baysal, S. Kureti, *Appl. Catal., B* **2020**, *262*, 118300; c) J. Kirchner, C. Zambrzycki, S. Kureti, R. Güttel, *Chem. Ing. Tech.* **2020**, *92*, 603.

[52] G. Zhou, T. Wu, H. Xie, X. Zheng, *Int. J. Hydrogen Energy* **2013**, *38*, 10012.

[53] a) M. C. Bacariza, I. Graça, J. M. Lopes, C. Henriques, *ChemCatChem* **2019**, *11*, 2388; b) M. Mihet, G. Blanita, M. Dan, L. Barbu-Tudoran, M. D. Lazar, *J. Nanosci. Nanotechnol.* **2019**, *19*, 3187.

[54] A. Beuls, C. Swalus, M. Jacquemin, G. Heyen, A. Karelovic, P. Ruiz, *Appl. Catal., B* **2012**, *113-114*, 2.

[55] a) R. Büchel, A. Baiker, S. E. Pratsinis, *Appl. Catal., A* **2014**, *477*, 93; b) A. Karelovic, P. Ruiz, *J. Catal.* **2013**, *301*, 141.

[56] G. Garbarino, D. Bellotti, P. Riani, L. Magistri, G. Busca, *Int. J. Hydrogen Energy* **2015**, *40*, 9171.

[57] a) K. P. Brooks, J. Hu, H. Zhu, R. J. Kee, *Chem. Eng. Sci.* **2007**, *62*, 1161; b) C. Janke, M. S. Duyar, M. Hoskins, R. Farrauto, *Appl. Catal., B* **2014**, *152-153*, 184; c) J. H. Kwak, L. Kovarik, J. Szanyi, *ACS Catal.* **2013**, *3*, 2449; d) K. Müller, M. Städter, F. Rachow, D. Hoffmannbeck, D. Schmeißer, *Environ. Earth Sci.* **2013**, *70*, 3771; e) D. C. Upham, A. R. Derk, S. Sharma, H. Metiu, E. W. McFarland, *Catal. Sci. Technol.* **2015**, *5*, 1783.

[58] G. Garbarino, P. Riani, L. Magistri, G. Busca, *Int. J. Hydrogen Energy* **2014**, *39*, 11557.

[59] S. He, C. Li, H. Chen, D. Su, B. Zhang, X. Cao, B. Wang, M. Wei, D. G. Evans, X. Duan, *Chem. Mater.* **2013**, *25*, 1040.

[60] J. Liu, C. Li, F. Wang, S. He, H. Chen, Y. Zhao, M. Wei, D. G. Evans, X. Duan, *Catal. Sci. Technol.* **2013**, *3*, 2627.

[61] S. Tada, T. Shimizu, H. Kameyama, T. Haneda, R. Kikuchi, *Int. J. Hydrogen Energy* **2012**, *37*, 5527.

[62] Y. Li, Q. Zhang, R. Chai, G. Zhao, Y. Liu, Y. Lu, F. Cao, *AIChE J.* **2015**, *61*, 4323.

[63] M. A. A. Aziz, A. A. Jalil, S. Triwahyono, A. Ahmad, *Green Chem.* **2015**, *17*, 2647.

[64] J. Kopyscinski, T. J. Schildhauer, S. M. Biollaz, *Fuel* **2010**, *89*, 1763.

[65] S. Weber, R. T. Zimmermann, J. Bremer, K. L. Abel, D. Poppitz, N. Prinz, J. Ilsemann, S. Wendholt, Q. Yang, R. Pashminehazar et al., *ChemCatChem* **2022**, *14*.

[66] H. Liu, X. Zou, X. Wang, X. Lu, W. Ding, *J. Nat. Gas Chem.* **2012**, *21*, 703.

[67] M. Guo, G. Lu, *Catal. Commun.* **2014**, *54*, 55.

[68] T. Abe, M. Tanizawa, K. Watanabe, A. Taguchi, *Energy Environ. Sci.* **2009**, *2*, 315.

[69] N. Perkas, G. Amirian, Z. Zhong, J. Teo, Y. Gofer, A. Gedanken, *Catal. Lett.* **2009**, *130*, 455.

[70] M. Yamasaki, H. Habazaki, K. Asami, K. Izumiya, K. Hashimoto, *Catal. Commun.* **2006**, *7*, 24.

[71] J. Ren, X. Qin, J.-Z. Yang, Z.-F. Qin, H.-L. Guo, J.-Y. Lin, Z. Li, *Fuel Process. Technol.* **2015**, *137*, 204.

[72] a) F. Ocampo, B. Louis, A.-C. Roger, *Appl. Catal., A* **2009**, *369*, 90; b) Q. Pan, J. Peng, T. Sun, D. Gao, S. Wang, S. Wang, *Fuel Process. Technol.* **2014**, *123*, 166.

[73] P. U. Aldana, F. Ocampo, K. Kobl, B. Louis, F. Thibault-Starzyk, M. Daturi, P. Bazin, S. Thomas, A. C. Roger, *Catal. Today* **2013**, *215*, 201.

[74] M. Cai, J. Wen, W. Chu, X. Cheng, Z. Li, *J. Nat. Gas Chem.* **2011**, *20*, 318.

[75] Y. Li, G. Lu, J. Ma, *RSC Adv.* **2014**, *4*, 17420.

[76] a) H. Takano, K. Izumiya, N. Kumagai, K. Hashimoto, *Appl. Surf. Sci.* **2011**, *257*, 8171; b) M. Yamasaki, M. Komori, E. Akiyama, H. Habazaki, A. Kawashima, K. Asami, K. Hashimoto, *Mater. Sci. Eng., A* **1999**, *267*, 220.

[77] S. Hwang, U. G. Hong, J. Lee, J. H. Baik, D. J. Koh, H. Lim, I. K. Song, *Catal. Lett.* **2012**, *142*, 860.

[78] a) T. Bligaard, J. K. Nørskov, S. Dahl, J. Matthiesen, C. H. Christensen, J. Sehested, *J. Catal.* **2004**, *224*, 206; b) M. P. Andersson, T. Bligaard, A. L. Kustov, K. E. Larsen, J. Eeley, T. Johannessen, C. H. Christensen, J. K. Nørskov, *J. Catal.* **2006**, *239*, 501.

[79] a) D. Tian, Z. Liu, D. Li, H. Shi, W. Pan, Y. Cheng, *Fuel* **2013**, *104*, 224; b) A. L. Kustov, A. M. Frey, K. E. Larsen, T. Johannessen, J. K. Nørskov, C. H. Christensen, *Appl. Catal., A* **2007**, *320*, 98.

[80] J. Sehested, K. E. Larsen, A. L. Kustov, A. M. Frey, T. Johannessen, T. Bligaard, M. P. Andersson, J. K. Nørskov, C. H. Christensen, *Top. Catal.* **2007**, *45*, 9.

[81] S.-H. Kang, J.-H. Ryu, J.-H. Kim, S.-J. Seo, Y.-D. Yoo, P. S. Sai Prasad, H.-J. Lim, C.-D. Byun, *Korean J. Chem. Eng.* **2011**, *28*, 2282.

[82] B. Mutz, M. Belimov, W. Wang, P. Sprenger, M.-A. Serrer, Di Wang, P. Pfeifer, W. Kleist, J.-D. Grunwaldt, *ACS Catal.* **2017**, *7*, 6802.

[83] D. Schmider, L. Maier, O. Deutschmann, *Ind. Eng. Chem. Res.* **2021**, *60*, 5792.

[84] L. Li, W. Zeng, M. Song, X. Wu, G. Li, C. Hu, *Catalysts* **2022**, *12*, 244.

[85] S. J. Choe, H. J. Kang, S. J. Kim, S. B. Park, D. H. Park, D. S. Huh, *Bull. Korean Chem. Soc.* **2005**, *26*, 1682.

[86] a) D. E. Peebles, D. W. Goodman, J. M. White, *J. Phys. Chem.* **1983**, *87*, 4378; b) J. Ren, H. Guo, J. Yang, Z. Qin, J. Lin, Z. Li, *Appl. Surf. Sci.* **2015**, *351*, 504.

[87] J. Sehested, S. Dahl, J. Jacobsen, J. R. Rostrup-Nielsen, *J. Phys. Chem. B* **2005**, *109*, 2432.

[88] Z. Wang in *Comprehensive organic name reactions and reagents* (Ed.: Z. Wang), John Wiley & Sons, Inc, Chichester, **2010**.

[89] a) C. Schild, A. Wokaun, R. A. Koeppel, A. Baiker, *J. Phys. Chem.* **1991**, *95*, 6341; b) X. Wang, Y. Hong, H. Shi, J. Szanyi, *J. Catal.* **2016**, *343*, 185.

[90] A. Westermann, B. Azambre, M. C. Bacariza, I. Graça, M. F. Ribeiro, J. M. Lopes, C. Henriques, *Appl. Catal., B* **2015**, *174-175*, 120.

[91] Q. Pan, J. Peng, T. Sun, S. Wang, S. Wang, *Catal. Commun.* **2014**, *45*, 74.

[92] C. Vogt, M. Monai, G. J. Kramer, B. M. Weckhuysen, *Nat. Catal.* **2019**, *2*, 188.

[93] a) C. Vogt, E. Groeneveld, G. Kamsma, M. Nachtegaal, L. Lu, C. J. Kiely, P. H. Berben, F. Meirer, B. M. Weckhuysen, *Nat. Catal.* **2018**, *1*, 127; b) C. Heine, B. A. J. Lechner, H. Bluhm, M. Salmeron, *J. Am. Chem. Soc.* **2016**, *138*, 13246; c) M.-C. Silaghi, A. Comas-Vives, C. Copéret, *ACS Catal.* **2016**, *6*, 4501.

[94] G. Weatherbee, *J. Catal.* **1982**, *77*, 460.

[95] X. Lin, S. Wang, W. Tu, Z. Hu, Z. Ding, Y. Hou, R. Xu, W. Dai, *Catal. Sci. Technol.* **2019**, *9*, 731.

[96] G. Bunker, *Introduction to XAFS*. *A practical guide to X-ray absorption fine structure spectroscopy*, Cambridge University Press, Cambridge, New York, **2010**.

[97] B. K. Teo, *EXAFS: Basic Principles and Data Analysis*, Springer, Berlin, **1986**.

[98] A. Sommerfeld, *Ann. Phys.* **1916**, *356*, 1.

[99] M. Siegbahn, *Nature* **1916**, *96*, 676.

[100] D. Attwood, *Soft X-Rays and Extreme Ultraviolet Radiation*, Cambridge University Press, Cambridge, **1999**.

[101] a) Z. Szakács, E. Vauthey, *J. Phys. Chem. Lett.* **2021**, *12*, 4067; b) C. W. Stark, M. Rammo, A. Trummal, M. Uudsemaa, J. Pahapill, M.-M. Sildoja, S. Tshepelevitsh, I. Leito, D. C. Young, B. Szymański et al., *Angew. Chem., Int. Ed.* **2022**, *61*, e202212581.

[102] P. Glatzel, U. Bergmann, *Coord. Chem. Rev.* **2005**, *249*, 65.

[103] R. D. Evans, *The atomic nucleus*, Krieger Publishing, Malabar, FL, **1985**.

[104] F. W. Lytle, *J. Synchrotron Radiat.* **1999**, *6*, 123.

[105] H. Fricke., *Phys. Rev.* **1920**, *16*, 202.

[106] G. Hertz, *Z. Physik* **1920**, *3*, 19.

[107] a) A. E. Lindh, *Z. Physik* **1921**, *6*, 303; b) A. E. Lindh, *Z. Physik* **1925**, *31*, 210; c) A. E. Lindh, *Z. Physik* **1930**, *63*, 106.

[108] a) D. Coster, J. Veldkamp, *Z. Physik* **1931**, *70*, 306; b) D. Coster, J. Veldkamp, *Z. Physik* **1932**, *74*, 191; c) G. A. Lindsay, *Z. Physik* **1931**, *71*, 735; d) B. Kievit, G. A. Lindsay, *Phys. Rev.* **1930**, *36*, 648.

[109] a) W. Kossel, *Z. Physik* **1920**, *1*, 119; b) R. d. L. Kronig, *Z. Physik* **1931**, *70*, 317; c) R. d. L. Kronig, *Z. Physik* **1932**, *75*, 191; d) R. d. L. Kronig, *Z. Physik* **1932**, *75*, 468.

[110] L. V. Azároff, *Rev. Mod. Phys.* **1963**, *35*, 1012.

[111] D. E. Sayers, E. A. Stern, F. W. Lytle, *Phys. Rev. Lett.* **1971**, *27*, 1204.

[112] E. A. Stern, *Phys. Rev. B: Condens. Matter Mater. Phys.* **1974**, *10*, 3027.

[113] F. W. Lytle, D. E. Sayers, E. A. Stern, *Phys. Rev. B: Condens. Matter Mater. Phys.* **1975**, *11*, 4825.

[114] F. W. Lytle, D. E. Sayers, E. B. Moore, *Appl. Phys. Lett.* **1974**, *24*, 45.

[115] E. A. Stern, D. E. Sayers, F. W. Lytle, *Phys. Rev. B: Condens. Matter Mater. Phys.* **1975**, *11*, 4836.

[116] a) L. Fang, S. Seifert, R. E. Winans, T. Li, *Small* **2022**, *18*, e2106017; b) H. Huang, A. E. Russell, *Curr. Opin. Electrochem.* **2021**, *27*, 100681.

[117] D. C. Koningsberger, B. L. Mojet, G. E. van Dorssen, D. E. Ramaker, *Top. Catal.* **2000**, *10*, 143.

[118] J. H. Sinfelt, G. H. Via, F. W. Lytle, *Catal. Rev.: Sci. Eng.* **1984**, *26*, 81.

[119] D. C. Koningsberger (Ed.) *A Wiley Interscience publication*, *Vol. 92*, Wiley-VCH, New York, NY, **1988**.

[120] G. F. Knoll, *Radiation detection and measurement*, Wiley-VCH, Hoboken, NJ, **2010**.

[121] S. Calvin, *XAFS for Everyone*, CRC Press, Hoboken, NJ, **2013**.

[122] H. Bertagnolli, T. S. Ertel, *Angew. Chem.* **1994**, *106*, 15.

[123] M. Bauer, H. Bertagnolli, *Bunsenmagazin* **2007**, *9*, 216.

[124] J. Yano, V. K. Yachandra, *Photosynth. Res.* **2009**, *102*, 241.

[125] M. D. Newton, *Chem. Rev. (Washington, DC, U. S.)* **1991**, *91*, 767.

[126] M. L. Baker, M. W. Mara, J. J. Yan, K. O. Hodgson, B. Hedman, E. I. Solomon, *Coord. Chem. Rev.* **2017**, *345*, 182.

[127] T. Yamamoto, *X-Ray Spectrom.* **2008**, *37*, 572.

[128] T. E. Westre, P. Kennepohl, J. G. DeWitt, B. Hedman, K. O. Hodgson, E. I. Solomon, *J. Am. Chem. Soc.* **1997**, *119*, 6297.

[129] a) M. Wilke, F. Farges, P.-E. Petit, G. E. Brown, F. Martin, *Am. Mineral.* **2001**, *86*, 714; b) M. Wilke, C. Schmidt, F. Farges, V. Malavergne, L. Gautron, A. Simionovici, M. Hahn, P.-E. Petit, *Chem. Geol.* **2006**, *229*, 144.

[130] N. Prinz, L. Schwensow, S. Wendholt, A. Jentys, M. Bauer, W. Kleist, M. Zobel, *Nanoscale* **2020**, 15800.

[131] J. W. Niemantsverdriet, *Spectroscopy in Catalysis*, Wiley-VCH, Weinheim, **2007**.

[132] P. A. Lee, J. B. Pendry, *Phys. Rev. B: Condens. Matter Mater. Phys.* **1975**, *11*, 2795.

[133] S. J. Gurman, R. F. Pettifer, *Philos. Mag. B* **1979**, *40*, 345.

[134] a) C. A. Ashley, S. Doniach, *Phys. Rev. B: Condens. Matter Mater. Phys.* **1975**, *11*, 1279; b) P. L. Lee, F. Boehm, P. Vogel, *Phys. Lett. A* **1977**, *63*, 251; c) B.-K. Teo, B. A. Averill, *Biochem. Biophys. Res. Commun.* **1979**, *88*, 1454; d) P. A. Lee, G. Beni, *Phys. Rev. B: Condens. Matter Mater. Phys.* **1977**, *15*, 2862.

[135] a) M. Benfatto, S. Della Longa, K. Hatada, K. Hayakawa, W. Gawelda, C. Bressler, M. Chergui, *J. Phys. Chem. B* **2006**, *110*, 14035; b) K. Hayakawa, K. Hatada, P. D'Angelo, S. Della Longa, C. R. Natoli, M. Benfatto, *J. Am. Chem. Soc.* **2004**, *126*, 15618; c) D.

Cabaret, P. Sainctavit, P. Ildefonse, A.-M. Flank, *J. Phys.: Condens. Matter* **1996**, *8*, 3691.

[136] C. T. Chantler in *International Tables for Crystallography (2021)* (Eds.: H. Fuess, T. Hahn, A. J. C. Wilson, U. Müller), Wiley–Blackwell, **2021**.

[137] a) W. H. Bragg, W. L. Bragg, *Proc. R. Soc. Lond. A* **1913**, *88*, 428; b) W. Friedrich, P. Knipping, M. Laue, *Ann. Phys.* **1913**, *346*, 971.

[138] W. H. Bragg, W. L. Bragg, *X rays and crystal structure*, George Bell and Sons, Ltd., London, **1915**.

[139] P. Glatzel, R. Alonso-Mori, D. Sokaras in *X-ray absorption and X-ray emission spectroscopy. Theory and applications* (Eds.: J. A. van Bokhoven, C. Lamberti), John Wiley & Sons, Inc, Chichester, **2016**, pp. 125–149.

[140] a) A. H. Compton, *Phys. Rev.* **1923**, *21*, 483; b) A. H. Compton, *Phys. Rev.* **1923**, *22*, 409.

[141] H. Moseley, *Philos. Mag. (1798-1977)* **1913**, *26*, 1024.

[142] H. H. Johann, *Z. Physik* **1931**, *69*, 185.

[143] T. Johansson, *Z. Physik* **1933**, *82*, 507.

[144] L. v. Hámos, *Naturwissenschaften (1913-2014)* **1932**, *20*, 705.

[145] a) B. B. Watson, *Rev. Sci. Instrum.* **1937**, *8*, 480; b) J. W. M. DuMond, B. B. Watson, *Phys. Rev.* **1934**, *46*, 316; c) C. Bonnelle, *Phys. Today* **2001**, *54*, 88; d) Y. Cauchois, *J. Phys. Radium* **1932**, *3*, 320.

[146] B. Beckhoff (Ed.) *Handbook of practical X-Ray fluorescence analysis*. *With 53 tables*, Springer, Berlin, **2006**.

[147] M. Rovezzi, P. Glatzel, *Semicond. Sci. Technol.* **2014**, *29*, 23002.

[148] a) H. A. Kramers, W. Heisenberg, *Z. Physik* **1925**, *31*, 681; b) J. J. Sakurai, *Advanced quantum mechanics*, Addison-Wesley, Reading, Mass., **1998**.

[149] M. Nowakowski, A. Kalinko, J. Szlachetko, R. Fanselow, M. Bauer, *J. Anal. At. Spectrom.* **2022**, *37*, 2383.

[150] B. D. Cullity, B. D. Cullity, *Elements of x-ray diffraction*, Addison-Wesley, Reading, Mass., **1978**.

[151] X. Wang, F. M. F. de Groot, S. P. Cramer, *Phys. Rev. B Condens. Matter* **1997**, *56*, 4553.

[152] a) R. Manne in *Inner-Shell and X-Ray Physics of Atoms and Solids* (Eds.: D. J. Fabian, H. Kleinpoppen, L. M. Watson), Springer - Verlag New York Inc., New York, NY, **1981**, pp. 699–706; b) I. Lindgren, *J. Electron Spectrosc. Relat. Phenom.* **2004**, *137-140*, 59.

[153] M. Vacher, K. Kunnus, M. G. Delcey, K. J. Gaffney, M. Lundberg, *Struct. Dyn.* **2020**, *7*, 44102.

[154] P. Glatzel, T.-C. Weng, K. Kvashnina, J. Swarbrick, M. Sikora, E. Gallo, N. Smolentsev, R. A. Mori, *J. Electron Spectrosc. Relat. Phenom.* **2013**, *188*, 17.

[155] J. T. Henthorn, S. DeBeer, *Inorg. Chem.* **2022**, *61*, 2760.

[156] P. Glatzel, *Dissertation*, Universität Hamburg, Hamburg, **2001**.

[157] a) G. Vankó, T. Neisius, G. Molnar, F. Renz, S. Karpati, A. Shukla, F. M. F. de Groot, *J. Phys. Chem. B* **2006**, *110*, 11647; b) G. Vankó, J.-P. Rueff, A. Mattila, Z. Németh, A. Shukla, *Phys. Rev. B: Condens. Matter Mater. Phys.* **2006**, *73*; c) J. P. Rueff, A. Shukla, A. Kaprolat, M. Krisch, M. Lorenzen, F. Sette, R. Verbeni, *Phys. Rev. B Condens. Matter* **2001**, *63*; d) J.-P. Rueff, C.-C. Kao, V. V. Struzhkin, J. Badro, J. Shu, R. J. Hemley, H. K. Mao, *Phys. Rev. Lett.* **1999**, *82*, 3284; e) G. Peng, F. M. F. deGroot, K. Hämäläinen, J. A. Moore, X. Wang, M. M. Grush, J. B. Hastings, D. P. Siddons, W. H. Armstrong, *J. Am. Chem. Soc.* **1994**, *116*, 2914; f) S. D. Gamblin, D. S. Urch, *J. Electron Spectrosc. Relat. Phenom.* **2001**, *113*, 179.

[158] U. Bergmann, C. R. Horne, T. J. Collins, J. M. Workman, S. P. Cramer, *Chem. Phys. Lett.* **1999**, *302*, 119.

[159] a) U. Bergmann, P. Glatzel, *Photosynth. Res.* **2009**, *102*, 255; b) F. de Groot, *Chem. Rev. (Washington, DC, U. S.)* **2001**, *101*, 1779.

[160] N. Lee, T. Petrenko, U. Bergmann, F. Neese, S. DeBeer, *J. Am. Chem. Soc.* **2010**, *132*, 9715.

[161] V. Martin-Diaconescu, K. N. Chacón, M. U. Delgado-Jaime, D. Sokaras, T.-C. Weng, S. DeBeer, N. J. Blackburn, *Inorg. Chem.* **2016**, *55*, 3431.

[162] C. J. Pollock, S. DeBeer, *J. Am. Chem. Soc.* **2011**, *133*, 5594.

[163] J. A. van Bokhoven, C. Lamberti (Eds.) *X-ray absorption and X-ray emission spectroscopy. Theory and applications*, John Wiley & Sons, Inc, Chichester, **2016**.

[164] M.-A. Arrio, S. Rossano, C. Brouder, L. Galoisy, G. Calas, *Europhys. Lett.* **2000**, *51*, 454.

[165] a) K. Hämäläinen, Siddons, J. B. Hastings, Berman, *Phys. Rev. Lett.* **1991**, *67*, 2850; b) F. de Groot, G. Vankó, P. Glatzel, *J. Phys.: Condens. Matter* **2009**, *21*, 104207.

[166] a) A. J. Atkins, C. R. Jacob, M. Bauer, *Chem. - Eur. J.* **2012**, 7021; b) M. Bauer, *Phys. Chem. Chem. Phys.* **2014**, *16*, 13827; c) N. J. Vollmers, P. Müller, A. Hoffmann, S. Herres-Pawlis, M. Rohrmüller, W. G. Schmidt, U. Gerstmann, M. Bauer, *Inorg. Chem.* **2016**, *55*, 11694.

[167] a) P. Eisenberger, B. M. Kincaid, *Chem. Phys. Lett.* **1975**, *36*, 134; b) B. M. Kincaid, P. Eisenberger, *Phys. Rev. Lett.* **1975**, *34*, 1361.

[168] J. C. Maxwell, *Phil. Trans. R. Soc.* **1865**, *155*, 459.

[169] S. Mobilio, F. Boscherini, C. Meneghini (Eds.) *Synchrotron Radiation*. *Basics, Methods and Applications*, Springer, Berlin, **2014**.

[170] H. Winick in *Proceedings of the 1997 Particle Accelerator Conference*. *Vancouver, B.C., Canada, 12 - 16 May 1997*, Institute of Electrical and Electronics Engineers (IEEE), Piscataway, NJ, **1998**, pp. 37–41.

[171] P. G. O'Shea, H. P. Freund, *Science* **2001**, *292*, 1853.

[172] a) M. A. Naumova, A. Kalinko, J. W. L. Wong, M. Abdellah, H. Geng, E. Domenichini, J. Meng, S. A. Gutierrez, P.-A. Mante, W. Lin et al., *J. Phys. Chem. Lett.* **2020**, *11*, 2133; b) A. L. Viotti, S. Alisauskas, A. Bin Wahid, P. Balla, N. Schirmel, B. Manschwetus, I. Hartl, C. M. Heyl, *J. Synchrotron Radiat.* **2021**, *28*, 36.

[173] K. Nass, L. Foucar, T. R. M. Barends, E. Hartmann, S. Botha, R. L. Shoeman, R. B. Doak, R. Alonso-Mori, A. Aquila, S. Bajt et al., *J. Synchrotron Radiat.* **2015**, *22*, 225.

[174] E. Kleimenov, A. Bergamaschi, J. A. van Bokhoven, M. Janousch, B. Schmitt, M. Nachtegaal, *J. Phys.: Conf. Ser.* **2009**, *190*, 12035.

[175] a) J. K. Kowalska, F. A. Lima, C. J. Pollock, J. A. Rees, S. DeBeer, *Isr. J. Chem.* **2016**, *56*, 803; b) P. Zimmermann, S. Peredkov, P. M. Abdala, S. DeBeer, M. Tromp, C. Müller, J. A. van Bokhoven, *Coord. Chem. Rev.* **2020**, *423*, 213466.

[176] a) W. A. Caliebe, V. Murzin, A. Kalinko, M. Görlitz in *AIP Conference Proceedings*, Author(s), **2019**, p. 60031; b) Deutsches Elektronen Synchrotron (DESY), "P64 - X-Ray Absorption Spectroscopy. Unified Data Sheet", can be found under https://photon-science.desy.de/facilities/petra_iii/beamlines/p64_advanced_xafs/unified_data_sheet/index_eng.html, **2023**.

[177] A. Kalinko, W. A. Caliebe, R. Schoch, M. Bauer, *J. Synchrotron Radiat.* **2020**, *27*, 31.

[178] a) Deutsches Elektronen Synchrotron (DESY), "P65 Applied X-ray Absorption Spectroscopy", can be found under https://photon-science.desy.de/facilities/petra_iii/beamlines/p65_applied_xafs/index_eng.html, **2023**; b) E. Welter, R. Chernikov, M. Herrmann, R. Nemausat in *AIP Conference Proceedings*, Author(s), **2019**, p. 40002.

[179] B. Ravel, M. Newville, *J. Synchrotron Radiat.* **2005**, *12*, 537.

[180] a) T. S. Ertel, H. Bertagnolli, S. Hückmann, U. Kolb, D. Peter, *Appl. Spectrosc.* **1992**, *46*, 690; b) M. Newville, *J. Synchrotron Radiat.* **2001**, *8*, 322.

[181] N. Binsted, S. S. Hasnain, *J. Synchrotron Radiat.* **1996**, *3*, 185.

[182] N. Binsted, F. Mosselmans (Eds.), Daresbury, UK.

[183] M. Bauer, H. Bertagnolli, *J. Phys. Chem. B* **2007**, *111*, 13756.

[184] J. J. Rehr, J. J. Kas, F. D. Vila, M. P. Prange, K. Jorissen, *Phys. Chem. Chem. Phys.* **2010**, *12*, 5503.

[185] M. Roy, S. J. Gurman, *J. Synchrotron Radiat.* **2001**, *8*, 1095.

[186] C. Lamberti, J. A. van Bokhoven (Eds.) *X-ray absorption and X-ray emission spectroscopy*. *Theory and applications*, John Wiley & Sons, Inc, Chichester, **2015**.

[187] J. J. Rehr, J. J. Kas, M. P. Prange, A. P. Sorini, Y. Takimoto, F. D. Vila, *C. R. Phys.* **2009**, *10*, 548.

[188] Ni, "WebAtoms. The Atoms.inp archive", can be found under https://millenia.cars.aps.anl.gov/atomsdb/.

[189] Ni3C, mp-7586, *Materials Data on Ni_3C by Materials Project*, Ernest Orlando Lawrence Berkeley National Laboratory (LBNL), United States: N. p., **2020**.

[190] J. Stöhr in *NEXAFS Spectroscopy* (Eds.: H. Lotsch, G. Ertl, R. Gomer), Springer, Berlin, **1996**, pp. 211–238.

[191] J. L. Campbell, T. Papp, *At. Data Nucl. Data Tables* **2001**, *77*, 1.

14 Appendices

14.1 Abbreviations

Table 2: List of abbreviations and symbols.

Abbreviation/Symbol	Description
$\hat{O}'^{\dagger}$	Outgoing transition operator
$\hat{H}$	Perturbation Hamiltonian
$\mu_0(E)$	Atomic background function
μE	Absorption coefficient
$\mu_{pre\text{-}edge}$	Pre-edge function
2D	Two dimensional
a. u.	Arbitrary unit
Abs	X-ray absorbing atom
A_{fac}	Amplitude reducing factor; cf. $S_i(k)$
$A_j(k)$	Amplitude of scattering intensitiy in j^{th} shell
ATR-IR	Attenuated total reflection – infrared spectroscopy
BASF	Badische Anilin- und Soda Fabrik
BDC	Benzene-1,4-dicarboxylate
BET	Brunauer-Emmett-Teller
BPI	Bavarian Polymer Institute
Bs	Backscattering atom
cf.	Confer (*latin:* compare*)*
CN	Coordination number
CtC	Core-to-core
d	Thickness
d (Eq. 37)	Distance between two parallel lattice planes
DCM	Double crystal monochromator
DESY	Deutsches Elektronen Synchrotron
DFG	Deutsche Forschungsgemeinschaft
DMF	Dimethylformamide
DOS	Density of states
dPDF	Differential PDF
DTG	Derivative thermogravimetry
E	Energy

E (Eq. 17)	Photon number
e. g.	exempli gratia (*latin*: for example)
E_0	Zero-point energy
E_{bind}	Binding energy
E_f (Eq. 35 and Eq. 36)	Final state
E_f / E_F	Fermi energy
E_g	Ground state
E_{kin}	Kinetic Energy
E_n	Intermediate state
Eq.	Equation
ESI	Electronic supplementary information
et al.	Et alia (*latin:* and others)
etc.	Et cetera (*latin:* and the rest)
EXAFS	Extended X-ray absorption fine structure
f (Eq. 21 and Eq. 22)	Final state
FD	Full dropout
FEL	Free electron laser
FFT	Fast Fourier Transform
Fig.	Figure
$F_j(k)$	Backscattering amplitude
FMS	Full Multiple Scattering
FTIR	Fourier transform infrared spectroscopy
FWHM	Full width half maxima
g	Gerade (*german*: even)
GC	Gas chromatography
h	Planck's constant (6.6260755 10^{-34} J s)
HERFD	High energy resolution fluorescence detected
HOMO	Highest occupied molecular orbital
HS	High-spin
$\hbar\omega$	Photon energy
i	Absorbing atom
i (Eq. 21 and Eq. 22)	Initial state
I(E)	Incident energy
i. e.	Id est (*latin:* that is)
$I_0(E)$	Transmitted energy

I_0, I_1, I_2	Ionization chambers
ICP-OES	Inductive coupled plasma optical emission spectroscopy
IR	Infrared spectroscopy
J	Total angular momentum
j	Index for atomic shells
$j(k)$	Inelastic mean free path length
k	Wave vector
L	Azimuthal quantum number
LC(F)	Linear combination (fitting)
LS	Low-spin
LUMO	Lowest unoccupied molecular orbital
m	Electron mass
MFC	Mass flow controller
MOF	Metal-organic framework
MOFMS	MOF mediated synthesis
MS	Mass spectrometry
n	Counting parameter
N_{ind}	Number of independent points
N_j	Number of nearby atoms in j^{th} shell
NMR	Nuclear magnetic resonance
norm. abs.	Normalized absorption
norm. abs. deriv	Normalized absorption of the derivative
norm. int.	Normalized intensity
$\hat{0}$	Incoming transition operator
O_h	Octahedral point group
p	Electron momentum
P	Position of the inflection point
P2X	Power-to-X
PD	Partial dropout
PDF	Pair distribution function
PNO	Pyridine-*N*-oxide
PXRD	Powder XRD
QMS	Quadrupole mass spectrometry
R (EXAFS analysis)	Fit index
r / R	Radius

RDF	Radial distribution function
r_j	Distance of the absorbing atom in j^{th} shell
RWGS	Reverse water gas shift reaction
S	Spin quantum number
s.	See
SCF	Self Consistency Field
SD	Stoichiometric dropout
SI	Supplementary Information
$S_i(k)$	Amplitude attenuating factor; cf. A_{fac}
ST	Static conditions
T_d	Tetrahedral point group
TEM	Transmission electron microscopy
TFFD	Temperature and flow controlled full dropout
TG	Thermogravimetry
TOS	Time-on-stream
TPR	Temperature programmed reduction
u	Ungerade (*german*: odd)
U_{iso}	Thermal displacement parameter
VtC	Valence-to-core
wt%	Weight percent
XAFS	X-ray absorption fine structure
XANES	X-ray absorption near edge structure
XAS	X-ray absorption spectroscopy
XES	X-ray emission spectroscopy
XRD	X-ray diffraction
XRF	X-ray fluorescence spectroscopy
Z	Atomic number
Γ_f	Lifetime broadening of the final state
Γ_G	Core hole lifetime in Ni 1 *s* level
Γ_n	Lifetime broadening of the intermediate state
δ	Dirac unit pulse function
$\Delta\mu_0(E_0)$	Normalization factor
$\Delta\theta$	Darwin width
θ	Bragg angle
λ	Wavelength

ν	Frequency
σ	Photoelectric absorption cross-section
σ_j	Debye-Waller like factor
σ_{stat}	Static disorders
σ_{vib}	Vibrational disorders
$\chi(E)$	Isolated, normalized energy-dependent fine structure
$\chi(k)$	$\chi(E)$ transferred to wave vector k
Ψ_{out}	Outgoing spherical wave
ω	Incident energy
$\phi_i(k)$	Phase shift of the absorbing atom
$\phi_{ij}(k)$	Total phase shift
$\phi_j(k)$	Phase shift of the backscattering atom

14.2 List of Figures

14.3 List of Tables